UNITED KINGDOM · CHINA · MALAYSIA

Blasco Giménez, Ramón (1995) High performance sensorless vector control of induction motor drives. PhD thesis, University of Nottingham.

Access from the University of Nottingham repository:
http://eprints.nottingham.ac.uk/13038/1/360194.pdf

Copyright and reuse:

The Nottingham ePrints service makes this work by researchers of the University of Nottingham available open access under the following conditions.

- Copyright and all moral rights to the version of the paper presented here belong to the individual author(s) and/or other copyright owners.
- To the extent reasonable and practicable the material made available in Nottingham ePrints has been checked for eligibility before being made available.
- Copies of full items can be used for personal research or study, educational, or not-for-profit purposes without prior permission or charge provided that the authors, title and full bibliographic details are credited, a hyperlink and/or URL is given for the original metadata page and the content is not changed in any way.
- Quotations or similar reproductions must be sufficiently acknowledged.

Please see our full end user licence at:
http://eprints.nottingham.ac.uk/end_user_agreement.pdf

A note on versions:

The version presented here may differ from the published version or from the version of record. If you wish to cite this item you are advised to consult the publisher's version. Please see the repository url above for details on accessing the published version and note that access may require a subscription.

For more information, please contact eprints@nottingham.ac.uk

High Performance Sensorless Vector Control of Induction Motor Drives

by **Ramón Blasco Giménez**

Thesis submitted to the University of Nottingham
for the degree of Doctor of Philosophy, December 1995

Salimos de la ignorancia y llegamos así nuevamente a la ignorancia, pero a una ignorancia mas rica, mas compleja, hecha de pequeñas e infinitas sabidurías.

Ernesto Sábato

... pero aun así, ignorancia.

Acknowledgements

I would like to express my most sincere gratitude to my supervisors, Dr. G.M. Asher and Dr. M. Sumner, for their guidance and support over the course of this project.

I would also like to thank Dr. J.C. Clare for his help on the design of the interface to the inverter, Dr. K.J. Bradley for his proofreading of part of Chapter 5 and Dr. M. Woolfson for his valuable comments on the signal processing aspects of this project and for the proofreading of Chapter 5.

Finally I would like to thank my friends and colleagues, especially R. Cárdenas, R. Peña and J. Cilia, for many useful comments and for their emotional support over the last three years.

Contents

List of Figures

List of Tables

Abstract

The aim of this research project was to develop a vector controlled induction motor drive operating without a speed or position sensor but having a dynamic performance comparable to a sensored vector drive. The methodology was to detect the motor speed from the machine rotor slot harmonics using digital signal processing and to use this signal to tune a speed estimator and thus reduce or eliminate the estimator's sensitivity to parameter variations. Derivation of a speed signal from the rotor slot harmonics using a Discrete Fourier Transform-based algorithm has yielded highly accurate and robust speed signals above machine frequencies of about 2 Hz and independent of machine loads. The detection, which has been carried out using an Intel i860 processor in parallel with the main vector controller, has been found to give predictable and consistent results during speed transient conditions. The speed signal obtained from the rotor slot harmonics has been used to tune a Model Reference Adaptive speed and flux observer, with the resulting sensorless drive operating to steady state speed accuracies down to 0.02 rpm above 2 Hz (i.e. 60 rpm for the 4 pole machine). A significant aspect of the research has been the mathematical derivation of the speed bandwidth limitations for both sensored and sensorless drives, thus allowing for quantitative comparison of their dynamic performance. It has been found that the speed bandwidth limitation for sensorless drives depends on the accuracy to which the machine parameters are known and that for maximum dynamic performance it is necessary to tune the flux and speed estimator against variations in stator resistance in addition to the tuning mechanism deriving from the DFT speed detector. New dynamic stator resistance tuning algorithms have been implemented. The resulting sensorless drive has been found to have a speed bandwidth equivalent to sensored drives fitted with medium resolution encoders (i.e. about 500 ppr), and a zero speed accuracy of ±8 rpm under speed control. These specifications are superior to any reported in the research literature.

Chapter 1 Introduction

1.1 Vector Control of Induction Machines

About fifty years elapsed from Faraday's initial discovery of electro-magnetic induction in 1831 to the development of the first induction machine by Nikola Tesla in 1888. He succeeded, after many years, at developing an electrical machine that did not require brushes for its operation. This development marked a revolution in electrical engineering and gave a decisive impulse to widespread use of polyphase generation and distribution systems. Moreover, the choice of present mains frequency (60 Hz in the USA and 50 Hz in Europe) was established in the late 19th century because Tesla found it suitable for his induction motors, and at the same time, 60 Hz was found to produce no flickering when used for lighting applications. Nowadays more than 60% of all the electrical energy generated in the world is used by cage induction motors. Nevertheless induction machines (and AC machines in general) have been mostly used at fixed speed for more than a century. On the other hand, DC machines have been used for variable speed applications using the Ward-Leonard configuration. This however requires 3 machines (2 DC machines and an induction motor) and is therefore bulky, expensive and requires careful maintenance.

With the arrival of power electronics, new impulse was given to variable speed applications of both DC and AC machines. The former typically use thyristor controlled rectifiers to provide high performance torque, speed and flux control. Variable speed IM drives use mainly PWM techniques to generate a polyphase supply of a given frequency. Most of these induction motor drives are based on keeping a constant voltage/frequency (V/f) ratio in order to maintain a constant flux in the machine. Although the control of V/f drives is relatively simple, the torque and flux dynamic performance is extremely poor. As a consequence, a great quantity of industrial applications that require good torque, speed or position control still use DC machines. The advantages of induction machines are clear in terms of robustness and price; however it was not until the development and implementation of field oriented control that induction machines were able to compete with DC machines in high performance applications. The principle behind field oriented control is that the machine flux and torque are controlled independently, in a similar fashion to a separately exited DC machine. Instantaneous stator currents are ''transformed'' to a rotating reference frame aligned with the rotor, stator or air-gap flux vectors, to produce a d axis component of current (flux producing) and a q axis component of current (torque producing). The basic field orientation theory is covered in Appendix 1.

The principle of field orientation for high performance control of machines was developed in Germany in the late sixties and early seventies [38, 6]. Two possible methods for achieving field orientation were identified. Blaschke [6] used Hall sensors mounted in the air gap to measure the machine flux, and therefore obtain the flux magnitude and flux angle for field orientation. Field orientation achieved by direct measurement of the flux is termed Direct Flux Orientation (DFO). On the other hand Hasse [38] achieved flux orientation by imposing a slip frequency derived from the rotor dynamic equations so as to ensure field orientation. This alternative, consisting of forcing field orientation in the machine, is known as Indirect Field Orientation (IFO). IFO has been generally preferred to DFO implementations which use Hall probes; the reason being that DFO requires a specially modified machine and moreover the fragility of the Hall sensors detracts the inherent robustness of an induction machine.

The operation of IFO requires correct alignment of the dq reference frame with the rotor flux vector. This needs an accurate knowledge of the machine rotor time constant T_r. However T_r will change during motor operation due to temperature and flux changes. On-line identification of the secondary time constant for calculation of the correct slip frequency in Indirect Rotor Flux Orientation is essential and has been addressed by different researchers [34, 84, 43, 3, 27, 64, 19, 18, 26, 53, 17, 71], thus providing a means of adapting T_r during the normal operation of the drive. An IRFO drive with on-line tuning of T_r can provide better torque and speed dynamics than a typical DC drive.

1.2 Vector Control without Speed or Position Transducers

The use of vector controlled induction motor drives provides several advantages over DC machines in terms of robustness, size, lack of brushes, and reduced cost and maintenance. However the typical IRFO induction motor drive requires the use of an accurate shaft encoder for correct operation. The use of this encoder implies additional electronics, extra wiring, extra space and careful mounting which detracts from the inherent robustness of cage induction motors. Moreover at low powers (2 to 5 kW) the cost of the sensor is about the same as the motor. Even at 50 kW, it can still be between 20 to 30% of the machine cost. Therefore there has been great interest in the research community in developing a high performance induction motor drive that does not require a speed or position transducer for its operation.

Some kind of speed estimation is required for high performance motor drives, in order to perform speed control. Speed estimation from terminal quantities can be obtained either by exploiting magnetic saliencies in the machine or by using a machine model. Speed estimation using magnetic saliencies, such as rotor slotting [31], rotor asymmetries [42] or variations on the leakage reactance [47], is independent of machine parameters and can be considered a true speed measurement. Some of these methods require specially modified machines [47] and the injection of disturbance signals [47, 42]. Generally, these techniques cannot be used directly as speed feedback signal for high performance speed control, because they present relative large measurement delays or because they can only be used within a reduced range of frequencies.

Alternatively, speed information can be obtained by using a machine model fed by stator quantities. These include the use of simple open loop speed calculators [87, 36], Model Reference Adaptive Systems (MRAS) [46, 89, 81, 56, 89] and Extended Kalman Filters [74]. All of these methods are parameter dependent, therefore parameter errors can degrade speed holding characteristics. It will be shown in this thesis that in some cases parameter errors can also cause dynamic oscillations. However these systems provide fast speed estimation, suitable for direct use for speed feedback.

It must be remembered that a high performance inner torque control loop is also required. The inner torque loop can be obtained by utilising Indirect Field Orientation using the rotor speed estimate from an MRAS [82, 72, 67] instead of the measured speed. However the use of a speed estimate for both speed control and for IFO makes the torque control loop sensitive to parameter errors in the MRAS speed estimator. A second option is to use a DFO inner loop whereby flux is measured using Hall probes [6], end windings [62] or tapped stator windings [90]. Clearly this demands the use of a modified machine and is unacceptable to drive manufacturers. Other strategies are only applicable to a particular machine configuration, like the use of the 3rd harmonic of the phase voltage to obtain the flux angle [54, 68] in star connected machines.

A third option is to derive the machine flux from a motor model, e.g. integration of the back e.m.f. [87, 36]; flux observers [55, 46, 89, 81, 56, 89]; the use of Extended Kalman Filters [3, 40, 15, 51, 60], Extended Luenberger Observers [27] and monitoring local saturation effects [74]. This broadens the definition of Direct Field Orientation to cover not only the methods of flux orientation that use a direct measurement of the flux, but also those that use a flux estimate for field orientation. There are benefits and disadvantages to each of these techniques of flux estimation and these will be presented and discussed. It should be noted that alternative inner torque control techniques such as Direct Self Control (DSC) [25] and Direct Torque Control (DTC) [36] inherently have similar features as DFO and these will also be covered in this thesis.

1.3 Parameter Adaption

The different methods of speed and flux estimation needed for sensorless vector control drives are model based and sensitive to the machine parameters; they require an *a priori* knowledge of the motor's electrical (and in some cases mechanical) characteristics. Therefore a sensorless vector control drive is more sensitive to machine parameters than a field oriented drive using a speed or position transducer. Hence it may be expected that the torque and/or speed dynamic performance of a sensorless vector control would be reduced with respect to that of a sensored vector control.

It is possible to measure the different parameters of the induction machine at stand still, and even tune the speed and current controllers accordingly [85, 49, 79, 78, 43, 52, 84, 28]. However, the parameters of the machine change during normal operation. For instance, stator and rotor resistances will vary due to thermal changes, the different inductive parameters are strongly dependent on the flux level in the machine and the leakage coefficient changes both with flux and load. Therefore some kind of parameter adaption is required in order to obtain a high performance sensorless vector control drive.

Identification of the rotor time constant T_r is of particular importance, because it will change during normal operation. Several methods of T_r identification have been proposed for speed sensored vector control applications [34, 84, 43, 3, 17, 27, 64]. However these methods are not easily applicable to the sensorless case since the machine slip ω_{sl} and T_r cannot be separately observed in the sinusoidal steady state [84, 27]. It is possible to estimate T_r from terminal quantities by superimposing a high frequency sinusoidal disturbance to the flux producing current (i_{sd}) of a vector controlled drive [55]. However effective identification implies the injection of disturbances of a relatively large amplitude, increasing therefore torque ripple and machine losses.

If an independent speed measurement is available, the value of the rotor time constant can be independently observed from stator terminals without injecting disturbance signals. Such independent speed measurement can be obtained by analyzing the rotor slot harmonics present in the line current of the induction machine.

A good knowledge of the stator resistance R_s is also important, since it determines the performance of the motor drive at low speed. In addition it will be shown in this thesis that R_s affects the dynamic performance of the sensorless drive presented in this work, moreover it will be shown that errors in the stator resistance estimate can eventually induce instability. Several methods of R_s estimation applicable to sensorless drives have been proposed based either on a steady state machine model [83] or using a Model Reference Adaptive System [89]. However these methods rely on an accurate knowledge of the remaining machine parameters and therefore the stator resistance estimate will exhibit errors if the other machine parameters are not accurately known. An alternative method of estimating the stator resistance that is independent of other machine parameters is presented in this thesis.

1.4 Speed Measurement using Rotor Slot Harmonics

The use of an independent speed measurement is not only desirable for on line adaption of T_r but what is more important, it can drastically improve the speed regulation and torque holding capabilities of the whole drive. It is a well known fact that the rotor slotting of the induction machine produces speed dependent harmonics in the line current. Therefore the machine rotational velocity can be obtained from these harmonics. The rotor slot harmonics are several orders of magnitude smaller than the fundamental component of the line current. In this respect, digital signal processing techniques are superior to analogue methods as will be shown in Chapter 5.

A reliable and accurate measurement of the rotor speed is obtained by estimating the line current spectrum using the Discrete Fourier Transform. The rotor slot harmonics are then identified from the estimated spectrum. Special attention has been paid to the robustness and accuracy of the proposed method. Obviously, if continual tuning of the rotor time constant is to be achieved, the speed detection from the rotor slot harmonics has to be performed on-line. Since the computation requirement for this process was not known, a specialised microprocessor was chosen in the form of a dedicated Digital Signal Processor (DSP). The DSP (an Intel i860) operates in parallel with the rest of the control hardware and provides continual speed updates. As far as the author is aware, the method presented is the first one to provide an on-line continual speed estimation from the rotor slot harmonics.

1.5 Project Objectives

The main aim of this research work is to implement and evaluate a high performance sensorless vector control drive. An MRAS flux and speed observer is employed to obtain flux and speed estimates needed to achieve field orientation and speed control. The torque and speed dynamic performance of such a sensorless system depends on the degree of accuracy by which the different parameters of the machine are known. A study to determine the extent up to which the different parameters affect the speed holding capability, speed dynamic performance and speed loop stability of the sensorless drive has been therefore carried out. It will be shown that the rotor time constant T_r is the most influential parameter regarding speed estimate accuracy and that an accurate knowledge of the stator resistance R_s is of paramount importance for attaining good speed loop bandwidths and for low speed operation. Therefore on-line adaption algorithms for stator resistance and rotor time constant are developed as a fundamental part of this work.

Speed measurement using the rotor slot harmonics present in the machine line current is employed to enhance speed regulation and at the same time obtain T_r adaption. Therefore an important part of this research is directed towards the development of and implementation of digital signal processing algorithms in order to obtain reliable and accurate speed information. These algorithms include the implementation of the Discrete Fourier Transform (DFT), the Short Time DFT (ST-DFT); the development of interpolation algorithms for high accuracy frequency measurement and the development of slot harmonic tracking algorithms. The advantages and limitations of this method of speed measurement will be fully discussed.

Finally the performance of both tuned and untuned sensorless systems are to be compared between themselves and with a speed sensored system. Obviously the term performance has to be defined in order to carry out the comparison between sensored and sensorless system. A comparison criteria is thus developed and used for such comparison.

Operation below base speed is assumed throught the project and the analysis and implementation of the proposed sensorless vector controlled drive for field weakening operation is considered as a topic for further study.

1.6 Thesis Overview

The present thesis is organized in the following way. Chapter 2 covers the practical hardware and software requirements and implementation. The control hardware consisting of a Transputer network and an Intel i860 processor is described in this chapter, as well as the different interfaces and power electronic components needed for the operation of the experimental rig. The guidelines for the software design are also covered in Chapter 2.

Chapter 3 presents a review of different methods of field orientation, discussing their suitability for sensorless operation. Several alternatives for flux and speed estimation are presented and discussed. In the view of the different alternatives, a particular sensorless technique (based on a MRAS) is chosen and used for the remain of the research work.

Chapter 4 covers the theoretical analysis of the effect of the different machine parameters on the stability and steady state speed accuracy of the proposed sensorless system. The influence of the machine parameters is studied by means of the small signal analysis of the closed loop sensorless system. The need for on-line identification of the rotor time constant and stator resistance derives from the results of this chapter.

There are two main alternatives of estimating T_r, one is to inject extra signals on the machine, and the other is to obtain an independent measurement of the rotor speed. The latter alternative has been chosen, and the procedures to obtain real-time rotor speed measurement from the rotor slot harmonics present in the line current are covered in Chapter 5. An all digital approach is presented in this chapter, as well as the discussion on the advantages and limitations of such a system. It will be shown that the proposed method is extremely accurate and therefore suitable for speed observer parameter tuning.

Chapter 6 covers the theoretical development and practical implementation of the rotor time constant and stator resistance tuning algorithms. The proposed T_r adaption mechanism ensures zero (or almost zero) steady state error on the estimated speed. The method of stator resistance estimation is completely independent of any other parameter, although speed transients through zero speed are required for its operation.

The effects of estimator parameter inaccuracies and the comparison of the proposed sensorless system with an Indirect Rotor Flux Orientation (IRFO) implementation are illustrated with experimental results in Chapter 7. The results shown in this chapter validate the theoretical results obtained in Chapter 4. Moreover, a criteria for the comparison of sensorless and sensored drives is derived.

Finally Chapter 8 includes the overall conclusions of this research work and highlights the direction of further research.

Chapter 2 Experimental Implementation

2.1 Introduction

This chapter describes the requirements and practical implementation of the different hardware and software components needed in order to proceed with the proposed investigation.

The criteria for selecting the components of the experimental system are:

- *Flexibility.* Different software and hardware modules are needed in order to investigate a variety of vector control strategies and signal processing routines. For this reason a transputer based control has been chosen, since transputer systems are extremely flexible and scalable [2].
- *Processing power.* The method of speed estimation proposed in Chapter 5 requires a great amount of computational power to be carried out in real time. This will normally involve dedicated hardware in form of a Digital Signal Processor (DSP). An alternative solution is the use of an INTEL i860 Vector Processor. The availability of the i860 in transputer compatible modules (TRAM) allows for an easy integration of the vector processor into the transputer network.
- *Realistic power level.* In order to obtain results that can be extrapolated to an ample range of induction machines, realistic power levels have to be used. On the other hand, an excessively large machine would increase drastically the hardware costs. A machine of 4 kW is chosen as a compromise. An IGBT inverter rated 10 kW will be used to drive the machine.

The following sections will explain in more detail the individual components of the experimental system.

Table 2.1 Parameters and characteristics of the induction machine

Frame	D112M	*Number of poles*	4
Rated speed	1420 rpm (50 Hz full load)	*Maximum speed*	3500 rpm
Rated i_{mrd}	2.2 A	*Rated* i_{sq}	4 A
Torque at rated i_{sq}	30.2 Nm		
No. of stator slots	36	*No. of rotor slots*	28
$R_s = 5.32\ \Omega$		$T_r = 0.168$ s	
$L_s = 0.64$ H		$L_0 = 0.6$ H	
$L_r = 0.633$ H		$\sigma = 0.11$	
$B = 0.02$ kgm^{2}s^{-1}		$J = 0.3$ kgm^2	

2.2 Motor Drive

2.2.1 Test Rig

The motor test rig consists of an ASEA closed slot squirrel cage induction machine rated at 4 kW and a corresponding DC dynamometer rated 10 kW in order to load it. The DC machine is controlled by a 4-quadrant DC converter. The DC drive provides a constant torque load throughout the whole speed range including stand still. The parameters and characteristics of the induction machine are listed in Table 2.1. Additionally, a separately powered fan has been fitted to the induction machine in order to provide forced cooling. Note the total inertia is several times bigger than that of the induction motor alone; this is due to the use of a rather old DC machine.

An incremental encoder providing 10000 pulses per revolution is fitted in order to provide a good position and speed resolution to verify the speed estimates obtained with the rotor slot harmonics and with the MRAC speed observer.

2.2.2 Power Electronics

The induction motor is fed using a commercial IGBT voltage fed inverter rated 10 kW. The inverter has been modified to allow for external PWM to be fed directly to the base drivers of the transistors. A dynamic braking unit, together with dynamic braking resistors, has been fitted in order to dissipate the energy generated by the induction motor during deceleration.

2.3 Control System Implementation

The practical implementation of the control system has been carried out in three stages. Firstly, all the required tasks were determined, then the procedures that can be carried out in parallel or pipelined were identified. Finally, the transputer network was designed and each task was assigned to the appropriate processor.

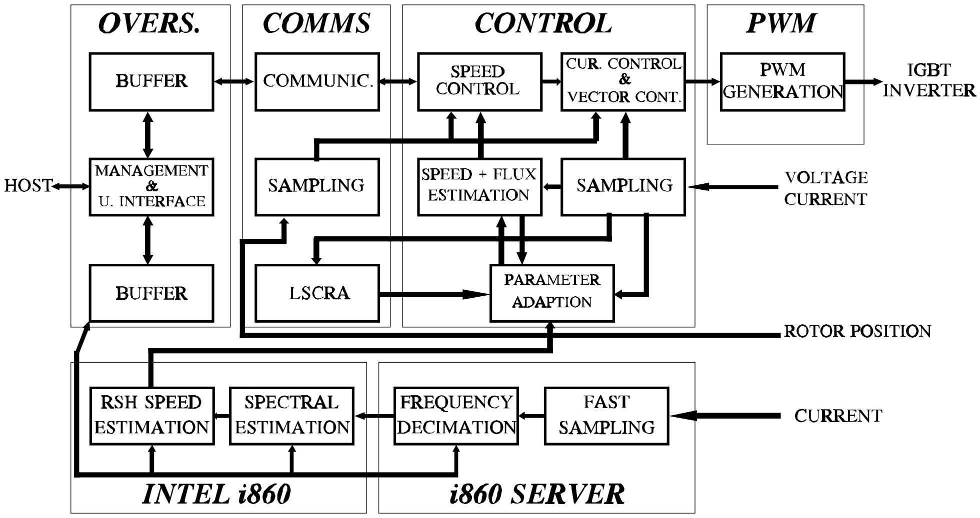

Figure 2.1 Allocation of the control procedures on the transputer network

2.3.1 Required Tasks

The block diagram of the induction motor drive control structure is shown in Fig. 2.1. The main tasks to be carried out in order to control the drive can be derived from this figure. These tasks are:

- *Signal measurement.* Acquisition of the signals to be used as inputs to the different control algorithms, to the signal processing algorithms and/or for validating purposes. The signals to be measured are two line voltages, two line currents and the rotor position.

- *Control calculations,* these provide the reference line voltages to be applied to the induction motor in order to achieve correct vector orientation.
- *Generation of actuation signals.* The voltage references from the control algorithms are processed to provide the correct switching signals for an IGBT voltage source inverter.
- *Observer based speed and flux estimation.* A fast speed estimation will be obtained from an observer based speed estimator using a motor model. At the same time flux estimation will be obtained in order to allow for Direct Field Orientation (DFO) vector control.
- *Speed measurement using Rotor Slot Harmonics (RSH).* Speed measurement will be extracted at the same time from the slot harmonics present in the line current.
- *Parameter identification.* On-line identification of the motor parameters will allow tuning of the motor model speed observer, in order to obtain a better performance.
- *Management and user interface.* Such a research drive also requires an efficient user interface, allowing on-line change of a wide range of parameters, real-time data capture of the most important variables and graphical representation of these variables, as well as performing the overall management of the system.

2.3.2 Task Classification

It is convenient to separate the above tasks in time-critical, time dependent and general non time dependent tasks.

- *Time critical tasks* are those that have to be carried out precisely at a particular instant of time, e.g. signal measurement and PWM generation.
- *Time dependent tasks* are those that do not need to be carried out at a particular instant of time, but their outputs are needed for time-critical tasks. Therefore their maximum execution time will be limited by the amount of time at which time-critical tasks need to be repeated. Time dependent tasks will be the PWM calculation algorithms, control calculations, parameter identification and observer based speed estimation.
- *Non time dependent tasks* will therefore be data acquisition and user interface, on-line change of parameters, diagnostics and RSH detection (as they are not used for the direct control of the induction machine). The amount of time allowed for procedure execution is in general different depending on the task.

Some of the previously described tasks can be carried out in parallel, while some others need to be performed sequentially. The latter is the case of the control algorithms. Firstly, the measured and reference quantities have to be provided to initiate the control loop. Then, the control algorithms generate several voltage references which in turn are used to generate the PWM switching times. However, these inherently sequential procedures can be easily pipelined onto different processors. This will reduce the overall computation time, and more importantly, will split the vector control task into different procedures as an entity in their own right. Therefore the vector control algorithm is divided into a pure control task and a PWM generation task. On the other hand, pipelining introduces a delay between the calculation of the voltage references and the actual control action.

Tasks that can be carried out in parallel with the vector control procedure are the observer based speed estimation using a motor model, parameter estimation, RSH based speed measurement, management and user interface.

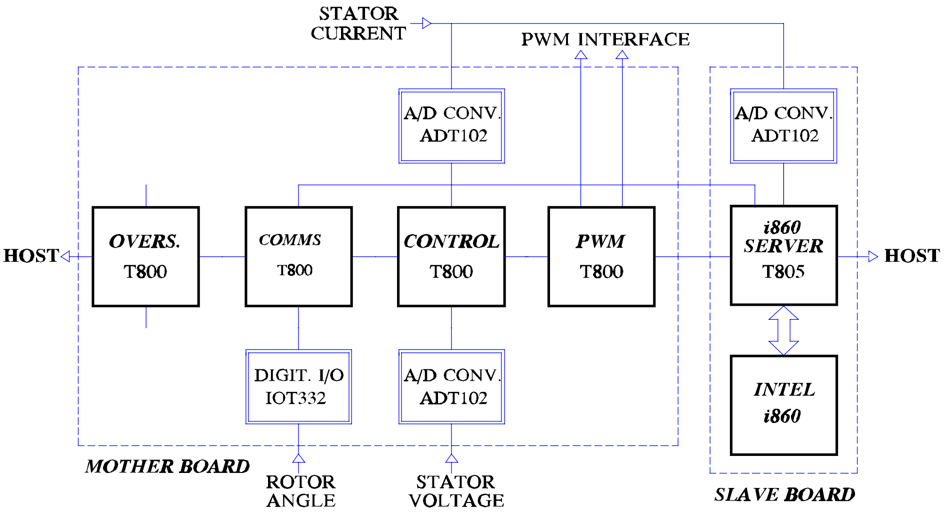

Figure 2.2 Layout of the transputer network

2.3.3 Task Allocation

There is a variety of techniques to realize the above tasks and therefore a very high degree of software and hardware flexibility is required from the control processor network. This inevitably implies the choice of processors of higher capacity than the required for a commercial application. This system has been implemented using four T800 transputers and one TTM110-i860 TRAM. The layout of the network can be seen in Fig. 2.2. Each one of the main tasks has been assigned to a different transputer as follows. A detailed description of the different software procedures running on each transputer is covered in Appendix 5.

- **PWM** *transputer*. The transputer labelled **PWM** generates the switching pattern that will be fed through the appropriate interfacing to the gate drivers of the IGBT inverter. This transputer receives the desired voltage reference from the **CONTROL** transputer. The voltage reference consists of two quadrature voltages (V_d, V_q) and the angle of the voltage phasor V_d (V_q is in quadrature to this angle). In a field oriented drive the angle of V_d corresponds to the flux angle, since V_d is aligned to the field phasor. The **PWM** transputer calculates the adequate switching patterns and sends then via two transputer links to the PWM interface (see Section 2.4.1). The transputer calculates the timing signals using regular asymmetric PWM. Due to the nature of this PWM strategy, two switching patterns must be calculated for each switching period [80]. Switching frequencies of 5 kHz are perfectly attainable with IGBT inverters. For a 5 kHz switching frequency, the switching period is 200 µs. Therefore, the maximum time available for the PWM calculations is 100 µs. Communications with the **CONTROL** transputer and with the interface circuitry to the IGBT gate drivers take a significant amount of the available processing time (16 µs). The use of look-up tables for sine and cosine operations is necessary since real time calculation of these functions would take longer than the time available for PWM generation. The total processing time for the PWM generation was found to be 74 µs including the 16 µs spent on communications.

  This transputer is also being used to generate the synchronising signals for the IGBT inverter and the current and vector control routines, carried out by the **CONTROL** transputer. In this particular software implementation, the time available for the current control and vector control routines is the same as the one for PWM calculation. This implies a 100 µs time slot for the execution of all of the procedures in the **CONTROL** transputer. Considering that communication time in the **CONTROL** transputer is about 35 µs, only 65 µs are available for the control calculations. Although it is possible to implement a sensorless vector control system on a transputer system within 65 µs, all the routines have to be optimised for speed. Therefore the use of a 100 µs time slot introduces unnecessary burden in the software development. Hence a longer time slot of 500 µs has been chosen for both control and PWM calculations. This time slot implies a switching frequency of 1 kHz. A possible alternative to reducing the switching frequency is the use of different sampling times for control and PWM calculations. This solution was not considered necessary, since a switching frequency of 1 kHz is considered adequate for the purposes of this research. The reduced switching frequency also contributes to reduce the possible adverse effects of the interlock delay (see Section 2.4.2).

- **CONTROL** *transputer*. Measurement of voltages and currents, current, speed and vector control loops, parameter estimation and model-based speed estimation procedures are allocated on the transputer labelled **CONTROL**.

  The A/D conversion of the analogue magnitudes is carried out by two SUNNYSIDE Adt102 TRAMs. This module has been chosen due to the simplicity to interface it to a transputer network, and to its high conversion speed.

  The flux and speed estimation procedure provides fast speed and flux estimates. However, both estimates depend on the different parameters of the machine. Therefore, there is another procedure running in parallel with the speed estimator to correct the deviation suffered by the different motor parameters.

  The vector orientation algorithms and the current control loops must be executed twice each switching cycle. The speed and flux estimation procedures are also carried out at the same frequency, since it makes its integration in the vector control routines easier. Therefore the basic time slot in which these routines have to be performed is 500 μs. However, the speed control can be much slower. This is because the speed response is mainly dominated by the inertia of the mechanical load. Therefore the speed loop sampling times are chosen between 5 and 20 ms. The routines to identify the different electrical parameters of the motor can be even slower, if only thermal effects are considered. It is worth remarking that most of the processing time available in this transputer is being used.

- **COMMS** *transputer*. To provide high flexibility, another transputer is connected between the **CONTROL** and **OVERSEER** transputers. This transputer will carry out the speed measurement from the shaft encoder, via a SUNNYSIDE Iot332 digital I/O TRAM. This transputer is also used for the communications between the **CONTROL** and **OVERSEER** transputers. This will not make full use of the capabilities of a T800 transputer and substantial quantity of processing time is available. Therefore simple signal processing routines are implemented on this transputer, i.e. the Least Squares Circular Regression Algorithm (LSCRA) described in Section 6.3.3.

- **OVERSEER** *transputer*. Diagnostic and user interface routines are implemented on the transputer labelled **OVERSEER**. This provides data capture facilities, on-line change of variables and decoding of the commands from the host. It will also implement the management routines of the overall system. This transputer also provides the necessary buffering of the data flowing to or from the host. The buffering consists of two procedures working in parallel. One of these procedures communicates to the transputer network, and the other one communicates to the host. Normally the transputer procedure will fill the buffer with data, and the host procedure will read from the buffer. In this way the transputer network can write to the buffer synchronously every 500 μs and the host can read from this buffer asynchronously without disturbing the operation of the transputer network. This system provides the possibility of on-line monitoring of up to eight different control variables.

- **i860 SERVER**. The transputer labelled **i860 SERVER** is on the same board as the INTEL i860. This transputer is memory mapped to the INTEL i860 and will perform all the auxiliary functions to ensure a correct operation of the vector processor routines. This includes:
  - all the procedures to control the interfacing with the i860,
  - sampling of the line current,
  - prefiltering of this current and frequency decimation, to obtain different sampling frequencies from a constant hardware sampling frequency.
  - interfacing with the rest of the network.

  Most of the computational power of this transputer will be used, since the sampling frequency has to be kept relatively high (5 to 10 KHz) in order to obtain a representation of the input signal with good frequency resolution.

- **i860** *vector processor*. As stated in the introduction, the **i860** vector processor will be dedicated to the signal processing routines. All of them will be separate processes running in parallel with the vector control drive. They will comprise windowing, fast fourier transform (FFT), power spectral density (PSD) calculation and rotor slot harmonic tracking algorithm.

2.3.4 Communications

It is worth noting that the amount of data flowing between procedures is very high. Therefore great attention has to be paid to the communication between tasks. In particular each procedure has to be synchronised with each other without disturbing their normal operation. It would never be acceptable if the PWM modulator has to stop because the **OVERSEER** is demanding the value of a particular variable.

Communications can be divided in three groups, those that are used for synchronising the different time-critical tasks, those that send reference values between time dependent tasks and those that carry information from or to the user (via overseeing transputer). The presence of several tasks working at different frequencies, and even asynchronously, makes necessary the design of routines to interface and buffer the signals from and to the different processes. Although serial links with a speed of 20 Mbit/s were used, the interprocessor communication time was found to be a significant proportion of the overall computation time. For instance, the communication time of the **PWM** transputer is 22 percent of the total execution time. Conversion of 32-bit floating point quantities into 16-bit integers for communication, does not make a significant difference, because of the overhead time required to convert and normalize the numbers. This highlights the only possible weakness of the use of transputers in real-time control applications. As more powerful floating point processors contribute to reduce the computation time, communication overheads start being more and more important. Such a problem does not exist with the communications between the i860 and the T805 on the same board, since the bulk of the input and output data is memory mapped into several buffers.

2.3.5 Reliability

Real time control systems require a high degree of reliability. In this particular case, a software or hardware failure could easily led to the destruction of very expensive equipment (especially the IGBT inverter). Such failures will just be unacceptable in an industrial application. The most common failure in a transputer network is deadlock, which occurs when a particular routine is waiting indefinitely to communicate with another procedure. This causes the programs that depend on the first routine to stop as well when they try to communicate with the first stopped procedure. Eventually all of the procedures running in parallel that depend on each other will stop. The initial communication failure can be caused by a hardware error or by wrong programming. The latter is particularly likely to occur in a research system, since the software will be probably changed several times every day. Hardware faults arise normally from electromagnetic interference on the transputer links. Electro-Magnetic Interference (EMI) could cause wrong data being read or even serial link communication failure and deadlock. The most sensitive links are those that connect to external interfaces, since they are relatively long and they are not shielded by the main computer case.

Elaborated Fault-Tolerant measures [23], that would usually be applied to a commercial product, will not be adequate for this system, since they will complicate both hardware and software unnecessarily. However, some measures are required to reduce faults or minimise their effects. Firstly, all the external links will be as short as possible, using appropriate double twisted-pair cable and placed away from sources of EMI (such as hard-switched inverters). Twisted pair was found to be sufficient, although differential and optical links could be used if necessary. Secondly, a hardware timer watch-dog is added to the protection already available in the inverter (such as overcurrent protection). When the transputer network fails to send a new switching pattern in a predetermined period of time, the IGBT inverter is disabled. This will provide protection against deadlock caused either by a hardware or software fault. These measures, although simple and easy to implement, have been proved very efficient, even at baud rates of 20 Mbit/s.

2.4 Interfaces

The transputer network communicates with the outside world by using transputer links. Each transputer has four serial bidirectional links that can be connected to another transputer, to specialised hardware, or to link adapters. The link adapters can convert the serial data from the link into parallel format suitable for use by a wide range of hardware. The signals flowing in and out the transputer links are unsuitable for direct connection to the IGBT inverter. Also, the analog signals need to be low pass filtered against noise and aliasing before the analog to digital conversion stage. Moreover, additional protections were built to prevent damage of the IGBT inverter. Therefore different interface circuits were designed to overcome these problems. The block diagram of the different interface circuits is shown in Fig 2.3. The diagrams of these interface boards are shown in Appendix 2.

2.4.1 PWM Counter Circuit

The **PWM** transputer generates the switching times of each inverter leg. However, these switching times need to be converted to the appropriate PWM pattern before they can be sent to the IGBT inverter. In order to do that, this interface circuit is built around an 8254 counter/timer. The 8254 provides three separate counters,

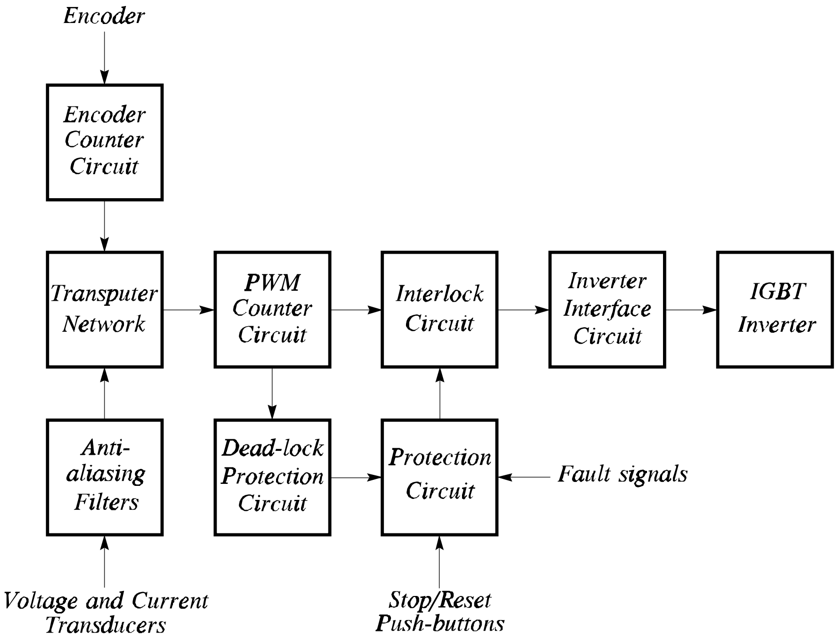

Figure 2.3 Block diagram of the different interface circuits

allowing for the three phase PWM patterns to be generated in one chip.

The 8254 is designed for direct connection to an 8-bit parallel bus. On the other hand, the transputer links use serial communication. Therefore two C011 link adapters have been used, in order to convert the serial data from the transputer into parallel data suitable for the 8254. One link adapter provides the data bus, and the other will generate the control signals. Hence two transputer links are required in order to interface with this board.

The 8254 is used in monostable mode, i.e. the output of each counter is normally high. When it is triggered, the output will become low, and the counter will start decrementing the preset counting value. When this value becomes zero, the output of the counter returns to its original high state. Three different counting values will be generated by the **PWM** transputer for each switching cycle, one for each phase. Normally, the three counters will be triggered at the same time. Extra circuitry is needed in order to provide high to low pulses, as well as the low to high pulses that the 8254 generates by default. The extra circuitry consists of three XOR gates, with one of their inputs connected to the 8254 output, and the other to the transputer network, via the control link adapter. These gates are used as programmable inverters. In order to synchronize the change on both inputs of the XOR gates, three latches have been added. Typical waveforms for one phase are shown in fig. 2.4.

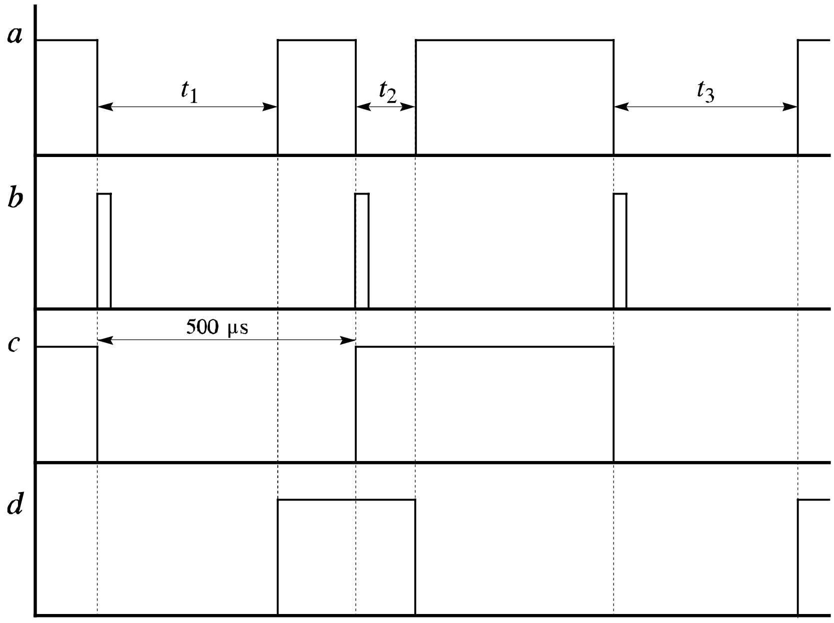

Figure 2.4 Typical waveforms of the PWM counter circuit. *a*) 8256 counter output, *b*) Trigger pulses, *c*) Inverting signal at the XOR gate input, *d*) PWM output

In this figure t_1, t_2, t_3 correspond to the timing values calculated by the **PWM** transputer.

The clock frequency used for the 8254 is 5 MHz. This provides a minimum timing of 400 ns, with a resolution of 200 ns. The 5 MHz oscillator is also used to provide an appropriate clock signal for the link adapters.

2.4.2 Interlock Circuit

Signals for the up and lower transistor of each leg must be generated from the three PWM signals provided by the previous circuit. A simple inversion of the PWM signal for the bottom transistor is not a good solution. Since the IGBT's do not switch off instantaneously, one of the transistors would still be on when the other is being turned on. Therefore a short circuit would occur, leading to a very fast increase in current through both transistors and to possible damage of the device. This effect is known as shoot-through. In order to avoid shoot-through, a mechanism preventing both transistors being on at the same time is required. This mechanism consists on delaying the turning on of the IGBT until the other IGBT is completely off. This delay is known as interlock delay. This is shown in Fig 2.5. The IGBT modules used in the inverter have a typical turn-off time of 2 μs, therefore an interlock delay t_i of 5 μs seems appropriate.

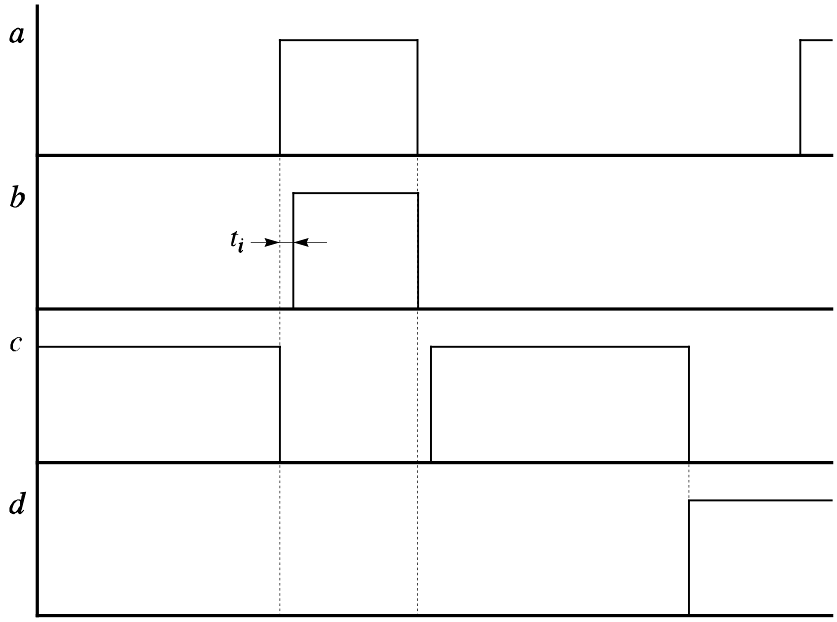

Figure 2.5 Typical waveforms of the interlock circuit. *a*) PWM, *b*) Top transistor gate signal, *c*) Bottom transistor gate signal, *d*) Shutdown signal

The circuit proposed is powered directly from the IGBT auxiliary 5 and 24 V supplies and provides the required optoisolation of the signals coming from the transputer network. The incoming PWM waveform is split into inverted and non-inverted signals for the upper and lower transistors, respectively. Then a delay is introduced in the positive edge of each of these signals, in order to retard the turning-on of the respective IGBT. The last transistor in the interlock circuit provides a low output impedance, needed for fast response. In order to provide a shutdown signal, an additional transistor is added. This transistor will pull both gate signals low when the shutdown signal is high.

The interlock delay must be easy to control, and at the same time has to be very accurate and with good repetitivity. In order to obtain these objectives, a 15 V precision power regulator and an accurate reference voltage are generated from the 24 V power supply, using a high quality, temperature compensated zener diode.

The interlock delay modifies the original PWM waveform, introducing a distortion on the obtained voltage. This distortion is proportional to the ratio t_i/T_s, where T_s is the overall switching time. Therefore the effect of the interlock delay can be reduced by decreasing t_i or by increasing T_s.

2.4.3 Inverter Interface Circuit

The inverter interface circuit adapts the signals generated by the interlock circuit for direct connection to the inverter gate driver optoisolators. Direct connection to the gate driver optoisolators permits the use of the inverter built-in gate drivers, greatly simplifying the hardware design. The interface circuit also provides pull down resistors, to keep the gate drives off when no PWM signal is present. Another feature of this circuit is that it allows selection of external or internal PWM. (Internal PWM is the one generated by the inverter itself). This permits normal (V/*f*) inverter operation without the need of any external source of PWM.

2.4.4 Protection Circuit

Any power electronics circuit requires adequate protection to prevent, as far as possible, damage to expensive power devices. Normal protections on AC inverters detect DC link overcurrent and overvoltage. Additional protections are DC link undervoltage, power supply loss and mains loss. The detection of a faulty condition will turn all the power devices off.

In this particular implementation, the PWM is generated externally and fed directly to the gate drivers. The ASIC that generates the inverter’s own PWM and provides the inverter built-in protection has been bypassed. Therefore an external protection circuit is required. On the other hand, the inverter will still produce the different fault signals. A shutdown signal that will turn-off all the IGBT’s is generated from these fault signals. All the fault signals are latched, and can only be reset by an external push-button.

Several LED’s are employed to indicate which fault actually triggered the protection circuit. A push-button generated fault, together with a reset button provide remote hardware on and off control of the drive. When the inverter is driven by internally generated PWM, it behaves like a standard inverter, and external protection is not necessary.

2.4.5 Dead-lock Protection Circuit

Dead-lock occurs in a transputer network when a transputer fails to send or receive a message to/from a channel (in our case, a channel is the same as a hardware link). This can be caused by a software error or by Electro-Magnetic Interference (EMI) on one of the external links.

Dead-lock will lead to immediate loss of the PWM signal. When this happens, the IGBT's will remain in the last switching pattern they received before dead-lock. This will not be a problem if a zero voltage vector was the last applied before dead-lock. However, if a non-zero voltage vector was the last applied, full DC link voltage will appear on the machine terminals, this will create a fast current build up, due to the relatively small stator resistance. Generally, an overcurrent fault will turn all the IGBT's off with no equipment damage

However, a dead-lock protection has being designed. This consists on a counter reset by the 8254 trigger signal. Since a trigger signal is required at the beginning of every switch period, the time between trigger signals will always constant and equal to the switching period (in our case 500 µs).

The eight bit counter is driven by a constant 0.5 MHz clock. If the trigger signal is received every 500 µs, the count will reach a maximum value of 250. However, if the delay between trigger signals is greater than 512 µs (because of dead-lock), the counter will reach a value of 255, and will generate a carry signal. This carry signal is then latched and used as a dead-lock fault signal, that is then fed to the protection circuit via an optoisolator.

2.4.6 Other Interface Circuits

Measurement of different magnitudes is required in order to control the induction machine and to verify the different results. These magnitudes are the machine line voltage and current, and the rotor position.

The line voltages are measured using two PSM voltage transposers, which provide an isolated signal proportional to the line voltage. They present a maximum voltage of 1000 V, an attenuation of 1:50 and a measurement bandwidth of 50 kHz. The line currents are measured using two LEM LA 50-S/SP1 hall effect transducers, with a measuring range of ±100 A and 1:2000 attenuation. These current transducers provide a maximum measuring bandwidth of 150 kHz.

The analog signals from the above transducers are buffered and low pass filtered to avoid aliasing problems in the analog to digital conversion stage. The antialiasing filters are second order Butterworth with a cut-off frequency of 600 Hz for the current and voltage measurements used for vector control, and speed and flux estimation. These signals are sampled at 2 kHz, therefore the 600 Hz cut-off frequency is adequate since it provides sufficient attenuation of frequencies above 1 kHz. The sampling frequency of the current measurement used for rotor slot harmonic identification is 5 kHz, therefore the corresponding antialiasing filter is also a second order Butterworth filter, but with a 1.5 kHz cut-off frequency.

The rotor position is measured using a 10000 pulses per revolution incremental encoder. The encoder provides three signals, the first one for clockwise pulses, the second for counter-clockwise pulses, and the third provides a single pulse per revolution (this is termed zero signal). The three lines are buffered using three line receivers. An absolute position signal is obtained by using 4-bit up/down counters. Therefore four of these counters are cascaded, allowing for a maximum count range from 0 to 65535, or from -32768 to +32767. The zero signal is used for resetting the counters, marking therefore the origin of the rotor position measurement. The counter outputs are connected through a latch to a parallel input/output TRAM, which is in turn connected to the transputer network.

2.5 Conclusions

The parallel implementation of the research test bed has been carried out by identifying all the necessary tasks and classifying them into time-critical, time-dependent and time-independent. Clearly the software design gives priority to time-critical procedures. The main tasks have been allocated to different transputers, and therefore executed in parallel. Some tasks have been pipelined, dividing the computational load between several processors. Pipelining will introduce extra delay. Of special importance is the delay between the calculation of control actions (stator voltage), and generation of the corresponding PWM patterns. Obviously, this delay is considered when designing the current loops.

The desired level of flexibility has been obtained, several control strategies can be selected on-line, at the same time speed and rotor flux estimation can be achieved and a number of signal processing routines can be carried out without disturbing the normal operation of the inverter motor drive. It is also possible to monitor interactively a considerable number of variables. This has been possible due to the modularisation of the tasks and to the choice of the appropriate software hierarchy.

Communication overheads have been found to be the only drawback of this multiprocessor approach. However they do not present a severe inconvenient, because of the amount of processing power left unused on each transputer. However this prevents the full use of the transputer processing capability.

The use of serial communication links in industrial environments is a cause of concern, especially when a transputer network is used in the proximity of hard switching electronic devices. However, if adequate twisted pair cables are used and prevented from running in parallel with power cables, a reliable communication with external circuitry is possible. In practice, reliable communication has been obtained for communication speeds up to 20 Mbit/s even though differential or optical line drivers and receivers are not being used.

It is emphasized that although a transputer implementation might be inadequate for a commercial product, it is very attractive for a research implementation, because it is very flexible and imposes almost no constraint in processing power (if more processing power is required, another transputer can always be added to the network).

Chapter 3 Sensorless Vector Control of Induction Machines

3.1 Introduction

The aim of this chapter is to review and select a configuration for the field orientation of induction motors that is suitable for a high performance sensorless drive. There are two basic ways of attaining field orientation: namely Direct and Indirect Field Orientation. Moreover, the synchronous reference frame can be aligned to stator, air gap or rotor flux. The behaviour of stator orientation and air gap orientation is very similar [41, 29], therefore only orientation on stator and rotor flux will be considered. Hence four basic implementations can be found: Indirect Rotor Field Orientation (IRFO), Direct Stator Field Orientation (DSFO), Direct Rotor Field Orientation (DRFO) and Indirect Stator Field Orientation (ISFO). Three of these four schemes have been practically implemented and compared in order to ascertain the relative merits of each implementation. An ISFO method has been modelled [30] but found to yield inferior results; it has therefore not been implemented and is not considered in this chapter.

Direct vector control implementations require flux estimation and this chapter also reviews several methods of attaining this. The characteristics of a particular vector control strategy depend on the frame of reference being used and on the use of either the stator or rotor dynamic equations for the purpose of field orientation. Hence the performance and parameter sensitivity of the relevant vector control implementations with respect to the use of either stator or rotor dynamic equations is discussed.

It is obvious that a vector control implementation without a rotor speed transducer needs some sort of speed estimation, at least for speed control. Several alternatives are reviewed, from simple open loop calculators to more complex systems such as Extended Kalman Filters (EKF), Extended Luenberger observers (ELO) and Model Reference Adaptive Systems (MRAS).

In conclusion, the chapter contains a discussion on the relative advantages and disadvantages of each system reviewed resulting in a decision on the scheme of field orientation to use for subsequent investigations.

3.2 Vector Control Implementations

3.2.1 Indirect Rotor Field Orientation (IRFO)

This method of field orientation was proposed as early as the late sixties [38], and is based on imposing the required slip into the machine so that rotor field orientation is forced. Using rotor flux and stator currents as state variables, and assuming a synchronous frame of reference aligned with the rotor flux ($\lambda_{rq} = 0$), we have (see App. 1)

$$v_{sd} = R_s i_{sd} + \sigma L_s p i_{sd} - \omega_e \sigma L_s i_{sq} + \frac{L_0}{L_r} p \lambda_{rd} \tag{3.1}$$

$$v_{sq} = R_s i_{sq} + \sigma L_s p i_{sq} + \omega_e \sigma L_s i_{sd} + \omega_e \frac{L_0}{L_r} \lambda_{rd} \tag{3.2}$$

$$\lambda_{rd} = \frac{L_0 i_{sd}}{1 + T_r p} \tag{3.3}$$

$$\omega_{sl} = \frac{L_0 R_r}{L_r \lambda_{rd}} i_{sq} \tag{3.4}$$

Considering operation below base speed at constant flux ($p\lambda_{rd} = 0$) the above equations simplify to

$$v_{sd} = R_s i_{sd} + \sigma L_s p i_{sd} - \omega_e \sigma L_s i_{sq} \tag{3.5}$$

$$v_{sq} = R_s i_{sq} + \sigma L_s p i_{sq} + \omega_e L_s i_{sd} \tag{3.6}$$

$$\lambda_{rd} = L_0 i_{sd} \tag{3.7}$$

$$\omega_{sl} = \frac{i_{sq}}{T_r i_{sd}} \tag{3.8}$$

Equation (3.8) provides an expression of the slip and can be used to force field orientation in the machine. The flux angle is obtained by integration of the electrical speed that in turn is obtained by adding the calculated slip and the measured rotor speed. This is shown in Fig. 3.1. This implementation uses fast current loops so the machine appears current fed and hence the stator dynamics can be neglected. Due to the high bandwidth of the current controllers, reference currents can be used instead of the measured ones for the calculation of the machine slip.

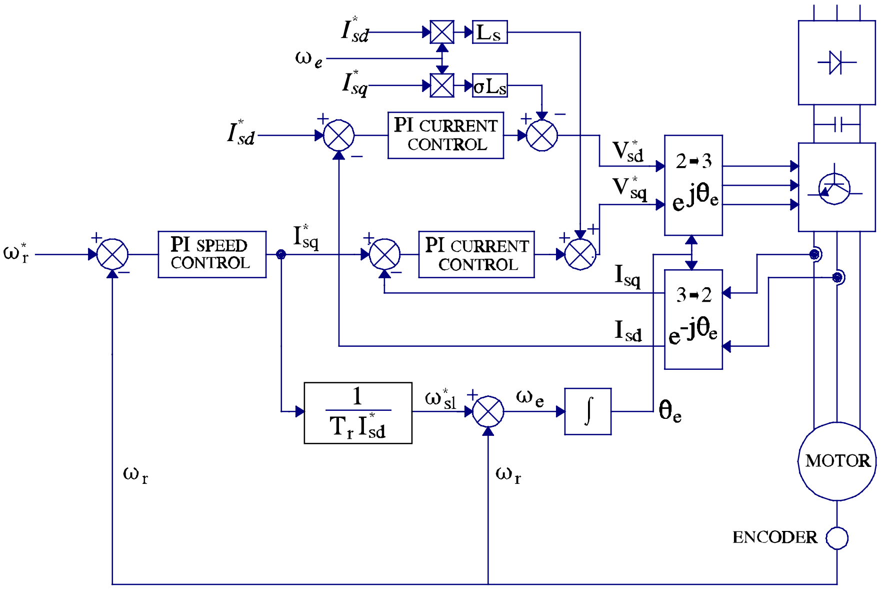

Figure 3.1 Indirect Rotor Flux Orientation Implementation

Correct field orientation is only dependent on the rotor time constant (T_r) and (3.3) shows that the rotor flux is independent of the q-axis current. Since simple techniques of T_r adaption have been devised [34] this method of field orientation can be considered very effective. Field orientation is kept regardless of the rotational speed of the machine and therefore IRFO can be used at standstill. This system provides a good torque response, due to the high bandwidth of the current controllers. Moreover, large changes of i_{sq} during transients will not affect the flux since there is a complete decoupling between i_{sq} and the rotor flux as seen from (3.7) and (3.8).

The performance of the IRFO implementation illustrated in Fig. 3.1 is shown in Figs. 3.2 to 3.4. Figure 3.2 depicts a speed reversal from 1000 rpm to -1000 rpm for the 4 kW machine whose parameters are given in Section 2.1. The constant deceleration rate is seen to be equal to the maximum limited torque (49 Nm) divided by the total inertia (0.3 kgm^{-2}) and verifies a good degree of field orientation.

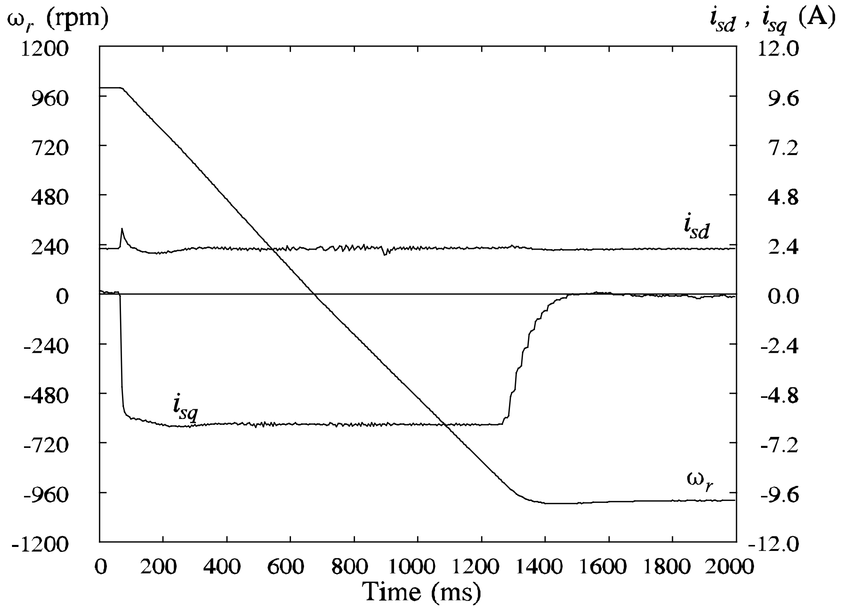

Figure 3.2 IRFO speed reversal

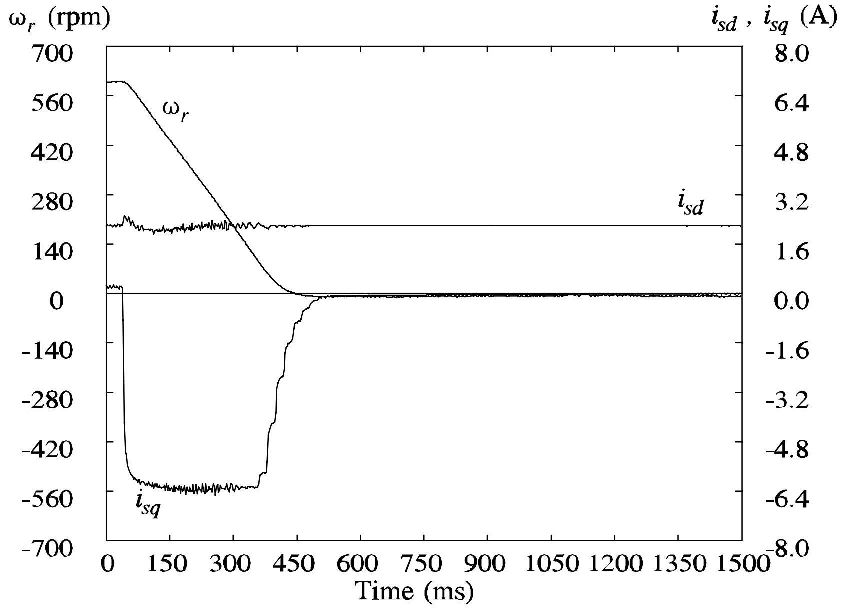

Figure 3.3 IRFO speed transient from 600 rpm to 0 rpm

Figure 3.3 illustrates the zero speed operation of the IRFO implementation in which there is a zero speed error in steady state. The high speed bandwidth attainable with this implementation is illustrated in Fig. 3.4. This figure shows a full load step

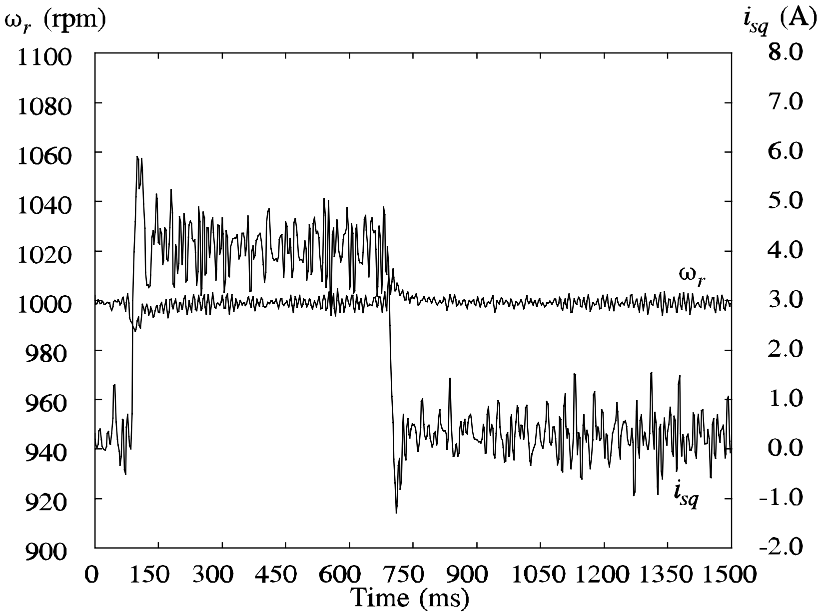

Figure 3.4 IRFO full load torque transient

transient at 1000 rpm and the maximum deviation from the preset speed is merely 10 rpm. The torque and speed in Fig. 3.4 are quite noisy due to the speed bandwidth being near its maximum limit. This is determined by speed encoder resolution. This limitation is discussed in Chapter 7 which compares the speed bandwidth performance of the sensored IRFO and the sensorless drive presented in this work.

However the performance of IRFO during field weakening is relatively poor [87]. When λ_{rd} is not constant the expression $\lambda_{rd} = L_0 i_{sd}$ is not longer true. Therefore the machine slip should be calculated using (3.4) rather than (3.8). In this situation field orientation does not only depend on T_r but also on L_0 and λ_{rd}. Since these three quantities vary greatly due to saturation effects [59], it is difficult to keep good field orientation during field weakening.

3.2.2 Direct Stator Field Orientation (DSFO)

The dynamic equations of the induction machine in a synchronous rotating frame aligned with the stator flux ($\lambda_{sq} = 0$) can be expressed as follows (see App. 1)

$$\begin{aligned} v_{sd} &= R_s i_{sd} + \frac{d}{dt}\lambda_{sd} \\ v_{sq} &= R_s i_{sq} + \omega_e \lambda_{sd} \end{aligned} \tag{3.9}$$

$$0 = (1 + T_r p)\lambda_{sd} - (L_s + \sigma L_s T_r p)\, i_{sd} + \omega_s \sigma L_s T_r i_{sq} \tag{3.10}$$

$$0 = -(L_s + \sigma L_s T_r p)\, i_{sq} - \omega_s \sigma L_s T_r i_{sd} + \omega_s T_r \lambda_{sd} \tag{3.11}$$

From (3.11) an expression to determine the slip frequency is derived

$$\omega_{sl} = \frac{(1 + \sigma T_r p) L_s i_{sq}}{T_r(\lambda_{sd} - \sigma L_s i_{sd})} \tag{3.12}$$

From (3.10) follows that the flux magnitude depends on both i_{sd} and i_{sq}. This is undesirable and a compensation term (i_{dq}) is calculated to decouple the flux from the torque producing current. Rearranging (3.10)

$$\lambda_{sd} = \frac{(1 + \sigma T_r p) L_s}{(1 + T_r p)} \left(i_{ds} - \frac{\sigma T_r \omega_s}{(1 + \sigma T_r p)} i_{sq} \right) \tag{3.13}$$

Hence

$$i_{dq} = \frac{\sigma T_r \omega_s}{(1 + \sigma T_r p)} i_{sq} \tag{3.14}$$

Substituting ω_s with its value from (3.12)

$$i_{dq} = \frac{\sigma L_s}{(\lambda_{sd} - \sigma L_s i_{sd})} i_{sq}^2 \tag{3.15}$$

The stator flux angle required for field orientation can be obtained from a direct measurement of the flux (using Hall probes [6], tapped windings [90], saturation effects [74], etc.) or by calculating the flux from the back e.m.f. of the machine [87]

$$\underline{\hat{\lambda}}_s = \int (\underline{v}_s - \hat{R}_s \underline{i}_s) dt \tag{3.16}$$

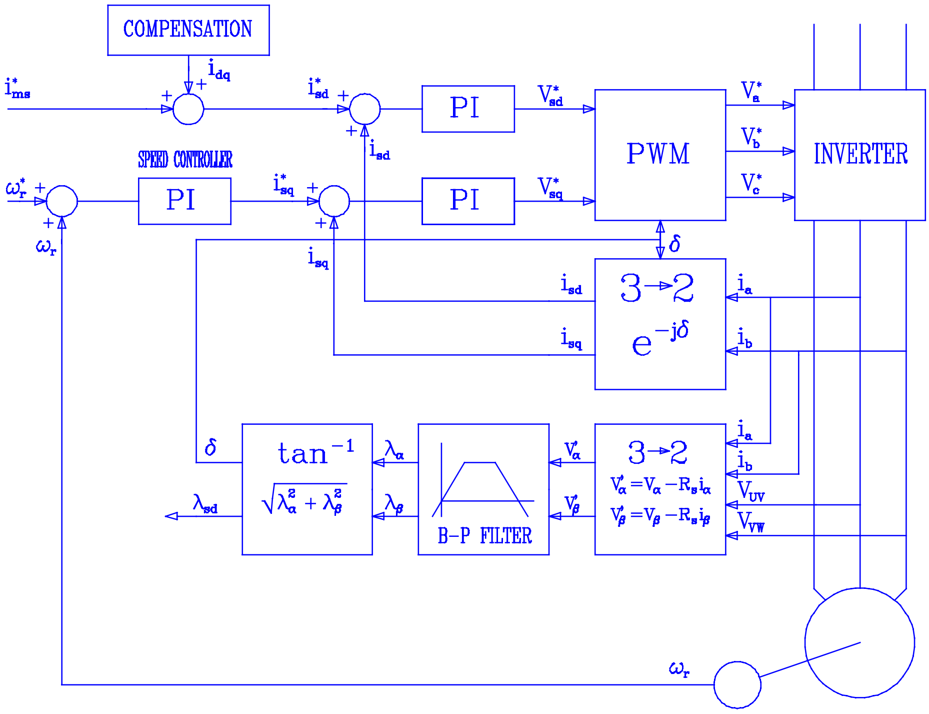

Figure 3.5 Basic Direct Stator Flux Orientation Scheme

A typical implementation of a DSFO drive is shown in Fig. 3.5. Note a band pass filter has been used instead of a pure integral, to avoid integrator drift problems. Therefore the DSFO implementation can only be used above a certain frequency which is slightly higher than the band pass filter cut-off frequency. Moreover flux orientation depends on the stator resistance R_s. The sensitivity to the stator resistance is frequency dependent; the voltage drop across R_s is negligible at high speed when compared with the back e.m.f. but at low speeds the term $R_s i_s$ will be of the same order of magnitude as the back e.m.f. Therefore good field orientation at low speed can only be achieved if the stator resistance is known with high accuracy. This is difficult to accomplish since R_s varies noticeably with temperature.

Note also the cross coupling term in the flux equation (3.13). This term causes the actual flux in the machine to drop when the magnitude of i_{sq} increases. In Fig. 3.5 a compensation term is added to the i_{sd} demand to cancel this cross coupling. However the practical cancellation of the cross-coupling term is difficult, since it requires a very accurate knowledge of all the magnitudes in (3.15). The presence of a i_{sq}^2 term makes the compensation extremely sensitive to errors in σL_s. For instance, for the 4 kW machine considered in this study, i_{sd} = 2.2 A and i_{sq} = 6 A during a speed transient. A 10% error on σL_s (typically 70 mH) would cause an error of 3.6 A in i_{sd}. The fact that σL_s is dependent on i_{sq}, especially in closed slot machines, contributes to exacerbate the sensitivity of the compensation term to changes in σL_s.

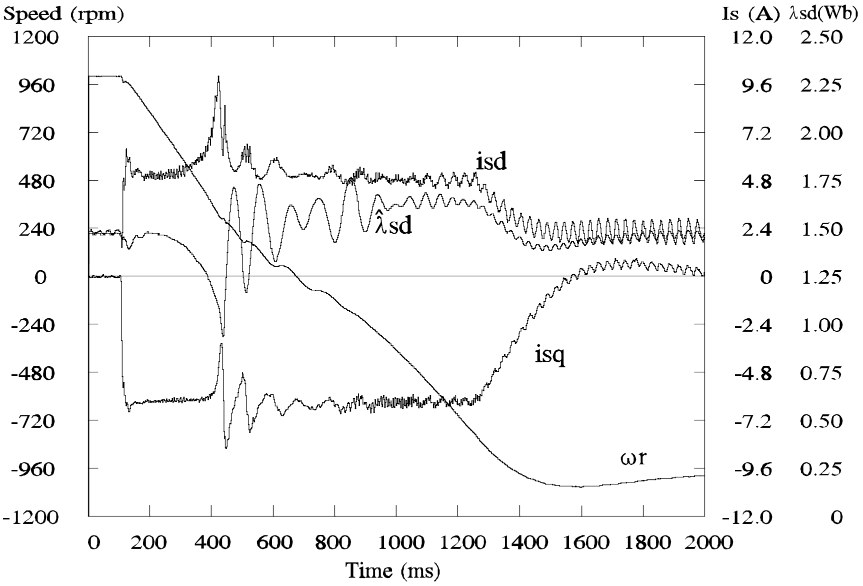

Figure 3.6 Speed reversal transient using sensored DSFO

Figure 3.6 shows a speed reversal transient from 1000 rpm to -1000 rpm using the DSFO scheme of Fig. 3.5. Field orientation is very good down to approx. 240 rpm. After that, there is a loss of orientation close to zero speed, due to the poor flux estimate at low speeds. When the machine reaches -240 rpm, the acceleration rate increases, showing that field orientation is retrieved gradually. The flux magnitude is not constant during the transient, indicating a possible overestimation of σL_s in the compensation term (i_{dq}). The cross-coupling problem between stator flux and i_{sq} can be ameliorated if a fast flux loop is introduced, in order to keep the stator flux constant against variations of the q-axis current. The bandwidth of this loop should be very high, since the reduction of flux due to changes in i_{sq} is also very fast [87]. Nevertheless the DSFO system will still be very sensitive to the stator resistance.

The DSFO implementation has the important advantage of not requiring speed or position feedback for field orientation. Therefore a basic sensorless system could be obtained from a DSFO by including a simple speed estimator for speed feedback [87]. Direct Stator Field Orientation also shows good performance during field weakening since the influence of R_s at high speed is negligible and therefore a good degree of field orientation can easily be obtained. Moreover the good stator flux estimate at high frequency will also imply good field control.

The characteristics of other methods of field orientation such as Direct Self Control DSC [25] or Direct Torque Control DTC [36] are very similar to that of a DSFO system with a fast flux loop; i.e. a speed sensor is not required for field orientation, the performance at high speed and during field weakening is probably better than IRFO, and they are both sensitive to the stator resistance at low speeds. Both DSC and DTC implement a direct control of flux and torque without using current controllers; DSC uses a bang-bang torque and flux control and DTC uses a dead beat controller. These systems provide a higher bandwidth for the flux control loop and therefore are less sensitive to σL_s estimation errors.

3.2.3 Direct Rotor Field Orientation (DRFO)

In a DRFO system, the rotor flux vector is computed directly for field orientation. The dynamic equations of the induction machine in a synchronous frame aligned with the rotor flux are the same as for the IRFO. However, no forcing condition is used for field orientation. The main advantage of rotor flux orientation (i.e. decoupled control of i_{sq} and flux) is retained with a DRFO system. The implementation of a DRFO based on a flux observer is shown in Fig. 3.7. Speed feedback could be obtained from a transducer or from a speed observer.

Computation of the rotor flux (or rotor angle) for field orientation from terminal quantities of the machine is normally preferred to searching methods based on Hall sensors [6], tapped windings [90] or similar methods that require special modification of the machine. Section 3.3 provides a review of several methods of rotor flux estimation of standard induction machines (i.e. without requiring special

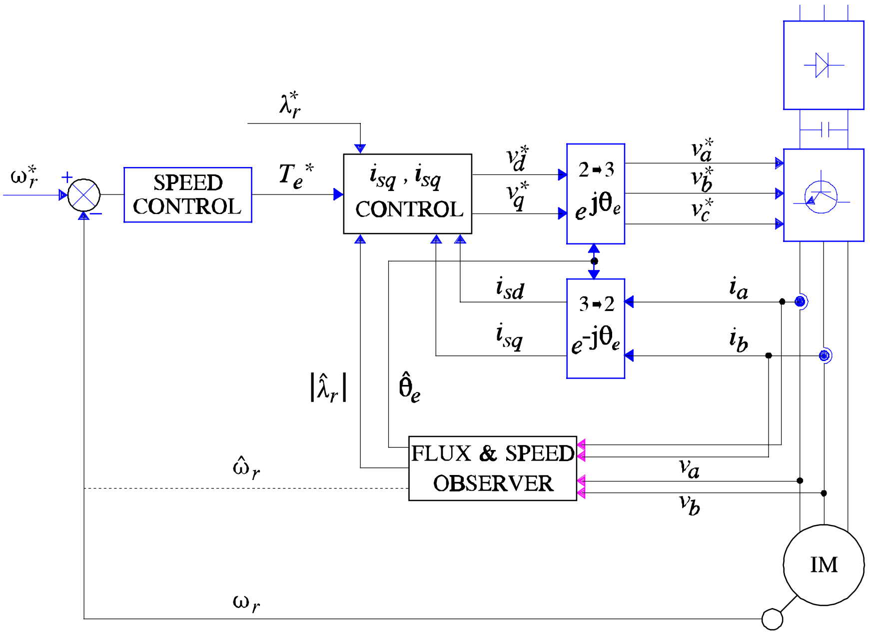

Figure 3.7 Direct Rotor Flux Orientation Diagram

modification of the machine). Most of these methods can be easily modified to provide a stator flux estimate rather than rotor flux, retaining most of their characteristics (parameter sensitivity, speed range, etc). However rotor flux orientation has been generally preferred in sensorless drives because of the inherent decoupling of i_{sq} and flux in the rotor frame [55, 46, 89, 81, 56, 89].

3.3 Rotor Flux Observers for DRFO

3.3.1 Open Loop Observers

The rotor flux can be calculated by using the stator equation of the induction machine

$$\underline{\lambda}_r = \int(\underline{v}_s - R_s\underline{i}_s)dt - \sigma L_s\underline{i}_s \tag{3.17}$$

This expression is also known as the *voltage model* of the machine. It presents similar problems and advantages as the DSFO described previously, since it requires a pure integration for flux estimation and it is sensitive to errors in the stator resistance at low speed. This makes the voltage model unsuitable for low speed operation. However, it does not require the rotor speed to produce a flux estimate. Unlike the DSFO, there is no cross coupling between i_{sq} and λ_{rd}, due to the orientation on the rotor flux. On the other hand field orientation in the DRFO depends on σL_s.

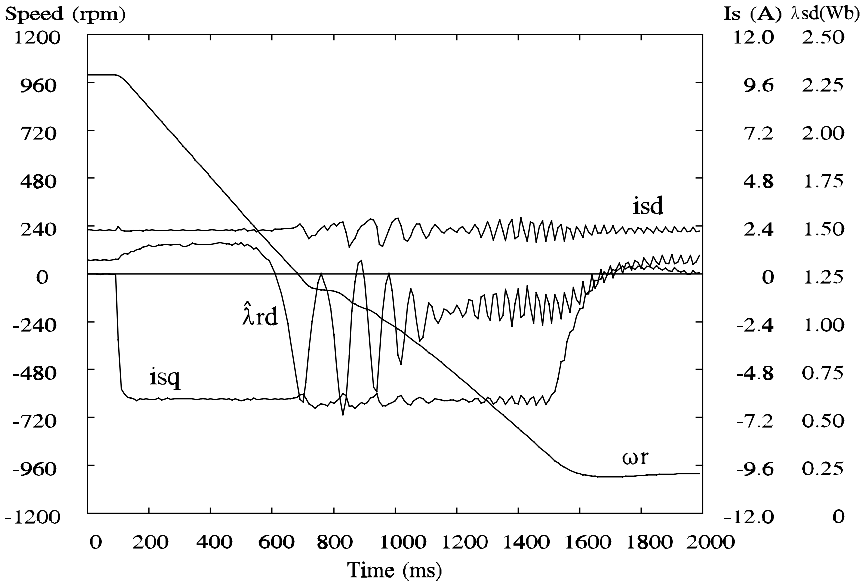

Figure 3.8 DRFO speed reversal using an open loop flux observer based on the voltage model

Figure 3.8 shows a DRFO speed reversal using an open loop flux observer based on the voltage model. During deceleration field orientation is very good down to almost 0 rpm. After that field orientation worsens, although a good degree of field orientation is recovered after approx. -240 rpm. Comparing this figure with Fig. 3.6 one can see that constant deceleration rate and constant flux is kept for longer time in the DRFO case. Moreover, the stator currents are controlled to their set values, unlike the DSFO. This is due in great extent to the better decoupling of the DRFO system. Both systems show orientation problems near zero speed, due to the use of the voltage model with a band-pass filter integrator. The acceleration rate is higher in the DSFO case due to the higher value of the torque constant in the stator reference frame ($3\frac{p}{2}\lambda_{sd} i_{sq}$) compared with $3\frac{p}{2}\frac{L_0}{L_r}\lambda_{rd} i_{sq}$ in the rotor frame. However this higher acceleration torque is obtained with a higher i_{sd} (needed to keep the stator flux constant), and therefore there is more power going into the machine in the DSFO case than in the DRFO implementation.

Rotor flux can also be obtained from the rotor equations of the machine

$$\dot{\underline{\lambda}}_r = \frac{L_0}{T_r}\underline{i}_s - \left(\frac{1}{T_r} - j\omega_r\right)\underline{\lambda}_r \qquad (3.18)$$

known as the *current model*. This model has similar advantages and disadvantages to the IRFO implementation. It requires knowledge of the rotor speed and it is dependent on the rotor time constant. The current model sensitivity to T_r is independent of the machine speed and a good degree of field orientation can be achieved even at stand-still, with appropriate speed measurement. The performance of this system degrades during field weakening, due to the difficulty of determining T_r and L_0 with changing flux. In fact, a DRFO implementation based on the current model with speed transducer yields identical performance to that of Indirect Rotor Flux Orientation.

3.3.2 Closed Loop Flux Observer

The advantages of both current and voltage models can be combined in what is known as a Closed Loop Flux Observer (CLFO) [48]. The structure of this observer is shown in Fig. 3.9.

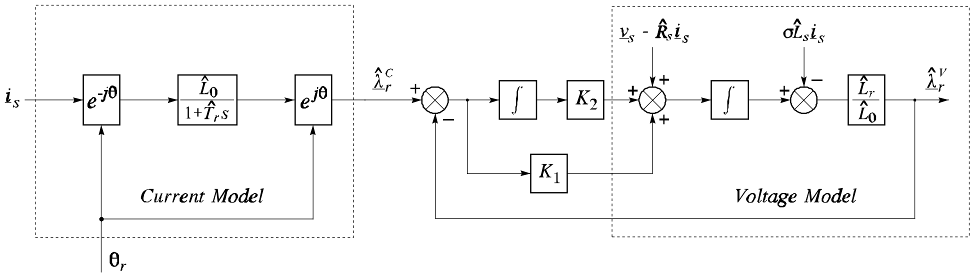

Figure 3.9 Closed Loop Flux Observer (CLFO)

The CLFO consists of the two models, based on (3.17) and (3.18), connected by a PI controller. Note the current model has been expressed in rotor coordinates rather than in stator fixed coordinates. The values K_1 and K_2 of the PI controller are designed to obtain a close loop bandwidth in the voltage model of ω_{cpl} (typically 1 or 2 Hz). For frequencies below ω_{cpl}, the CLFO output ($\hat{\underline{\lambda}}_r^V$) follows the flux estimate from the current model ($\hat{\underline{\lambda}}_r^C$). For frequencies above ω_{cpl} (outside the bandwidth of the PI controller), the two models are not coupled any more.

Therefore the output $\hat{\underline{\lambda}}_r^V$ corresponds to that of the voltage model. This behaviour can also be understood from the overall CLFO transfer function

$$\begin{aligned}\underline{\lambda}_r^V = {} & K_p \frac{L_r}{L_0} \frac{(s+a)}{s^2 + K_p \frac{L_r}{L_0} s + K_p \frac{L_r}{L_0} a} \underline{\lambda}_r^C + \\ & + \frac{s^2}{s^2 + K_p \frac{L_r}{L_0} s + K_p \frac{L_r}{L_0} a} \frac{L_r}{L_0} \left(\frac{1}{s} (\underline{u}_s - R_s \underline{i}_s) - \sigma L_s \underline{i}_s \right)\end{aligned} \tag{3.19}$$

where the PI controller is expressed as $K_p(s + a)/s$. The first term of the transfer function corresponds to a low pass filter applied to the output of the current model. The second term is equivalent to a high pass filter applied to the flux estimate obtained from direct integration of the stator back e.m.f. The equivalent diagram of the CLFO is shown in Fig. 3.10. The cut off frequency of both filters (ω_{cpl}) is the same and provided that $a > \omega_{cpl}$ the resulting phase shift of the combined filters is very close to zero for the whole range of frequencies.

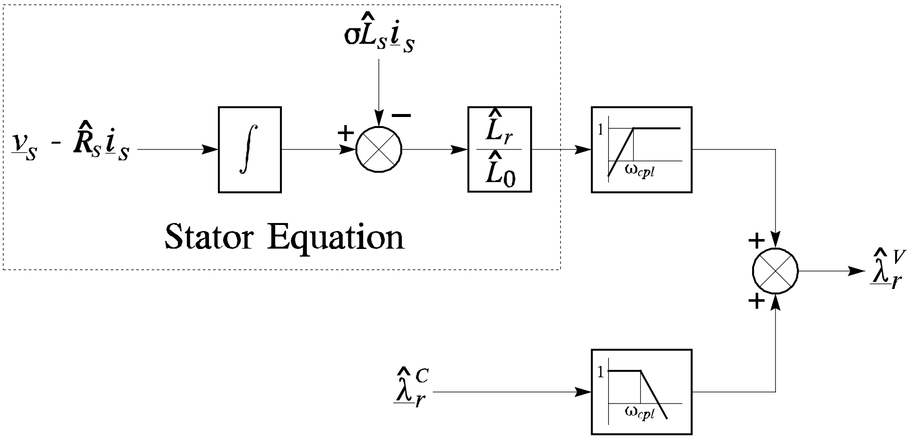

Figure 3.10 Equivalent diagram of the Closed Loop Flux Observer

Therefore the CLFO can operate properly at zero speed, due to the use of the current model which offers the same performance as indirect rotor field orientation. Figure 3.11 shows a speed reversal transient using a CLFO-DRFO implementation. This transient shows a very good field orientation, and it is almost identical to the IRFO speed reversal shown in Fig 3.2. The only difference is the small spike in the i_{sd} current at the beginning of the transient in Fig 3.2 caused by the fact that the IRFO ω_{sl} calculator uses the reference value of i_{sq} and the actual i_{sq} takes a small time to respond to changes in i_{sq}^*. This spike does not appear in Fig 3.11 because the DRFO flux angle ie derived from measured quantities and hence independent of the current controller's limited bandwidth. Reliable operation at zero speed is shown in Fig 3.12.

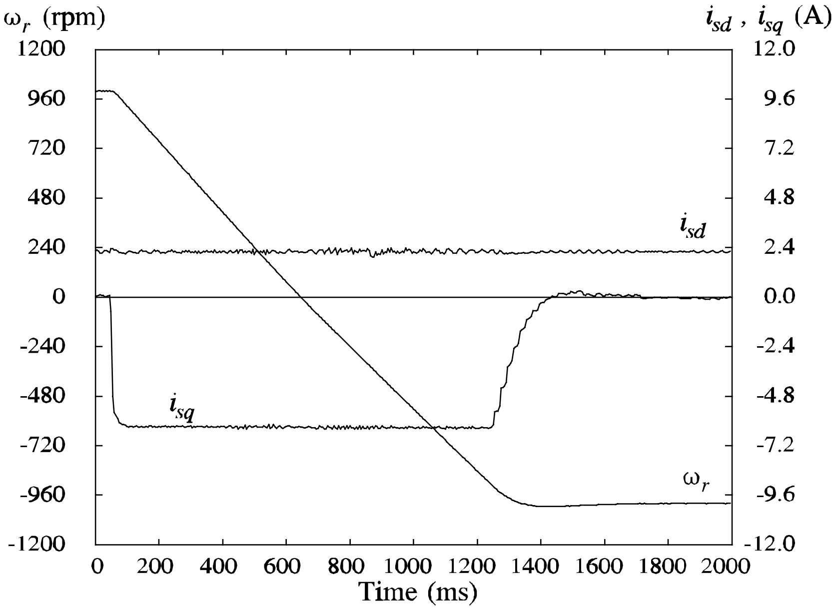

Figure 3.11 Speed reversal using DRFO based on a CLFO with position transducer

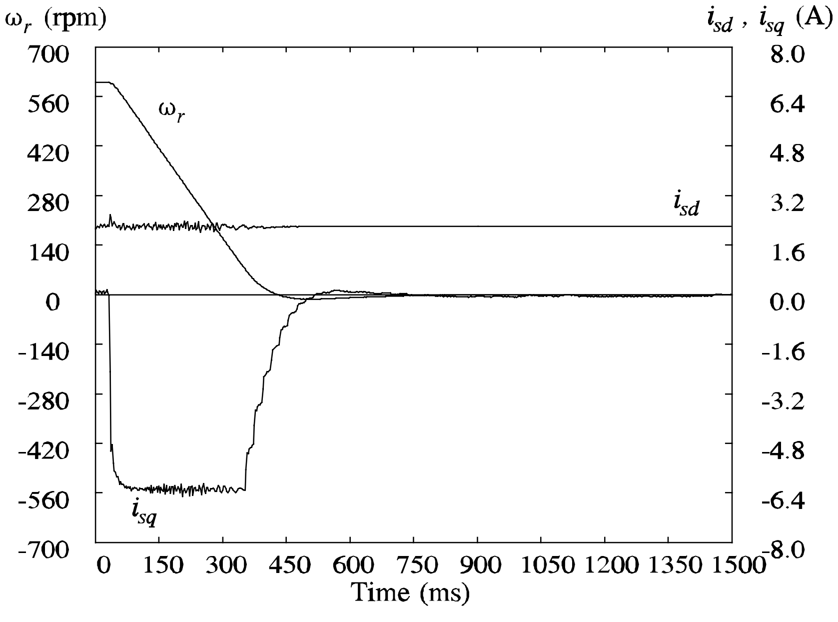

Figure 3.12 Speed transient to stand still using sensored CLFO-DRFO

3.3.3 Other Flux Observers

Besides the previous mentioned open and closed loop flux observers, several methods have been proposed for the estimation of the rotor flux. In [3], the Extended Kalman Filter (EKF) was used to produce estimates of rotor currents and secondary time constant, requiring a speed transducer for its operation. The EKF can also be used for estimating rotor flux and rotor speed [40]. Extended Kalman Filters use the difference between a measured quantity (e.g. the stator current) and its value from a machine model as error vector. The error vector is then used to drive the observed flux estimate towards that of the machine. Since the observer equations contain both the stator and rotor dynamic equations there is no fundamental reason why the observer should not exhibit good flux estimation through the whole speed range. However the EKF is computationally intensive and presents the difficulty of choosing the adequate values for the P and Q weighting covariance matrices [66]. Alternatively, the rotor flux can also be estimated by using an Extended Luenberger Observer (ELO) [27]. The main difference between the EKF and the ELO is that the latter ensures a predetermined position of the observer eigenvalues whilst the former places automatically the observer eigenvalues based on the selection of the P and Q matrices. Although the ELO approach does not present the problem of choosing weighting covariance matrices, it also requires great number of calculations to be solved in real time.

Alternative methods of measuring the rotor flux have also been derived exploiting magnetic saliencies in the machine, generally due to saturation. In [74], the local saturation of the rotor teeth is used in order to obtain the position of the rotor flux vector. The main advantage of this method is that the flux estimate is independent of the machine parameters. However, this approach requires the injection of a short high frequency disturbance and is only applicable to low speed, due to the required large magnitude of the disturbance at high speed. As a result of the high frequency of the disturbance, the sampling frequency of this method has to be very high. This method is also computationally intensive and the resulting estimated flux is generally very noisy.

3.4 Speed Observers

Some sort of speed estimation is needed for speed and/or field orientation of sensorless induction motor drives. Different kinds of speed estimators have been developed, using techniques such as open loop slip calculation [87, 88, 65], Extended Kalman Filters [15, 40], Luenberger observers [27], Least Squares Regression Models [84], or Model-Reference Adaptive Systems (MRAS) [82, 72, 81, 55, 89, 46].

Open loop slip calculation is relatively easy to implement. The stator frequency (ω_e) can be calculated using [87]

$$\omega_e = \frac{\underline{\lambda}_s \times (\underline{v}_s - R_s \underline{i}_s)}{|\underline{\lambda}_s|^2} \tag{3.20}$$

The excitation frequency (ω_e) can also obtained by differentiating the flux angle or directly from the control system in the case of IRFO. The calculation of the slip can be carried out by using [87]

$$\omega_{sl} = \frac{(1 + \sigma T_r s) L_s i_{sq}}{T_r(\lambda_{sd} - \sigma L_s i_{sd})} \tag{3.21}$$

and assuming $\lambda_{sq} = 0$ (Stator Field Orientation SFO). Assuming Rotor Flux Orientation (RFO), the machine slip can also be calculated by [65]

$$\omega_{sl} = \frac{i_{sq}}{T_r\, i_{sd}} \tag{3.22}$$

A system that calculates the rotor speed of the machine based on the above expressions is bound to be extremely sensitive to parameter errors and in some cases very noisy. Equation (3.20) requires knowledge of the stator flux. Calculation of the stator flux from the voltage model is sensitive to stator resistance errors. Moreover, (3.20) itself depends on R_s, so that this method of calculating ω_e is bound to be very inaccurate at low speed. The alternative of calculating ω_e by direct differentiation of the flux angle is bound to be noisy. Moreover, slip calculation based either on (3.21) or (3.22) depends strongly on an accurate knowledge of the machine parameters and also on good field orientation. An experimental result of open loop speed estimation using (3.21) is shown in Fig. 3.13. During deceleration the speed error is about 35 rpm. At speeds close to zero, the estimate is extremely poor, due to the low frequency limitation of the ω_e calculation based on (3.20). Typical steady state error at full load is approximately 20 to 25 rpm. These figures represent 25 to 30% rated slip (80 rpm). Therefore speed holding and speed accuracy at medium/low speed is very poor. In conclusion, open loop speed calculation can only be used in very low performance applications in which speed accuracy and speed holding capability are not important.

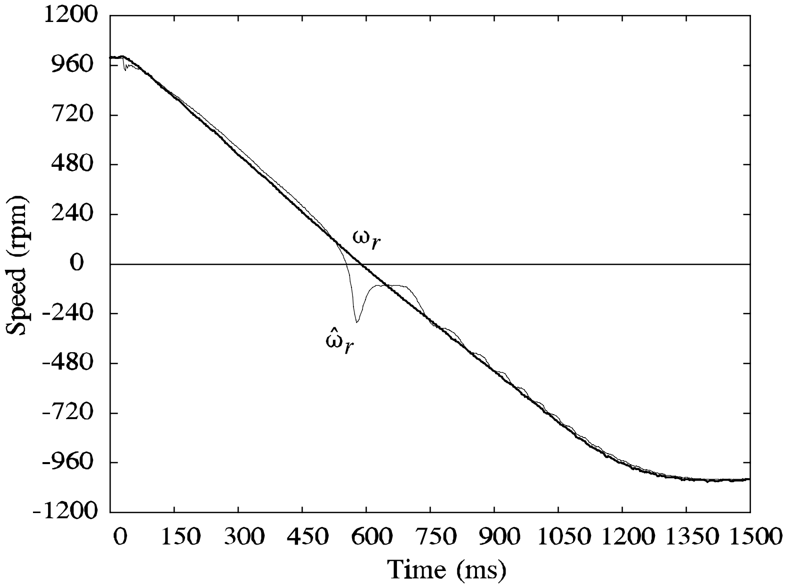

Figure 3.13 Open loop speed estimation during speed reversal

More sophisticated methods such as extended Kalman filters [40] or Luenberger observers [27] have also been used for joint rotor speed and rotor flux/current estimation. However they present the disadvantages noted in Section 3.3.3. The use of a least squares regression algorithm for the identification of the all the machine parameters together with the rotor speed has also been reported [84]. This method of speed estimation requires the use of a high sampling frequency of the machine voltages and currents and is computationally intensive. Therefore it is very difficult to implement in real time, and as far as the author is aware no results of a real time implementation have been published.

The rotor speed can be obtained by using an estimator based on the MRAS principle [58], in which an error vector is formed from the outputs of two models both dependent on different motor parameters. The error vector is driven to zero through adjustment of a parameter that influences one model and not another. In this case the parameter is the rotor speed (ω_r). The MRAS approach has an immediate advantage in that the models are simple, very easy to implement and have direct physical interpretation. There is a choice of error vectors which may or may not give a wider flexibility in achieving design goals. The most common choice of error vector is that of rotor flux [82, 72, 46, 81] which also has the advantage of producing a rotor flux angle estimate that could be used for DRFO vector control. At very low speeds however all flux calculators are very sensitive to the effects of stator resistance and integrator drift and in order to overcome these problems, back e.m.f. and reactive power have both been suggested as error vectors [67]. However these quantities themselves disappear at low speed and also give rise to highly non-linear gains in the adaptive MRAS controllers [20, 77].

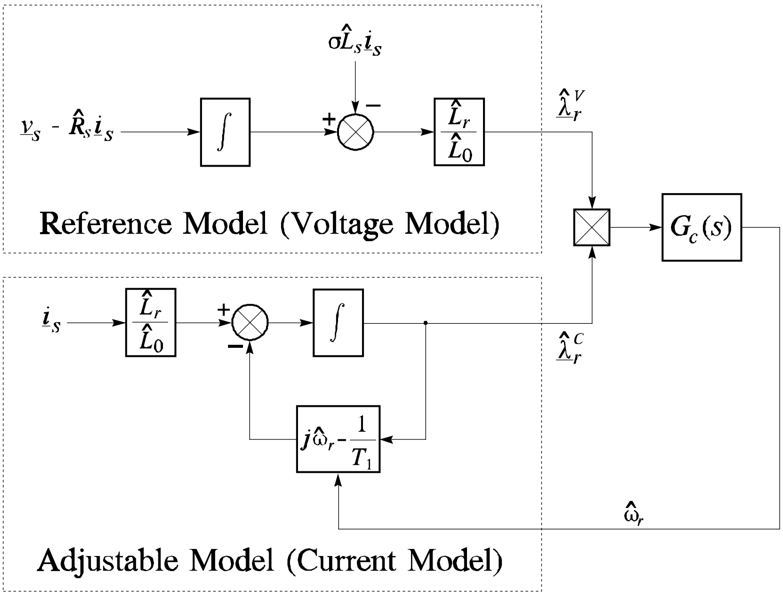

Figure 3.14 Basic MRAS speed identification using the rotor flux as error vector

A basic MRAS implementation using the rotor flux as error vector is shown in Fig. 3.14. This system is based on the fact that the rotor flux can be obtained from either the voltage or current model. The flux estimate produced by the former ($\hat{\lambda}_r^V$), does not depend on the rotor speed, and is used as a reference model. The latter produces a flux estimate ($\hat{\lambda}_r^C$) that is dependent on the rotor speed. Therefore the rotor speed in the current model can be adjusted to force an error function between the estimated fluxes to zero. The loop that drives this error function to zero is termed the speed adaption loop, and the function $G_c(s)$ is known as the adaptive controller. Any error function that satisfies the hyperstability criteria (i.e. that results in a stable system) can be chosen. The cross product of the flux estimates has been shown to satisfy the hyperstability criteria [82] and will therefore be used here

$$\varepsilon = \hat{\lambda}^{C}_{rd}\hat{\lambda}^{V}_{rq} - \hat{\lambda}^{C}_{rq}\hat{\lambda}^{V}_{rd} = \left|\hat{\lambda}^{V}_{r}\right|\left|\hat{\lambda}^{C}_{r}\right|\sin\left(\hat{\theta}^{C}_{r} - \hat{\theta}^{V}_{r}\right) \tag{3.23}$$

where $\hat{\theta}^{V}_{r}$ and $\hat{\theta}^{V}_{r}$ are the rotor flux angles estimated by the voltage and current model respectively. For small differences between estimated flux angles, the error function can be expressed as

$$\varepsilon = \left|\hat{\lambda}^{V}_{r}\right|\left|\hat{\lambda}^{C}_{r}\right|\left(\hat{\theta}^{C}_{r} - \hat{\theta}^{V}_{r}\right) \tag{3.24}$$

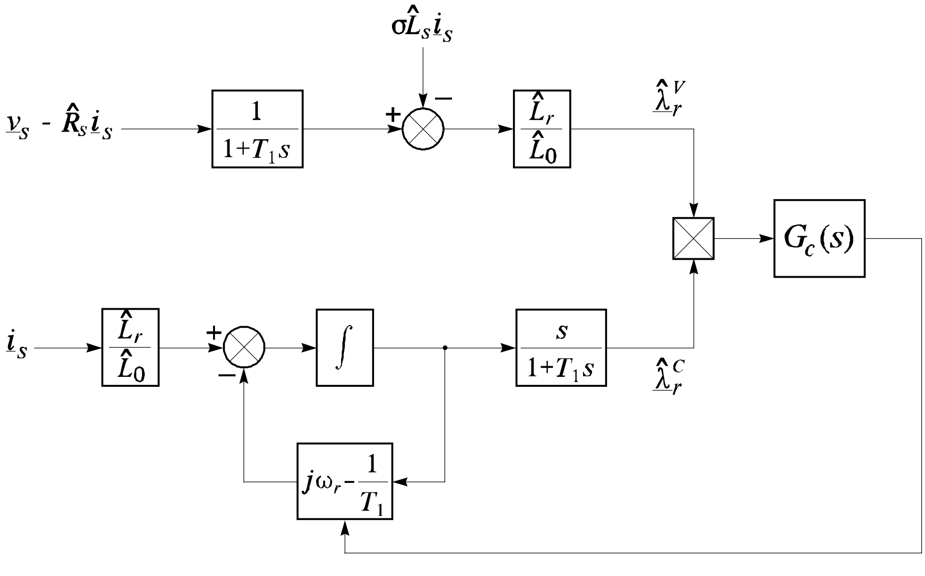

Figure 3.15 MRAS speed observer with DC blocking filters

The voltage model obtains the rotor flux by integration so that in practice dc offsets must be removed by employing a dc-blocking filter so that the error vector becomes an ac-coupled rotor flux signal (Fig. 3.15) [82, 72]. MRAS speed observers using a voltage model with dc-blocking filters present the disadvantage that at low speeds misidentification of R_s and the distorting effects of the dc-blocking filter cause the rotor flux estimate to become inaccurate and both the speed estimate and the field orientation breaks down below 1 or 2 Hz. An improvement in both rotor flux and speed estimate at very low speed may be obtained by using a closed loop flux observer (CLFO) instead of two independent flux models [46]. This structure, depicted in Fig. 3.16, is termed a closed loop flux observer MRAS (MRAS-CLFO).

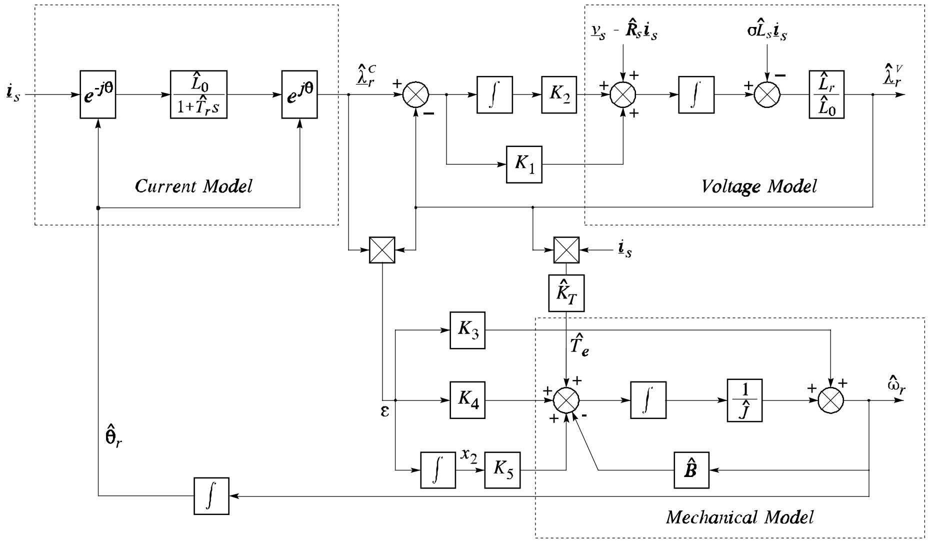

Figure 3.16 MRAS-CLFO flux and speed observer

At frequencies above ω_{cpl} the voltage and model loops are effectively independent and the system is equivalent to the basic MRAS shown in Fig. 3.14. However, as the frequency approaches zero, $\hat{\lambda}_r^V = \hat{\lambda}_r^C$ and speed estimate forcing is lost. A mechanical model can compensate for this effect in that flux and speed estimates are produced even when $\hat{\lambda}_r^V = \hat{\lambda}_r^C$. The structure of the mechanical model is also shown in Fig. 3.16 in which an estimated torque signal is used to drive a first order drive train model. This model is also driven by the ε signal through a PI controller which will help compensate model errors. The feedforward term K_3 weights the effect of the pure MRAS-CLFO and the mechanical model upon $\hat{\omega}_r$. At low frequencies, the MRAS-CLFO is equivalent to the speed observer shown in Fig. 3.17 since $\hat{\lambda}_r^V = \hat{\lambda}_r^C$. Therefore operation at very low speed is dependent on a good knowledge of the mechanical parameters. However, if the mechanical parameters are not accurately known, then the compensation will merely be less effective but still an improvement over the case when no mechanical model is used at all. In practice it is found that field orientation and the speed estimate start to deteriorate for excitation frequencies below ω_{lim}, a frequency slightly higher than ω_{cpl} (eg if ω_{cpl}

is designed at 0.8 Hz, ω_{lim} is about 1.5 Hz). The degree of deterioration depends on the accuracy of the of the estimated voltage model and mechanical parameters.

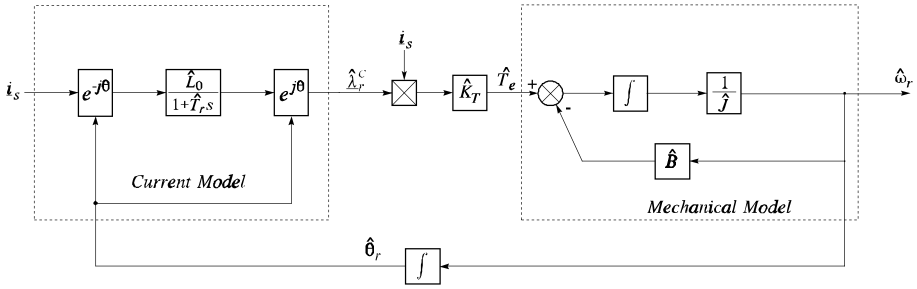

Figure 3.17 MRAS-CLFO low frequency equivalent diagram

3.5 Discussion and Conclusions

When deciding on a particular vector control implementation three main factors should be taken into account, namely performance, sensitivity to parameters and suitability for speed sensorless operation. Three different vector control implementations have been presented in this chapter: IRFO, DSFO and DRFO. Air-gap field orientation has not been considered, since it is substantially similar to stator field orientation. Indirect Stator Field Orientation (ISFO) has not been included since it requires a speed sensor for its operation, it is very sensitive to parameter errors and its performance is much worse than other sensored methods, therefore there is no relative advantage in using ISFO.

The first method reviewed, IRFO, probably gives the highest performance under base speed of any vector control system when properly tuned, due to the complete decoupling between flux and torque control. It can also operate indefinitely at low and zero speed without noticeable performance degradation. Field orientation depends only on a good knowledge of the rotor time constant (T_r). On the negative side of this implementation we have that a speed or position sensor is required and that operation during field weakening is difficult and very sensitive to parameter errors.

Direct Stator Field Orientation based on integration of the back e.m.f. presents the major advantage of not requiring a speed sensor for field orientation. Its performance at medium and high speeds and during field weakening is very good.

However field orientation at low speeds depends on an accurate knowledge of the stator resistance and zero speed operation is generally impossible even when a speed transducer is used. Moreover there is a cross coupling term between flux and torque loops, and a fast flux controller is required in order to compensate for this cross coupling. If a fast field controller is not used, DSFO is also very sensitive to errors in σL_s. More elaborated methods like Direct Self Control or Direct Torque Control improve the performance of a DSFO implementation, since flux and torque are controlled directly in a dead beat fashion therefore compensating for the cross coupling effects.

The characteristics of Direct Rotor Field Orientation are a combination of those of IRFO and DSFO, and depend strongly on the method used for calculating the rotor flux. It can be easily shown that a DRFO system based on flux calculation from the current model (hence requiring a speed sensor) is equivalent to Indirect Rotor Flux Orientation. If the rotor flux is calculated from the voltage model, the characteristics are more similar to those of DSFO, i.e. no speed transducer is required for field orientation, the system is very sensitive to R_s errors at low speed and zero speed operation is not possible. The main difference between DSFO and DRFO is that the latter does not present cross coupling between flux and torque producing current at the expense of being sensitive to σL_s even when high bandwidth flux controllers are used.

From the study of these implementations it can be concluded that the presence or absence of a cross coupling term between flux and torque producing current depends only on the frame of orientation. Therefore Rotor Flux Orientation is preferred to Stator Field Orientation, due to the absence of cross coupling. Sensitivity to parameters and the requirement of speed or position transducers is determined by the use of stator or rotor equations (voltage and current model respectively) for field orientation. In general the voltage model can be used without speed sensor and is sensitive to R_s errors whereas the current model needs knowledge of the rotor speed and is sensitive to T_r errors. The voltage model is preferred at high speed and during field weakening and the current model should be used at low speeds. The Closed Loop Field Observer exhibits these characteristics; however it requires knowledge of the machine speed for its operation at low speed. This speed information can be obtained from a speed observer for sensorless operation.

The solution chosen for sensorless operation is based on a MRAS-CLFO implementation. This implementation performs differently at high and low speeds, due to the nature of the CLFO. At high speeds field orientation is obtained from the voltage model, which is also used as reference model of the MRAS speed observer, while the current model is used as adjustable model. In this condition field orientation depends on R_s (not very important at high speed) and on σL_s, whereas speed estimation depends mainly on T_r. At low speeds, the contribution of the voltage model is negligible, and the field orientation is obtained from an observer based on the current and mechanical models of the machine. Therefore field orientation *and* speed estimates will depend mainly on T_r and on the mechanical parameters. Since it is very difficult to know the mechanical parameters accurately (especially at low speeds), zero speed operation will not be possible in the general case (although Section 7.2 shows that it is possible under certain circumstances). However the alternative of using a flux observer based on the voltage model at low speeds is generally worse due to integration drift, extreme sensitivity to R_s and to measurement quantisation errors. Therefore the use of the current model and the mechanical model, although is not optimal, is better than the use of a voltage model alone.

An alternative to a DRFO sensorless scheme could be the implementation of an IRFO system that uses a speed estimate rather than actual speed for field orientation [82, 72]. However field orientation in this case will be very sensitive to speed estimation errors. Therefore the degree of field orientation is determined by the quality of the speed estimator and sensitive to errors in the parameters of the speed estimator. In this respect some researchers [82, 72] have suggested that an error in the rotor time constant used for speed estimation is compensated by the use of the same (erroneous) value of T_r for indirect flux orientation. Therefore an error on T_r would affect the speed estimate but not field orientation. Although this is true during steady state, during transient operation the cancellation of T_r errors does not generally occur due to the dynamics of the speed estimator. Therefore a sensorless IRFO approach is bound to exhibit cross-coupling effects during transients due to inaccurate parameters being used for speed estimation. In contrast field orientation using the proposed DRFO approach is insensitive to speed observer parameter errors in most of the speed range, being only sensitive to inaccurate speed observer parameters at low frequencies (typically below 1 Hz).

For the above reasons, the research work carried out is based on a DRFO implementation using the MRAS-CLFO shown in Fig. 3.16, and all the results presented in following chapters use this structure unless otherwise stated. A Model Reference Adaptive structure has been preferred for speed and flux estimation to other solutions based on Extended Kalman Filters or on Luenberger observers for reasons of simplicity and flexibility; however no thorough comparison between these methods and MRAS speed estimators has yet been published.

Chapter 4 MRAS-CLFO Sensorless Vector Control

4.1 Introduction

The performance of sensorless drives is generally compared with the open-loop V/f PWM drive over which the sensorless vector exhibits improved flux holding both at low speeds and under disturbance torque rejection. In the research community however, recent years have also seen the development of effective speed and flux estimators which allow good rotor-flux orientated (RFO) performance at all speeds except those close to zero. The independent control of torque and flux implied by RFO itself implies that a good speed and load torque rejection bandwidth should be attainable and that in these respects sensored vector drives rather than open-loop PWM drives should provide the benchmark for sensorless vector performance. However such a comparison (or results which allow a comparison to be deduced) has not hitherto been reported. This chapter, together with Chapter 7, provides such a comparison.

The observer/estimator structures for deriving estimates of the speed and flux were reviewed in Chapter 3. It was shown in Section 3.4 that the Model Reference Adaptive System Closed Loop Flux Observer (MRAS-CLFO) exhibits advantages in terms of sensitivity to parameters and simplicity and therefore this observer structure is used throughout the remainder of the thesis. In this chapter it will be shown that the speed bandwidth of a sensorless drive is limited by stability considerations arising from incorrect estimator parameters. These limitations are verified experimentally in Chapter 7.

To study the effect of errors in the model parameters the small signal stability analysis will be carried out with the MRAS-CLFO structure. The global stability of the adaptive MRAS loop based on the structure due to Schauder has been reported [82, 72]. A similar proof for the MRAS-CLFO structure can proceed on similar lines but has not been included here since taking the effect of inaccurate model parameters into account is beyond the scope of this work. A small signal stability analysis however yields stability margins for specific model parameter errors and is thus more useful from an engineering view point. The small signal stability analysis in Section 4.3 will be subject to case study using the machine parameters listed in Chapter 2. These parameters are those of the 4 kW experimental rig.

Figure 4.1 shows the structure of a general sensorless DRFO implementation. The flux angle and magnitude required for field orientation and flux control are obtained from a flux observer. The inputs to the flux observer are the stator voltages and currents. The observer also provides a speed estimate for speed control.

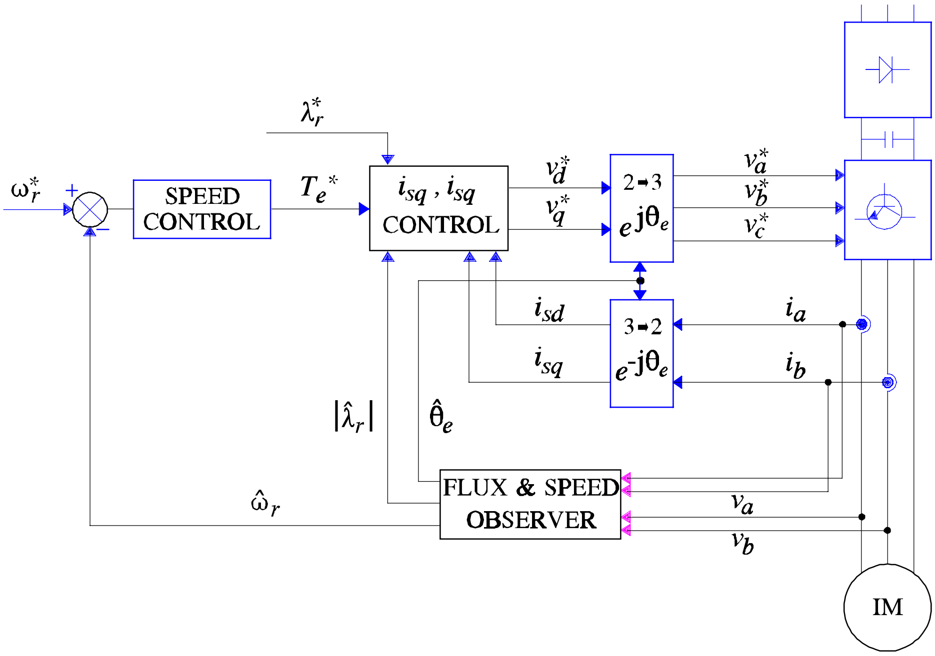

Figure 4.1 General sensorless DRFO structure

The particular observer used in this work is the previously mentioned MRAS-CLFO, which is shown in Fig. 4.2. As explained in Section 3.4, the MRAS-CLFO consists of the voltage model of the machine, which is used as a reference model; the current model (adjustable model) and the mechanical model, used for improving the speed estimation dynamics and the flux estimate at speeds close to zero.

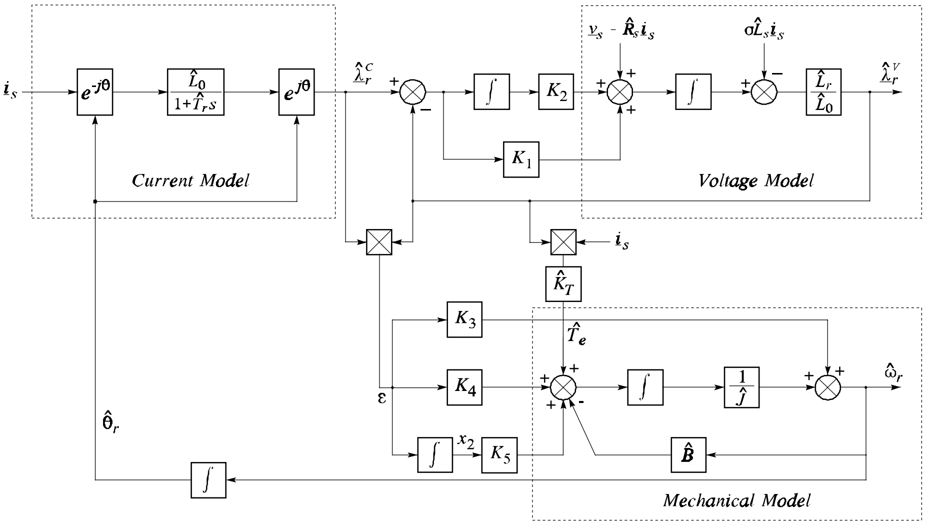

Figure 4.2 MRAC-CLFO speed and flux observer including the mechanical model

4.2 Design of Adaptive Control Parameters

The guidelines for designing the control parameters of the MRAS-CLFO are included here since the controller equations are used later in the stability analysis. Also an explicit treatment has not hitherto appeared in literature.

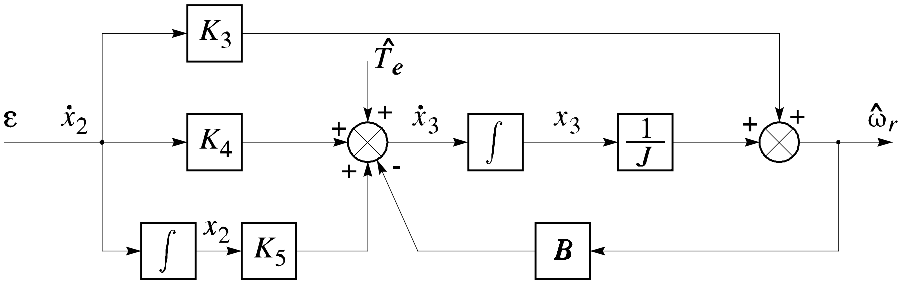

Figure 4.3 Adaptive controller and mechanical compensation

The adaptive controller structure together with the mechanical compensation is shown in Fig. 4.3. The PI controller plus the feedforward gain is equivalent to a PID controller on which K_4, K_5 and $K_3 J$ are the proportional, integral and derivative gains respectively. If the PID controller is written as $k(s+x)(s+y)/s$, then the controller constants for Fig. 4.3 are given by

$$K_3 = k/J; \quad K_4 = k(x+y); \quad K_5 = kxy \tag{4.1}$$

The resulting equivalent adaptive control loop is shown in Fig. 4.4. The input to the control system is considered as the actual flux in the machine, since for frequencies above ω_{cpl} the voltage model gives an accurate estimate of the rotor flux vector. Moreover the coupling between current and voltage models can be neglected (again working at frequencies higher than ω_{cpl}). In order to derive the PID parameters a linearised transfer function between $T'(s)$ and $\varepsilon(s)$ is obtained as follows. Since all voltages, currents and fluxes of Fig. 4.3 are 2-axis sinusoidal quantities, the linearisation is facilitated by transforming the defining equations of the estimator into a synchronously rotating reference frame.

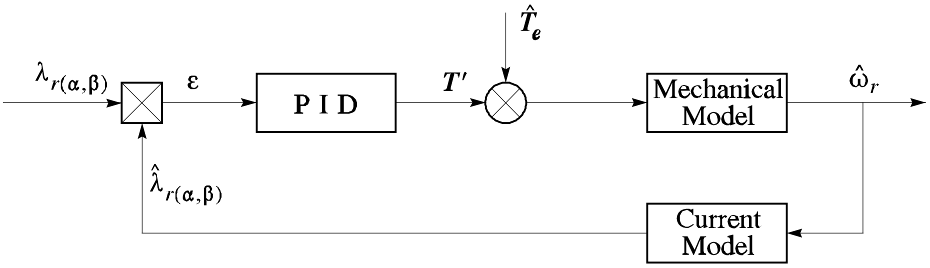

Figure 4.4 Equivalent adaptive control loop

With reference to Fig. 4.4, we have

$$\hat{\omega}_r = \frac{p}{2}\frac{(T' + \hat{T}_e)}{(Js + B)} \tag{4.2}$$

In the dq synchronously rotating frame, we have

$$\varepsilon = \hat{\lambda}_{rd}\lambda_{rq} - \hat{\lambda}_{rq}\lambda_{rd} \tag{4.3}$$

$$s\hat{\lambda}_{rd} = -\frac{1}{T_r}\hat{\lambda}_{rd} + \hat{\omega}_{sl}\hat{\lambda}_{rq} + \frac{L_0}{T_r}i_{sd} \tag{4.4}$$

$$s\hat{\lambda}_{rq} = -\frac{1}{T_r}\hat{\lambda}_{rq} - \hat{\omega}_{sl}\hat{\lambda}_{rd} + \frac{L_0}{T_r}i_{sq} \tag{4.5}$$

Linearising (4.3)

$$\delta\varepsilon = \delta\hat{\lambda}_{rd}\lambda_{rq} + \delta\lambda_{rq}\hat{\lambda}_{rd} - \delta\hat{\lambda}_{rq}\lambda_{rd} - \hat{\lambda}_{rq}\delta\lambda_{rd} = -\delta\hat{\lambda}_{rq}\lambda_{rd0} \tag{4.6}$$

assuming field orientation and that the voltage model flux is ideal and constant.

Linearising (4.2)

$$\delta\hat{\omega}_r = \frac{P}{2}\frac{\delta T^{/}}{(Js+B)} \tag{4.7}$$

Assuming field orientation and that i_{sd} and i_{sq} are constant we can linearise (4.4) and (4.5) to yield

$$s\delta\hat{\lambda}_{rd} = -\frac{1}{T_r}\delta\hat{\lambda}_{rd} + \delta\hat{\lambda}_{rq}\hat{\omega}_{sl0} \tag{4.8}$$

$$s\delta\hat{\lambda}_{rq} = -\frac{1}{T_r}\delta\hat{\lambda}_{rq} - \hat{\omega}_{sl0}\delta\hat{\lambda}_{rd} - \hat{\lambda}_{rd0}\delta\hat{\omega}_{sl} \tag{4.9}$$

and eliminating $\delta\hat{\lambda}_{rd}$ gives

$$\delta\hat{\lambda}_{rq} = -\frac{\hat{\lambda}_{rd0}\delta\hat{\omega}_{sl}\left(s+\dfrac{1}{T_r}\right)}{\left((s+\dfrac{1}{T_r})^2+\hat{\omega}_{sl0}^2\right)} \tag{4.10}$$

Substituting (4.7) into (4.10) and (4.10) into (4.6) noting that $\hat{\lambda}_{rd0} = \lambda_{rd0}$ and $\delta\hat{\omega}_{sl} = -\delta\hat{\omega}_r$ gives

$$\frac{\delta\varepsilon(s)}{\delta T^{/}(s)} = -\frac{\lambda_{rd0}^2 P}{2J}\frac{\left(s+\dfrac{1}{T_r}\right)}{(s+\dfrac{B}{J})\left((s+\dfrac{1}{T_r})^2+\omega_{sl0}^2\right)} \tag{4.11}$$

Therefore, the dynamics of the adaptive loop vary only with the motor slip. The PID controller demands the placement of two zeros. One possibility is to cancel the slip dependent poles which will make the control independent of the operating point albeit with a slip dependent controller. Alternatively, one of the zeros can be used to cancel the mechanical pole (*B*/*J*). This approach is the one used henceforth and is depicted in the root loci of Fig. 4.5. At very low gains a slow real pole will dominate. As the gain is increased the dominant real pole approaches the zero at

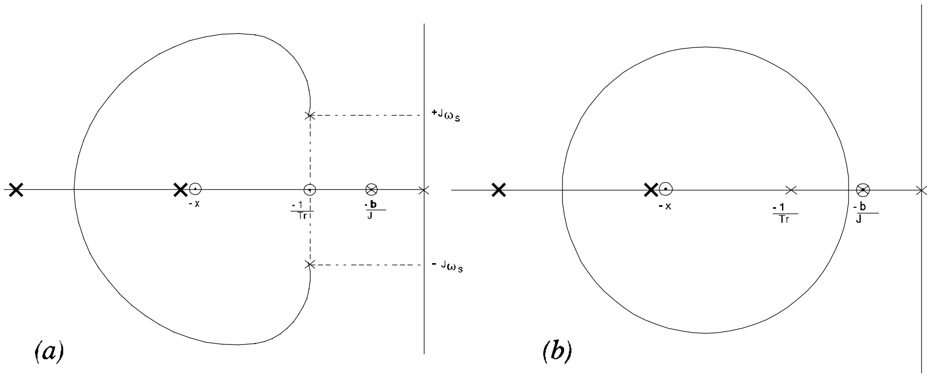

Figure 4.5 Root loci for the adaptive loop. ***(a)*** Rated slip; ***(b)*** Zero slip

$1/T_r$ and since this zero is also in the closed loop transfer functions for ω_r (see eq. (4.11)), the effect of this slow real pole will become negligible. Therefore the dominant poles can be freely placed in order to obtain a given bandwidth. One criteria for the placement of these poles is to obtain two real poles in such a way that one of them lies, at the high gain, very close to the second PID zero. The closed loop natural frequency is then determined by the second fast pole. A typical "fast adaptive loop" can be designed to give a natural frequency of 125 rads^{-1} (or 20 Hz) for the case of full load. Fig. 4.5b shows the no-load case of $\omega_{sl} = 0$ and in which the slip-dependent poles lie on the $1/T_r$ zero. The position of the "fast" closed loop poles are almost identical to the full load case and the design is practically load independent.

To allow for the fact that the "fast" design may be noisy or destabilizing, a slower design can of course be made. In this case both the residual from the slow real pole and the slip dependence of the closed-loop poles are larger for the slow design.

4.3 State Equations and Linearised Dynamic Model

To study the effects that incorrect estimator parameters have on the stability of the MRAS-CLFO, a state space analysis is carried out using a small signal linearised model. The system pole-zero positions will thus vary with speed and load. However it will be shown that for excitation frequencies greater than a certain frequency (ω_{lim}), the pole-zero positions move in a predictable and experimentally verifiable manner. The practical value of ω_{lim} is determined by the closed loop frequency of the coupling loop (ω_{cpl}), as explained in Section 3.4. For frequencies below ω_{lim}, the movement is large even for very small changes in the quiescent stator frequency. In practice, the usefulness of the linearisation is restricted to excitations frequencies greater than ω_{lim}.

For the following analysis it has been assumed that the machine is current fed (due to the large bandwidth of the current controllers), and that field orientation is always kept. This is valid since with DRFO, the flux angle calculation from the flux estimates is largely independent of poor speed estimates.

4.3.1 Machine Dynamics

The rotor dynamics of the machine can be expressed as

$$\dot{\underline{\lambda}}_r = -\left[\frac{1}{T_r} + j(\omega_e - \omega_r)\right]\underline{\lambda}_r + \frac{L_0}{T_r}\underline{i}_s \tag{4.12}$$

However, if the flux in the machine is constant under field orientation (and therefore i_{sd} is constant as well), this equation has no dynamics and can be used to obtain a relationship between the quiescent values λ_{r0} and i_{sd0}.

The mechanical dynamics for the machine is

$$\dot{\omega}_r = -\frac{B}{J}\omega_r + \frac{K_T\left(\underline{\lambda}_r \times \underline{i}_s\right)}{J} - \frac{T_m}{J} \tag{4.13}$$

where K_T is the torque constant and T_m the load torque.

4.3.2 Estimator Dynamics

The equation for the current model is

$$\dot{\hat{\underline{\lambda}}}{}_r^C = -\left[\frac{1}{\hat{T}_r} + j(\omega_e - \hat{\omega}_r)\right]\hat{\underline{\lambda}}{}_r^C + \frac{\hat{L}_0}{\hat{T}_r}\underline{i}_s \tag{4.14}$$

To derive the equations for the voltage model, the block diagram in Fig. 4.6 is used.

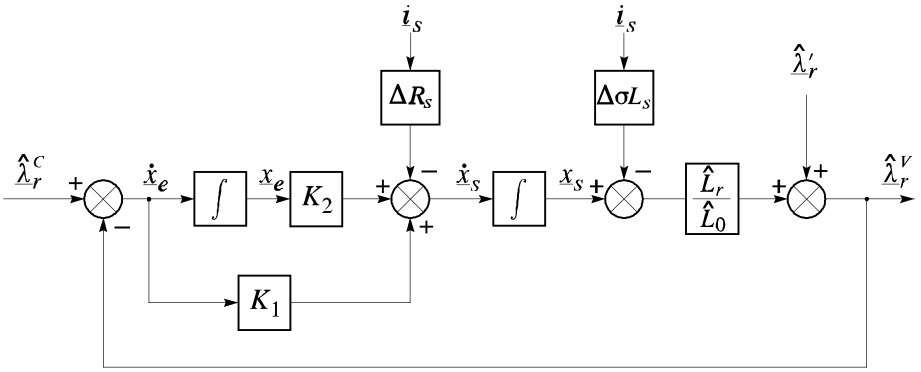

Figure 4.6 Voltage model equivalent diagram

To reflect errors in voltage model parameters, the following variables are defined

$$\begin{aligned} \Delta R_s &= \hat{R}_s - R_s \\ \Delta\sigma L_s &= \sigma\hat{L}_s - \sigma L_s \\ \hat{\underline{\lambda}}_r^{/} &= \frac{\hat{L}_r L_0}{\hat{L}_0 L_r}\underline{\lambda}_r \end{aligned} \tag{4.15}$$

Hence the equations for the voltage model in stator fixed coordinates are

$$\dot{\underline{x}}_{s(\alpha,\beta)} = K_2\underline{x}_{e(\alpha,\beta)} + K_1\dot{\underline{x}}_{e(\alpha,\beta)} - \Delta R_s\underline{i}_{s(\alpha,\beta)} \tag{4.16}$$

$$\dot{\underline{x}}_{e(\alpha,\beta)} = \hat{\underline{\lambda}}^C_{r(\alpha,\beta)} - \hat{\underline{\lambda}}^V_{r(\alpha,\beta)} = \hat{\underline{\lambda}}^C_{r'(\alpha,\beta)} - \hat{\underline{\lambda}}^{/}_{r(\alpha,\beta)} - \frac{\hat{L}_r}{\hat{L}_0}\underline{x}_{s(\alpha,\beta)} + \frac{\hat{L}_r}{\hat{L}_0}\Delta\sigma L_s\underline{i}_{s(\alpha,\beta)} \tag{4.17}$$

Therefore the corresponding equations in synchronous coordinates are

$$\dot{\underline{x}}_s = K_2\underline{x}_e - \left(K_1\frac{\hat{L}_r}{\hat{L}_0} + j\omega_e\right)\underline{x}_s + K_1\hat{\underline{\lambda}}_r^C - K_1\hat{\underline{\lambda}}_r^{/} + \left(K_1\frac{\hat{L}_r}{\hat{L}_0}\Delta\sigma L_s - \Delta R_s\right)\underline{i}_s \tag{4.18}$$

$$\dot{\underline{x}}_e = -j\omega_e\underline{x}_e + \hat{\underline{\lambda}}_r^C - \hat{\underline{\lambda}}_r^{/} - \frac{\hat{L}_r}{\hat{L}_0}\underline{x}_s + \frac{\hat{L}_r}{\hat{L}_0}\Delta\sigma L_s\underline{i}_s \tag{4.19}$$

The equations for the adaptive loop and mechanical model may be obtained from Fig. 4.3. Two states x_2 and x_3 are defined and have state equations

$$\dot{x}_2 = (\hat{\underline{\lambda}}_r^C \times \hat{\underline{\lambda}}_r^V) \tag{4.20}$$

$$\dot{x}_3 = K_t(\hat{\underline{\lambda}}_r^V \times \underline{i}_s) + K_5 x_2 + K_4 \dot{x}_2 - \hat{B}\hat{\omega}_r \tag{4.21}$$

4.3.3 Combined Equations

The resulting state equations in synchronous coordinates are linearised to give the standard form

$$\begin{aligned} \delta\dot{x} &= A\delta x + B\delta u \\ \delta y &= C\delta x + D\delta u \end{aligned} \tag{4.22}$$

where the state, input and output vectors are defined as

$$\delta x \triangleq (\delta\omega_r \quad \delta\hat{\lambda}_{rd}^C \quad \delta\hat{\lambda}_{rq}^C \quad \delta x_{sd} \quad \delta x_{sq} \quad \delta x_{ed} \quad \delta x_{eq} \quad \delta x_2 \quad \delta x_3)^T \tag{4.23}$$

$$\delta u \triangleq \delta i_{sq} \tag{4.24}$$

$$\delta y \triangleq \delta\hat{\omega}_r \tag{4.25}$$

In general the values of the different matrices depend on the operating point and on the different parameter errors (Appendix 3).

It is seen that $\delta y(s)/\delta u(s)$ can form the transfer function of the estimator dynamics and thus the open loop transfer function for designing the speed controller. However to use this approach for speed controller design is only possible when the estimator and motor parameters are equal. When they are not, $\delta y(s)/\delta u(s)$ yields root loci or Bode gain-phase plots which are too complex to be useful. The approach taken therefore is to design the speed controller on the basis of perfect estimator parameters (see Section 4.4) and to study the resulting closed loop system. The above matrix equations are thus augmented by a speed controller which for simplicity is assumed to be a conventional PI controller

$$\begin{aligned} \dot{x}_1 &= u_1 \\ y_1 &= K_{is}x_1 + K_{ps}u_1 \end{aligned} \tag{4.26}$$

Hence the resulting (still open loop) system can be written

$$\delta x' = (\delta x \quad \delta x_1)^T; \quad \delta y' = \delta y; \quad \delta u' = \delta u_1 \tag{4.27}$$

$$A' = \begin{pmatrix} A & BK_{is} \\ 0 & 0 \end{pmatrix}; \quad B' = \begin{pmatrix} BK_{ps} \\ 0 \end{pmatrix}; \quad C' = \begin{pmatrix} C & 0 \end{pmatrix}; \quad D' = 0 \tag{4.28}$$

Finally the estimated speed feedback signal can include a 1st order filter expressed as

$$\begin{aligned} \dot{x}_4 &= -ax_4 + au_4 \\ y_4 &= x_4 \end{aligned} \tag{4.29}$$

where x_4 is the filtered value of $\hat{\omega}_r$ and u_4 the unfiltered. Incorporating (4.27) and closing the loop gives

$$\delta x'' = (\delta x' \quad \delta x_4)^T; \quad \delta y'' = \delta y'; \quad \delta u'' = \delta u' + \delta y_4 \tag{4.30}$$

$$A'' = \begin{pmatrix} A' & -B' \\ aC' & -a \end{pmatrix}; \quad B'' = \begin{pmatrix} B' \\ 0 \end{pmatrix}; \quad C' = \begin{pmatrix} C & 0 \end{pmatrix}; \quad D' = 0 \tag{4.31}$$

From (4.31) the pole-zero positions of the closed loop transfer function $\delta y''(s)/\delta u'(s) = \delta\hat{\omega}_r/\delta\omega_r^*$ can be derived.

4.3.4 Calculation of Quiescent Points

Once the linear equations are obtained, they need to be evaluated at the particular operating point. Since the speed controller and feedback filters are linear, only the linearised matrices $\boldsymbol{A}$, $\boldsymbol{B}$ and $\boldsymbol{C}$ in (4.22) need to be considered ($\boldsymbol{D}$ = 0). The operating point $(x_0, u_0, T_{m0}, \underline{\hat{\lambda}}'_{r0})$ is obtained by solving

$$0 = f_i(x_0, u_0, T_{m0}, \underline{\hat{\lambda}}'_{r0}) \tag{4.32}$$

Since the system (4.32) consists of nine equations and the initial condition vector is of dimension thirteen, the initial conditions can be uniquely determined by choosing the values of three independent variables. The natural choice would be $(u_0 = i_{sq0}, T_{m0}, \underline{\hat{\lambda}}'_{r0})$, however ω_{r0} is preferred to T_{m0}; and i_{mrd0} is used instead of $\underline{\hat{\lambda}}'_{rd0}$ $(\underline{\hat{\lambda}}'_{rq0} = 0)$ since the frame of reference is assumed to be aligned with the rotor flux, without loss of generality. Therefore the conditions determining the operating point of the linearised system are i_{sq0}, ω_{r0} and i_{mrd0}. However most of the functions f_i in (4.32) also depend on the parameter estimates used in the MRAS-CLFO. Hence the value of x_0 also depends on these parameters; i.e. for a given set of values $(i_{sq0}, \omega_{r0}, i_{mrd0})$, there are different values of x_0 depending on the parameter errors (and even for different adaptive and coupling controllers). Equation (4.32) is solved for a particular set of observer parameters by using the software package MAPLE as a function of $(i_{sq0}, \omega_{r0}, i_{mrd0})$, and solved numerically for each operating point by using MATLAB.

4.3.5 Effect of Parameter Inaccuracies on Steady State Speed Error

The calculation of the quiescent values permits an easy calculation of the errors in steady state speed estimate caused by parameter inaccuracies. The value of the estimated speed is obtained as follows

$$\hat{\omega}_{r0} = \frac{1}{\hat{J}} x_{30} \tag{4.33}$$

where x_{30} is calculated following the procedure in the previous section. Equation (4.33) is calculated considering full load (i_{sq0} = 4 A), rated flux (i_{mrd0} = 2.2 A) for different operating speeds and parameter errors. Full load is chosen since it represents the worst situation with respect to speed estimate errors. The effect of incorrect estimator parameters on the accuracy of the speed estimator is shown in Fig. 4.7 and agrees with previous results [46]. The speed error is defined as $\hat{\omega}_r - \omega_r$.

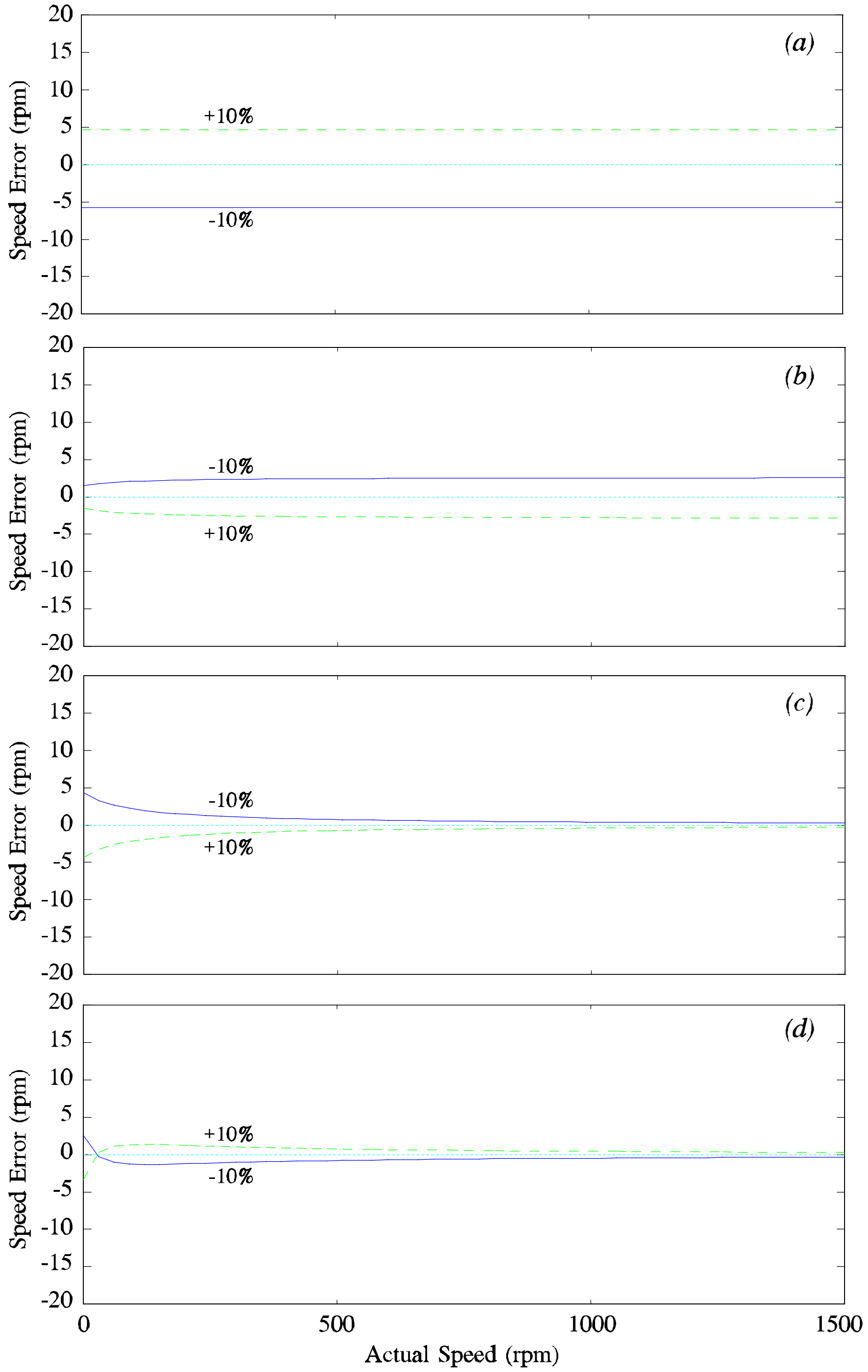

Figure 4.7 Estimated speed error for inaccurate parameters. ***(a)*** T_r; ***(b)*** σL_s; ***(c)*** L_0; ***(d)*** R_s

The conclusion is that errors in T_r have most effect on steady state accuracy. The second parameter in importance is σL_s, whereas the effect of R_s and L_0 is only significant at low speeds. These results are presented to illustrate the effects of errors on the different parameters and to obtain a quantitative measure of the steady state speed errors produced by each parameter. The effect of the adaptive MRAS loop bandwidth on the speed error has not been considered in any depth. The parameter variation used in this test (±10%) is considered to reflect a realistic situation, since it is difficult to calculate parameters like σL_s with accuracy higher than 10%; stator and rotor resistances can easily vary by this amount due to thermal changes; and L_0 can vary easily by 10% with changing flux (or even with changing load). For constant flux operation, magnetising inductance can be determined with an accuracy higher than 10%. This confirms the result of Fig. 4.7d which shows that errors in L_0 have a lesser effect on steady state speed accuracy. It is worth noting that these results have been obtained for the MRAS system alone, without closing the speed loop and therefore are only valid provided that the resulting closed loop system is stable.

4.3.6 Plots of the Closed Loop Pole-Zero Loci

An analytical solution of the transfer function between reference and estimated speed from (4.31) is generally too cumbersome to be useful. A graphical representation of the poles and zeroes of this transfer function for different parameters is more useful in order to study the small signal stability of the closed loop sensorless system. In all studies that follow, the pole-zero positions are plotted with ω_{r0} as a parameter. The principal pole-zero movement derives from the ω_e-dependent pole-zero pairs of the estimator deriving in turn from the implicit transformation into synchronous coordinates.

These estimator pole-zero pairs can be shown to be cancelling if the estimation parameters are correct. If not, the pole and zero of each pair will diverge causing the loci of the closed loop roots (for variable loop gain and at a given value of ω_{r0}) to branch between them. It is not possible to infer from such plots what the shape of these branches will be. This is why all studies will show the loci of the closed loop poles and zeros for varying ω_{r0} and fixed controller gain. All the plots have been obtained considering rated flux (i_{mrd0} = 2.2 A) and full load (i_{sq0} = 4 A). Only results at full load are presented since it exacerbates the effect of zero-pole divergence. It is also noted that since the pole-zero pairs derive from the estimator, they will be present in any closed loop transfer function that includes it. Thus there is no loss of generality in using the reference speed demand as the closed loop input.

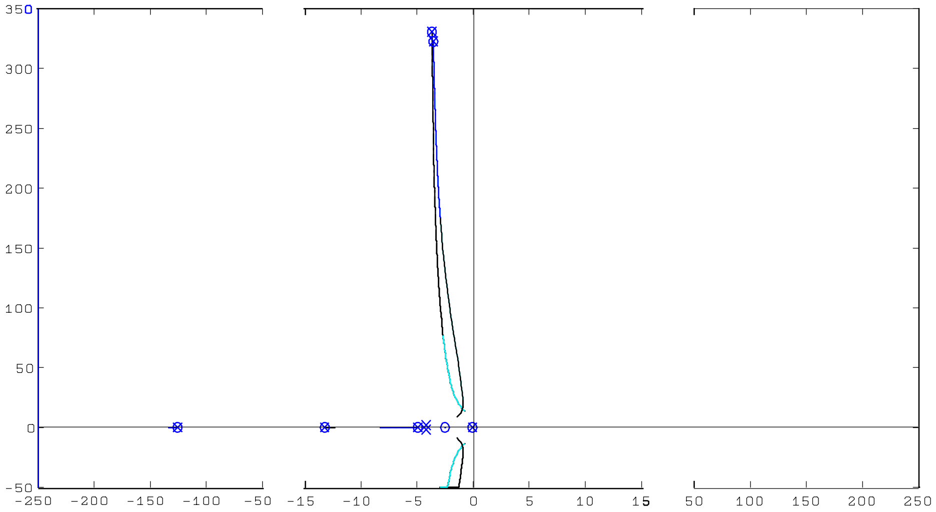

Figure 4.8 Pole-zero loci for perfect estimator parameters

The loci are plotted for ω_{r0} varying from 0 to 50 Hz (electrical). However ω_{r0} is not shown on the loci since the value is very close to the frequency of the oscillatory poles and thus can be approximated from the imaginary axis of the plot (in rads^{-1}). The pole-zero loci for the case when the estimator parameters are perfect are shown in Fig. 4.8. Only the closed loop poles and zeros deriving from the speed controller design remain. For perfect estimator parameters, the transfer function of the MRAS-CLFO reduces to

$$\frac{\hat{\omega}_r}{i_{sq}} = \frac{K_t \lambda_{rd0}}{sJ + B} \tag{4.34}$$

and the speed controller can be designed assuming a 1st order mechanical pole.

It may be noted that the moment of inertia of the experimental drive is 0.3 kgm^2 which is large for the power rating. This arises from the motor being loaded by an old DC machine dynamometer whose inertia is nearly 90% of the total. Since experimental results are used to verify the analysis, the large inertia is used in the simulations also. Fortunately, the effect of inertia on the results is simple to predict (and is discussed in Section 4.5) so that the use of a high inertia is of no particular import.

4.4 Effect of Incorrect Estimator Parameters

In Sections 4.4.1 to 4.4.4, the closed-loop pole-zero positions are plotted for variations in ω_{r0}. The results are for the adaptive MRAS loop design with ω_{ad} = 20 Hz as described in Section 4.2, and for a speed loop natural frequency ω_n of about 4 rads^{-1}. It is emphasized that the degree of pole-zero divergence illustrates in this chapter reduce as ω_n and i_{sq0} are reduced. Values of ω_n and i_{sq0} have been chosen to exacerbate the effect of pole-zero divergence. No filter is included in the speed estimate feedback path.

4.4.1 Variations in the Magnetising Inductance - L_0

Figures 4.9 and 4.10 show the closed loop pole-zero positions when the estimated value of L_0 varies by -10% and +10% from the true value respectively. The non-cancellation of the (nearly) ω_e-dependent poles is immediately evident. For the case when L_0 is underestimated (Fig. 4.9), the separation is not severe and the residuals of the closed loop poles are small. Nevertheless, since the poles cause very lightly damped oscillations at near ω_e, corresponding transient oscillations may appear in the response. The overestimated case is more serious in that the zeros have significantly diverged. The transient oscillations caused by the pole-pairs will therefore be increased. The close proximity of the closed loop poles to the imaginary axis is cause for concern.

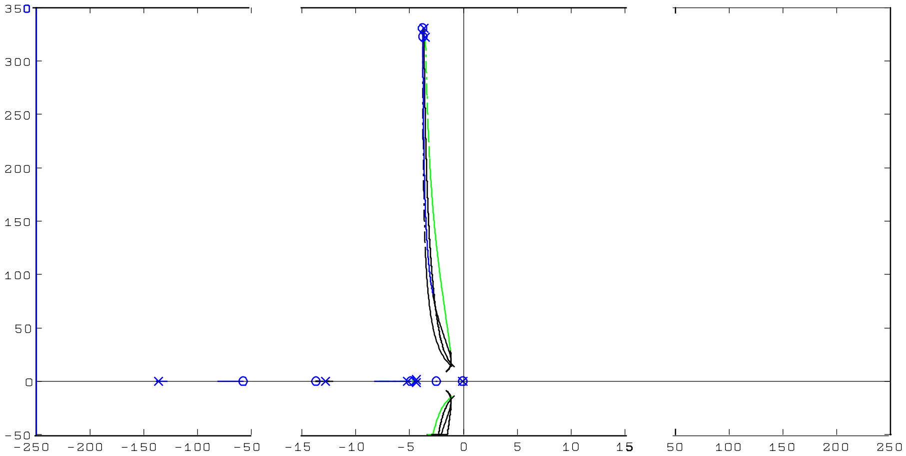

Figure 4.9 Pole-zero loci for varying speed and estimated L_0 = 0.9L_0

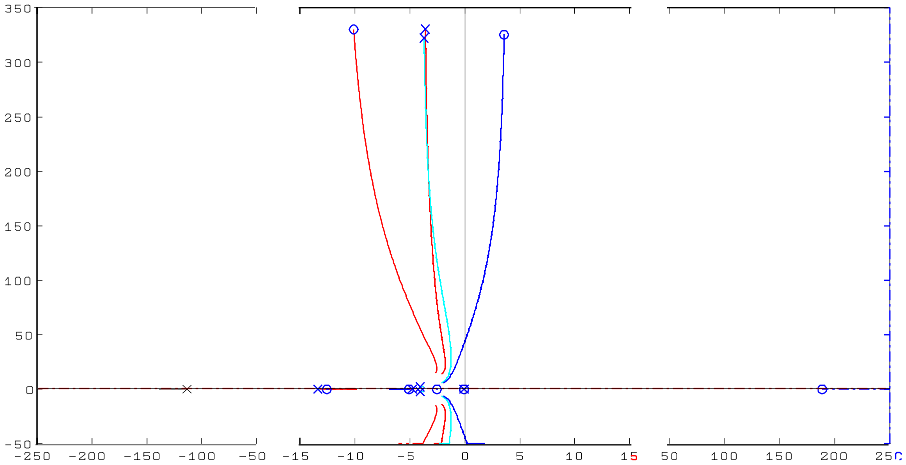

Figure 4.10 Pole-zero loci for varying speed and estimated $L_0 = 1.1L_0$

4.4.2 Variations in the Rotor Resistance - R_r

Figures 4.11 and 4.12 show the loci when the estimate of R_r is -10% and +10% from the true value. Of interest is the right-hand half zero in Fig. 4.12 (which also occurred in Fig. 4.10) which implies that the estimated speed will initially go in an opposite direction to that demanded by a step input in speed demand. This is in fact a very common observation in experimental closed loop sensorless drives and will be seen in the results of Chapter 7.

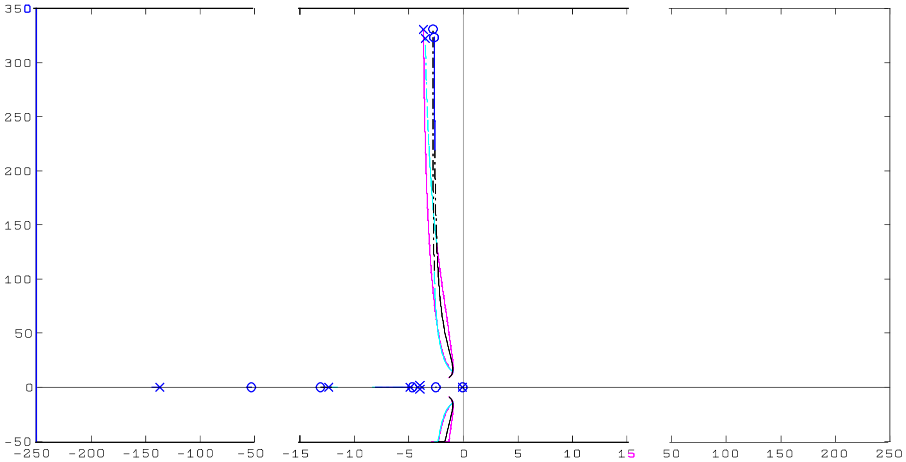

Figure 4.11 Pole-zero loci for varying speed and estimated $R_r = 0.9R_r$

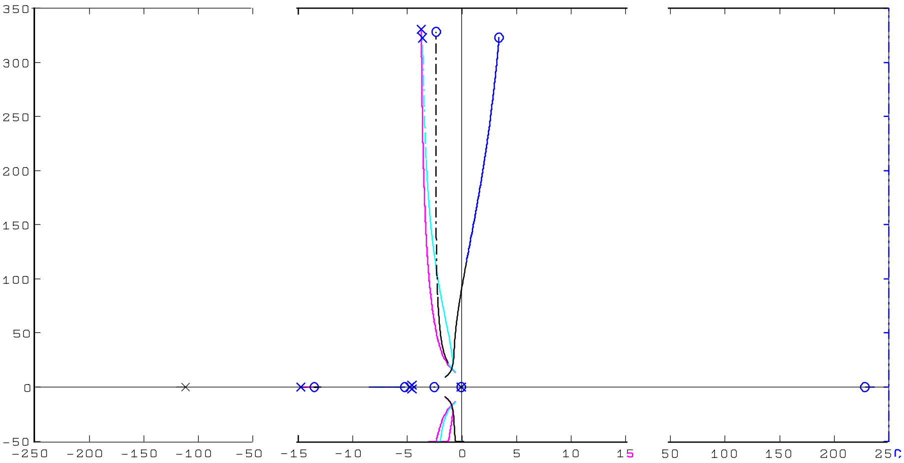

Figure 4.12 Pole-zero loci for varying speed and estimated R_r = 1.1R_r

4.4.3 Variations in the Motor Leakage - σL_s

A variation of -10% and +10% in this parameter causes the loci of Figs. 4.13 and 4.14 respectively. For both under and overestimates there is a significant residual from the one of the closed loop poles for speeds above approx. 15 Hz, so that oscillations in the system behaviour are easily induced. Further the residual and hence the size of transient oscillation will increase for an increase in speed.

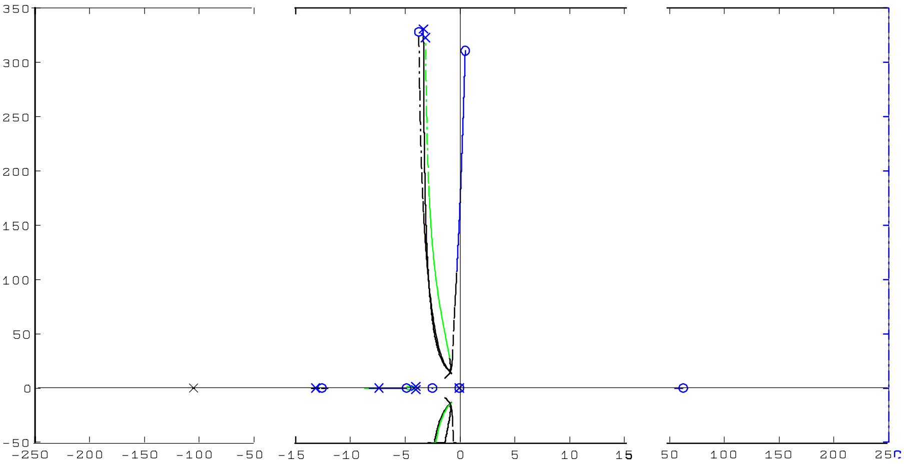

Figure 4.13 Pole-zero loci for varying speed and estimated σL_s = 0.9σL_s

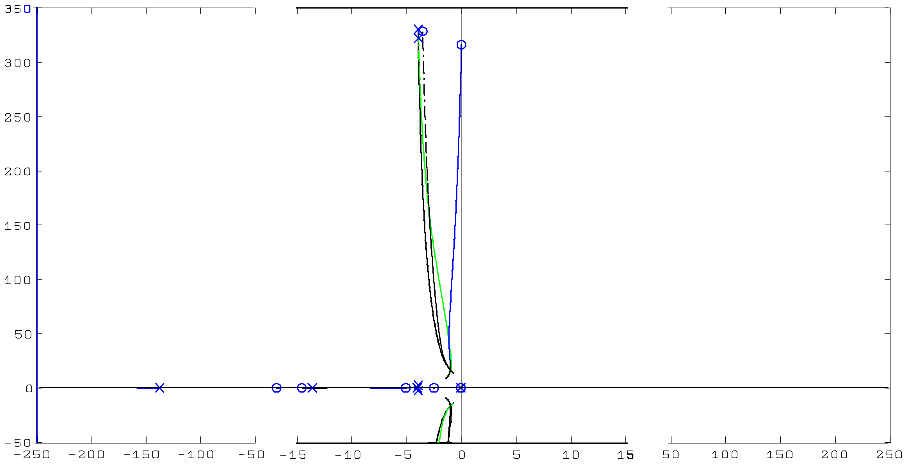

Figure 4.14 Pole-zero loci for varying speed and estimated σL_s = 1.1σL_s

4.4.4 Variations in the Stator Resistance - R_s

The 10% variations are shown in Figs. 4.15 and 4.16. Of all the parameters, R_s is found to have the most influence on system stability. For the underestimated case, the poles are always seen to shift to the left; however the pole-residuals are large causing substantial, albeit stable oscillations. For the overestimated case, the poles travel in the opposite direction and in this case instability occurs for all but very low frequencies.

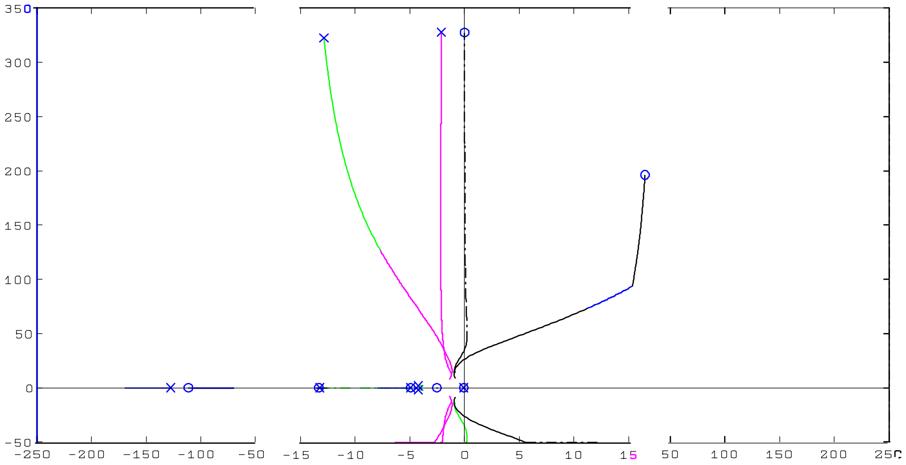

Figure 4.15 Pole-zero loci for varying speed and estimated R_s = 0.9R_s

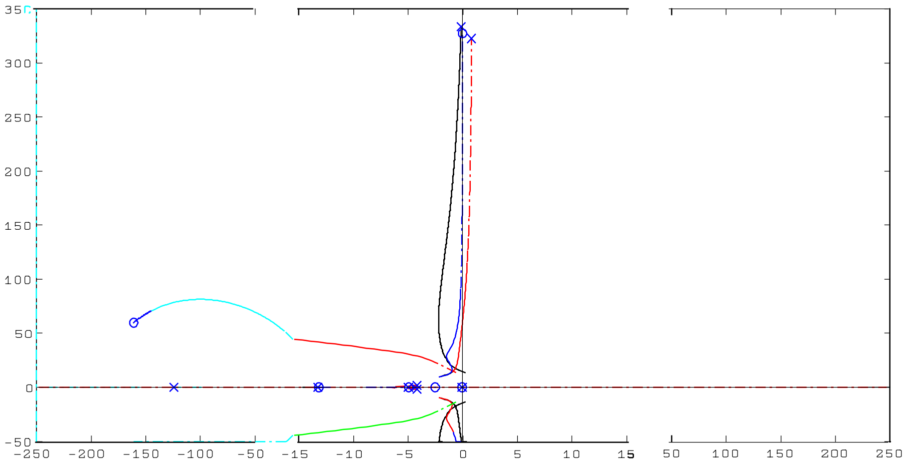

Figure 4.16 Pole-zero loci for varying speed and estimated R_s = 1.1R_s

This result is experimentally verified in Fig. 4.17 showing the estimated and real speed when the value of $\hat{R}_s$ is changed from 6.1 to 6.72 Ω (i.e. a 10% increase). As a consequence, the real and estimated speeds begin to oscillate, reaching a limit cycle when the speed controller saturates. The presence of this limit cycle will cause the average speed of the motor to drop. When the estimated R_s is restored to its original value, the oscillations decrease and eventually disappear. At the same time the machine returns to its original speed.

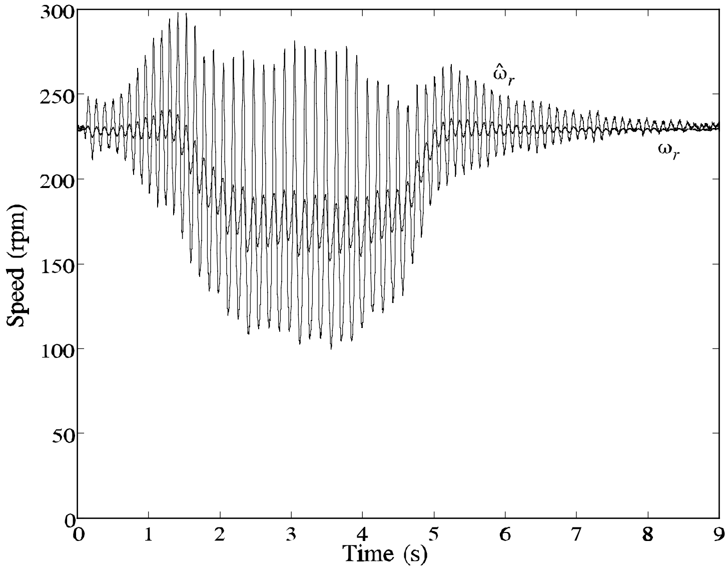

Figure 4.17 Instability in real and estimated speeds when the estimated R_s = 1.1R_s

Figure 4.18 shows the behaviour of the sensorless MRAS-CLFO system when $\hat{R}_s$ is reduced by 10%. As expected from Fig. 4.15, the operation of the system is stable, although small oscillations appear due to the excitation of the lightly damped poles by the step change in estimated resistance.

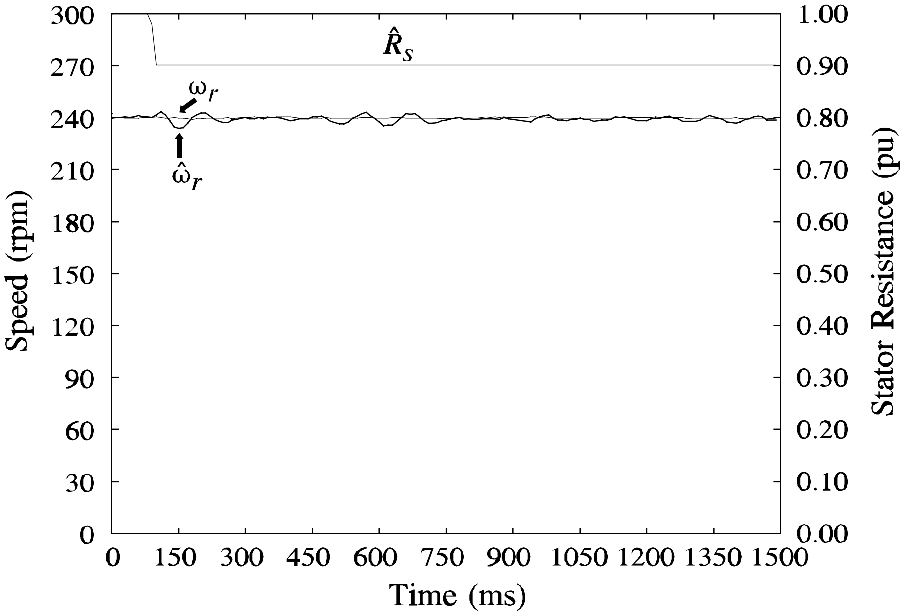

Figure 4.18 Stable operation when the estimated R_s is changed from $1.0R_s$ to $0.9R_s$

4.5 Effect of Loop Bandwidths

The movement of the pole-zero pairs with incorrect parameters is itself dependent on the natural frequencies of the adaptive loop - ω_{ad}, and the main speed loop - ω_n. Since the movement due to overestimation of R_s are always the most serious, results are shown for the condition that $\hat{R}_s = 1.1R_s$. Figures 4.19, 4.20 and 4.21 show the effect with ω_{ad} as 10 Hz, 20 Hz and 40 Hz respectively.

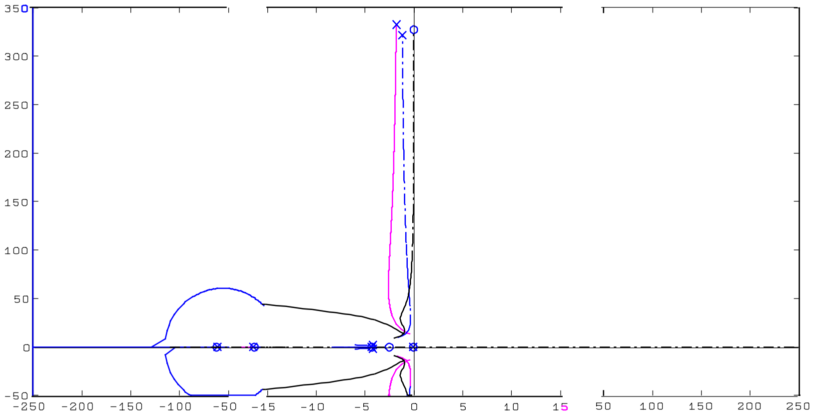

Figure 4.19 Pole-zero loci for ω_{ad} = 10 Hz with estimated $R_s = 1.1R_s$

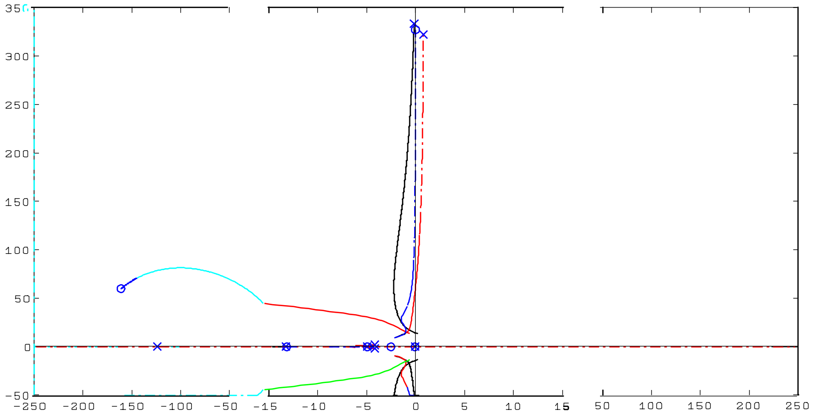

Figure 4.20 Pole-zero loci for ω_{ad} = 20 Hz with estimated $R_s = 1.1R_s$

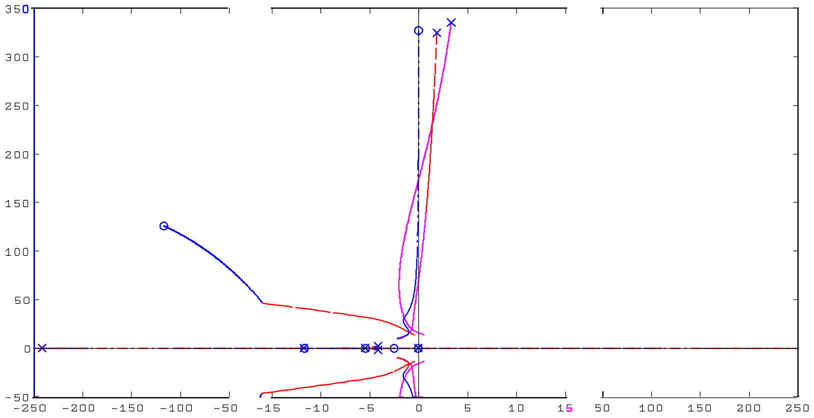

Figure 4.21 Pole-zero loci for ω_{ad} = 40 Hz with estimated $R_s = 1.1R_s$

It can be surmised that with ω_n = 4 rads^{-1}, the maximum ω_{ad} that can be attained before instability is about 15 Hz. With varying ω_{ad} a similar qualitative pole-zero movement with variations in the other parameters are also obtained. Since the movements are of less consequence than those due to R_s, they are not given here.

For investigating the variation with ω_n, the damping factor was set at 0.8 and ω_{ad} at 20 Hz. The results for ω_n of 2, 4 and 8 rads^{-1} are shown in Figs. 4.22 to 4.24. Increasing instability is seen which is not surprising since the speed controller can be viewed as a feedback gain between the output and input of the estimator. For a PI controller controlling a purely inertial plant, the proportional and integral gains can be easily shown to be

$$K_p = 2\zeta\omega_n J\,; \qquad K_i = K_p\zeta\omega_n \tag{4.35}$$

Thus if purely proportional control is used then for a given damping factor, the degree of oscillation or instability (for a given error in the estimator parameters) increases with the quantity $\omega_n J$ (and not ω_n). Other statements follow:

i) for a given set of parameter errors, then if $\omega_n J$ is held constant, the degree of oscillations increases with ω_{ad}.

ii) for a given set of parameter errors, $\omega_n J$ and ω_{ad} have an inverse relationship for a given stability (ie if one is increased the other must be decreased)

iii) *the less the error in the estimator parameters, the greater $\omega_n J$ can be before a specified degree of system oscillation occurs.*

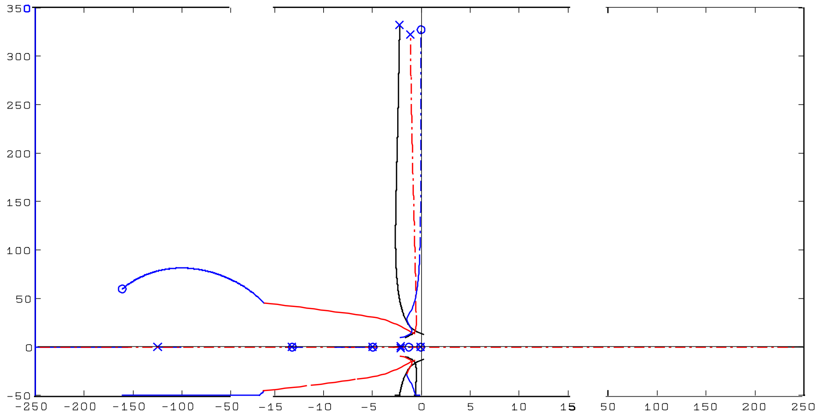

Figure 4.22 Pole-zero loci for ω_n = 2 rads^{-1}, ω_{ad} = 20 Hz and estimated R_s = 1.1R_s

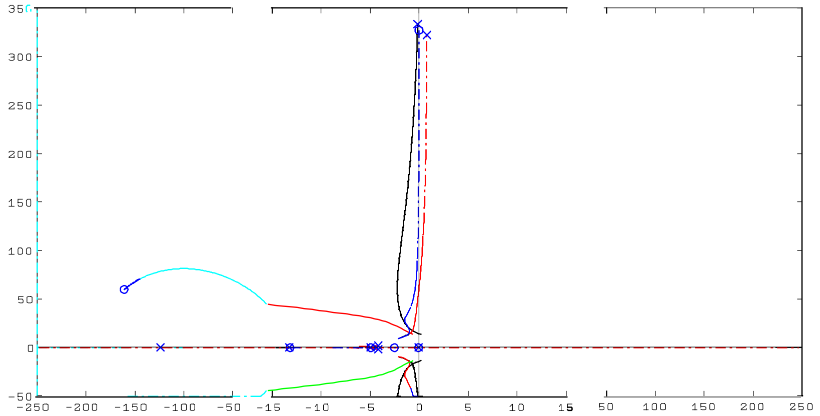

Figure 4.23 Pole-zero loci for ω_n = 4 rads^{-1}, ω_{ad} = 20 Hz and estimated R_s = 1.1R_s

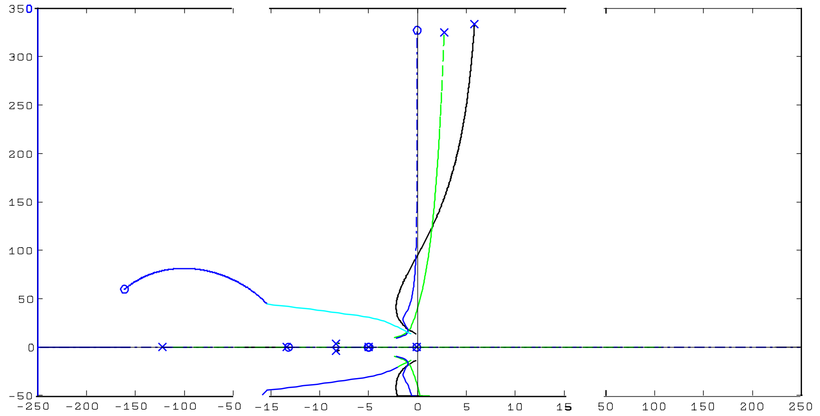

Figure 4.24 Pole-zero loci for ω_n = 8 rads^{-1}, ω_{ad} = 20 Hz and estimated R_s = 1.1R_s

For a given parameter error, ζ and ω_{ad}, the adjustment of ω_n and J keeping $\omega_n J$ constant does not result in exactly the same pole-zero movement due to the integrating term whose constant is not dependent on J. This can be seen in Fig. 4.25 in which J is reduced by a factor of 10 and ω_n is increased by 10, all other conditions being identical to the case of Fig. 4.20. Comparison with Fig. 4.20 shows the difference to be relatively small. However both sets of oscillatory poles have become marginally less oscillatory. This is a general trend; the integrating term has a secondary but stabilizing influence.

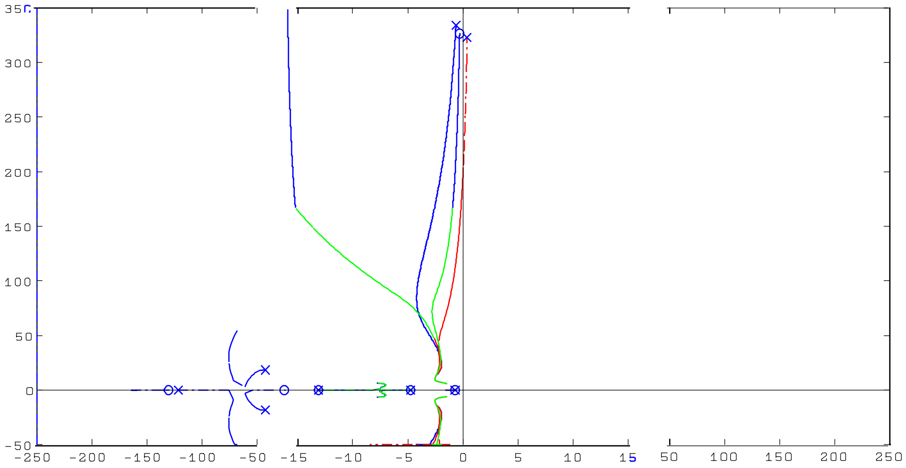

Figure 4.25 Pole-zero loci for J reduced by a factor of 10

Finally an increased value of $\omega_n J$ can be attained at higher operating frequencies through filtering the estimated speed signal. With the conditions pertaining to that of Fig. 4.20, Fig. 4.26 shows the effect of a 1st order 15 Hz filter. The poles are bent left at the higher frequencies. Care must be taken of course to ensure acceptable operation at frequencies that are within the filter bandwidth.

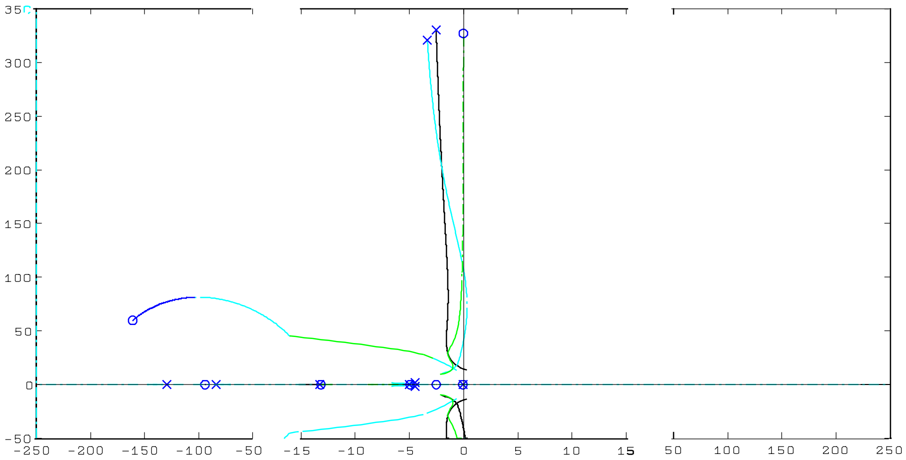

Figure 4.26 Effect of a 15 Hz filter in the feedback path

4.6 Discussion

The results of Sections 4.4 and 4.5 show that, from a practical viewpoint, a MRAS speed estimator with incorrect parameters can be considered as an encoder with inherent transient ripple. The improving effects of the speed estimate filter and the integrating component of the speed controller can be viewed in this light. The ripple is however closely related to the motor speed and at low speeds will be inside the speed controller bandwidth. It also constrains the magnitude of the design parameter $\omega_n J$ which if too high results in the ripple magnitude growing into instability. In an effort to reduce this ripple and hence to achieve as high a value of $\omega_n J$ as possible, a number of ground rules may be deduced:

1. The sensorless system is most sensitive to errors in R_s. Unless this parameter is identified on-line it is important that it is underestimated rather than overestimated. Fortunately a ‘cold’ R_s measure obtained during self-commissioning fortuitously provides this since the motor R_s can only increase during operation. Although underestimation may avoid instability, the ripple induced by even small errors in this parameter is likely to be the most significant factor in limiting $\omega_n J$ and thus obtaining comparable performance with sensored vector drives.
2. The estimated values of L_0, R_r and σL_s are of less importance but still cannot be ignored. Underestimation is preferred with respect to R_r and a "cold" value is appropriate. With respect to σL_s, overestimation is preferred, therefore the

value of σL_s obtained through self-commissioning [79] should be obtained under no load current since the reduced stator tooth saturation provides for a higher leakage value. A slightly "overfluxed" value of L_0 is also appropriate during parameter identification. Flux orientation is relied upon to keep L_0 and σL_s reasonably constant during motor operation. However it is noted that the ripple dependence on L_0 and σL_s may cause problems during field weakening operation. Errors in the R_r estimate are well known to be the biggest single factor effecting the accuracy of the speed estimate. On-line tuning for R_r can thus provide both for increased accuracy and the removal of the ripple dependence on this parameter.

3. The adaptive loop natural frequency ω_{ad} should be kept as low as possible whilst still obeying the natural observer condition $\omega_{ad} > \omega_n$ for good tracking. It is emphasised that ω_{ad}-induced ripple is dependent on $\omega_n J$ and not on ω_n. The nominal value of ω_{ad} used in this paper (which is high with respect to the nominal ω_n used) envisages ω_n values of up to 10 Hz which is still feasible for smaller drives.
4. The use of extra controller zeros, either with PID or with lead-type controllers, should be avoided as these will only amplify the ripple in the system.

A very significant result derives from the statement (iii) of Section 4.5. For a specified ripple, then the less the error in the estimated parameters, the greater $\omega_n J$ can be. Thus $\omega_n J$ can be used as a measure of goodness for the sensorless drive. The quantity $\omega_n J$ can be termed the closed loop natural angular momentum of the drive. Since it can also be derived for sensored vector drives, the measure provides for a direct quantitative comparison of sensorless and sensored drives. This will be considered in Chapter 7.

Although the stability analysis has been carried out on the MRAS-CLFO estimator, the results have a wider significance. For the rotor flux based MRAS estimators developed by Tamai and Schauder [82, 72], an almost identical behaviour is observed. It is felt that the oscillatory poles arise from an implicit transform of the motor equations into synchronous coordinates. If this is true then the system oscillation is likely to affect speed estimators based on observer or EKF techniques. In fact, in observer theory, it is known that the poles and zeros of the plant are cancelled by those of the observer model (so that the closed loop system poles are the union of the closed loop observer and controller poles considered separately). However, the cancellation is incomplete if the observer model parameters are in error. The effect of this for observer based sensorless drives having large $\omega_n J$ values certainly merits further study.

4.7 Conclusions

In an effort to obtain closed loop speed bandwidths from sensorless vector controlled induction motor drives that are comparable to sensored drives, it has been found that MRAS based speed estimators yield speed estimates corrupted by transient oscillations at very near the excitation frequency. This chapter has analyzed the small signal stability of a MRAS-CLFO estimator embedded in a closed loop drive. It has been shown that the transient oscillations derive from incorrect estimator parameters. The oscillations, which can lead to unstable operation, are also dependent on the natural frequency of the adaptive MRAS loop and, more importantly, upon the closed loop natural angular momentum of the drive - $\omega_n J$. This parameter represents a goodness measure of the closed loop sensorless drive and one which can be used for comparisons between sensorless and sensored drives. In order to increase this measure towards that of a sensored drive, on-line parameter tuning is necessary.

Chapter 5 Speed Measurement Using Rotor Slot Harmonics

5.1 Introduction

Rotor speed estimation from terminal magnitudes of the induction machine is needed for sensorless drives since rotor speed is required for field orientation and/or for speed control. Different kinds of speed estimators have been developed in the past (see Section 3.4). These methods often assume linear models of the machine and time-invariant parameters, and therefore will give a speed estimate with poor accuracy. Moreover, the accuracy of these methods will also change for different operating points, since the actual parameters of the machine will vary for different load conditions, flux level and temperature.

In this work the speed estimate is only used for purposes of speed control and the field orientation is obtained from a rotor flux observer that in general is independent of the speed estimate dynamics. As discussed in Chapter 3 the direct field orientation thus obtained provides better torque control than an indirect field orientation requiring the speed estimate for flux angle calculation. Nevertheless there are many applications in which accurate speed signals are required in the control loop. These include speed holding, speed matching, electronic gearboxes and speed regulation under load torque disturbances.

The problem of accuracy can be overcome if any form of speed estimate which is independent of the machine parameters can be obtained. Constructional characteristics of the induction machine can be used to obtain rotor speed or position estimation. Methods based on constructional characteristics can be considered as actual speed measurements, since they do not depend on non-linear time-varying parameters. Constructional factors used for speed estimation are usually the ones producing magnetic saliencies that are dependent on the rotor position. These normally occur due to the existence of stator and rotor slotting, and also to the difficulty in manufacturing the rotor as an ideal cylinder or even aligning rotor and stator perfectly. Therefore a rotor position dependent term will appear in the inductive parameters of the machine which in turn can be used to derive the rotor speed and/or position. Magnetic saliencies can be enhanced or even intentionally introduced in order to increase these rotor position dependent terms and ease the task of rotor speed and position measurement.

Attempts to measure the rotor position using magnetic saliencies include the use of complicated state observers to model these saliencies [24]. This technique requires extensive testing of the machine and considerable computation, therefore its application to real-time control systems is unlikely. An alternative method is the tracking of eccentricity harmonics [42]. In this work only results for rated speed are presented. Since important aspects, such as accuracy, robustness, dynamics and measurement range are not discussed, it is difficult to evaluate the validity of this method. Nevertheless, it is reasonable to expect poor dynamic performance and poor robustness to load and speed changes, due mainly to the analog implementation using high order switch capacitor filters. Injection of short high frequency pulses has also been used [74], but it is only applicable to highly saturated machines. A more promising technique consists on modifying the machine rotor to create a periodic variation of the leakage inductance [47]. To obtain position information with this method, a high frequency modulating signal needs to be injected in the machine, following a similar method to the one employed for Permanent Magnet Synchronous Machines (PMSM) [51]. Although this method gives very good results for machines with pronounced saliencies, like the PMSM, its reliable application to induction motors is still under development and restricted to very low speeds.

It is also possible to derive the rotor speed from the harmonics in the stator current produced by the rotor slotting. Figure 5.1 shows for example the current spectrum, with two harmonics of the fundamental (f_{11} and f_{13}) and two harmonics produced by the rotor slots ($f_{sh(1)}$ and $f_{sh(-3)}$). The frequency of these harmonics is a function of the rotor speed, therefore the machine rotational speed can be derived from the measurement of the rotor slot harmonics frequency.

The existence of such speed related rotor slot harmonics (RSH) present in the stator line current or voltage can provide an independent speed measurement and it will be shown in this chapter that the accuracy and tracking robustness attainable is of a sufficient quality as to justify the exploitation of the measurement in a sensorless vector control scheme. Since, as will be shown, the principal limitation is the measurement bandwidth, it is envisaged that the measurements will be used to tune MRAS speed estimators against motor parameter variations.

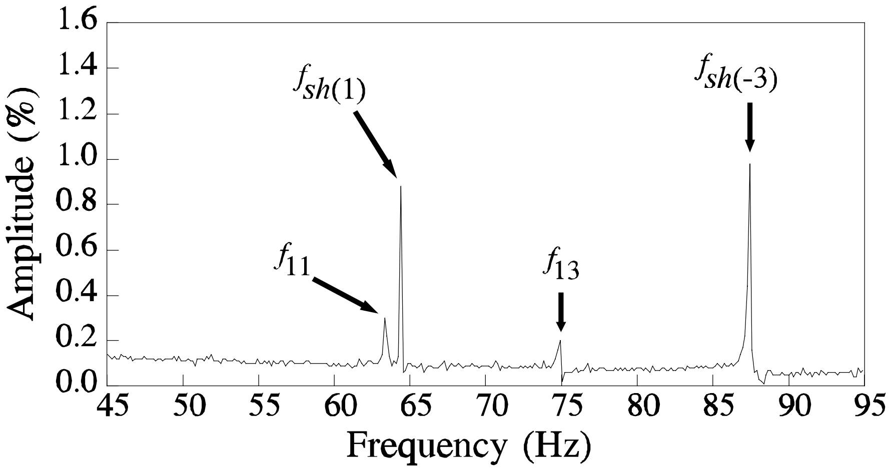

Figure 5.1 Line current spectrum showing two rotor slot harmonics

The principle of speed detection using rotor slot harmonics is in itself not new. Analogue filtering techniques have been used to provide steady state slip control [45, 76], whilst an improved analogue technique using switched capacitor filters has been exploited [86]. The use of a phase locked loop to track the harmonics derived from stator voltages has also been reported [90] but this demanded the use of a specially modified motor.

An all digital approach based on a Discrete Fourier Transform (DFT) is superior to analogue tracking techniques for a number of reasons:

i) digital techniques do not suffer from analogue component tolerance or drift, hence greater accuracy is attainable.

ii) tracking algorithms can be developed to discern the rotor slot harmonics from inverter harmonics which interfere with each other in the low speed range. Analogue techniques would certainly fail in such situations.

iii) the dynamic characteristics of a digital solution based on a DFT are entirely predictable and not subject to the oscillatory dynamic characteristics of low bandwidth band-pass filters.

Initial investigations into a DFT based identifier [31] was carried out using batch processing ‘off-line’ to validate the basic feasibility of this technique. An alternative digital technique for speed measurement from rotor slot harmonics was presented in [44]. The technique consisted in an intentional aliasing of the spectrum, by sampling the stator current at a frequency twice the fundamental ($2f_0$). This would create an aliased spectrum with only two peaks, one related to the fundamental component and another one related to the slot harmonic. However this technique presents disadvantages in terms of accuracy for a given record duration. This is due to the long samples required at low speed ($36/f_0$) and to the need of a previous knowledge of f_0 for the spectral aliasing (by using this technique the errors on f_0 estimation will also be present in the rotor slot harmonic). Moreover this method will certainly run into difficulties when the rotor slot harmonic is close to an f_0 harmonic of relatively high amplitude, since the existence of a high amplitude f_0 component very close to a rotor slot harmonic makes difficult the accurate measurement of the RSH frequency. For these reasons, the performance of this method cannot be better than that of the non-interpolated DFT method presented in this chapter, and substantially worse than the interpolated DFT algorithm.

This chapter describes the work carried out in order to obtain a robust, reliable and accurate ‘on-line’ speed measurement based on the rotor slot harmonics, suitable to tune an MRAS based speed estimator against parameter variation. To accomplish this objective, tracking algorithms to enhance the robustness of the measurement have been developed. Moreover this is the first work that investigates the performance of an RSH-based speed measurement system during speed transients. Methods for obtaining maximum speed accuracy from the sampled line currents are fully discussed and implemented. Furthermore, the performance of the DFT with regard to record length, sampling frequency and motor speed and load conditions is also assessed.

5.2 Speed Detection using the Rotor Slot Harmonics

A rigorous derivation of the effects produced by slotting in induction machines is beyond the scope of this work and good in depth texts can be found in [32, 39, 4]. However a summary will be given here, focusing on the demonstration of speed measurement using the rotor slot harmonics.

The slotting of rotor and stator of an induction machine produces a regular variation of the air gap flux density B. For convenience, the flux density B is

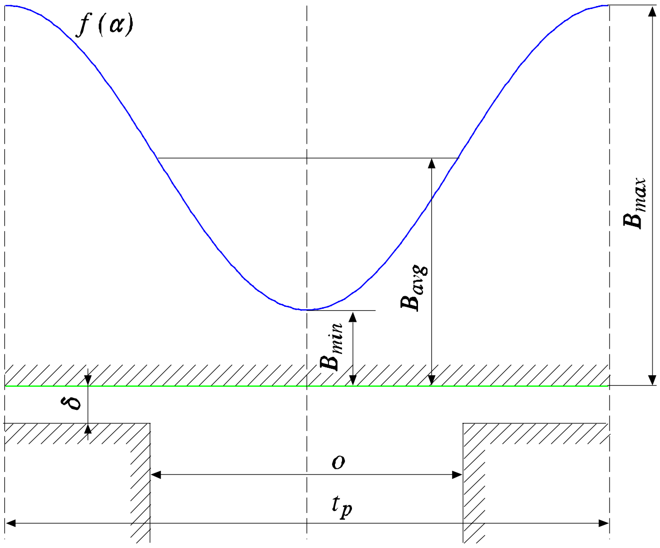

Figure 5.2 Effect of slotting on the air gap magnetic induction

defined as the flux density on the stator surface, in this way all the flux lines are perpendicular to the considered surface, since the permeance of the stator is considered infinity. Figure 5.2 shows the typical distribution of B for a one-side slotted machine for unit magnetic potential (F) difference between rotor and stator. The average flux density is B_{avg}. However, an ideal machine formed by two smooth (unslotted) cylinders would have a flux density of B_{max}. Therefore, the presence of slotting implies an increase of the average effective air gap thickness.

To consider the regular variation of the air gap, λ is defined as the reciprocal of the effective air gap length. Therefore the following equation will hold

$$H(\alpha,t) = F(\alpha,t)\,\lambda(\alpha) \tag{5.1}$$

H being the magnetic field intensity and F the magnetomotive force. It is possible to obtain an expression for λ from the following relation

$$B(\alpha,t) = \mu_0\,H(\alpha,t) = \mu_0\,F(\alpha,t)\,\lambda(\alpha) \tag{5.2}$$

In general F, B and λ are functions of the mechanical angle α. From Fig. 5.2 it can be seen that $f(\alpha)$ is equal to the variation of B for unit magnetic potential ($F = 1$), hence

$$f(\alpha) = \mu_0 \lambda(\alpha) \tag{5.3}$$

Therefore, knowing the flux density distribution over the slot pitch $f(\alpha)$, an expression for $\lambda(\alpha)$ can be easily derived. For a machine with slotted stator and smooth rotor the reciprocal of the effective air gap length will vary with a period equal to the tooth width. Therefore, the corresponding expansion in Fourier series will be

$$\lambda_1(\alpha) = a_o - \sum_{k=1}^{k=\infty} a_k \cos k Z_1 \alpha \tag{5.4}$$

where Z_1 is the number of stator slots. A similar equation can be derived for the case of a machine with slotted rotor and smooth stator

$$\lambda_2(\alpha) = b_o - \sum_{k=1}^{k=\infty} b_k \cos k Z_2 \alpha \tag{5.5}$$

where Z_2 is the number of rotor slots. When the rotor is turning at the mechanical angular velocity ω_r, the term $\omega_r t$ has to be added to the mechanical angle (α), to compensate for the angular displacement of the rotor with respect to the stator

$$\lambda_2(\alpha) = b_o - \sum_{k=1}^{k=\infty} b_k \cos k Z_2 (\alpha + \omega_r t) \tag{5.6}$$

On the other hand, assuming a sinusoidal supply of angular frequency ω_0, the magnetomotive force can be expressed as

$$F(\alpha,t) = \sum_{v=1}^{v=\infty} F_v \sin\left(\omega_0 t \mp v p \alpha\right) \tag{5.7}$$

where the term $\nu p\alpha$ represents the space harmonics due to the windings distribution. Considering a singly slotted machine and substituting (5.6) and (5.7) into (5.1)

$$\begin{aligned} H(\alpha,t) &= \sum_{v=1}^{v=\infty} \Big\{ F_v b_0 \sin(\omega_0 t \mp vp\alpha) - \\ &- \frac{F_v}{2} \sum_{k=1}^{k=\infty} b_k \{ \sin[(\omega_0 - kZ_2\omega_r)t + (kZ_2 \mp vp)\alpha] + \\ &+ \sin[(\omega_0 + kZ_2\omega_r)t - (kZ_2 \pm vp)\alpha] \} \Big\} \end{aligned} \tag{5.8}$$

The magnetic flux distribution in a coil parallel to the longitudinal axis of the machine is

$$\Phi(t) = \mu_0 l \int_{-1/2\alpha_y}^{+1/2\alpha_y} H(\alpha,t)\,\mathrm{d}\alpha \tag{5.9}$$

l being the axial length of the machine, and α_y the periphery angle corresponding to the coil pitch. Hence the induced electromotive force in a coil is

$$e(t) = -\mu_0 l \frac{\mathrm{d}}{\mathrm{d}t} \int_{-1/2\alpha_y}^{+1/2\alpha_y} H(\alpha,t)\,\mathrm{d}\alpha \tag{5.10}$$

Therefore the resulting electromotive force will be

$$\begin{aligned} e(t) &= \sum_{v=1}^{v=\infty} \Big\{ E_v \sin(\omega_0 t + \Psi_v) - \\ &- \sum_{k=1}^{k=\infty} E_{v,k} \{ \sin[(\omega_0 - kZ_2\omega_r)t + \Psi'_{v,k}] + \\ &+ \sin[(\omega_0 + kZ_2\omega_r)t + \Psi''_{v,k}] \} \Big\} \end{aligned} \tag{5.11}$$

The induced emf consists of a fundamental of frequency ω_0 plus two sidebands at frequencies $kZ_2\omega_r \pm \omega_0$. This could have been deduced from a direct observation of (5.6) and (5.7), considering that (5.1) represents the *amplitude modulation* of λ and F. These emf harmonics will result in current harmonics of the same frequency.

So far the above analysis has considered a machine with slots only in the rotor, and fed by a sinusoidal supply. It can be shown [39] that the presence of stator slotting does not introduce any additional speed dependent harmonics. However a non-sinusoidal supply and saturation within the machine will introduce new speed dependent harmonics. If a non-sinusoidal supply is considered (5.7) can be expressed as

$$F(\alpha,t) = \sum_{n=0}^{n=\infty} \sum_{v=1}^{v=\infty} F_v \sin\left(n\omega_0 t \mp vp\alpha\right) \tag{5.12}$$

n being the order of the supply harmonic. Each supply harmonic will introduce a new set of speed dependent air-gap flux harmonics, in a similar fashion as the fundamental supply harmonic. Saturation will introduce a regular variation of the iron magnetic permeance. If this variation is included in (5.9), it can be shown following a similar procedure that new rotor slot harmonics will also be produced. Therefore a general expression for the rotor slot harmonic frequencies is

$$\omega_{sh} = kZ_2\omega_r + \kappa\omega_0 , \qquad \kappa = 0, \pm 1, \pm 2, \ldots \tag{5.13}$$

where the factor κ is introduced to take account of these new rotor slot harmonics. From this equation, the rotor speed (in electrical Hz) can be expressed as

$$f_r = \frac{p}{kZ}\left(f_{sh} + \kappa f_0\right) \tag{5.14}$$

Not all of the air-gap flux harmonics will induce current harmonics which are detectable. The coefficients of α in (5.8) define the pole numbers of the fundamental harmonics (νp) and the slots harmonics ($kZ_2 \pm \nu p$, or more generally $kZ_2 \pm \kappa\nu p$). When the pole numbers of air-gap flux harmonics are $3j$ multiples of the pole number of the fundamental flux, j being a positive non-zero integer, the voltages induced in all three phases of a balanced machine are in phase and have the same amplitude. These zero sequence components of voltage have no path through a three wire supply and therefore do not produce harmonic line currents. However they will produce circulating currents in the winding of a delta connected machine.

A slot harmonic where $k = 1$ and $\kappa = 1$ will always exist. For the closed rotor slot, 4 kW, 4-pole, 415 V, 50 Hz, ASEA induction motor used in this study, the number of rotor slots (Z) is 28, and under motoring conditions $\kappa = +1, -3$ were always detected, whilst $\kappa = -5, +7, -9$ and -11 were detectable under loaded conditions. Note that although slot harmonics for $k > 1$ have also been observed, their amplitude is very small, and from now on it is assumed that $k = 1$.

Defining the number of rotor slots may seem at first sight to be a problem with this method of speed estimation should the information not be available from the manufacturer. In reality however, there are few combinations of rotor and stator slotting for the machine designer to choose which give acceptable performance. The number of rotor slots influences crawling, cogging, acoustic noise, stray loss and shaft voltages. Die casting requirements for mass production normally favour the larger slots consequent upon choosing a lower number of rotor than stator slots. Typically, for the most common 4-pole machines, a rotor with 8 fewer slots than the stator is frequently chosen. Much rarer combinations would be within ±3 slots of this value. The stator slot numbers for 4-pole machines range from 36, for a small 4 kW design, through 48 and 60 to 72 for a machine of about 100 kW rating. The increment of 12 slots being fixed by the 3 phases and the 4 poles for normal, integral-slot windings. This explains why the ASEA motor, which has 36 stator slots, has the expected 28 rotor slots.

5.3 Spectral Analysis using the Discrete Fourier Transform

Knowledge of the frequency of the fundamental component of the stator current and of the rotor slot harmonic provides an immediate measurement of the rotor speed. Therefore, spectral analysis of the line current is carried out to obtain the above mentioned frequencies.

The DFT of a sequence $x(n)$ is defined as [5]

$$X(k) = \sum_{n=0}^{N-1} x(n) W_N^{nk} \qquad k = 0,\ 1,\ \cdots,\ N-1 \tag{5.15}$$

where $W_N = e^{-j(2\pi/N)}$. Direct computation of the DFT is very inefficient, and therefore almost never carried out in practice. Normally most efficient algorithms, based on the Fast Fourier Transform (FFT) are used to compute the DFT. In this particular case a real valued FFT based on a split radix algorithm [75] is recommended in that it minimises the number of multiplications and additions. The algorithm acts on 2^N samples over a acquisition time T_{aq} with sampling frequency f_{samp}. This gives a spectrum of base resolution $f_{res} = 1/T_{aq}$ over the frequency range 0 to $f_{samp}/2$.

The frequency of the fundamental component of the stator current (f_0) can be easily obtained from the result of the FFT. However the resulting spectrum will include the inverter PWM harmonics of f_0. These will interfere with the detection of the slot harmonics and make speed tracking a non-trivial task even when the spectral record is available for algorithmic perusal. In fact the severity of the interference at low speed results in a low speed limit for the speed tracking. The methods proposed for rotor slot harmonic detection are illustrated in section 5.7.

An additional problem is the inaccurate frequency information provided by the FFT when the frequencies to be detected are not integer multiples of f_{res}. This has two important effects. The first is that the measured frequency will be subject to quantization error with respect to the real frequency. This is caused by the fact that the FFT only computes the spectrum at discrete frequencies. This error is said to affect the *accuracy* and is considered in section 5.4. The second effect is that of spectral leakage. This effect becomes very important when small amplitude harmonics are close to large amplitude ones since they become hidden by the energy distribution of the larger harmonic. The effect is exacerbated at low speeds when the slot harmonics will be close to the PWM harmonics in absolute terms. To reduce the effect, windowing must be applied to sampled time data. Spectral spreading is said to affect the *resolving capability* and is considered in section 5.6.

5.4 Accuracy

The speed measurement accuracy is directly related to the accuracy by which f_0 and f_{sh} in (5.14) can be detected. Since frequency measurement accuracy is so much dependent on acquisition time T_a (or frequency resolution f_{res}), the relationship between these two factors and speed measurement accuracy should be taken into account.

In the case of the standard FFT, the average error of the detected harmonic is $f_{res}/2$. Therefore, the error on the measured speed (in electrical Hz) will be

$$\varepsilon^*(f_r) = \frac{p}{Z}\Big[\left|\varepsilon^*(f_{sh})\right| + \left|\kappa\,\varepsilon^*(f_0)\right|\Big] = \frac{p}{Z}\left[\frac{f_{res}}{2} + |\kappa|\frac{f_{res}}{2}\right] = \frac{p}{Z}\frac{f_{res}}{2}\left(1+|\kappa|\right) \qquad (5.16)$$

where $\varepsilon^*(f_{sh})$ and $\varepsilon^*(f_0)$ is the average error in f_{sh} and f_0 respectively. For minimum error, the calculation should be carried on slot harmonics corresponding to the κ that minimises the magnitude of (5.16). It is interesting to observe that if one were to count the pulses of a N-line encoder over a period $T_{aq} = 1/f_{res}$, the average measurement error would be half the speed resolution that corresponds to a count of one pulse i.e.

$$\varepsilon_{rpm} = \frac{60\, f_{res}}{2N} \tag{5.17}$$

Putting this equal to $\varepsilon_{\mathrm{rpm}}*$ from (5.16) with $\kappa = 1$ yields

$$\frac{60\, f_{res}}{2\,N} = \left(\frac{60}{p}\right)\frac{p\, f_{res}}{Z} \tag{5.18}$$

giving $N = Z/2$. Thus the speed error arising from the FFT spectral estimate of the fundamental slot harmonic is equivalent to that obtained from a $Z/2$ line encoder. The reason why the equivalent encoder lines is half the slot number (and independent of pole number) derives from (5.16). An error $f_{res}/2$ is introduced for both $\varepsilon*(f_{sh})$ and $\varepsilon*(f_0)$. For $Z = 28$, $N = 14$ and this is of course rather crude. Some improvement in accuracy can be obtained by deriving f_0 from the n-th harmonic. In this case the error will become

$$\varepsilon^{*}(f_r) = \frac{p\, f_{res}}{2\,Z}\left(1 + \frac{|\kappa|}{n}\right) \tag{5.19}$$

If n is high, then for $\kappa = 1$, the error from the FFT will approach that of a Z-line encoder.

5.5 Interpolated Fast Fourier Transform

The speed measurement accuracy is limited by the signal acquisition time T_{aq}. However, some assumptions can be made on the behaviour of the signal which can be used to enhance the speed estimate accuracy without incurring longer acquisition times (and hence longer delays). In general these assumptions are related to the behaviour of the signal *outside* of the acquired sample. It is assumed that the input signal consists of a finite number of purely sinusoidal components that extend infinitely in time plus some amount of noise. This assumption is acceptable when the machine is operating in steady state at a constant speed, provided that the duration of the signal sample is not excessively long (then it would be questionable whether the rotor speed is constant). Using the previous assumption, it is possible to increase the measurement accuracy by means of the interpolation technique presented below.

It is common practice in signal processing to multiply the desired signal in the time domain by a function (known as time window) that generally vanishes at both ends of the record sample. This technique reduces the frequency spreading of each spectral component when its frequency is not an integer multiple of f_{res}. The pre-windowing of the incoming signal (product of the signal and the window in the time domain) will imply the convolution of the desired signal spectrum with the Fourier transform of the applied window in the frequency domain. Assuming a pure sinusoid of unity amplitude, the corresponding Fourier transform of the windowed signal will be

$$H(\omega) = W(\omega_0 - \omega) \tag{5.20}$$

$W(\omega)$ being the Fourier transform of the window and ω_0 the frequency of the sinusoid. The DFT can be obtained as this resulting spectrum sampled at regular intervals[1]

$$G(k) = H(k\Delta\omega), \quad k = 0,1,2,3,\ldots,\frac{N}{2} \tag{5.21}$$

where $\Delta\omega = 2\pi f_{res}$. This is illustrated in Fig. 5.3, where the dotted line represents the original sinusoid (of frequency ω_0).

The resulting DFT presents several spectral lines due to the use of the time window. Moreover the frequency of the maximum peak ($x_i\Delta\omega$) does not correspond to that of the original sinusoid (ω_0). However it is possible to take advantage of the extra information provided by the set of spectral peaks to obtain an accurate measurement of both amplitude and frequency of the original sinusoid. Several methods are proposed in [70, 1], depending on whether two or more spectral peaks are employed. An alternative method is presented here, similar to *method 3* in [70]. Only the two spectral peaks that present the highest amplitude are used, since they present the highest signal to noise ratio.

---

[1] This is only true for a continuous signal in the time domain. For a sampled signal, the DFT presents infinite spectral bands around integer multiples of the sampling frequency. To take account of this effect Dirichlet kernels will be used for the derivation of the window frequency response $W(\omega)$.

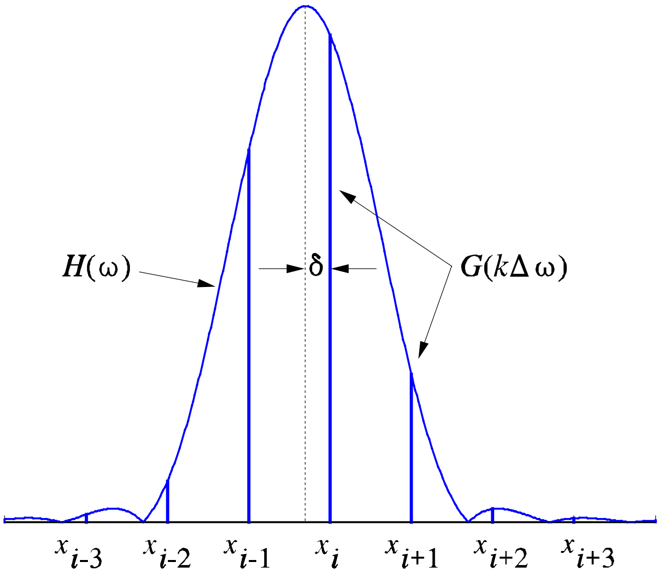

Figure 5.3 Spectrum resulting from the convolution of a pure sinusoid (dotted line) with that of the time window. The lines represent the obtained DFT

As previously stated, ω_0 will not generally be a multiple of $\Delta\omega$, therefore it is possible to express

$$\omega_0=(n+\delta)\Delta\omega;\ n\in\mathbb{N},\ \delta\in\mathbb{R} \tag{5.22}$$

where δ represents a frequency correction coefficient (see Fig. 5.3).

A number of windows obtained by adding Dirichlet kernels are considered here. The Dirichlet kernel represents the Discrete Fourier Transform of the rectangular window [57]

$$D(\omega) = \frac{\sin\left(\pi\frac{\omega}{\Delta\omega}\right)}{\sin\left(\pi\frac{\omega}{\Delta\omega N}\right)} e^{j\pi\frac{\omega}{\Delta\omega}\frac{N-1}{N}} \tag{5.23}$$

The data windows considered correspond to the following expression

$$w(n)=\sum_{m=0}^{N/2}(-1)^m a_m \cos\left[\frac{2\pi}{N}mn\right]; \qquad n=0,1,\dots,N-1 \tag{5.24}$$

where N is the number of points of the data record and a_m are $N/2$ weighting coefficients, assuming N even. In general only a small number of weighting coefficients will be different from zero. The rectangular, Hanning, Hamming, Blackmann-Harris and Rife-Vincent windows, among others, can all be expressed with appropriate a_m coefficients. However, several windows, like the Kaisser-Bessel and Dolphy-Chebyshev windows cannot. Nevertheless they can be approximated with a good degree of accuracy choosing the right a_m values.

The resultant spectral window corresponding to (5.24) can be expressed as an addition of Dirichlet kernels

$$W(\omega) = \sum_{m=0}^{N/2} \frac{a_m}{2}\left[D(\omega+m\Delta\omega) + D(\omega-m\Delta\omega)\right] \tag{5.25}$$

If the number of samples N is sufficiently high, and assuming $\sin x = x$ for x small and $(N\text{-}1)/N = 1$,

$$D(\omega) \approx N\frac{\sin\left(\pi\frac{\omega}{\Delta\omega}\right)}{\pi\frac{\omega}{\Delta\omega}} e^{j\pi\frac{\omega}{\Delta\omega}} = N e^{j\pi\frac{\omega}{\Delta\omega}} \,\mathrm{sinc}\left(\pi\frac{\omega}{\Delta\omega}\right) \tag{5.26}$$

Substituting (5.26) in (5.25) leads to

$$W(\omega) = 2N\frac{\omega\Delta\omega}{\pi} e^{j\pi\frac{\omega}{\Delta\omega}} \sin\left(\frac{\pi\omega}{\Delta\omega}\right)\sum_{m=0}^{N/2}\frac{a_m}{\omega^2-m^2(\Delta\omega)^2} \tag{5.27}$$

Defining r as the ratio between the i-th and the $(i+1)$-th spectral peaks, and using (5.20) and (5.21) it is possible to express r as

$$r = \frac{|G(i)|}{|G(i+1)|} = \frac{|H(i\Delta\omega)|}{|H((i+1)\Delta\omega)|} = \frac{|H(\omega_0-\delta\Delta\omega)|}{|H(\omega_0-(\delta-1)\Delta\omega)|} = \frac{|W(\delta\Delta\omega)|}{|W((\delta-1)\Delta\omega)|} \tag{5.28}$$

Combining (5.28) and (5.27) it is possible to obtain the following relationship between r and δ

$$0 = \delta \sum_{m=0}^{N/2} \frac{a_m}{\delta^2 - m^2} - r(\delta - 1) \sum_{m=0}^{N/2} \frac{a_m}{(\delta - 1)^2 - m^2} \tag{5.29}$$

This equation results in a general polynomial solution for the correction coefficient δ, and therefore provides a way of obtaining a more accurate frequency measurement. The solution of the previous equation is first order for the Rectangular and Hanning windows. Inserting the values of a_m (see table 5.1) for these two windows into (5.29) yields

$$\begin{aligned} &\text{Rectangular:} \qquad \delta = \frac{1}{1+r} \\ &\text{Hanning:} \qquad \delta = \frac{2-r}{1+r} \end{aligned} \tag{5.30}$$

5.5.1 Sources of Error in the Interpolated FFT

In theory it is possible to obtain an infinite improvement on the frequency measurement of any signal by using the above method. However, the presence of measurement noise, and the existence of systematic errors limit the maximum attainable accuracy.

So far the above analysis assumes that the input signal is purely sinusoidal. When two or more frequencies are present in the spectrum, an error will be introduced into the above expressions. This error is negligible when the frequency components have similar magnitude and are not very close in the frequency domain. It can be reduced by decreasing f_{res} using appropriate record lengths and sampling frequencies. The error is larger for windows exhibiting larger spectral leakage, such as the rectangular window.

Note (5.26) implies the use of Fourier kernels (sinc functions) instead of Dirichlet kernels (periodic sinc functions), i.e. the effect of spectral folding around integer multiples of the sampling frequency is neglected. In practice, the errors introduced by this assumption are much smaller than the ones introduced by the presence of more than one sinusoid in the spectrum. As with the previous case, the use of longer record lengths and windows with small spectral leakage will reduce the error.

The method presented here does not consider the contribution of the negative frequency axis. This source of error will add to the previous two, and will improve greatly if time windows with reduced leakage are used [73].

In practice, the contribution of the last two effects to the overall error is very small for the record lengths used, and can be neglected in most cases. Note the measurement dynamic range is 98 dB, and to this we must add the noise present in the signal.

5.6 Resolution and Low-load Limit

Resolution is the ability to resolve a slot harmonic from a close PWM harmonic. It will obviously determine the low-load limit at which a speed measurement can be made. Let the basic (non-interpolated) FFT algorithm detect two harmonics as two spectral lines f_i and f_j at the *i*-th and *j*-th spectral lines separated by *n* bins (i.e. nf_{res}). Given the mechanism of interpolation, it follows that the theoretical minimum bin number whereby two harmonics can be resolved is 2 if the spectral line separating the two peaks has a smaller amplitude than both, this ensures that two different peaks can be detected from the spectrum. In practice this overall minimum will depend strongly on the particular window being used. Even when two different peaks are detected, the resulting interpolated estimates will be subject to error caused by the overlapping of the spectral spreads. This error can be investigated for various windows.

The FFT algorithm was simulated in MATLAB using the eight different windows shown in Table 5.1. Note the Kaiser-Bessel and the Dolphy-Chebyshev windows cannot be obtained by addition of Dirichlet kernels. The coefficients shown in Table 5.1 for these two windows are close approximations to the actual windows. Two close frequency sinusoids of variable relative amplitudes were used as test signals. For each window, the frequency separation of the sinusoids was decreased until the interpolated estimation matched the original test frequencies to an accuracy of 0.1 bin. The results are shown in Fig. 5.4 (the ‘discontinuities’ in the figure are due the to simulation at discrete points).

Table 5.1 a_m coefficients for different time windows

Time Window	a_0	a_1	a_2	a_3
Rectangular	1	-	-	-
Hanning	0.5	0.5	-	-
Hamming	0.54	0.46	-	-
Blackman	0.42	0.5	0.08	-
67dB *Blackman-Harris*	0.42323	0.49755	0.7922	-
74dB *Blackman-Harris*	0.40217	0.49703	0.09392	0.00183
69dB *Kaiser-Bessel* †	0.40243	0.49804	0.09831	0.00122
60dB *Dolphy-Chebyshev*†	0.460352	0.492	0.047695	0.000047

† These windows cannot be expressed as additions of Dirichlet kernels, and the values of a_m are given for an approximation to the respective window

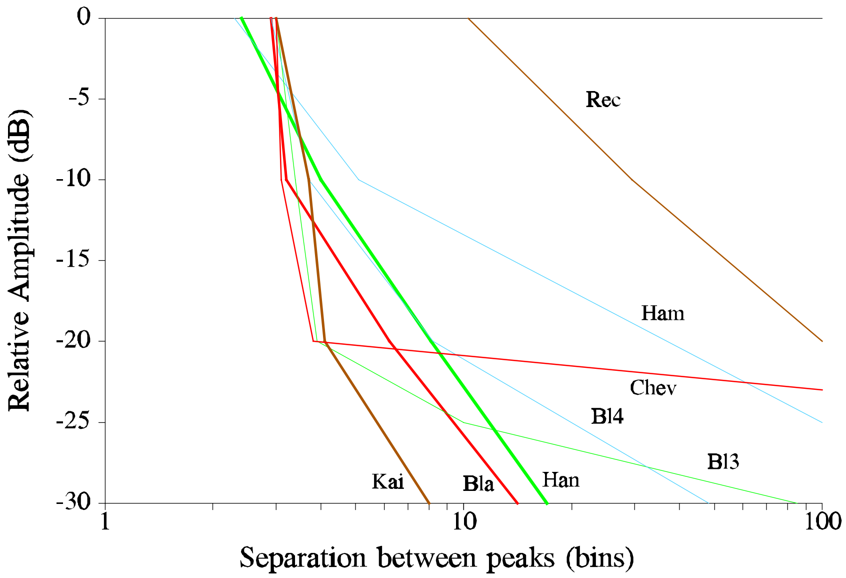

Figure 5.4 Performance of various data windows for resolving two close harmonics x bins apart in frequency and of relative amplitude y

For signals of the same amplitude, the Hanning and Hamming windows give the best results. The Chebyshev window gives the best performance down to an amplitude separation of 20 dB, below which the Kaiser-Bessel window is superior. This is expected from the well known trade-off between the main lobe width and sidelobe attenuation of the spectral windows [37]. However, the performance of the Chebyshev window for signals of similar amplitude is slightly worse than initially expected, since this window presents one of the narrowest main lobes. A possible explanation might be the use of an approximation instead of the actual window. Experimental results in section 5.9.2 show that a 20 dB separation of the slot and PWM harmonic is not unrealistic. The results above show that the low load resolution of the slot harmonic can be written βf_{res} where β lies between 3 and 5 depending on the accuracy of the interpolated result. The lower load limit can be investigated.

Under rotor flux orientated control, the slip frequency f_s (in electrical Hz) is given by

$$f_s = \left(\frac{2\pi}{T_r i_{sd}}\right) i_{sq} \tag{5.31}$$

where T_r is the rotor time constant and i_{sq}, i_{sd} are the torque and field producing currents of the stator current. The rotor resistance will vary with i_{sq}. For constant rated flux conditions ($i_{sd} = i_{sd}^b$) we can define the per unit torque as $T_{pu} = i_{sq}/i_{sq}^b$. If T_r^b is the rotor time constant at i_{sq}^b we can write

$$\frac{f_s}{f_s^b} = \frac{T_r^b}{T_r} T_{pu} = \frac{T_{pu}}{T_{r(pu)}} \tag{5.32}$$

Since the slip frequency resolution is $(p/Z)\beta f_{res}$, we have the load resolution as

$$T_{pu(res)} = \frac{\beta p T_{r(pu)} f_{res}}{Z f_s^b} \le T_{min} \tag{5.33}$$

where T_{min} is the minimum per unit load for a particular application. For the test rig T_{min} is about 0.05 as a result of friction and windage in the motor-generator set. With $\beta = 5$, $T_{r(pu)} = 1.1$ at T_{min}, and $f_s^b = 1.7$ Hz, f_{res} must be less than 0.22 Hz corresponding to T_{aq} of nearly 4.6 s. For $\beta = 3$, T_{aq} drops to 2.7 s.

5.7 Searching Algorithms

As seen in previous sections, the task of obtaining the rotor slot harmonic from the line current spectrum is not trivial. A particular rotor slot harmonic can only be present within a particular range of frequencies, giving the normal operating conditions of the machine. Therefore the computational time required to find the rotor slot harmonic can be substantially improved by using only this reduced range of frequencies. Two searching algorithms are proposed, depending on whether one or more slot harmonics are present in the spectrum.

5.7.1 Slot Harmonic Tracking Window

At no load the rotor revolves at synchronous speed ($f_r = f_0$), assuming $k = 1$ and rearranging (5.14) yields the no-load slot harmonic frequencies as

$$f_{sh0} = \left(\frac{Z}{p} - \kappa\right) f_0 \qquad (5.34)$$

Since Z/p is usually even, f_{sh0} will normally lie on an odd harmonic of the fundamental (for $Z = 28$, $\kappa = +1, -3$, then f_{sh0} lies at $13f_0$ and $17f_0$). The slot harmonic frequency is

$$f_{sh} = f_{sh0} - \frac{Z}{p} f_s \qquad (5.35)$$

where f_s is the slip frequency in Hz. Therefore each rotor slot harmonic will be present in a precise range of frequencies. A tracking window of width Δf_{sh} can be defined as

$$\Delta f_{sh} = \frac{Z}{p} f_{s(\max)} \qquad (5.36)$$

where $f_{s(max)}$ is the maximum value of operational slip and can be chosen equal to the motor's rated slip frequency $f_{s(rated)}$. Under motoring the window will be placed at $[f_{sh0} - \Delta f_{sh}, f_{sh0}]$ whilst for both motoring and generating the window is placed at $[f_{sh0} - \Delta f_{sh}, f_{sh0} + \Delta f_{sh}]$. Note that the window is independent of motor speed and is the same for any value of κ. For the motor under test $f_{s(rated)}$ is 1.7 Hz giving a minimum window frequency of 24 Hz.

5.7.2 Using One Slot Harmonic

The basic rotor slot harmonic tracking algorithm can be summarized in the steps below. The algorithm is applied upon the calculation of a new frequency spectrum.

i. search non-interpolated spectrum and identify the fundamental frequency f_0
ii. determine the no load slot harmonic frequency $f_{sh0(\kappa)}$. The value of κ (1 or -3) will be chosen depending on f_0. For values of f_0 larger than 12 Hz, $\kappa = 1$ will be used, due to its larger magnitude. For $f_r < 12$ Hz, the slot harmonic $\kappa = -3$ is used, since this was not only the largest in magnitude in this range of frequencies but allows for lower speed operation before the slot and PWM harmonics crossover.
iii. define the searching window $[f_{sh0} - \Delta f_{sh}, f_{sh0}]$ considering $\Delta f_{sh} = 24$ Hz.
iv. search for largest amplitude harmonic that is not a triplen harmonic of f_0. If no harmonic is found, set a No-Result (NR) flag. This flag can be used to increase the robustness of any control of tuning system that uses the rotor speed obtained from the rotor slot harmonics.
v. after the RSH is found, apply interpolation to increase measurement accuracy.

5.7.3 Using Two Slot Harmonics

The reliability and robustness of the basic algorithm can be improved if it is known that two or more slot harmonics exist and are readily detectable. This derives from the fact that the frequency difference between two slot harmonics is independent of speed and is always equal to $k_d f_0$ (k_d integer). This can be derived from (5.34) and (5.35). Given two detectable slot harmonics, the algorithm can be summarized as:

i. eliminate noise on the basic spectrum by eliminating all spectral lines whose amplitude is less than a small threshold.
ii. apply interpolation algorithm to all remaining peak spectra to obtain a spread-free spectrum.
iii. remove all PWM harmonics nf_0.
iv. search for a spectral pair $k_d f_0$ apart. If found, the lower of the pair is $f_{sh(1)}$ and the higher is $f_{sh(-3)}$. If more than one pair is found, or if no pair is found then
v. bring back the spectrum of (ii). Search for a $k_d f_0$ pair such that the lower and higher lay respectively in the frequency windows $[f_{sh0(1)} - \Delta f_{sh}, f_{sh0(1)}]$, and

[$f_{sh0(-3)}$ - Δf_{sh}, $f_{sh0(-3)}$]. If found, the lower of the pair is $f_{sh(1)}$ and the higher is $f_{sh(-3)}$. If more than one such pair exists, or if no pair is found the NR flag is set.

5.8 Short Time Fast Fourier Transform Recursive Calculator

The FFT acts on a record set of N samples acquired over T_{aq} with a sampling frequency of f_{samp}. A batch calculator collects successive batches of N samples with a speed update time $T_{up} = T_{aq} + T_c$ where T_c is the time for computation and data communications overhead. Alternatively a recursive calculator is possible in which the oldest m samples are discarded from the record buffer, the buffer then being filled with m new ones. This is shown in Fig. 5.5. The speed update time is therefore $T_{up} = m/f_{res}$. This way of recursively performing the FFT is known as Short Time Fast Fourier Transform (ST-FFT). The use of the ST-FFT allows for a smaller update time and can be used during transients, therefore it is preferred to the standard *batch* FFT.

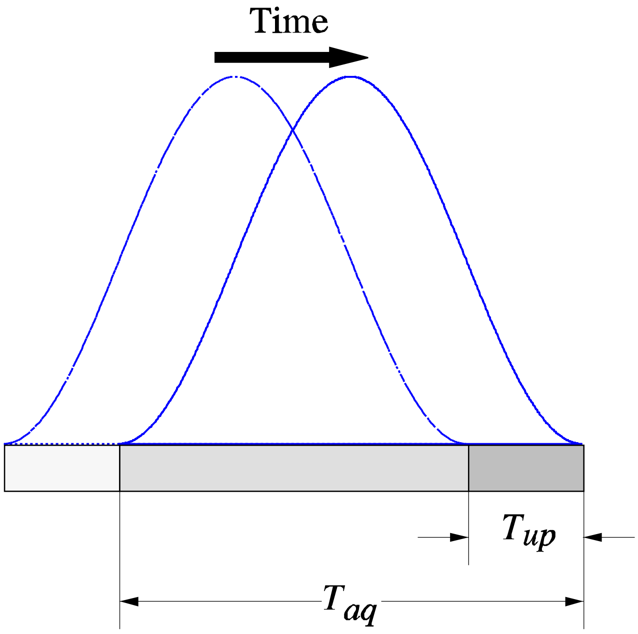

Figure 5.5 Short Time Fast Fourier Transform (ST-FFT)

All the following results are obtained using the recursive calculator although for steady state conditions, the batch and recursive calculators yield identical results.

5.9 Experimental Results

5.9.1 Prefiltering and Frequency Decimation

In the practical implementation, it is convenient to be able to access different sampling frequencies and different record lengths. It is very easy to vary the record length of the acquired sample. However, the selection of different sampling frequencies implies the necessity of anti-aliasing filters with variable cut-off frequencies. It is possible to use switched capacitor filters to provide low pass filters with different bandwidths, however the solution proposed here obviates the necessity of extra hardware.

The machine line current is sampled at a constant frequency after the hardware anti-aliasing filter. Lower sampling frequencies can be obtained by frequency decimation of the incoming signal. The frequency decimation consists on the resampling of the original signal at multiples of the initial sampling period T_s. This will provide sampling periods of T_s, $2T_s$, $3T_s$..., that correspond to sampling frequencies of f_s, $f_s/2$, $f_s/3$, etc. To prevent spectral aliasing, a second order Butterworth low pass filter with different cut-off frequencies is implemented in software before the frequency decimation. The constant sampling frequency is fixed at 5 kHz. Lower frequencies could also be acceptable, following Shannon's theorem for the maximum frequency of interest (1360 Hz for a fundamental frequency of 80 Hz). However a higher sampling frequency is preferred since it gives a broader range of decimated sampling frequencies.

5.9.2 Illustration of Slot Harmonics

The spectrograms of Fig. 5.6 illustrate the slot harmonic amplitudes $f_{sh(1)}$ and $f_{sh(-3)}$ for different loads when the motor speed is 150 rpm (f_r = 5 Hz). For these results, N = 4096 with a sampling frequency of 625 Hz giving f_{res} = 0.152. The rotor speed is kept constant by an indirect rotor flux orientated control system. The no-load harmonics $f_{sh0(1)}$ and $f_{sh0(-3)}$ are 65 and 85 Hz (13 f_0 and 17 f_0) respectively. The PWM harmonics are denoted f_7, f_{11}, f_{13} and f_{17}. The slot harmonic amplitude clearly increases with load, as does their separation from their no load values as predicted by (5.35). The slot harmonic for T_{pu} = 0.05 is clearly resolved as predicted from (5.33). Note that $f_{sh(1)}$ is not less than 20 dB down on f_{13} for this low load case.

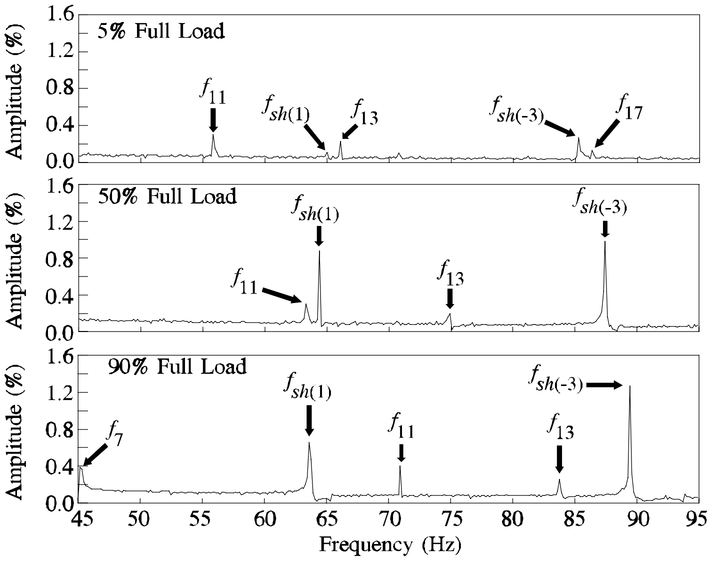

Figure 5.6 Spectrograms illustrating the presence of rotor slot harmonics in the stator line current for different loads

The difficulties in tracking is clearly shown by the movement of the slot harmonics crossing the lower order PWM harmonics as the load is increased. For example, it will be very difficult for an analogue tracking filter to distinguish between $f_{sh(1)}$ and f_{11} in certain conditions (around 50% load in Fig. 5.6). The per unit load at which the slot and PWM harmonics cross can be easily calculated. From (5.34)

$$f_{sh} = (\frac{Z}{p}-\kappa)f_0-\frac{Z}{p}f_s = (\frac{Z}{p}-\kappa-2l)f_0 \qquad l=1,2,3... \tag{5.37}$$

giving

$$f_s = \frac{2plf_0}{Z} \tag{5.38}$$

from which

$$T_{pu} = \frac{2plT_{r(pu)}f_0}{Zf_s^b} = \frac{T_{r(pu)}f_r}{\left(\frac{Z}{2pl}-1\right)f_s^b} \tag{5.39}$$

following a similar argument to that contained in section 5.6. Note that for some values of l, the slot harmonic will cross a triplen harmonic of the fundamental and will not be a problem. Generally however, the crossing of the slot harmonics with the lower order PWM harmonics complicates the task of speed tracking and this is considered in section 5.9.4.

5.9.3 Accuracy

Figure 5.7 shows the experimental accuracy obtained for the basic FFT algorithm (without interpolation) as a function of the frequency resolution.

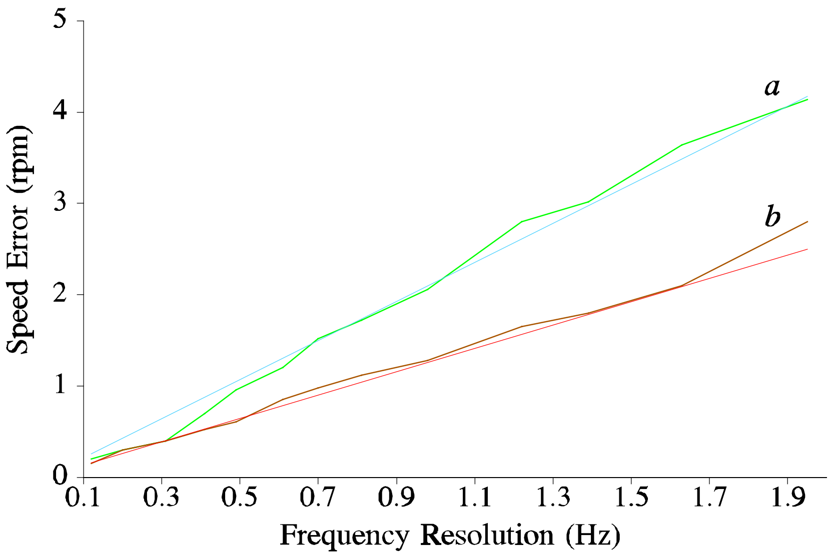

Figure 5.7 Speed measurement accuracy when no interpolation is used, and comparison with expected error. ***a)*** $\kappa = 1$, $n = 1$; ***b)*** $\kappa = 1$, $n = 5$.

In this case a Hanning window is employed, however, when no interpolation is used, the data window does not affect significantly the measurement accuracy, and in general, any other window could have been used. The accuracy is displayed as an absolute speed error $\varepsilon_{\mathrm{rpm}}$ obtained from m successive steady state measurements where

$$\varepsilon_{rpm} = \frac{60}{2\pi}\frac{1}{m}\sum\left|\omega_i^{FFT} - \omega_i^{enc}\right| \tag{5.40}$$

The actual rotor speed ω^{enc} is calculated as an average over a 6 s acquisition time using a 10000 pulses per revolution encoder which results in measurement accuracies better than 0.01 rpm. The particular frequency resolution is determined by the number of samples N and by the discrete sampling frequencies obtained from the decimation of the 5 kHz maximum sampling frequency. For N values of

1024, 2048 and 4096, only particular discrete f_{res} values could be investigated. In general it is possible to obtain a given frequency resolution using different values of N, and selecting an appropriate sampling frequency. For the values of N used, the accuracy is almost wholly determined by f_{res}, the maximum variation in accuracy between N = 1024 and N = 2048 generally being less than 0.1 rpm. For the results shown N = 4096 when $f_{res} < 0.65$ and N = 2048 otherwise.

From (5.19) the accuracy is dependent on κ and the PWM harmonic order n. Figure 5.7 shows both experimental and theoretical accuracies for two cases: $\kappa = 1$, $n = 1$ (which also correspond to a 14-pulses per revolution encoder) and $\kappa = 1$, $n = 5$. The theoretical cases are derived from (5.19). The experimental results agree well with prediction.

The improved accuracy obtainable using interpolation techniques is clearly shown in Fig. 5.8. The relationship between measurement accuracy and acquisition time (T_{aq}) can clearly be seen, even when the interpolation algorithm is used. A Hanning window has been used in both cases.

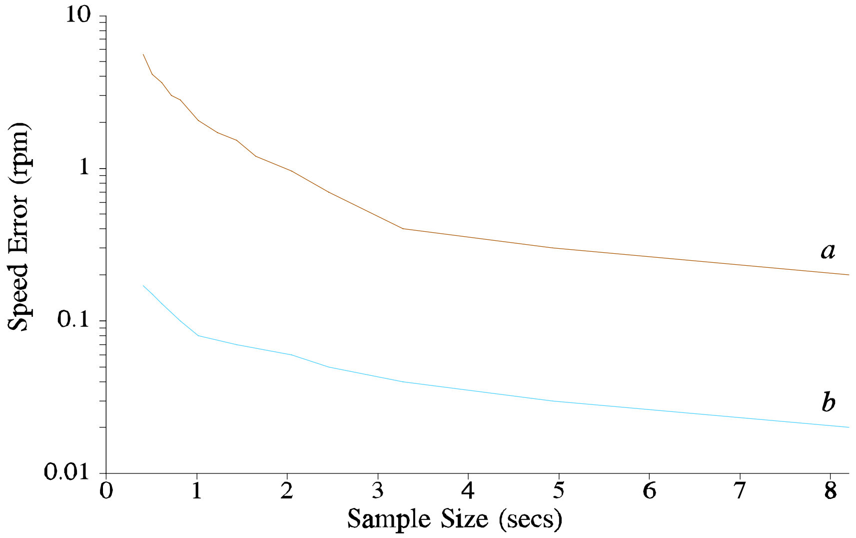

Figure 5.8 Speed measurement accuracy for different acquisition times (T_{aq}). ***a)*** When no interpolation is used. ***b)*** When interpolation algorithm is used.

In Fig. 5.9, interpolation algorithms corresponding to 7 different windows were investigated. The Hanning window is one of those that give the best improvement even for larger values of f_{res}. Given the simplicity of the Hanning interpolation

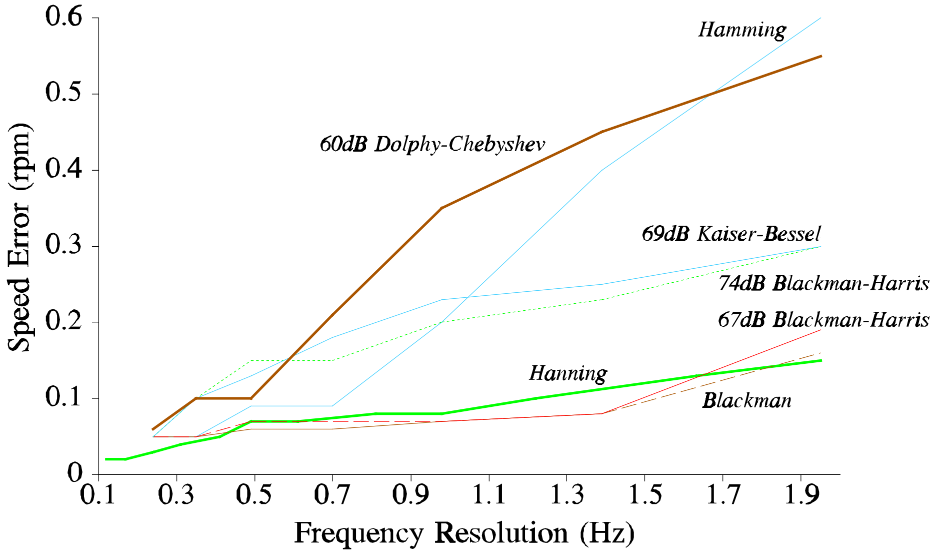

Figure 5.9 Speed measurement accuracy for different windows using the interpolation algorithm

formula, the argument for using this window would appear to be decisive. The results showing accuracies of less than 0.1 rpm should be viewed in context with the maximum accuracy of the encoder measured speed of 0.01 rpm. Nevertheless, it can be seen that a 30 to 40 fold increase in accuracy is possible. In this instance, this corresponds to that attainable from a 400 to 500-line encoder.

5.9.4 Speed Tracking and Low Speed Limit

Figure 5.10 shows the performance of the basic algorithm using a single rotor slot harmonic (section 5.7.2) for particular (integer) values of f_r in electrical Hz at low speeds. For $f_r < 12$ Hz, the slot harmonic $\kappa = -3$ is used, since this was not only the largest in magnitude but allows for lower speed operation before the slot and PWM harmonics crossover. Equation (5.39) is plotted with $f_s^b = 25$ Hz and $R_{r(pu)} = 1$; the actual PWM harmonics involved in the crossover being shown. Above 5 Hz, the speed detector proves 100% reliable, the reliability breaking down near the crossovers. In this situation the RSH will be hidden by the spectral leakage of the f_0 harmonics. This problem can be overcome by using a recursive interpolation algorithm [69] and/or by reducing the spectral leakage by using longer data records in order to enhance the resolution of the individual spectral components. This will generally impose a low frequency limit to the proposed method of speed measurement, since it is impractical to extend the data record duration to extremely

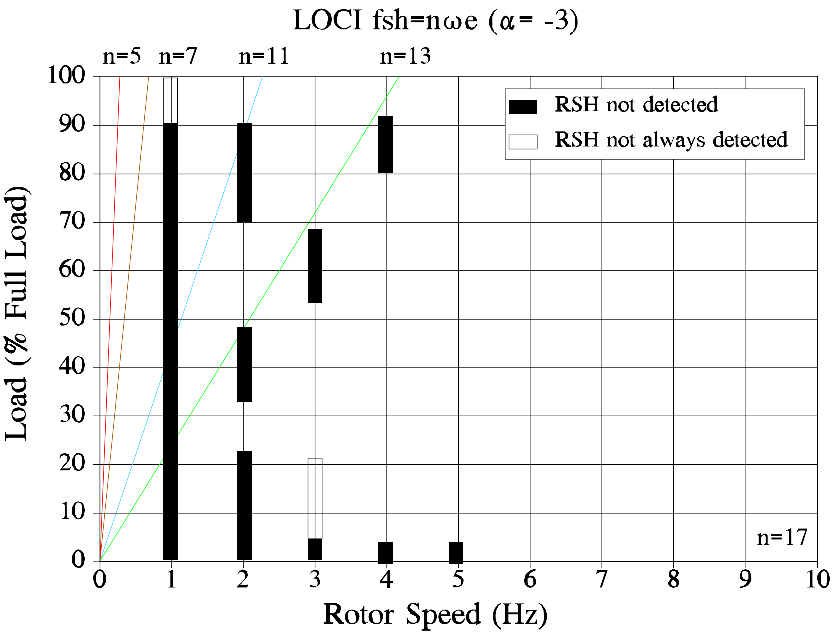

Figure 5.10 Speed detection robustness using one slot harmonic

high values. This low frequency limit will strongly depend on the machine characteristics. Machines with large number of rotor slots develop rotor slot harmonics at higher frequencies. Hence the frequency at which RSH's become very close to large PWM harmonics is lower, therefore allowing for speed measurement at lower operating frequencies.

The results of the algorithm using two slot harmonics (section 5.7.3) are shown in Fig. 5.11, the crossover uncertainties having been largely removed. The degradation in the low load result at f_r = 3, 4 and 5 Hz is due to the amplitude of $f_{sh}(1)$ being less than the selected threshold. This algorithm shows a great improvement in robustness, reducing substantially the amount of wrong speed estimates. It is emphasised that a no-result is preferable to a high probability result when the occasional wrong result is 'very wrong'. If the speed detector is used for the on-line tuning of a MRAS algorithm, a no-result merely suspends the tuning process and does not lead to an erroneous perturbation.

Neither of the tracking algorithms described use the torque current i_{sq}. In a vector controlled system, i_{sq} can be made available to the speed detector and can be used to reduce the uncertainty still further at low speeds and loads.

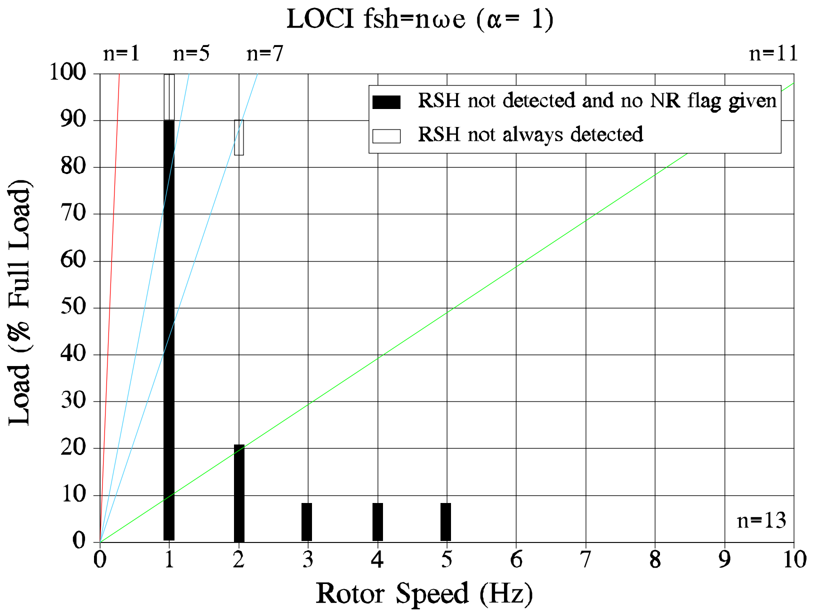

Figure 5.11 Speed detection robustness using two rotor slot harmonics

5.9.5 Transient Conditions

The FFT recursive calculator of section 5.8 allows the performance of the harmonic speed detector to be ascertained for changing speeds. The speed update time has to be greater than the computation time T_c. Table 5.2 shows the i860 computation times for various record lengths.

Table 5.2 Calculation times for different record lengths and searching algorithms

Samples	Window	FFT	Search 1	Search 2	Total 1	Total 2
1024	0.7	6.0	2.3	1.4	9.0	8.1
2048	1.3	11.3	4.2	2.6	16.8	15.2
4096	2.5	39.5	8.2	5.0	50.2	47.0

All figures given in milliseconds

The largest component is that due to the FFT. The search times are for the basic algorithm and for the 2-harmonic algorithm. It is worth noting that the search times for the 2-harmonic algorithm are slightly lower than those of the basic algorithm. All the i860 algorithms were written in FORTRAN so that the times shown can almost certainly be reduced if they were directly implemented in assembler code. These figures therefore determine the minimum update time for each sample size.

Figure 5.12 shows the response to a fast transient in which the transient time is much less than T_{aq}. For this case f_{samp} = 1 kHz, N = 4096, $T_{aq} \approx 4$ s, T_{up} = 100 ms and $i_{sq(max)}$ = 2 pu. The load torque is held constant at 0.2 pu. It can be seen that the speed detector jumps to the correct speed after a delay $T_d = T_{aq}/2 + T_{up}$. This can be understood from Fig. 5.13 which shows the current spectrum at different instances of time during the transient. For clarity only the fundamental is shown although all other components behave in a similar way. At the beginning of the transient the spectrum corresponds to the starting speed. New data then fills the buffer and old data is discarded. The spectrum shows two peaks, the peak corresponding to the new speed becoming the largest when more than half the buffer contains data corresponding to the new speed.

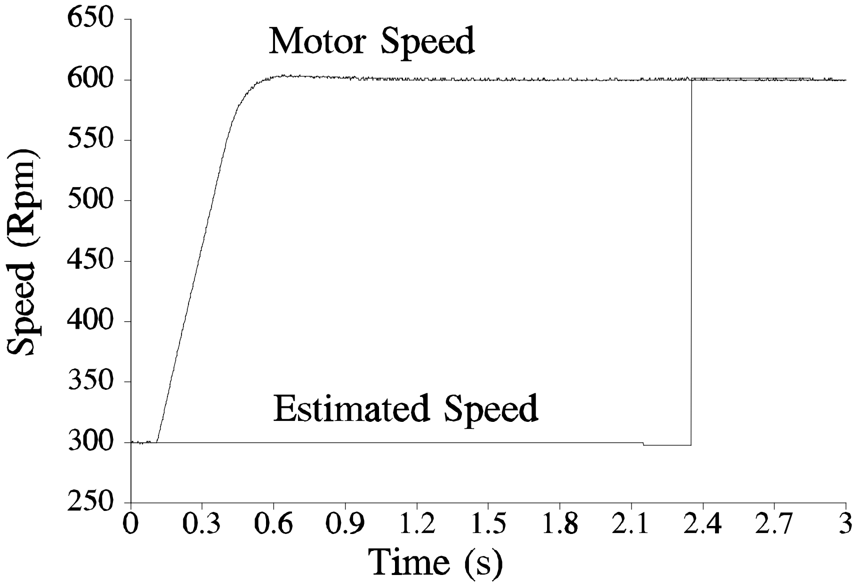

Figure 5.12 Actual and detected speed for a fast speed transient from 300 to 600 rpm

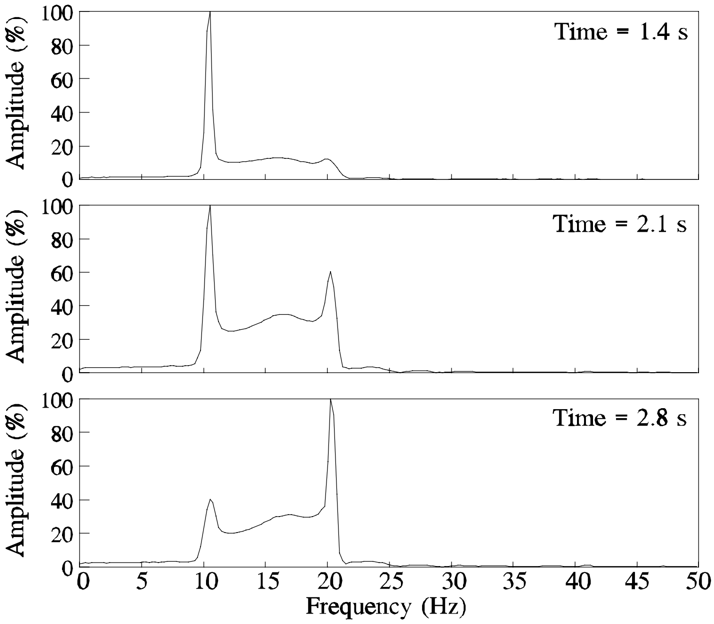

Figure 5.13 Fundamental component of the line current at different instants in time during the transient of fig. 5.12

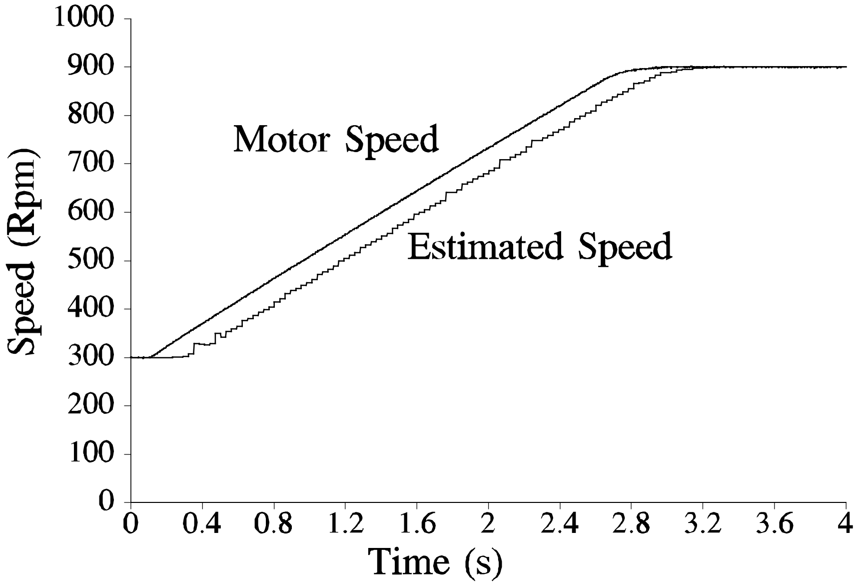

Figure 5.14 Actual and detected speed for slower rate transients, 300 to 900 rpm with i_{sq} = 0.5 pu

Figures 5.14 and 5.15 show the response for two slower transients with $i_{sq(max)} = 0.5$ and 0.75 pu respectively. T_{aq} is reduced to 400 ms with $N = 1024$, $f_{samp} = 2.5$ kHz. The update time T_{up} is 30 ms. The speed detector again follows the real speed with a delay $T_d = T_{aq}/2 + T_{up}$. However in this case the splitting of the harmonics during

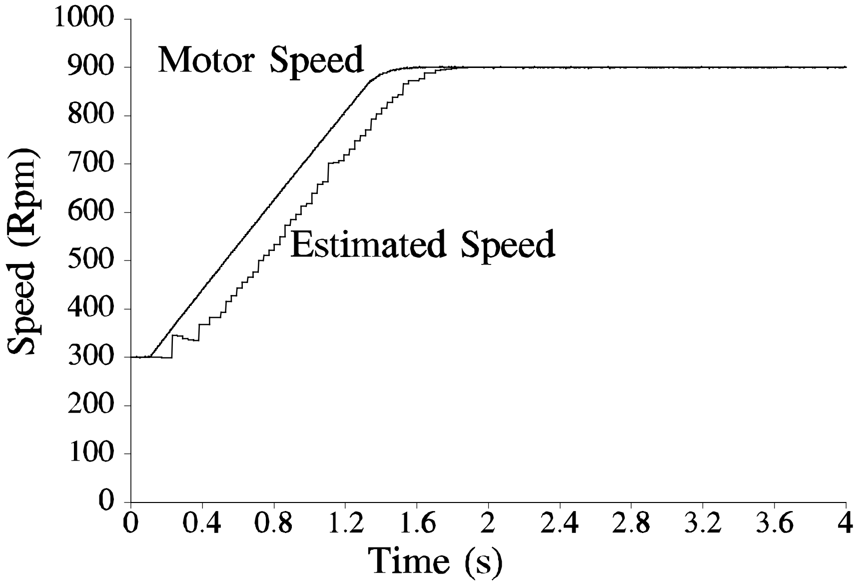

Figure 5.15 Actual and Detected speed for slower rate transients. 300 to 900 rpm with i_{sq} = 0.75 pu

the transient does not occur and the T_{aq} delay component is due to the fact that the Hanning window enhances the harmonics present at the centre of the record sample. The spectral peaks also exhibit an increased spread during the speed change and this results in less accuracy and resolution. Interpolation does not result in increased accuracy since the assumptions that give rise to the interpolation algorithm do no longer hold.

The principal conclusion of these studies is the predictability of the speed detection behaviour during transients assuming of course that the tracking algorithm gives a result. It is seen that the detector can be represented as a delay element e^{-sT} where T is T_d/T_s.

5.10 Discussion

5.10.1 Slot Harmonic Detection for the General Cage Induction Machine

It is first emphasised that even for closed slot rotors, at least one slot harmonic is readily detectable with 16-bit sampling, even at low loads. Indeed, under load, the amplitude of the principal slot harmonics are comparable or larger than the PWM harmonics that lie close to them. Therefore it is almost certain that the slot harmonic speed detector would prove effective for all induction machines. However, for detection, the rotor slot number per pole (Z/p) and the principal slot harmonics present (κ_i) must be known (the principal slot harmonics can be considered to be those which are less than 25 dB down upon the close PWM harmonic at no load).

Of course, the easiest way of obtaining Z/p is from manufacturers data. An automated commissioning procedure for finding Z/p and κ_i is a possibility. If only $\kappa = 1$ exists and if f_0 and f_{sh} are detected in a spectral search, then Z/p is easily derivable. It is noted that the theoretical derivation of κ_i from motor design data is a problem which has not been sufficiently studied and further research would be of interest. The problem however is a little academic since if Z/p is known, then the principal slot harmonics can be obtained algorithmically from a spectral search.

5.10.2 Accuracy and Robustness

General expressions have been derived for steady state resolution and the measurement accuracy for interpolated and non-interpolated algorithms has been thoroughly studied for a broad class of windows. It has also found that the absolute speed measurement error is generally independent of the machine speed, provided the rotor slot harmonic is detected by the tracking algorithm.

For the machine tested, speed measurements have proved to be reliable for rotor speeds between 4 and 50 Hz under all load conditions. This has been achieved with acquisition times (T_{aq}) from 0.4 to 8 s, therefore measurement at lower speeds can be obtained with acquisition times longer than 8 s. With simple tracking algorithms, the robustness is lost when slot harmonics cross lower order PWM harmonics as predicted by (5.39) which shows the same (cancelling) dependence on Z/p and f_s^b as discussed above. More complex tracking algorithms can improve the reliability down to 2 Hz but the gains made are not substantial, provided the acquisition time is not increased. For a larger machine, this low speed limit for a given record time duration is likely to be smaller, due to the larger Z/p and to the smaller f_s^b. If the speed measurements are used for model tuning, then providing the algorithm can give certain results and certain no-results, the low speed limitation is not a severe handicap. For such application, the basic tracking algorithm with interpolation would be recommended.

A 1 kHz PWM carrier was used in the experiments. Higher carrier frequencies result in lower amplitude PWM harmonics in the line currents which is of course not a problem. Neither is it likely that slot harmonics could interfere with the carrier harmonics; at rotor speeds greater than 50 Hz, the motor voltage waveforms become quasi-square waves and the carrier harmonics in the line currents will disappear. Variable carrier frequency schemes (for reducing acoustic noise) are also unlikely to be a problem since the frequencies of the main fundamental harmonics are not functions of the carrier frequency.

5.10.3 Transient Performance

The results in section 5.9.5 suggest that the speed signal derived from the slot harmonics can be used directly for speed control, at least for large drives. For the case where $T_{up} \approx 200$ ms, a good control response can be obtained for closed loop speed bandwidths down to 1 Hz with speed accuracies in the region of 1 rpm in the steady state. Reliability is critical however for such a direct use of the speed signal and in practice a minimum speed and load would probably be imposed. If the signal is used indirectly for observer tuning, the transient capability becomes academic in that tuning need only take place in steady state intervals. Further, the dynamics of an adaptive loop to tune the observer against changes in rotor resistance can be very slow (since the changes are determined by thermal time constants) which in turn allows a slow speed update time (eg $T_{up} \approx 1$ s) and a corresponding relaxation in T_c.

5.10.4 Speed Direction and Controller-Detector Interaction

In all investigations to date, the slot harmonic detector has been self contained in that one motor current has been the only input. Others are available, of particular interest being i_{sq}, f_0 and sgn(f_0). The torque current i_{sq} is strictly available only for vector drives. It can be used to enhance the reliability of the tracking algorithm since it is very closely proportional to slip frequency for operation up to base speed. The use of i_{sq} certainly makes the crossover problems of section 5.9.2 easier to solve. The fundamental inverter frequency f_0 is available in open loop V/f drives and often in indirect vector schemes. It can obviously be used to accelerate the search for the slot harmonics. However, for sensorless vector drives, the direct approach to flux orientation is used in which the rotor flux angle (derived from a flux observer) is used to determine the demanded motor voltages. Thus f_0 is not explicitly available and must be obtained from the flux angle through differentiation. This can be noisy and experience suggests that obtaining f_0 by spectral estimation is superior in steady state. Of real interest however is sgn(f_0) which can be used to find the direction of rotation. This direction cannot be determined from harmonic analysis of a single line current. The quantity sgn(f_0) is actually the rotational direction of the rotor flux vector which is the same as that of the stator current vector except in cases of high rates of change of i_{sq} (at the onset of braking) which are very transitory. Once the direction of the stator current vector is known, the direction of the rotor follows from the position of the slot harmonics relative to their no-load positions.

5.10.5 Microprocessor Implementation

The selection of the i860 as a development processor was mentioned in Section 4.2. Its unit price is approximately £200 which is comparable to a mid-range incremental encoder. However other more specialized Risc DSPs offer similar performance at a reduced price. For example, the Motorola M56001 and the Hitachi HD81831 are able to compute a 1024-point FFT in less than 4 ms and both cost in the region of £60 to £80. If the slot harmonic calculator is for tuning motor models or MRAS systems, a considerable relaxation in T_c is allowable and conventional fast processors in the range £10 to £20 may be used. This discussion must also be viewed against a continual fall in processor costs.

5.11 Conclusions

The main objective of this chapter was to obtain a robust, reliable and accurate speed measurement from the rotor slot harmonics, suitable to tune an MRAS based speed estimator against parameter variations. This objective has been completely fulfilled. The dependence of the speed measurement error with the data acquisition time T_{aq} has been thoroughly investigated, and accuracies of 0.03 and 0.02 rpm for a data records of 5 and 8 s, respectively, have been obtained. Moreover, expressions for speed accuracy and resolution have been derived for motors of general rotor slot numbers and slot harmonic orders, and windowing and interpolation methods have been derived and described. These allow the user to predict the performance and limitations of the detector for a given machine. Speed tracking and the problems at low speed have been discussed. The recursive collection of data has allowed the performance under changing speed conditions to be investigated and it has been shown that the calculator is equivalent to a predictable delay element. Practical considerations relating to the general application of the technique have also been discussed.

It is felt that it is extremely unlikely that better accuracy could be obtained using non parametric spectral estimation techniques (i.e. the ones that do not use a model of the signal, like the FFT) for the same acquisition time (T_{aq}).

Chapter 6 Parameter Tuning

6.1 Introduction

It was seen in Chapter 3 that a sensorless drive system uses a rotor speed estimator based either on slip calculation, observer techniques or, more commonly, Model Reference Adaptive Systems (MRAS). All these approaches give estimates that are sensitive to the machine parameters and require a prior knowledge of the motors electrical characteristics. The sensitivity of the speed estimate to the rotor and stator resistance is a particular cause for concern, since the resistances vary greatly with temperature, and therefore their values cannot be completely predetermined by using off-line tests.

The rotor speed and the rotor time constant cannot be independently observed from stator quantities when the machine is excited by single frequency sinusoidal waveforms [84, 27]. If an independent speed measurement is available then the rotor time constant can be obtained. The existence of speed related rotor slot harmonics (RSH) present in the stator line current or voltage can provide such a independent measurement and it has been shown that the accuracy and tracking robustness attainable is of a sufficient quality as to justify the exploitation of the measurement to tune MRAS speed estimators against machine parameter variations. The mechanisms of tuning the MRAS estimator, principally against T_r variations, will be presented in this chapter.

This chapter will also present a new algorithm for tuning the MRAS against R_s variation. The new approach is proposed for stator resistance estimation that does not require rotor speed measurement and does not depend on any other machine parameter. It will be shown that the use of more accurate R_s estimate leads to enhanced dynamic performance for sensorless vector control drives. Special regard will be paid to dynamic performance through zero speed.

The MRAS observer used in this work provides flux and speed estimates, and permits a straightforward implementation of a flux oriented control of the induction machine. The schematic of the tuned estimator system and Direct Rotor Flux Orientation control (DRFO) is illustrated in Fig. 6.1, which shows the adaption processes for T_r and R_s. The adaption for T_r is achieved by feeding the difference between the estimated speed from the MRAS-CLFO and the measured speed from the rotor slot harmonics to an adaption algorithm. Stator resistance R_s adaption is also carried out during transients in order to enhance dynamic behaviour. The purpose and methodologies of the tuning methods are introduced below.

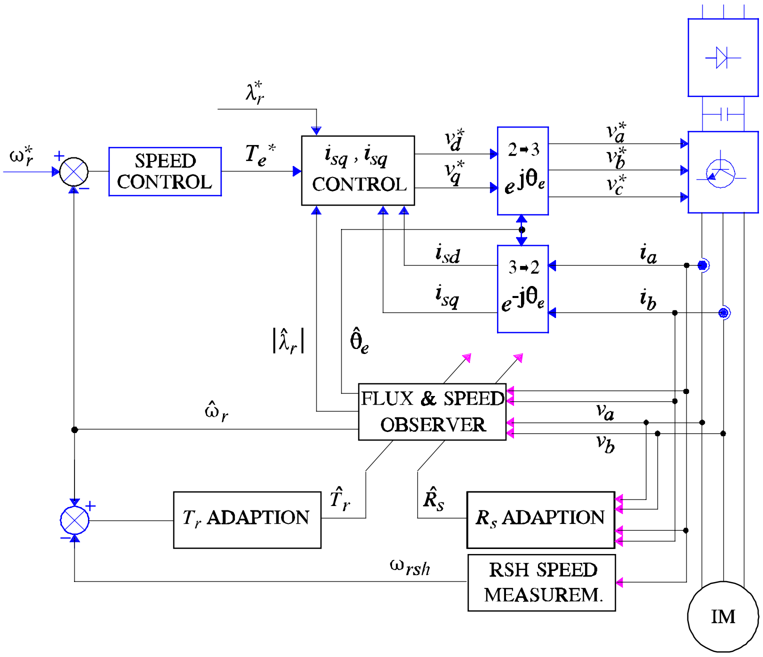

Figure 6.1 Diagram of the DRFO sensorless drive with T_r and R_s adaption

6.1.1 Tuning of T_r

This parameter varies with thermal drift of R_r, which is generally larger than the variation due to L_r which may be about 5% due to saturation effects. The parameter T_r (or R_r) is the largest single factor in determining the accuracy of the speed estimate. It was shown in Chapter 4 that incorrect R_r estimates can also induce oscillation.

The identification of T_r in sensorless drives is a problem since for a sinusoidally fed machine in which only the stator quantities are measured, ω_r and T_r cannot be simultaneously estimated in steady state. It can be shown [82, 72] that the relationship between the real and estimated slip frequency is

$$\hat{T}_r \hat{\omega}_{sl} = T_r \omega_{sl} \tag{6.1}$$

where ω_{sl} and T_r are actual slip and rotor time constant in the machine whereas $\hat{\omega}_{sl}$ is the estimated slip from the MRAS-CLFO and $\hat{T}_r$ is the estimated rotor time constant used in the MRAS observer. Equation (6.1) shows that slip (and hence speed) cannot be estimated independently of T_r. Under dynamic flux conditions however, T_r becomes observable. In [55] for example, T_r is derived through the sinusoidal perturbation of the field current demand i_{sd}^*. These method also corrects for variations in the stator resistance. However this kind of T_r adaption is based on a linear machine model and is therefore sensitive to machine inductances. Since T_r and speed estimates are both parameter dependent, this method of T_r identification does not ensure zero speed error. Moreover, the injection of current harmonics of relatively large amplitude (typically 5% rated i_{mrd}) will increase losses and therefore the machine will have to be derated.

A more effective way of ensuring speed accuracy through T_r tuning is to derive the motor speed by tracking the speed dependent rotor slot harmonics present in the stator currents. This method does not require the injection of extra signals into the machine and it will be shown in Section 6.2 that such a system ensures zero (or close to zero) speed error. In [63], the only previous work to use a slot harmonic derived speed estimate (denoted $\hat{\omega}_{rsh}$) to tune for R_r, results are shown which give an $\hat{\omega}_r$ estimate compensated against thermal drift. The rotor slot harmonic frequency was estimated by using switched capacitor tracking filters [86]. However, filter methods suffer from resolution problems especially at low loads. They cannot distinguish the slot harmonics when they lie close to or cross PWM inverter harmonics, the latter occurring in the lower speed range. Moreover the accuracy of this analogue method is worse than that of the FFT-based speed measurement shown in Chapter 5. Finally, the use of narrow bandpass filters results in very poor tracking dynamics. The poor dynamics of a bandpass filter thus restricts the compensation of $\hat{\omega}_r$ to very slow thermal effects. Therefore this system cannot provide rapid compensation for faster effects due to changes on the inductive terms or to errors in other parameters. Hence speed holding capability during load changes is degraded. The performance of the proposed system during load transients is shown in Section 6.2.1.

The use of digital FFT techniques to extract the slot harmonics shown in Chapter 5 provides substantial improvements in accuracy, robustness and dynamic performance over analogue techniques, allowing absolute speed accuracies down to 0.02 rpm to be obtained with record lengths of approximately 6 s. Enhanced resolution and tracking algorithm performance gives robust operation down to natural no-load and speeds down to 2 Hz, even in the presence of PWM harmonics. Most significantly however, absolute accuracies of 0.2 rpm could be obtained with record lengths as low as 0.5 s. Section 6.2 shows how this can be exploited to yield ω_{err} dynamics in the region of 4 to 6 s such that the compensation of $\hat{\omega}_r$ to load changes is considerably enhanced.

6.1.2 Tuning of R_s

This parameter varies with thermal drift. At very low speeds it has a fundamental effect on the flux calculation and thus the quality of field orientation. In Chapter 4 it was also shown that oscillations and sensorless drive stability was more sensitive to inaccuracies in R_s than any other parameter. On-line tuning is therefore necessary.

Several methods of stator resistance estimation have been devised in the past. Different approaches have been used such as Extended Kalman Filtering [60] or some kind of observer based estimation [35]. However these strategies require speed measurement for their operation, and are therefore unapplicable to speed sensorless drives. Previous methods of tuning R_s in a sensorless environment include [83] which used the steady state model of the machine. However this method is very sensitive to the machine inductive parameters. Also in [89] a method was shown based on a full state observer and a MRAS for joint rotor speed and stator resistance estimation. However, it is also based on a machine model and therefore dependent on the rest of the machine parameters. In section 6.3 an alternative method is proposed. This method does not rely on the knowledge of any other parameter. It will be shown that accuracies down to 1% are attainable repeatedly and the consequent performance improvement is illustrated.

6.2 Rotor Time Constant Adaption

To devise an adaption mechanism for the rotor time constant T_r, the following equation can be derived from (6.1)

$$T_r = \hat{T}_r - \frac{\hat{\omega}_r - \omega_r}{\omega_{sl}} \hat{T}_r \tag{6.2}$$

where $\omega_r = \hat{\omega}_{rsh}$ is the actual speed of the machine (obtained from the rotor slot harmonics), $\hat{\omega}_r$ is the output of the MRAS-CLFO speed estimator, and ω_{sl} is the slip of the machine. It is possible to define a new magnitude ΔT_r as

$$\Delta T_r = \frac{\hat{\omega}_r - \omega_r}{\omega_{sl}} \hat{T}_r \qquad \text{where} \qquad T_r = \hat{T}_r - \Delta T_r \tag{6.3}$$

Therefore it is possible to estimate the actual value of the rotor time constant by driving ΔT_r to zero. The calculation of ΔT_r is carried out according to (6.3), and its implementation is shown in Fig. 6.2. Note that this implies that the difference between actual and estimated speed will also be driven to zero.

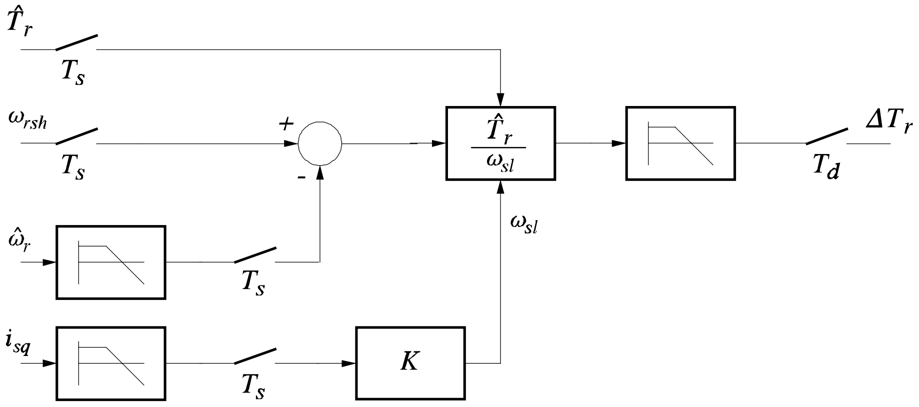

Figure 6.2 ΔT_r identifier

The values $\hat{\omega}_{rsh}$ and $\hat{T}_r$ are available to the calculator every T_s and there is a delay in $\hat{\omega}_{rsh}$ of $T_d = T_{aq}/2$. The machine slip is calculated assuming field orientation and constant flux and is thus proportional to i_{sq}. Both i_{sq} and $\hat{\omega}_r$ are sampled at 500 μs and are filtered with a moving average filter to introduce a delay T_d. The value of ΔT_r is then sampled at T_d after appropriate low pass filtering. The low pass filter is introduced to avoid spectral aliasing.

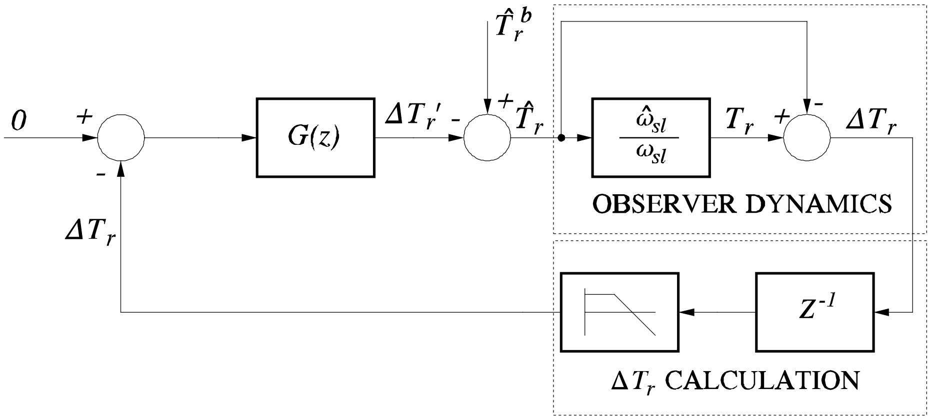

Figure 6.3 Equivalent control structure for ΔT_r identifier dynamics

The control system for driving ΔT_r to zero is shown in Fig. 6.3. The observer dynamics between T_r and $\hat{T}_r$ (that constitute the plant) are represented by (6.1). The ΔT_r calculator is represented as a low pass filter in series with a pure delay (z^{-1}) block as shown. The delay corresponds to the FFT measurement delay and the low pass filter is the previously mentioned antialiasing filter. The remaining dynamics of the ΔT_r calculator are much faster than the combination of the low pass filter and the pure delay and can therefore be neglected. The signal ΔT_r is forced to zero using a controller *G(z)* (nominally a PI controller) to give a bandwidth appropriate to the loop sample time T_d. For the following studies, T_s = 100 ms and T_d = 1 s giving an absolute speed accuracy of 0.08 rpm (see Chapter 5). The T_r adaption loop has a natural frequency of 1 rads^{-1}. Faster bandwidths are of course attainable given a reduction in T_d (i.e. T_{aq}) with a subsequent deterioration in speed accuracy.

6.2.1 Results of T_r tuning

The effects of an untuned $\hat{T}_r$ value used for speed estimation are first illustrated. Figure 6.4 shows how the error between real and estimated speed ($\omega_{err} = \hat{\omega}_{rsh} - \hat{\omega}_r$) varies depending on the temperature of the machine. In Fig. 6.4, the motor has been operated at full load for 12 minutes, at 150 rpm. The rotor time constant tuning has been disabled so that ω_{err} increases as the temperature of the machine increases. This is expected from 6.1, since the actual value of T_r will decrease with temperature whilst $\hat{T}_r$ remains constant. Typical errors of approximately ±8 rpm are found when no T_r tuning is used.

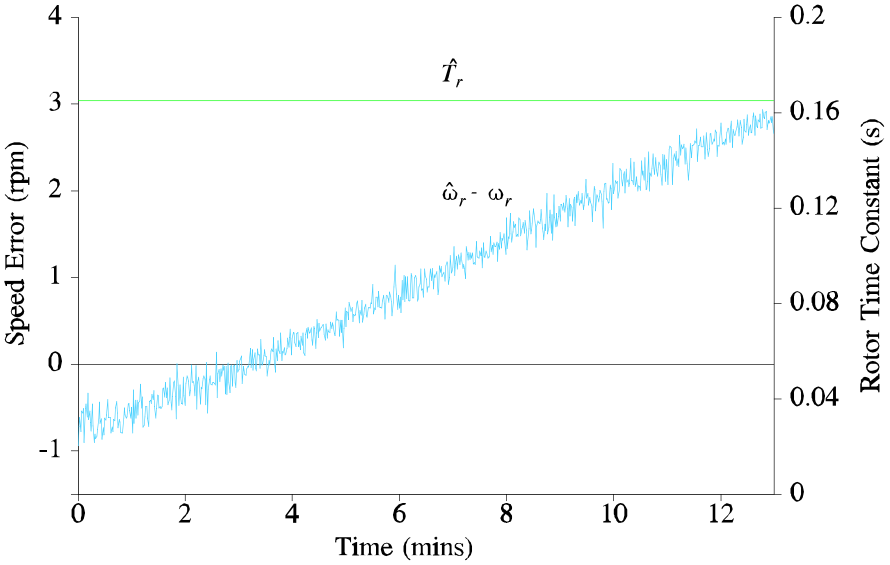

Figure 6.4 Speed drift with untuned rotor time constant (T_r)

Figure 6.5 shows the effectiveness of the proposed method. When the adaption algorithm is disabled, ω_{err} increases steadily, since $\hat{T}_r$ is constant. At t = 60, the rotor time constant adaption is enabled. The error ω_{err} is driven to zero in approximately 6 s. As with the previous case, this test has been carried out with the machine at 150 rpm and at full load. The estimated speed is seen to have an average error of very near zero. In general the speed estimate average error will coincide with the accuracy of the FFT-RSH speed measurement, in Fig. 6.5 the speed measurement accuracy is 0.1 rpm.

The robustness of the adaption algorithm to load changes is shown in Fig. 6.6. Initially the machine is operating at 600 rpm and 10% load, using sensorless DRFO. The load torque is then suddenly increased to 90%. Note that $\hat{\omega}_{rsh} = \omega_r$ is tracked during the speed transient itself with a delay of T_d. There is a difference between ω_r and $\hat{\omega}_r$ after the torque transient with a reduction of T_r. This reduction is not due to thermal changes in R_r.

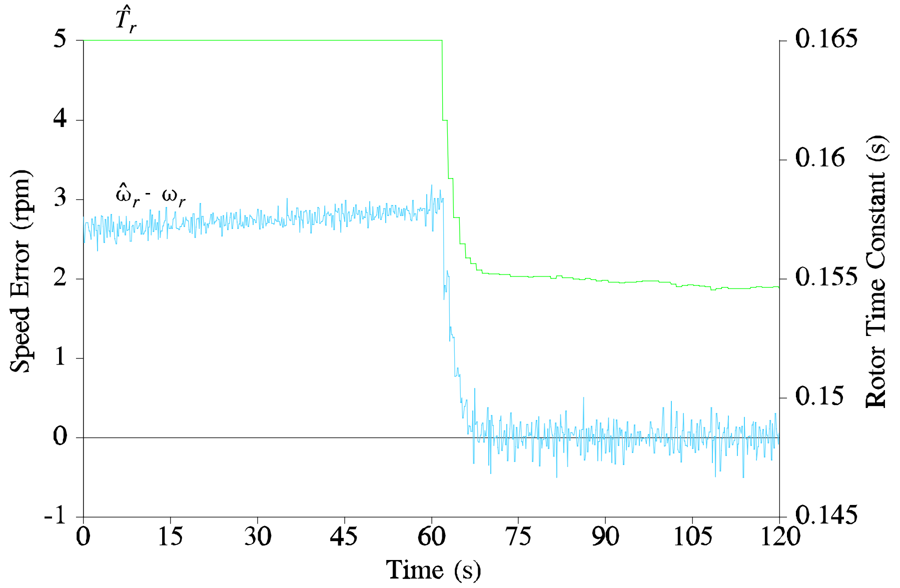

Figure 6.5 Effect of activating rotor time constant identifier

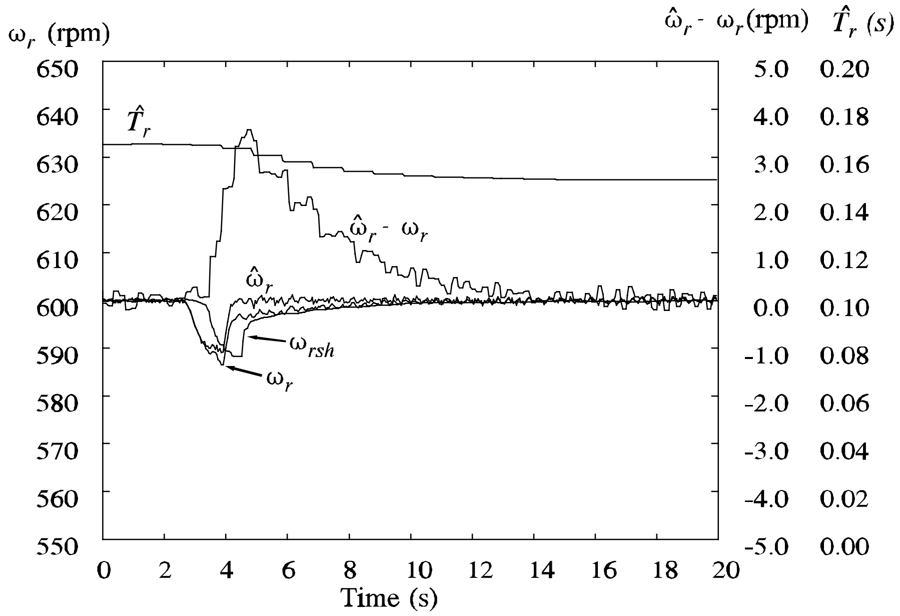

Figure 6.6 Performance of the rotor time constant identifier during a load transient

Initially it was thought that the reduction in $\hat{T}_r$ was due to the influence of errors in σL_s on the estimated speed and the identifier is compensating for this. However when σL_s is decreased (to take account of the increased i_{sq}), the reduction in $\hat{T}_r$ was found to be even greater (a study of Figs. 4.7a and 4.7b will show that this is what should happen). Further the reduction was not very sensitive to changes in σL_s. The observed reduction in $\hat{T}_r$ is thus thought to be a real effect caused by the reduction of L_r with i_{sq}. This could be due to local saturation effects [79, 59] under high i_{sq} current; these include cross-saturation caused by the non-sinusoidal distribution of the saturated flux, and also skew and axial saturation. Since this effect would seem to be of greater magnitude than the effect due to variations in σL_s, it should become possible to use the T_r identifier to tune variations in L_r.

6.3 Tuning of the Stator Resistance

6.3.1 Estimated Flux Trajectory

A large number of sensorless vector control techniques use the induction machine stator equation in some form to obtain stator or rotor flux estimates [72, 36, 46, 87]

$$\hat{\lambda}_s = \int(\boldsymbol{u}_s - \hat{R}_s \boldsymbol{i}_s)dt \qquad (6.4)$$

where $\hat{\lambda}_s$ is the estimated stator flux vector, $\hat{R}_s$ is the estimated stator resistance, and $\boldsymbol{u}_s$ and $\boldsymbol{i}_s$ are the measured stator voltage and current of the machine. An estimate of the rotor flux could be easily obtained from the above equation. Therefore it is possible to concentrate on the study of the estimated stator flux without loss of generality.

In a complex plane, the flux vector in the machine will describe a circular trajectory centred at the origin, provided the flux magnitude is constant. It is possible to rewrite (6.4) as

$$\hat{\lambda}_s = \int \boldsymbol{u}_s dt - \hat{R}_s \int \boldsymbol{i}_s dt = \lambda_s - \Delta R_s \int \boldsymbol{i}_s dt \qquad (6.5)$$

being $\Delta R_s = \hat{R}_s - R_s$. In general, the integral of the stator current describes a circular trajectory only in steady state, and will diverge from it during transients. This deviation from a circular trajectory will appear on the estimated flux vector when the stator resistance is not accurately known.

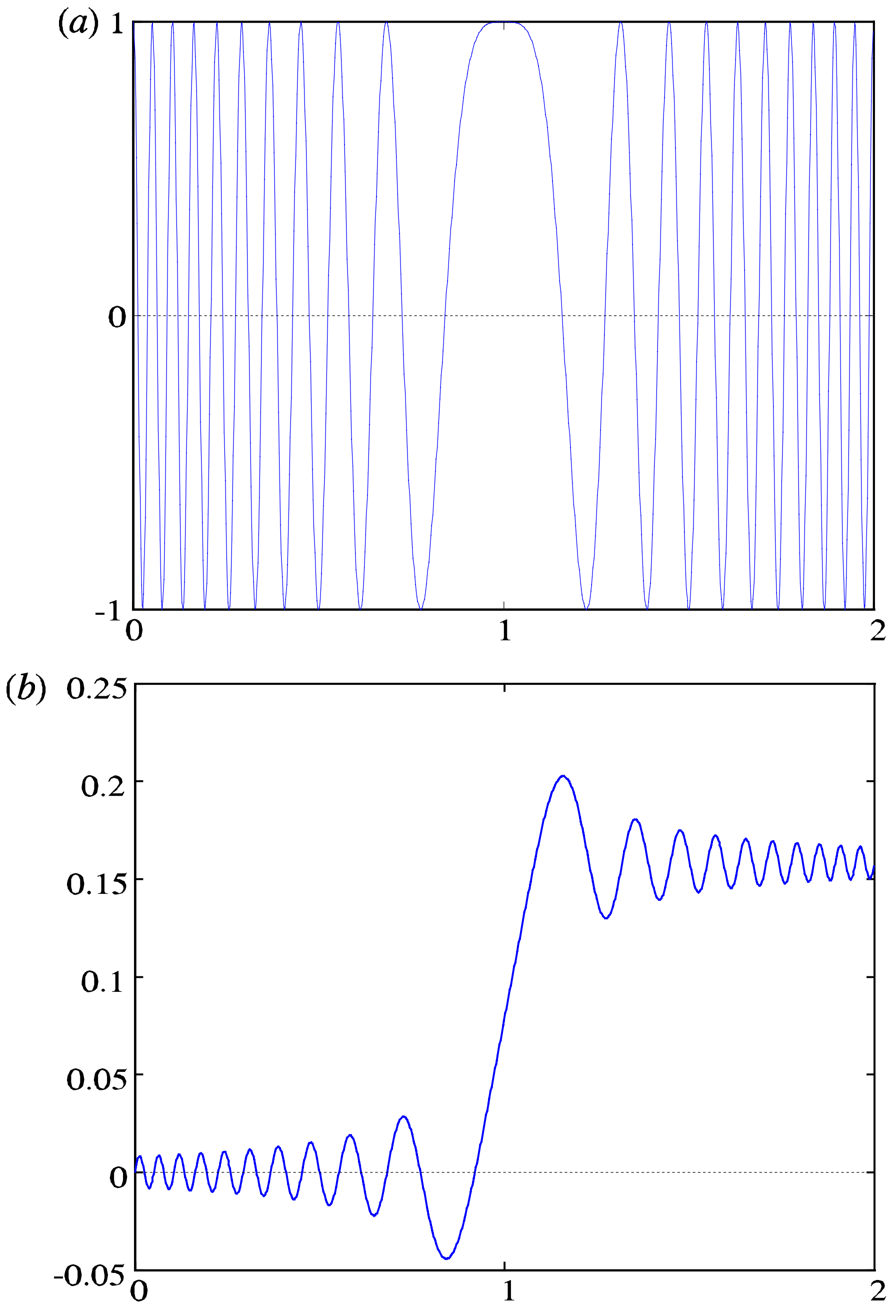

Figure 6.7 (**a**) Simulated general signal of unity amplitude varying linearly from 20 Hz to -20 Hz. (**b**) Integral of signal (**a**).

To illustrate this, Fig. 6.7a shows a waveform similar to the stator current of a vector controlled induction machine during speed reversal. The frequency of this waveform changes linearly in frequency, while its magnitude remains constant.

Figure 6.7b shows the integral of the stator current depicted in Fig. 6.7a. When $\Delta R_s \neq 0$, functions like the ones shown in Fig 6.7b will appear in each one of the components of the estimated flux. These functions will cause deviations of the flux trajectory from a circle centred on the origin during transients, as depicted in Fig. 6.8. This transient corresponds to the same speed reversal as in 6.7.

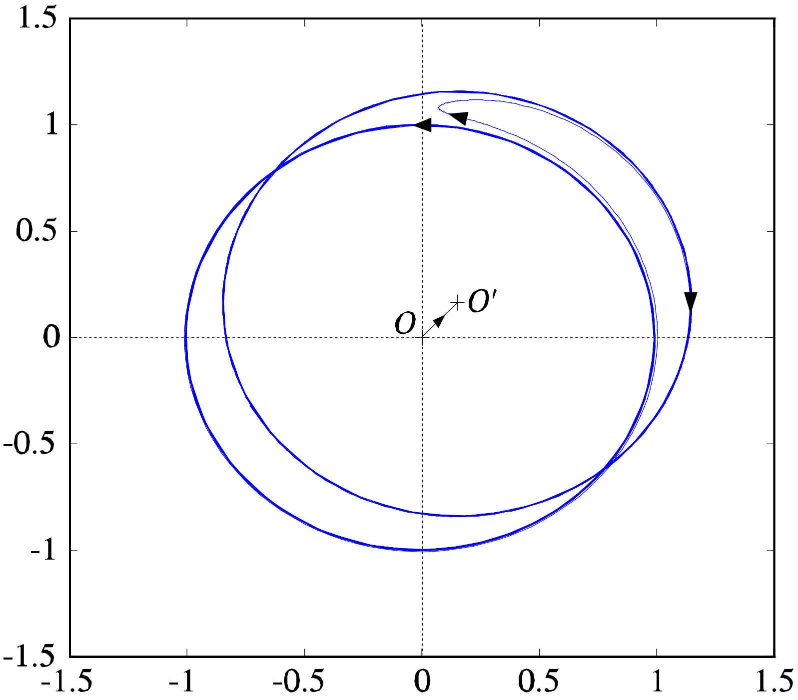

Figure 6.8 Flux trajectory with incorrect estimated stator resistance

The effects of an inaccurate stator resistance estimate can be calculated as follows. It is possible to define the stator current as

$$\boldsymbol{i}_s(t) = A(t)\, e^{j\varphi(t)} \tag{6.6}$$

where $A(t)$ and $\varphi(t)$ are respectively the current magnitude and phase. Therefore we have

$$\int_a^b \boldsymbol{i}_s\, dt = \int_a^b A(t)\, e^{j\varphi(t)}\, dt \tag{6.7}$$

If $A(t)$ varies slowly, while $\varphi(t)$ varies over 2π, then positive and negative values of the previous integrand will tend to cancel each other, and the main contributions to the integral will arise from the end points (*a*,*b*) and from neighbourhoods containing the stationary phase points that satisfy

$$\frac{d}{dt}\varphi(t) = 0 \tag{6.8}$$

If $\varphi'(t)$ is monotonic then (6.8) has only one solution (at $t = t_0$). Provided that the distances from a and b to t_0 are large so the effect of the end points can be neglected and assuming that

$$\left|\varphi^{/}(t_0)\right| >> \left|A^{/}(t_0)\right| \tag{6.9}$$

then it is possible to obtain an approximate expression for (6.7) using the method of stationary phase [22]

$$\int_a^b \boldsymbol{i}_s\,dt \simeq A(t_0)\sqrt{\frac{2\pi}{|\,\varphi^{//}(t_0)\,|}}\;e^{j[\varphi(t_0) \pm \pi/4]} \tag{6.10}$$

The above expression has been validated both experimentally and with numerical simulations. Table 6.1 shows the values obtained by applying (6.10) to the transients in Figs. 6.7 and 6.17 (trace *d*). The simulated and practical results shown in these graphs agree with the theoretical results. Table 6.1 compares the obtained values of $\int_a^b i_s\,dt$ from the simulation and from the practical experiment with the result of applying (6.10) to the corresponding transients.

Table 6.1 Verification of expression (6.10)

	$A(t_0)$	$\varphi''(t_0)$	Obtained value	Result from (6.10)
Simulation (Fig. 6.7)	1 A	251.33 rads^{-2}	0.158	0.1581
Experiment (Fig. 6.17)	6.86 A	380.8 rads^{-2}	0.87	0.8815

Substituting (6.10) in (6.5)

$$\hat{\lambda}_s \simeq \lambda_s - \Delta R_s A(t_0) \sqrt{\frac{2\pi}{|\varphi^{//}(t_0)|}}\; e^{j[\varphi(t_0) \pm \pi/4]} \tag{6.11}$$

Since λ_s describes always a circular trajectory provided that the flux magnitude is constant, the shift from the centre of the estimated flux trajectory is dependent only on the integral of the current, and proportional to ΔR_s.

Therefore the distance $\overline{OO^{/}}$ in Fig 6.8 corresponds to the absolute value of the second term of (6.11), i.e.

$$\overline{OO^{/}} \simeq \left| \Delta R_s A(t_0) \sqrt{\frac{2\pi}{|\varphi^{//}(t_0)|}} \right| \tag{6.12}$$

6.3.2 Effect of Wrong R_s Estimate on the Performance of Sensorless Drives

In many cases the estimated flux angle $\hat{\theta}_e$ is used for Direct Field Orientation (DFO) and the estimated flux magnitude $|\hat{\lambda}_s|$ is used for providing the feedback for flux control. It is clear that an incorrect stator resistance estimate would degrade both flux angle and flux magnitude estimates at low speed. Moreover it will also cause steady state fluctuations around the actual values of $\hat{\theta}_e$ and $|\hat{\lambda}_s|$ as illustrated in Fig. 6.9. This ripple is caused because the estimated flux trajectory is not centred at the origin.

Although the shift from the origin will occur at or very near zero speed, the centre of the estimated flux trajectory will remain indefinitely at the new location. Therefore the ripple caused by this shift will be present at *any frequency*. It can be easily seen that the ripple frequency is that of the estimated flux, i.e. the fundamental electrical frequency in the machine. The effect of this ripple on the performance of the sensorless drive depends on the sensorless technique being used, but it will usually lead to fluctuations around the point of field orientation and to undesirable oscillations on the machine output torque.

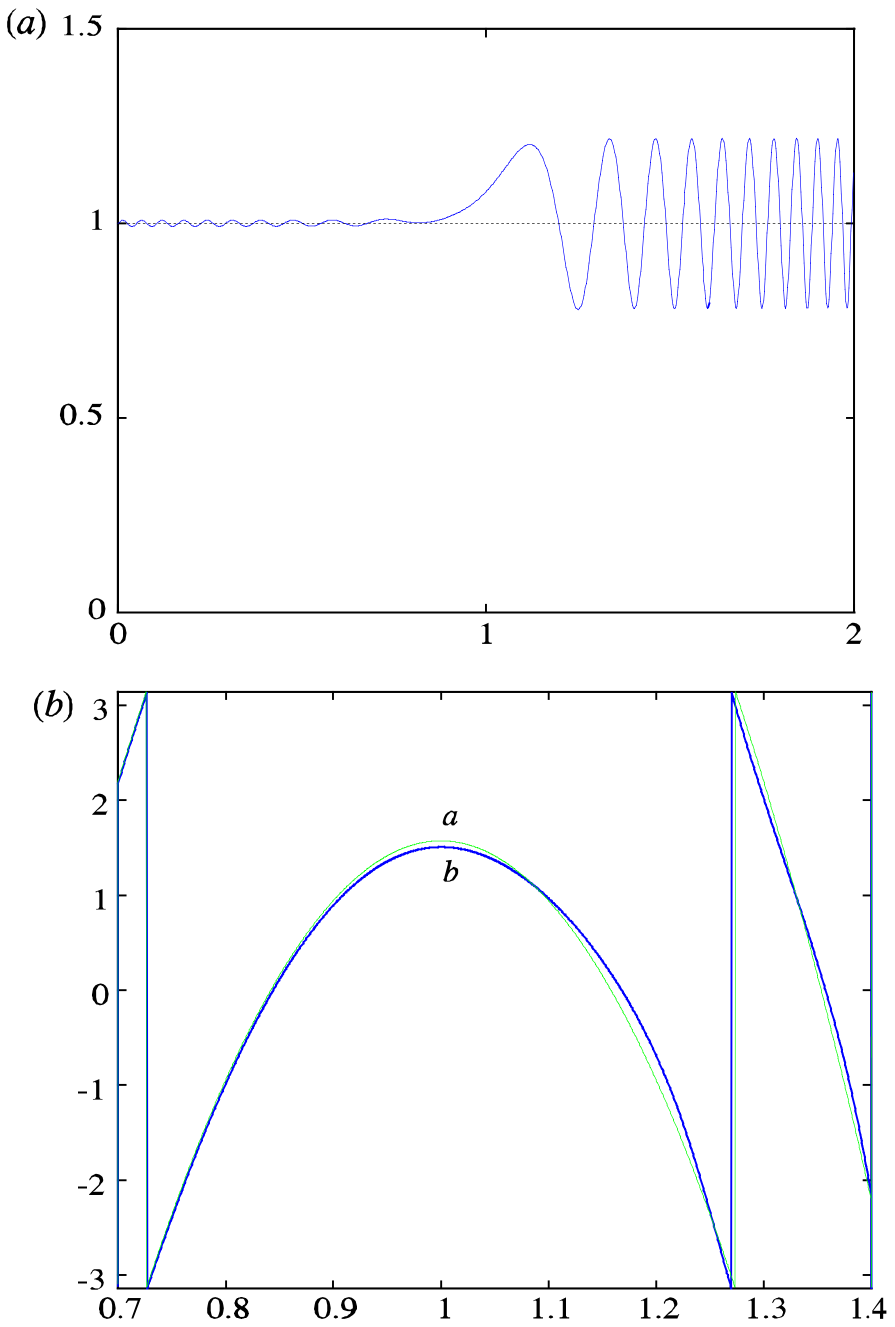

Figure 6.9 a) Oscillation in estimated flux magnitude. **b**) Oscillation in estimated flux angle: *a*) Actual angle, *b*) Estimated angle

Obviously (6.4) is never implemented directly in practice due to drift and initial value problems that are associated with pure integrators. Therefore some sort of low pass or band pass filter is utilised to implement the integrator. In this case, the rotor flux estimate will return to the circular trajectory centred on the origin following the dynamics of the filter. It is easy to understand this if the origin shift is seen as step-like terms added to both components of the estimated flux. However, the time constants of the integrating filters are very large if a good approximation to an ideal integrator is to be obtained. Therefore, the convergence to the actual trajectory will also be very slow. Because of this, the previously mentioned oscillations will persist for a long period of time. This is considered to be a plausible explanation for the estimated flux magnitude ripple observed in [46, 87] during transients through or near zero speed. Note this ripple is not the same effect as that due to oscillations caused by wrong R_s values at general motor speed as seen in Chapter 4.

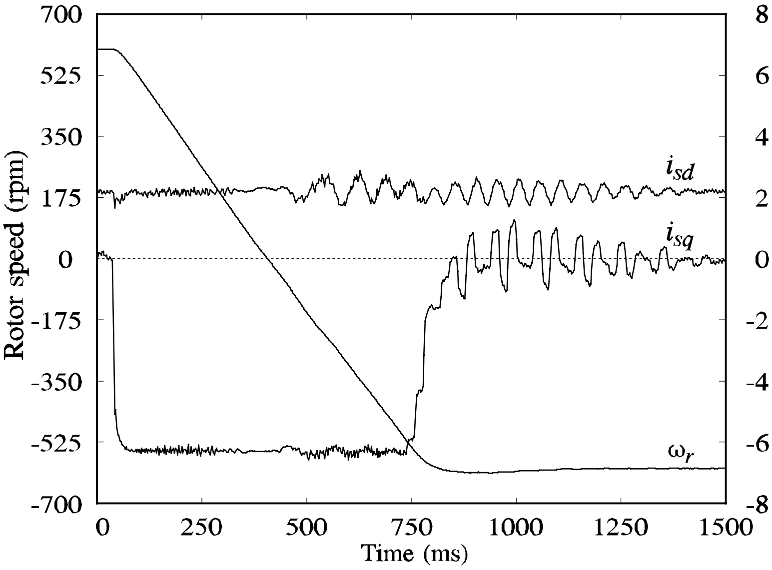

Figure 6.10 Speed transient with incorrect stator resistance

Figure 6.10 shows the waveforms of a speed reversal carried out using a DRFO sensorless vector controlled drive based on the MRAS-CLFO with incorrect stator resistance. Oscillations on i_{sd} and i_{sq} caused by an R_s mismatch during a transient through zero speed are clearly seen. This can be compared with Fig. 6.11 that shows a speed reversal transient on the same conditions, but with properly tuned stator resistance.

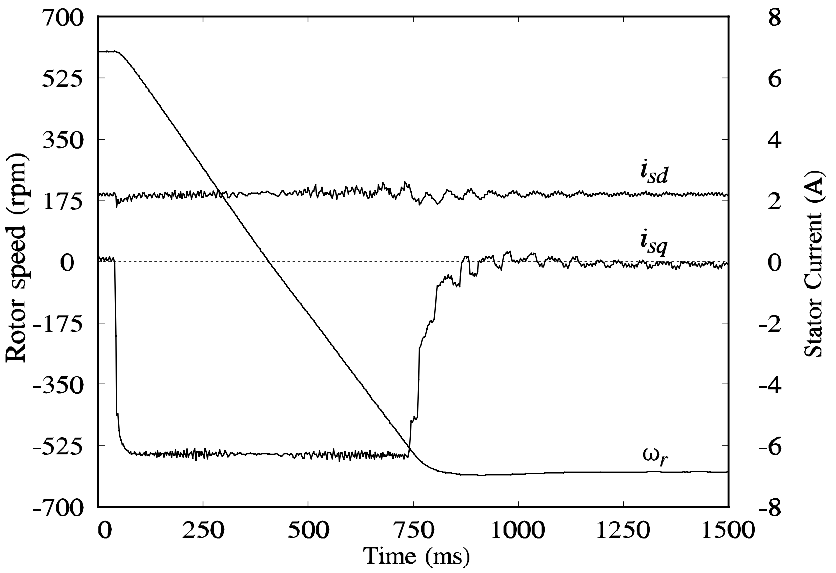

Figure 6.11 Speed transient with correct stator resistance

6.3.3 Circular Regression Algorithm

A system that corrects for the previously mentioned oscillations caused by wrong R_s has been devised by using a least squares circular regression algorithm (LSCRA). The inputs to the LSCRA are N points in the plane, expressed by their coordinates (x_i, y_i). The LSCRA obtains then a least squares fit to a circle of these points. The outputs of the LSCRA are the coordinates of the centre of the circle (x_c, y_c) and its radius (r). To correct for errors in R_s, the inputs to this algorithm are the two components of the estimated flux; i.e. $x_i = \hat{\lambda}_{s\alpha}$, $y_i = \hat{\lambda}_{s\beta}$. The outputs will therefore be the flux magnitude ($r = |\hat{\lambda}'_s|$) and the two components of the centre of the flux trajectory ($x_c = \hat{\lambda}_{s\alpha 0}$, $y_c = \hat{\lambda}_{s\beta 0}$). Therefore the magnitude $\overline{OO'}$ in (6.12) can be expressed as

$$\overline{OO'} = \sqrt{\hat{\lambda}^2_{s\alpha 0} + \hat{\lambda}^2_{s\beta 0}} \tag{6.13}$$

The LSCRA is derived as follows. As previously explained, the LSCRA calculates the values of x_c, y_c and r in

$$(x - x_c)^2 + (y - y_c)^2 = r^2 \tag{6.14}$$

that minimise the error function

$$\varepsilon = \sum_{i=1}^{N} \left[(x_i - x_c)^2 + (y_i - y_c)^2 - r^2 \right]^2 \tag{6.15}$$

In order to do that, the following partial derivatives are obtained and equated to zero

$$\frac{\partial \varepsilon}{\partial x_c} = -4 \sum_{i=0}^{N} (x_i - x_c) \left[(x_i - x_c)^2 + (y_i - y_c)^2 - r^2 \right] = 0 \tag{6.16}$$

$$\frac{\partial \varepsilon}{\partial y_c} = -4 \sum_{i=0}^{N} (y_i - y_c) \left[(x_i - x_c)^2 + (y_i - y_c)^2 - r^2 \right] = 0 \tag{6.17}$$

$$\frac{\partial \varepsilon}{\partial r} = -4r \sum_{i=0}^{N} \left[(x_i - x_c)^2 + (y_i - y_c)^2 - r^2 \right] = 0 \tag{6.18}$$

Solving the above equations for x_c, y_c and r gives

$$x_c = \frac{\alpha\eta - \beta\delta}{\beta^2 - \gamma\eta} \tag{6.19}$$

$$y_c = \frac{\gamma\delta - \alpha\beta}{\beta^2 - \gamma\eta} \tag{6.20}$$

$$r^2 = x_c^2 + y_c^2 + \frac{1}{N} \left[\sum_{i=1}^{N} x_i^2 + \sum_{i=1}^{N} y_i^2 - 2 \left(x_c \sum_{i=1}^{N} x_i + y_c \sum_{i=1}^{N} y_i \right) \right] \tag{6.21}$$

where

$$\alpha = \sum_{i=1}^{N} x_i^3 + \sum_{i=1}^{N} x_i y_i^2 - \frac{1}{N} \sum_{i=1}^{N} x_i \left(\sum_{i=1}^{N} x_i^2 + \sum_{i=1}^{N} y_i^2 \right) \tag{6.22}$$

$$\beta = -2\sum_{i=1}^{N} x_i y_i + \frac{2}{N}\sum_{i=1}^{N} x_i \sum_{i=1}^{N} y_i \tag{6.23}$$

$$\gamma = -2\sum_{i=1}^{N} x_i^2 + \frac{2}{N}\left(\sum_{i=1}^{N} x_i\right)^2 \tag{6.24}$$

$$\delta = \sum_{i=1}^{N} y_i^3 + \sum_{i=1}^{N} x_i^2 y_i - \frac{1}{N}\sum_{i=1}^{N} y_i \left(\sum_{i=1}^{N} x_i^2 + \sum_{i=1}^{N} y_i^2\right) \tag{6.25}$$

$$\eta = -2\sum_{i=1}^{N} y_i^2 + \frac{2}{N}\left(\sum_{i=1}^{N} y_i\right)^2 \tag{6.26}$$

N is the number of samples taken to obtain an estimate of x_c, y_c and r. In the practical implementation of the LSCRA, the new input values (x_i, y_i) will be stored in an N-sample buffer, while the oldest sample in the buffer is discarded. Then the values of the centre and radius of the circle are recalculated. In this way, this algorithm will produce an estimate every sample, with an average delay of $NT_s/2$ seconds, being T_s the sampling time.

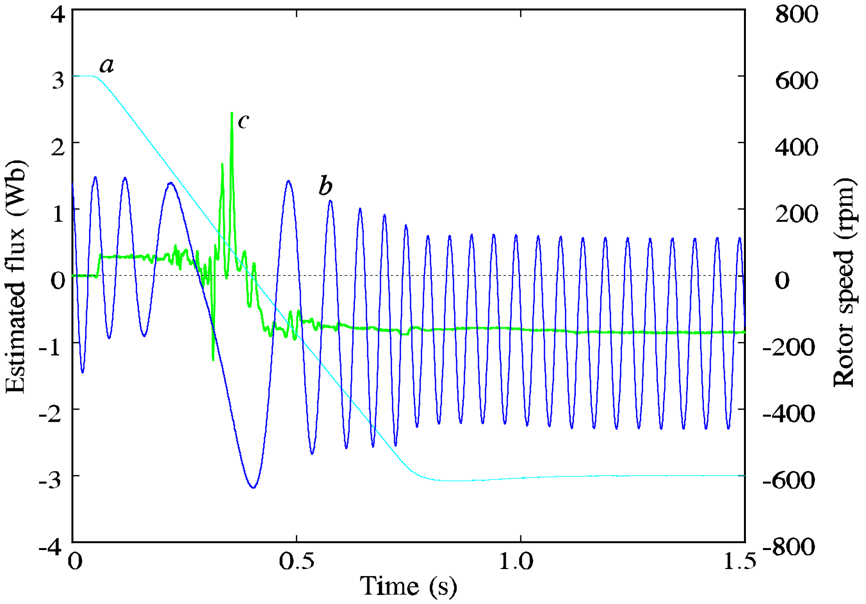

Figure 6.12 Effectiveness of the LSCRA. *a*) Rotor speed, *b*) Integral of the stator voltage, *c*) Output x_c of the LSCRA

The performance of this algorithm is illustrated in Fig. 6.12. This figure shows the estimated flux waveform during speed reversal transient. The flux estimate has been obtained using a pure integrator and considering $\hat{R}_s = 0$, therefore the trace shown corresponds to the integral of the voltage. The value of x_c obtained from the LSCRA is also shown. It is possible to see that x_c tracks successfully the average value of the voltage integral. This average value presents two significant changes. The first one occurs at the beginning of the transient (when i_{sq} is suddenly changed from its no load value to 150% rated i_{sq}). The second and most noticeable change occurs near zero speed, as expected. The use of a pure integrator has been possible since the LSCRA can also track the drift caused by measurement offsets.

6.3.4 Stator Resistance Estimation using the LSCRA

Using the LSCRA it is possible to obtain an estimate of the distance $\overline{OO'}$. To calculate the value of ΔR_s, it is necessary to know the values of the current magnitude $A(t)$ and acceleration $\varphi''(t)$. The current magnitude is very easy to calculate from i_{sq} and i_{sd} reference values. However, direct calculation of $\varphi''(t)$ will in general be very noisy. An alternative approach is to apply the LSCRA not only to the flux estimate, but also to the integral of the stator current; therefore the value

$$\overline{OO'_I} \simeq \left| A(t_0) \sqrt{\frac{2\pi}{|\varphi''(t_0)|}} \right| \qquad (6.27)$$

will be obtained, according to (6.10). Hence an estimation of the stator resistance can be obtained from

$$|\Delta R_s| = \frac{\overline{OO'}}{\overline{OO'_I}} \qquad (6.28)$$

The signum of ΔR_s can be obtained from the comparison of the quadrants where O' and O'_I lie. If both centres are in the same quadrant ΔR_s is negative, being positive otherwise.

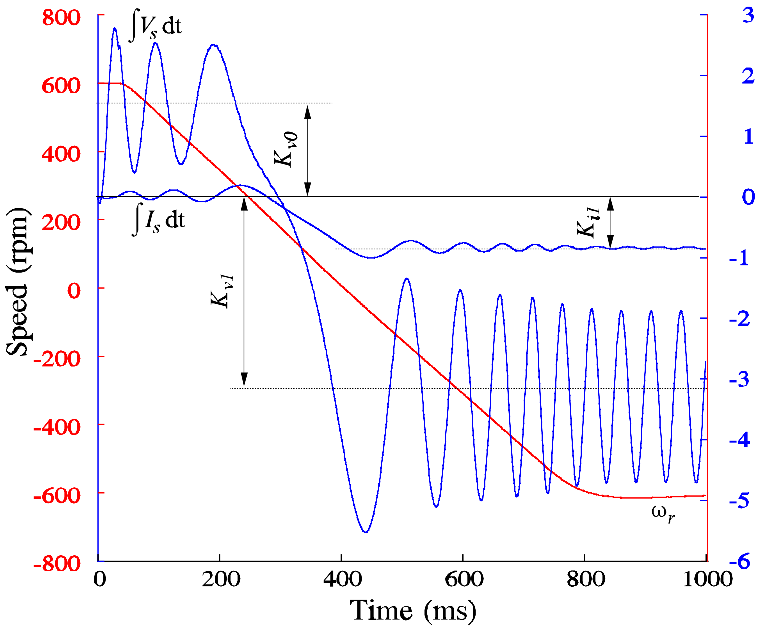

Figure 6.13 Voltage and current integrals during speed reversal

Figure 6.13 shows the waveforms of one component of the stator voltage and current integrals during speed reversal. Note the integral of the stator voltage is used instead of the stator flux (hence $\Delta R_s = R_s$). In this figure $K_{v1} - K_{v0}$ is proportional to $\overline{OO'}$ and $K_{i1} - K_{i0}$ to $\overline{OO'_I}$, and therefore the ratio between them is the stator resistance.

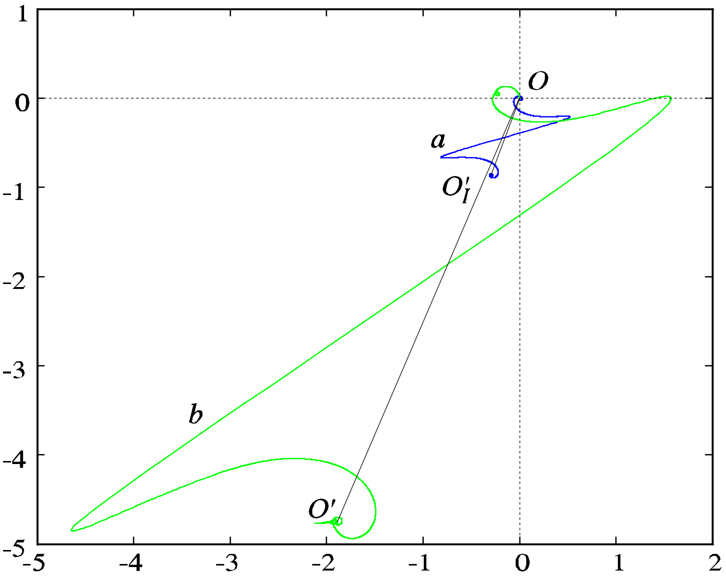

Figure 6.14 Loci of the centre of the voltage and current integrals trajectories. *a*) Locus of O'_I, *b*) Locus of O'

Figure 6.14 illustrates the trajectories of the centres of the voltage and current integrals (i.e. O' and O'_I) during the previous speed reversal transient. The two trajectories are very similar, and the scaling factor between them is again R_s, according to (6.28).

6.3.5 Simplified Method of Stator Resistance Estimation

The LSCRA is computationally intensive and requires a relatively large memory storage. A simpler method of stator resistance estimation can be devised considering

$$\boldsymbol{u}_s(t) = \frac{\mathrm{d}}{\mathrm{dt}}\lambda_s(t) + R_s\boldsymbol{i}_s(t) \tag{6.29}$$

Obtaining the Fourier transform of both sides we have

$$\mathcal{F}\{\boldsymbol{u}_s(t)\} = j\omega\mathcal{F}\{\lambda_s(t)\} + R_s\mathcal{F}\{\boldsymbol{i}_s(t)\} \tag{6.30}$$

Using $X(\omega)$ to denote the Fourier transform of $\boldsymbol{x}(t)$ and the definition of stator current in (6.6)

$$U_s(\omega) = j\omega\Lambda_s(\omega) + R_s\int_{-\infty}^{+\infty} A(t)e^{j[\varphi(t) - \omega t]}dt \qquad (6.31)$$

Applying the stationary phase method (given the same conditions as for the derivation of (6.10)

$$U_s(\omega) = j\omega\Lambda_s(\omega) + R_s A(t_0)\sqrt{\frac{2\pi}{\left|\varphi^{//}(t_0)\right|}}\,e^{j[\varphi(t_0) - \omega t \pm \pi/4]} \qquad (6.32)$$

By evaluating this expression at $\omega = 0$, an estimate of R_s can be obtained

$$R_s = \frac{U_s(0)}{A(t_0)\sqrt{\dfrac{2\pi}{\left|\varphi^{//}(t_0)\right|}}} \qquad (6.33)$$

Therefore it is possible to obtain an estimate of the stator resistance by dividing the average values of stator voltage and stator current taken during a transient. This is equivalent to a direct application of Ohm’s law, since it has been proven that the average value of the stator current is not zero during transients through zero speed. However, (6.33) cannot be applied during steady state, since the average value of the stator currents and voltages will be zero. The immediate implementation is rather simple, requiring only a low pass filter for the current, and another one for the voltage.

The implementation of the proposed method is illustrated in Fig. 6.15. In this implementation two first order low pass filters have been combined to obtain a second order low pass filter. The output of the first low pass filter can be considered as an approximation to the stator voltage and current integrals. In order to obtain a good measurement of the DC components, the time constants of the low pass filters should be large; however, it should not be so large as to cause problems with measurement offsets. Favourable time constants are in the range of 1-2 s. Two problems will arise in practice: the presence of a DC offset in the input signal and the division by very small values of $\boldsymbol{K}_i$. The latter is solved by computing the division only when $\boldsymbol{K}_i \geq \varepsilon$. If not then the division output $\boldsymbol{r}_s$ is held constant. The measurement offset can avoided by resetting the output of the second low pass filter when the machine has been in a steady state for a certain amount of time. To avoid

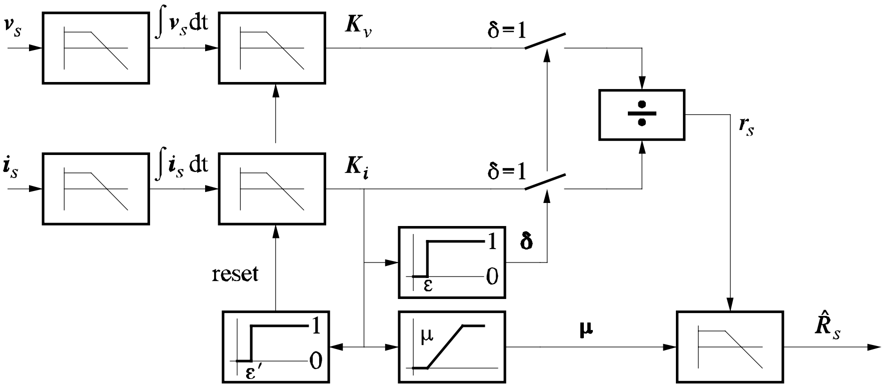

Figure 6.15 Implementation of stator resistance identifier

a sudden change in the R_s estimate when the offset is zeroed, resetting is only carried out when the resistance estimation is disabled. This occurs when $|\boldsymbol{K}_i| \leq \varepsilon' \leq \varepsilon$.

Two different R_s estimates are obtained, one from each component of the stator equation. A weighting function is applied to each R_s estimate (**μ** in Fig. 6.15) depending on the value of their respective K_i. For instance, if $K_{i\alpha}$ is bigger than $K_{i\beta}$, then the contribution of $R_{s\alpha}$ to the overall R_s will also be bigger than that of $R_{s\beta}$. This can be expressed mathematically as

$$R_s = \frac{\mu_\alpha}{\mu_\alpha + \mu_\beta} R_{s\alpha} + \frac{\mu_\beta}{\mu_\alpha + \mu_\beta} R_{s\beta} \tag{6.34}$$

μ_α and μ_β being the weighting factors corresponding to each of the R_s estimates. Finally the resulting R_s estimate will be low pass filtered to minimize noise and ripple.

6.3.6 Experimental Results

Figure 6.16 illustrates the performance of the LSCRA. The magnitude of the estimated rotor fluxes $|\hat{\lambda}_r|$ and $|\hat{\lambda}_r'|$ is shown. The flux estimate $|\hat{\lambda}_r|$ is obtained using a closed loop flux observer (MRAS-CLFO). The stator resistance error is set at approximately 10%. Both flux estimates are very similar until about 200 rpm, then oscillations of a relatively big amplitude appear in $\left|\hat{\lambda}_r\right|$. Note the waveforms are very similar to that of Fig 6.9a, although the oscillations decrease with a time constant determined by the characteristics of the CLFO. However, these oscillations are completely filtered out by the LSCRA.

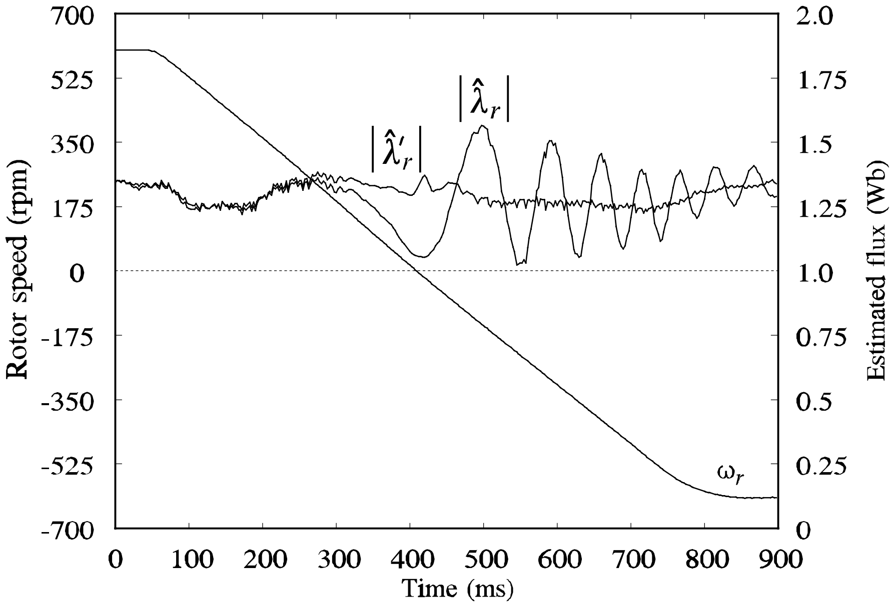

Figure 6.16 Estimated flux magnitude using the LSCRA during speed reversal

The calculation of the stator resistance is illustrated in Fig 6.17. In this case $\hat{R}_s = 0$, therefore ΔR_s will give directly the value of R_s. Two LSCRA filters are used on the integral of the voltage and the integral of the current, and the estimated stator resistance is calculated by dividing their outputs, according to (6.28). Initially the obtained value of R_s is extremely noisy, due principally to the small value of $\overline{OO'_I}$. However when the machine electrical speed approaches 0 Hz, the magnitudes of both $\overline{OO'}$ and $\overline{OO'_I}$ increase, and therefore a consistent estimation of R_s is obtained, after about 500 ms. Since the algorithm gives a wrong stator resistance estimate for part of the transient, some kind of management system needs to be included to determine whether the actual estimate is correct or not. This management system is easy to implement by checking the magnitude of $\overline{OO'_I}$.

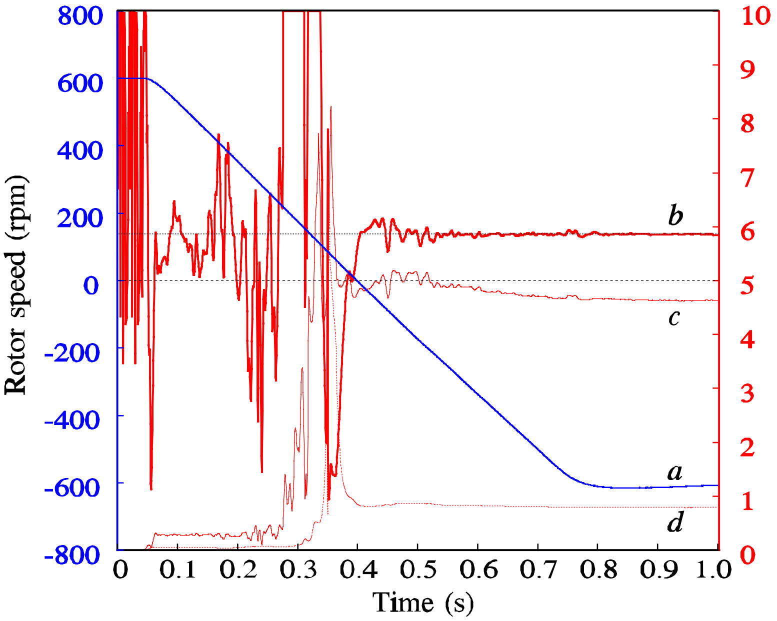

Figure 6.17 *a*) Rotor speed, *b*) Estimated stator resistance, *c*) Distance OO', *d*) Distance OO'_I

When this value is greater than a certain level, the output of the R_s estimator is considered valid.

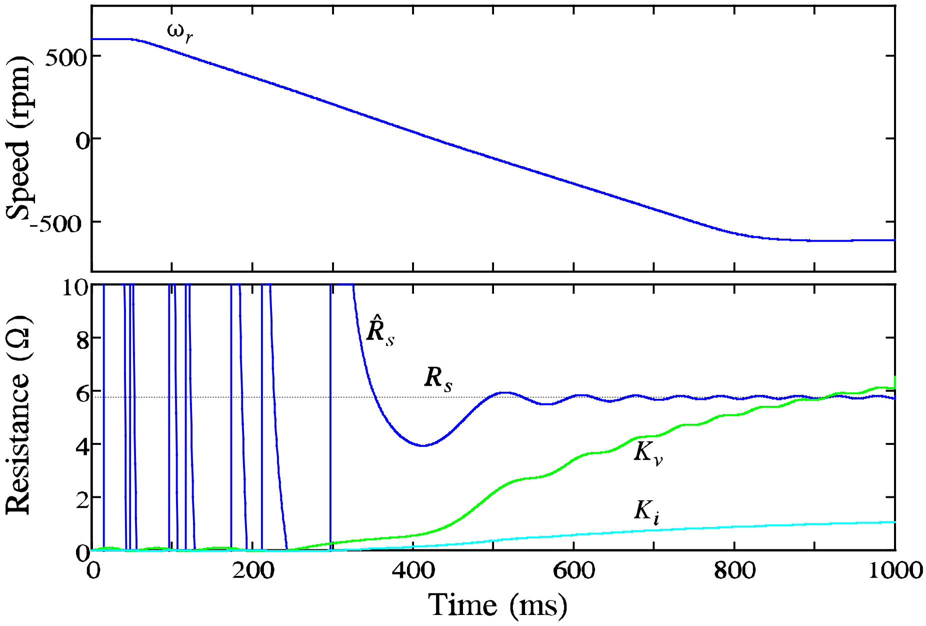

Figure 6.18 Top: Rotor speed. Bottom: Actual and estimated stator resistance; K_v, K_i outputs of the voltage and current low pass filters

Figure 6.18 shows a similar transient, but using the simplified method of stator resistance estimation. An estimate is always calculated, even when K_i is very small.

Therefore big oscillations are present before the system converges to a constant value. A stable value of R_s is obtained after about 700 ms. Since no filtering of the resulting R_s estimate has been carried out, the output also presents a small ripple. Although the implementation of this method is much simpler than that of the LSCRA, the stator resistance estimate takes a longer time to converge. Moreover, the correction of the magnitude and phase of the estimated flux cannot be attained with this approach.

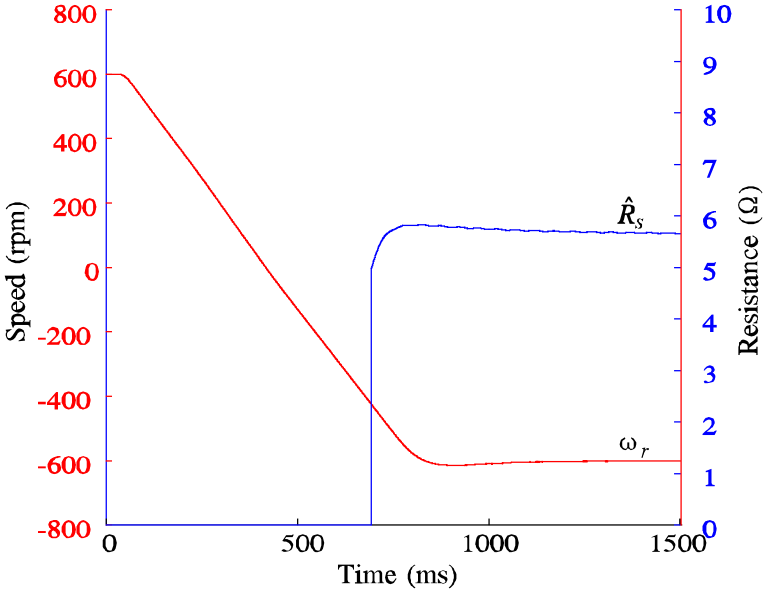

Figure 6.19 Stator resistance estimation transient, $R_s = 0$ at $t = 0$

Figure 6.19 shows the results for the previous transient when the system is fully implemented, i.e. switching off the estimation when K_i is too small, combining both R_s estimates and filtering the resulting estimate. The initial value of the R_s estimate is set to zero. It is possible to see that the ripple present in Fig. 6.18 has been completely cancelled. It is also possible to use previous R_s estimates during the transient, and update the value of R_s only when K_i is sufficiently high. This is shown in Fig. 6.20.

The evaluation of the accuracy of this method of R_s measurement was obtained by using the following procedure. First, the machine was operated at constant speed and full load until it reached constant temperature, then a speed transient was carried out to obtain a stator resistance estimate. After that, the machine was switched off and driven externally to stand still. The stator resistance was then measured at regular intervals (each minute, during 10 minutes). The real stator

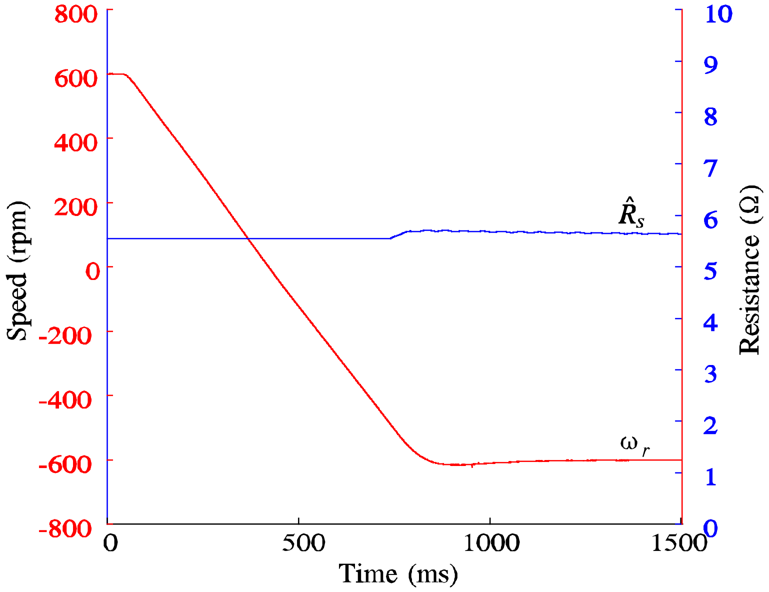

Figure 6.20 Stator resistance estimation. R_s at t = 0 obtained from a previous transient

resistance was calculated from this measurements by correlating them to an exponential and extrapolating the resulting exponential to $t = 0$. It was found that the proposed method showed an accuracy better than 1%.

6.4 Discussion and Conclusions

6.4.1 Rotor Time Constant Identification

The proposed method of rotor time constant identification uses the interpolated Short Time Fast Fourier Transform to obtain an independent speed measurement from the rotor slot harmonics. With this method it is possible to obtain extremely good accuracy for a given data record duration. This method has proven to be very robust, since it is parameter independent and can be applied to almost any induction machine.

A T_r identification method has been devised by using the above mentioned speed measurement. Therefore a more accurate speed estimate is obtained from the rotor speed estimator. By using this method the speed holding characteristic of a sensorless vector controlled drive has been notably enhanced. Typical figures show a maximum average error of 0.08 rpm between actual and reference speed in steady state.

The availability of a speed estimate with high accuracy and small delay has made possible the observation of rapid changes of the rotor time constant estimate which cannot be attributable to thermal variations of the rotor resistance. Possible causes of this change on the estimated T_r are inaccuracies on the rest of the speed estimator parameters and actual changes in the motor quantities. However the error between estimated and actual speed is driven to zero, although in this case the obtained $\hat{T}_r$ would in general differ from the actual machine rotor time constant. It is emphasised that the technique of forcing $\omega_{err} = \hat{\omega}_r - \hat{\omega}_{sh}$ to zero also compensates $\hat{\omega}_r$ for variations in all parameters including σL_s, L_0, L_s and L_r all of which vary with load.

6.4.2 Stator Resistance Identification

This chapter explains the effects of incorrect stator resistance in deriving the flux estimate from integration of the stator back emf during speed transients through or near zero speed. A qualitative and quantitative explanation of these effects is given. The effect of an incorrect R_s can be likened to a step function added to each one of the estimated flux components, causing oscillations in the estimated flux magnitude and angle. These oscillations will generally cause undesirable oscillations in the machine torque. The amplitude of the step like disturbance is proportional to the magnitude of the stator current and inversely proportional to the square root of the machine acceleration. Therefore this effect is more pronounced in machines with large inertia.

A solution to the above problem has been presented, by adjusting the trajectory of the estimated flux to a circle, using a least squares method (LSCRA). The output of the LSCRA is used in two ways: firstly, the flux estimates are corrected, and therefore the previously mentioned ripple in flux magnitude and angle is considerably reduced. Secondly, the stator resistance estimate is corrected at the same time. Therefore the performance of a sensorless vector controlled induction machine during speed transients thorough or near zero speed is improved.

An alternative method of R_s estimation has also been proposed. This method consists on dividing the average values of stator voltage and current calculated over a time period which includes a transient. However it is slower than the LSCRA and does not allow for correction of the flux estimates.

The main drawback of the proposed methods of stator resistance estimation is the impossibility of obtaining an estimate in steady state. This is because the denominators of (6.28) and (6.33) vanish at this point. However both methods of resistance estimation are very robust, since no extra signals have to be injected into the machine, no speed measurement is required and no previous knowledge of any other machine parameter is needed.

Chapter 7 Dynamic Performance Study

7.1 Introduction

The work carried out in this chapter was motivated by the aim of attaining the maximum speed loop bandwidth from a sensorless vector controlled induction motor drive. The torque response of sensorless drives is known to be as good as sensored drives except at very low speed (1 Hz and below) when field orientation deteriorates. However the closed loop speed bandwidth limitations for sensorless drives has never been studied.

Generally, the maximum performance of a speed sensored drive in terms of speed loop bandwidth is determined by noise considerations. The maximum acceptable torque ripple and the speed transducer noise/quantisation error are the main limiting factors. However this is not the case for MRAS based sensorless vector control implementations. In this case the most important limiting factor in terms of performance is stability considerations. It is shown in Chapter 4 that a rotor-flux based MRAS system exhibits transient speed-dependent oscillations in the speed estimation signal due to incomplete cancellation of the underdamped oscillatory estimator poles by the estimator zeros. Inaccuracies in all the required estimator parameters, R_s, R_r, L_0 and σL_s, can induce incomplete cancellation, with the stator resistance R_s being the most serious with even a +10% overestimate causing possible instability at most operating frequencies. The sensitivity to oscillation increases with the bandwidth of the adaptive speed estimation represented by the natural frequency ω_{ad}. This is chosen to be 20 Hz (or 125 rads^{-1}) to allow for good speed dynamics for low power industrial drives below 5 kW. The sensitivity also increases with the closed loop parameter $\omega_n J$ which can be used as a goodness factor for the sensorless drive in comparison with sensored drives.

This chapter investigates the dynamic performance limits of a sensorless cage induction motor drive utilizing a MRAS based speed and flux estimator operating within a Direct Rotor Flux Orientated (DRFO) vector controller. The effects of incorrect estimator parameters in zero speed operation, speed holding accuracy and speed transients are presented. These results are discussed in context with the theoretical results in Chapter 4, as a means of providing a practical validation of the aforementioned theoretical results.

To provide a means of comparing the performance of sensored and sensorless drives, the parameter $\omega_n J$ is discussed in relation to encoder resolution in sensored drives and speed estimate signal ripple for sensorless drives. The load torque rejection performance of any drive is also strongly determined by $\omega_n J$. As such, load torque transients form the main mode of comparison between sensored and sensorless drives. Finally the effect of the adaptive loop bandwidth in the sensorless drive performance is also discussed.

7.2 Sensorless Field Orientation at Zero Speed

The purpose of these tests is to evaluate the performance of the MRAS-CLFO system at low speed. The first test involves the system being run under sensored IRFO and then comparing the MRAS-CLFO estimated flux angle with the flux angle used for IRFO. The second test investigates the influence of the stator resistance estimate on the performance of the sensorless DRFO at full load at zero speed.

For the first test the drive is operated under sensored IRFO control in which T_r is set at its tuned value. The estimated values of $\hat{\theta}_e$ and $\hat{\omega}_r$ are computed from the MRAS-CLFO but are used only for comparison with the rotor flux angle obtained from the IRFO (θ_e) and the measured rotor speed (ω_r). In the tests the motor is driven to zero speed under no load which represents the worst case for the MRAS-CLFO since ω_e is approximately zero and the estimator is hypersensitive to errors in the stator parameters. Figure 7.1 shows $\hat{\theta}_e, \theta_e, \hat{\omega}_r, \omega_r$ when R_s is derived from the identifier of Section 6.3, and σL_s is the no-load value taken from self-commissioning [79]. Although an angle error $(\theta_e - \hat{\theta}_e)$ exists at $\omega_r = 0$, the angle $\hat{\theta}_e$ stays close to θ_e for upto a minute before slowly diverging. Figure 7.2 shows the effect of a +10% error in R_s where it is found that $\hat{\theta}_e$ diverges after approximately 1 s.

Under sensorless DRFO, when $\hat{\omega}_r$ and $\hat{\theta}_e$ are used for speed and vector control respectively, no-load at zero speed was found to be unattainable due to the poor

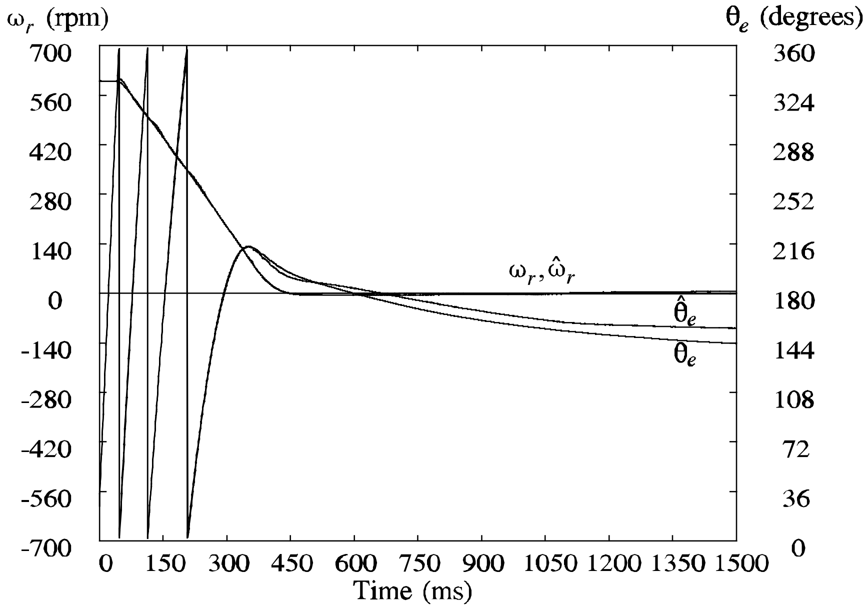

Figure 7.1 Comparison of ω_r, θ_e (IRFO) with estimated ω_r, θ_e (DRFO) for transient to zero speed under no-load

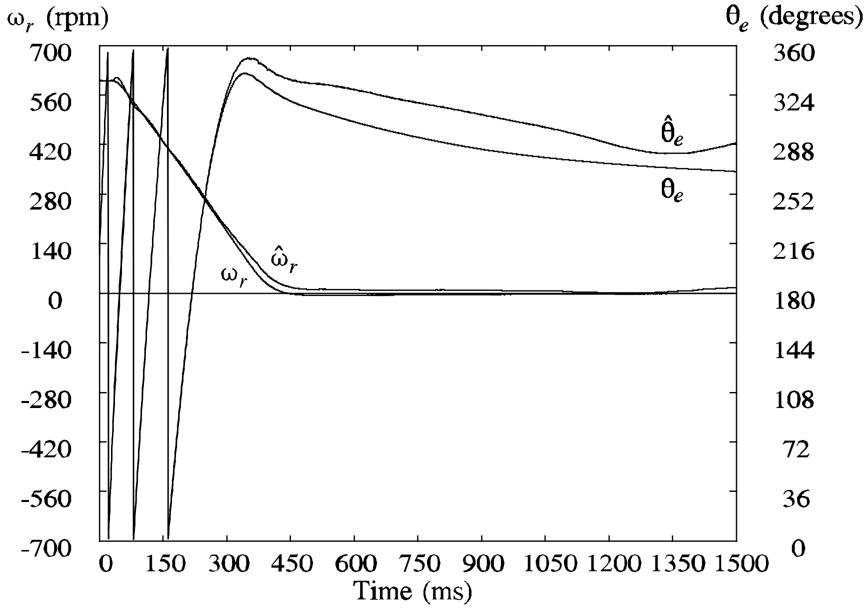

Figure 7.2 Comparison of ω_r,θ_e (IRFO) with estimated ω_r,θ_e (DRFO) for transient to 0 rpm at no-load 10% error in R_s

quality of speed and flux angle estimates. Therefore transients at full load have been used to perform the second test on a sensorless DRFO implementation. Transients to zero speed under full load are shown in Figs. 7.3 to 7.7. The full-load i_{sq} current is approximately 4 A whilst the demand limit i_{sq}^* is set at 6.5 A.

Identification for T_r is off whilst R_s is kept tuned in all the transients except for Figs. 7.4 and 7.5. The control natural frequencies are $\omega_n = 4$ rads^{-1} and $\omega_{ad} = 125$ rads^{-1}. When all the parameters are tuned (Fig. 7.3), the estimated speed follows the actual speed very closely with a typical steady state speed error of ±5 rpm. There is also good field orientation down to zero speed. Moreover, the system is stable at zero speed and continuous operation is possible. There is a short period during settling when the i_{sq} response presents some oscillations due to the relatively poor speed estimate. However after a period of approximately 0.5 s, speed and currents settle to their respective steady state values.

However if R_s is in error by ±10%, field orientation is lost completely with i_{sq} settling at the limit value. The speed feedback is very poor and the speed control is also lost. This can be easily seen in Fig. 7.4, where the machine accelerates without control, and in Fig. 7.5, where the machine never settles at zero speed.

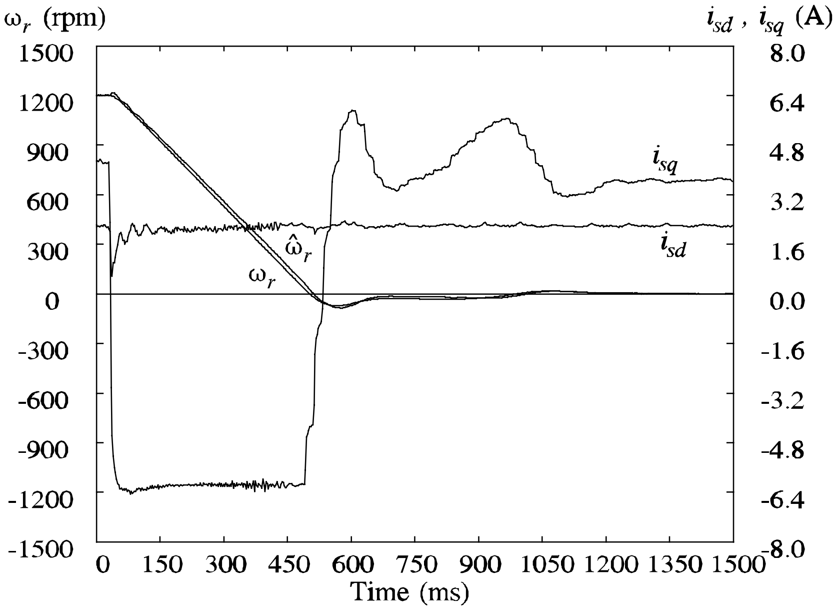

Figure 7.3 Sensorless DRFO transient to zero speed under full load. Tuned parameters

When the full load transient to zero speed is carried out with ±10% error in σL_s and tuned R_s, the results in Figs. 7.6 and 7.7 are obtained. Stable and continuous zero speed operation is achieved. However the rotor speed estimate presents a noticeable error during the moment of settling (compare with Fig. 7.3). This causes i_{sq} to reach the positive current limit before reaching its steady state value. Otherwise field orientation is acceptable, since control over the output torque is never lost.

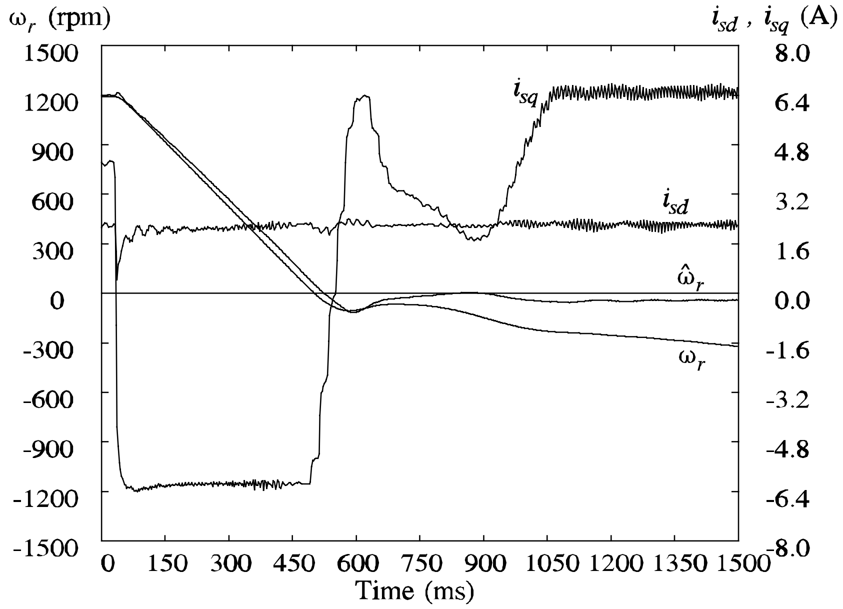

Figure 7.4 Sensorless DRFO transient to zero speed under full load. +10% error in R_s

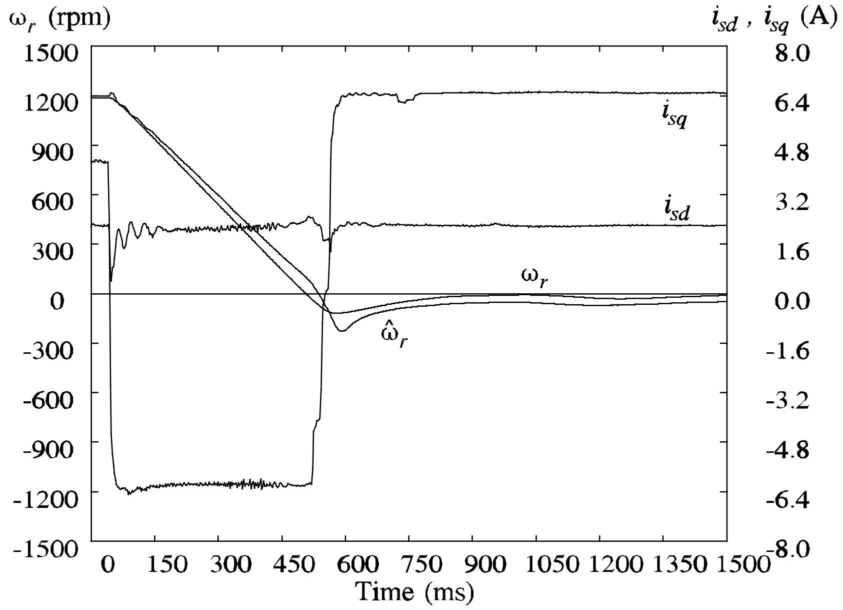

Figure 7.5 Sensorless DRFO transient to zero speed under full load. -10% error in R_s

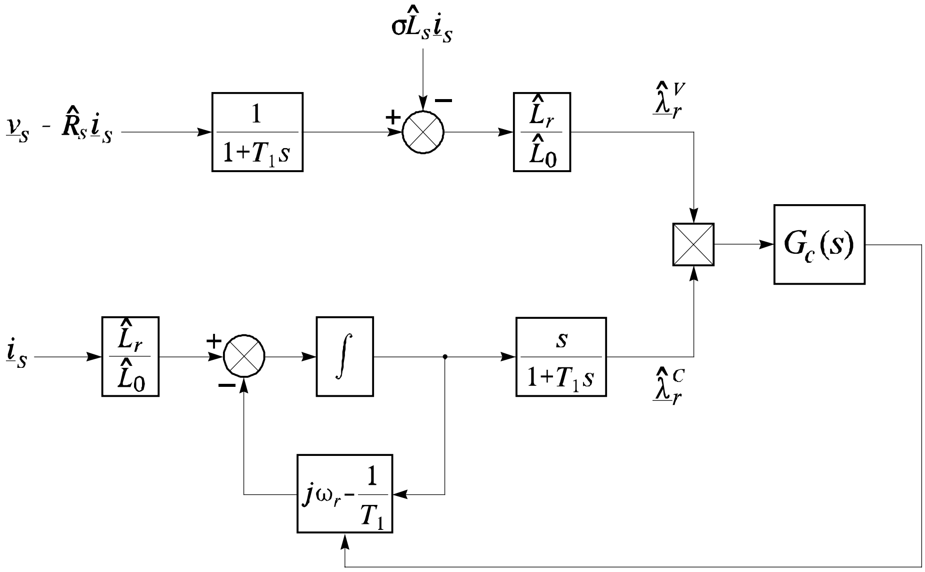

Figure 7.6 Sensorless DRFO transient to zero speed under full load. +10% error in σL_s

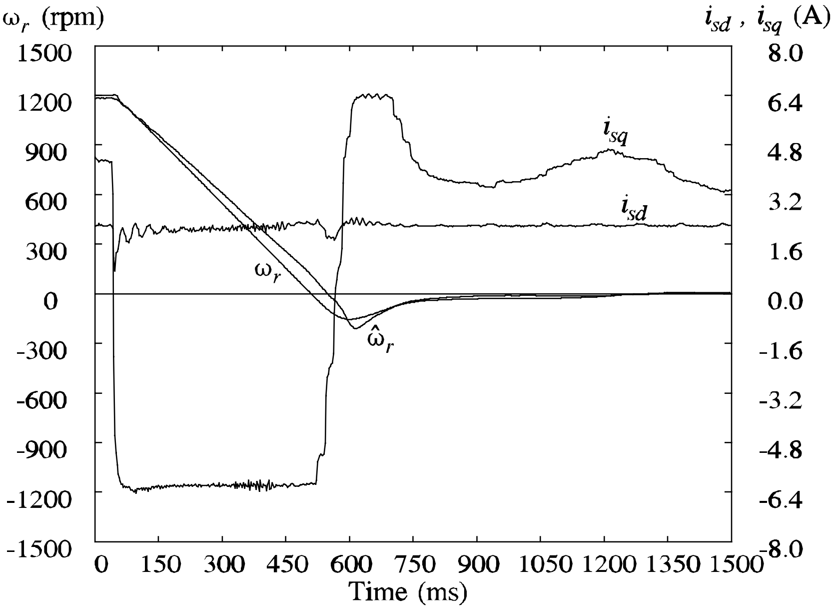

Figure 7.7 Sensorless DRFO transient to zero speed under full load. -10% error in σL_s

7.3 Speed Holding Accuracy

Section 4.3.5 showed the theoretical speed error ($\hat{\omega}_r - \omega_r$) for different parameter errors. The experimental results in this section aim to validate these theoretical results. The following results have been produced using the sensorless MRAS-CLFO with ω_n = 4 rads^{-1}, ω_{ad} = 125 rads^{-1} and using a speed feedback filter of 25 Hz. The induction machine is driven at full load (i_{sq} = 4 A) to exacerbate the effects of incorrect parameters. At the beginning of each transient, all the estimator parameters are tuned, then a particular parameter is changed and after a few seconds the parameter is reset to its original tuned value. The effect of the speed feedback filter in this transients is negligible because the filter exhibits unity gain at low frequencies and therefore does not affect the speed value in steady state. The results for variation on the stator resistance (R_s) have already been shown in Figs. 4.17 and 4.18, and therefore are not repeated here. In all cases the ripple observer in $\hat{\omega}_r$ is principally at the excitation frequency (or very close) which is about 10 Hz in this case. This is consistent with the analysis in Chapter 4.

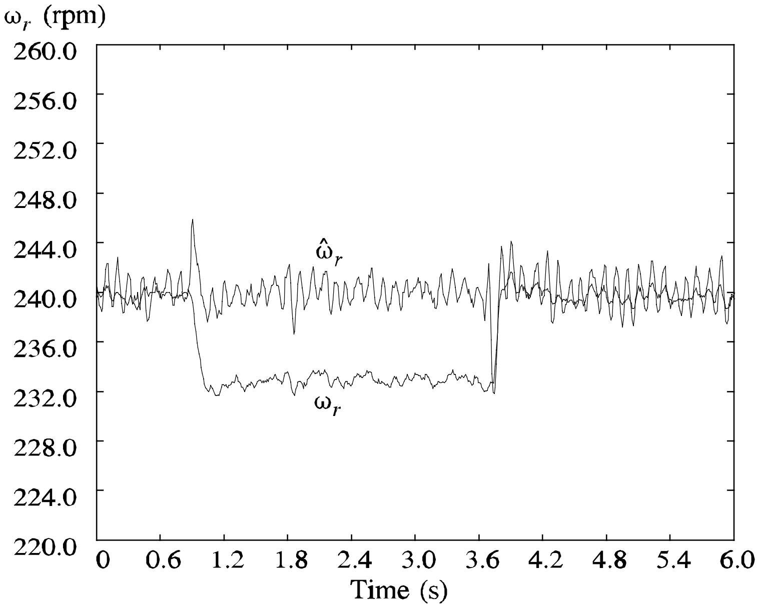

Figure 7.8 Speed holding accuracy for an error of +10% on the estimated T_r

Figures 7.8 and 7.9 show the steady state speed error of the sensorless system when the tuned value of the rotor time constant used in the MRAS speed estimator is increased or decreased by a 10%. These results agree with the theoretical results shown in Fig. 4.7a, and also validate experimentally expression (6.1), which is used as starting point for the T_r identification method described in Chapter 6. The machine slip frequency at full load is approximately 70 rpm, therefore a change of 10% in the estimated T_r implies a proportional error on the estimated slip frequency (7 rpm). The theoretical speed error of about 5 rpm in Fig. 4.7a is consistent with the practical results, since the value of the machine rotor time constant used for calculating the theoretical error was 0.168 s, which implies a slip

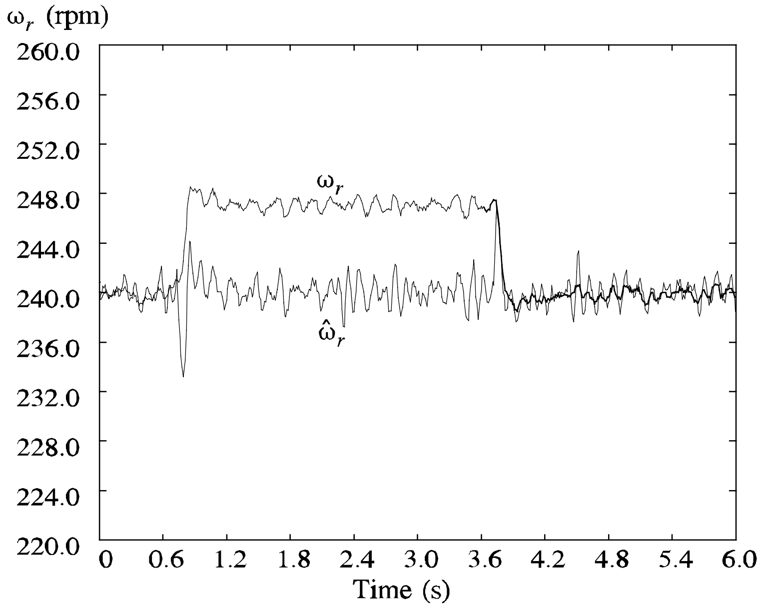

Figure 7.9 Speed holding accuracy for an error of -10% on the estimated T_r

frequency of 51 rpm. This value of T_r corresponds to the cold value of T_r in the 4 kW machine used for experimental purposes. However in Figs. 7.8 and 7.9 the value of the actual T_r is about 0.145 s, due to thermal variation of R_r.

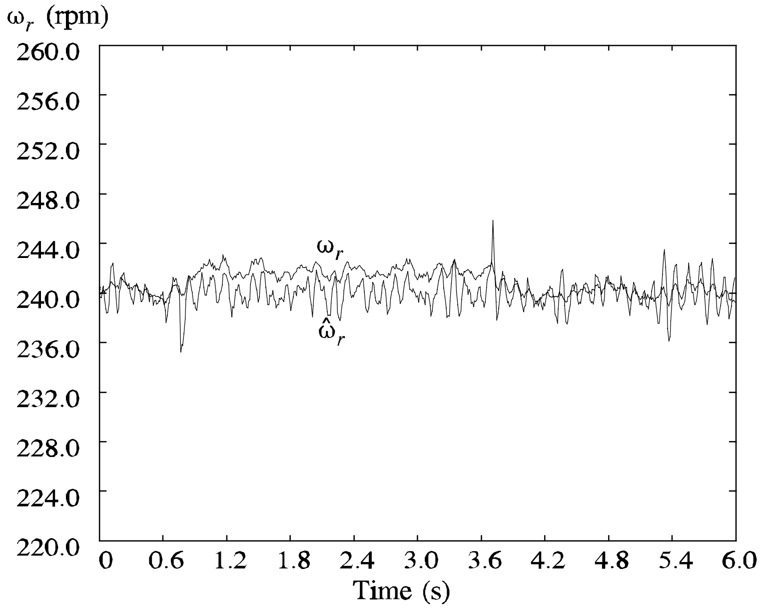

Figure 7.10 Speed holding accuracy for an error of +10% on the estimated σL_s

The effect of errors on the estimated σL_s is shown in Figs. 7.10 and 7.11. The steady state error is approximately 2-3 rpm. This result agrees with the theoretical

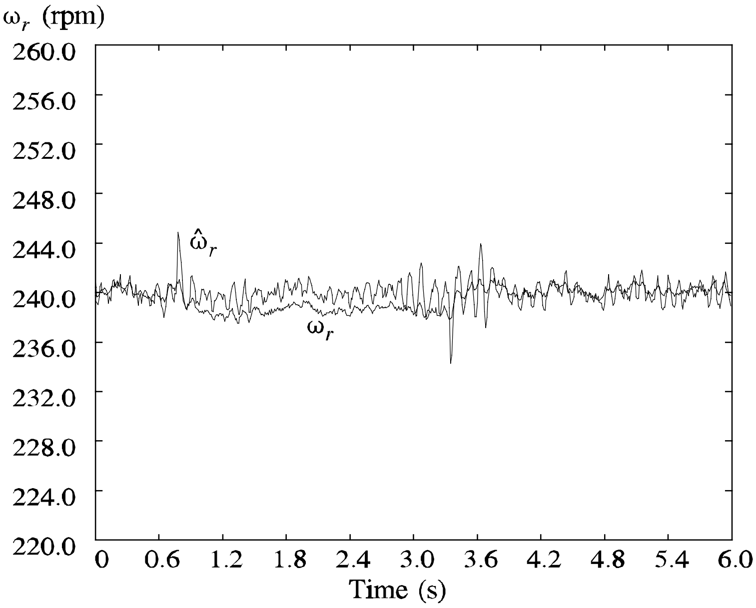

Figure 7.11 Speed holding accuracy for an error of -10% on the estimated σL_s

result in Fig. 4.7b. It can be seen that after T_r, σL_s is the second most important parameter affecting steady state accuracy. However the sensitivity to changes in σL_s is smaller than the sensitivity to T_r.

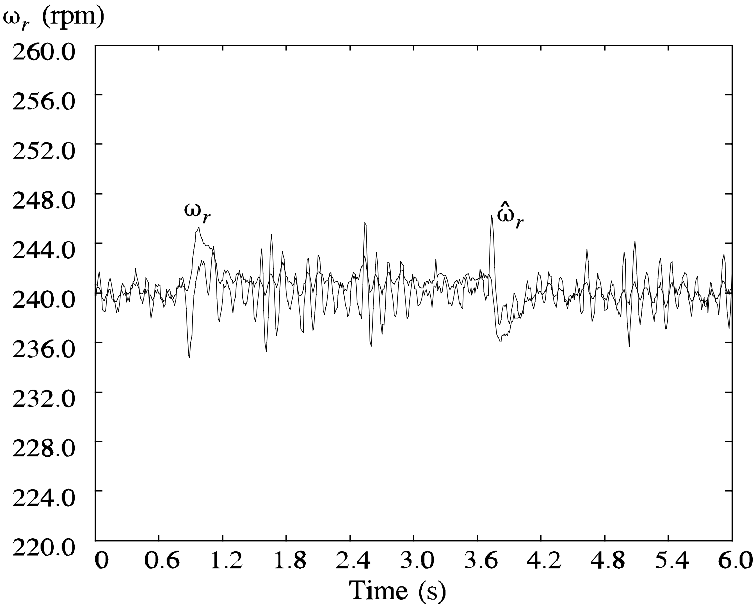

Figure 7.12 Speed holding accuracy for an error of +10% on the estimated L_0

Figures 7.12 and 7.13 show the effect on the steady state accuracy of incorrect values of L_0. Both figures present a small speed error when L_0 is incorrect, agreeing

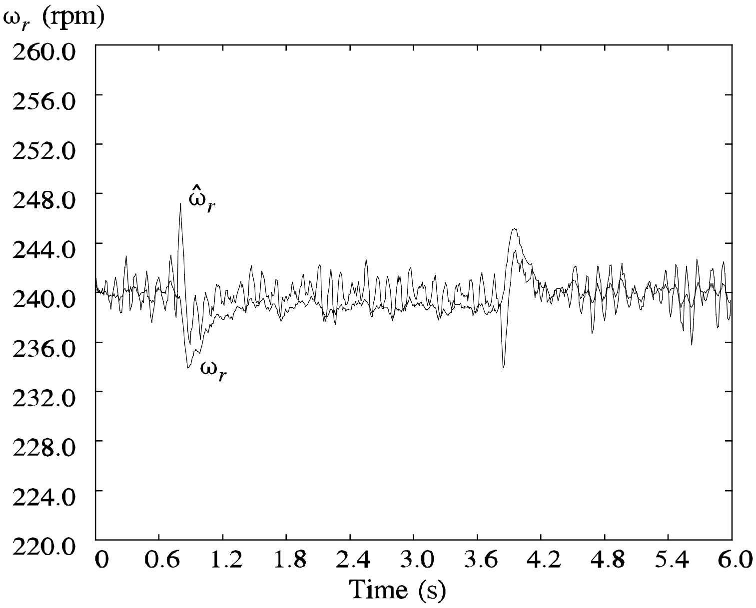

Figure 7.13 Speed holding accuracy for an error of -10% on the estimated L_0

with the theoretical results of Fig. 4.7c. Note the estimated speed ripple in Fig. 7.12 is higher than that in Fig. 7.13. This effect can be explained by considering the MRAS-CLFO structure depicted in Fig. 4.2, in which L_0 can be seen as a multiplicative factor in the numerator of the current model. Effectively L_0 contributes to the overall gain of the adaptive loop. Therefore an increase in L_0 implies an increase in the adaptive loop gain and hence an increase in steady state ripple.

7.4 Speed Reversal Transients

Sensorless no-load DRFO speed reversal transients with ω_n = 4 rads^{-1}, ω_{ad} = 125 rads^{-1} and using a speed feedback filter of 15 Hz are shown in Figs. 7.14 through to 7.21. Rotor time constant tuning is on except for Figs. 7.22 and 7.23 and that for stator resistance is on for all transients except Figs. 7.16 and 7.17. The speed transient in Fig. 7.14 was carried out with all the estimator parameters tuned. It compares very favourably with the sensored IRFO transient shown in Fig. 7.15 which has the same speed and current controllers. The transient time is roughly the same in both cases. Therefore the degree of field orientation of the tuned sensorless DRFO is similar (or even better) than that of the standard sensored IRFO.

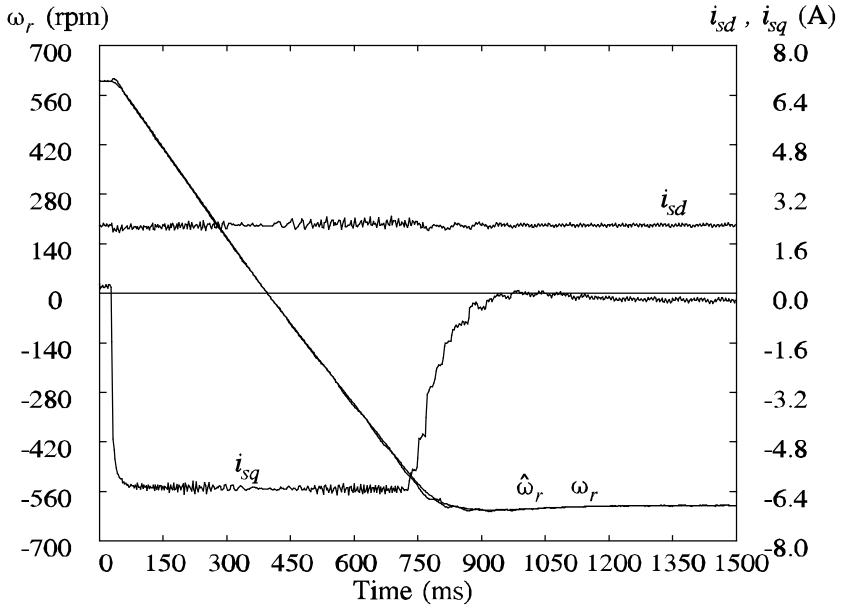

Figure 7.14 Sensorless DRFO speed reversal under no load. Tuned parameters

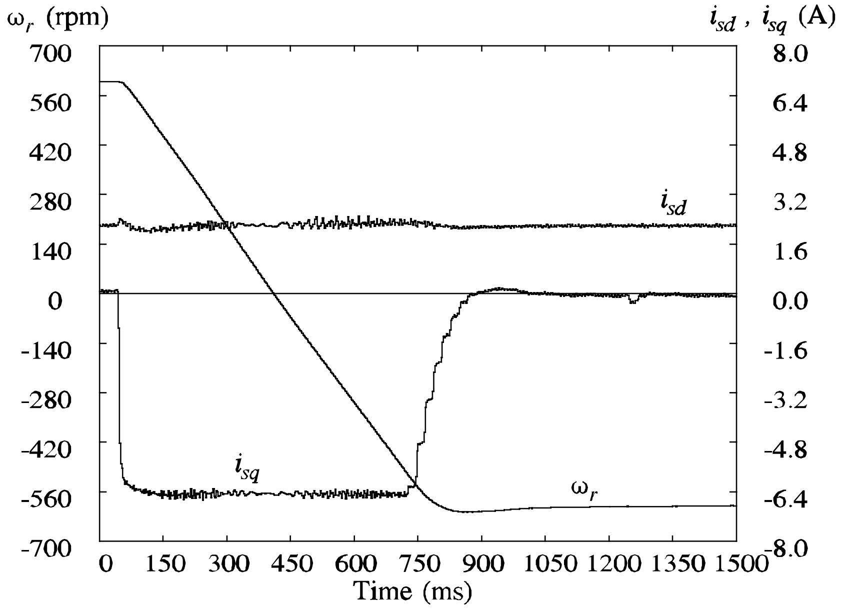

Figure 7.15 Sensored IRFO speed reversal under no load

Errors in the stator resistance cause a deterioration in field orientation as the speed approaches and passes through zero as seen in Figs. 7.16 and 7.17. This causes a visible, but not overly significant, increase in the transient time (compare with Fig. 7.14). There is also an increase in transient oscillation in the motor currents.

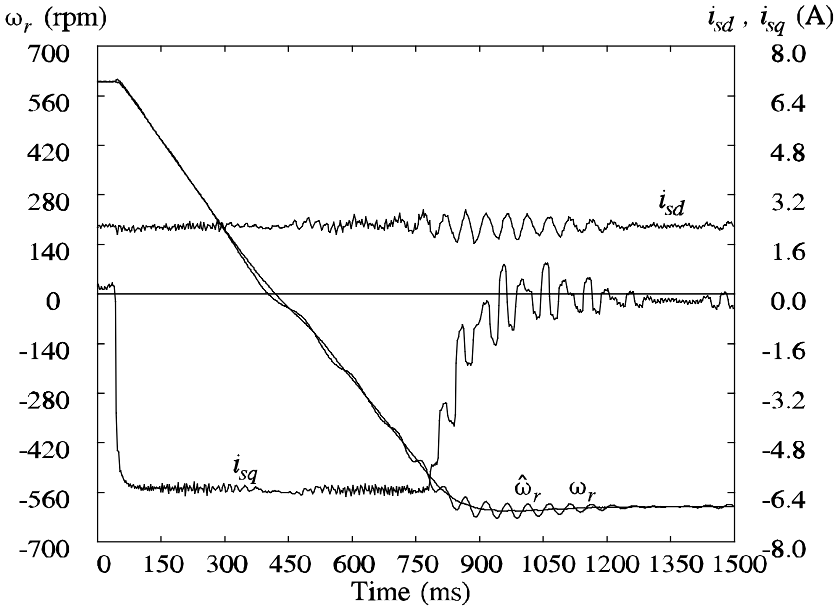

Figure 7.16 Sensorless DRFO speed reversal under no load. -10% error in R_s

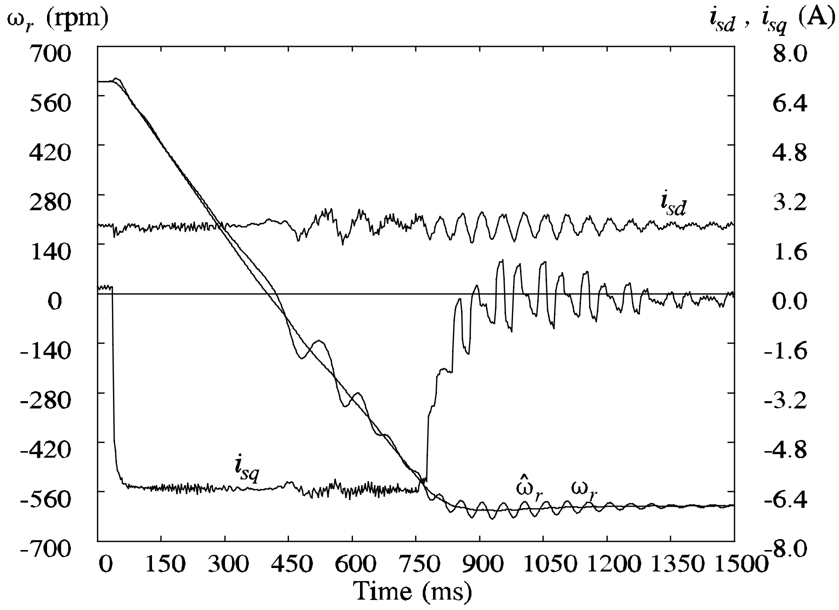

Figure 7.17 Sensorless DRFO speed reversal under no load. +10% error in R_s

Note the system is stable regardless of R_s being overestimated by 10%. Stability is achieved by the use of a speed feedback low pass filter as described in Section 4.5 (pole-zero loci in Fig. 4.26). The transient oscillations appear when the rotor speed goes below approx. 140 rpm ($\omega_e \approx 1.7$ Hz). These transient oscillations are caused by the presence of DC terms appearing in the flux estimate components due to errors in the stator resistance estimate (see Section 6.3.2). These flux estimate oscillations cause in turn oscillations in the estimated speed. The frequency of the oscillations is close to ω_e and both the rate and decay of the oscillations are determined by ω_{cpl} Section 6.3.2. The speed oscillations shown in Fig. 7.17 are larger than those in Fig. 7.16. However, equation (6.12), which is repeated here

$$\overline{OO'} \simeq \left| \Delta R_s A(t_0) \sqrt{\frac{2\pi}{|\varphi''(t_0)|}} \right| \tag{7.1}$$

predicts that the amplitude of the DC term that appears in the estimated flux should be the same for both under and overestimated R_s. The fact that they are not equal is due to the MRAS-CLFO structure used for field and speed estimation which exhibits lightly damped speed dependent poles that are exited by errors on R_s during a system transient. For the case of stator resistance errors, the pole-zero loci are shown in Figs. 4.15 and 4.16. Albeit the pole-zero loci were calculated for small perturbations, the practical results are consistent with these pole-zero loci.

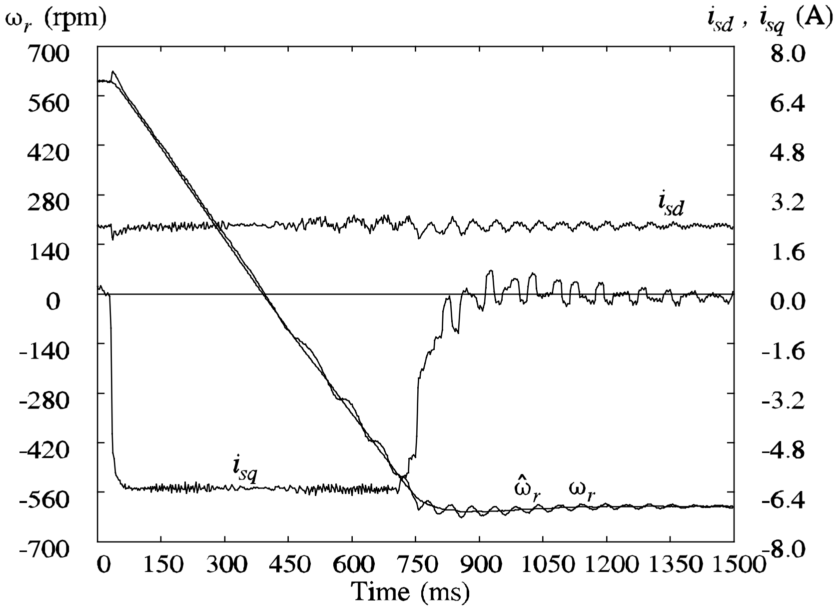

Figure 7.18 Sensorless DRFO speed reversal under no load. +10% error in σL_s

The effects of a ±10% variation in σL_s are shown in Figs. 7.18 and 7.19. Again the speed oscillations are caused by excitation of lightly damped speed dependent poles, probably by small errors on R_s. Note these errors are very small, since the tuning mechanism for R_s obtains its value with an accuracy of 1-2%. However small, these errors always exist and therefore will excite the effects of the speed dependent poles. The speed oscillations are of about the same magnitude in both

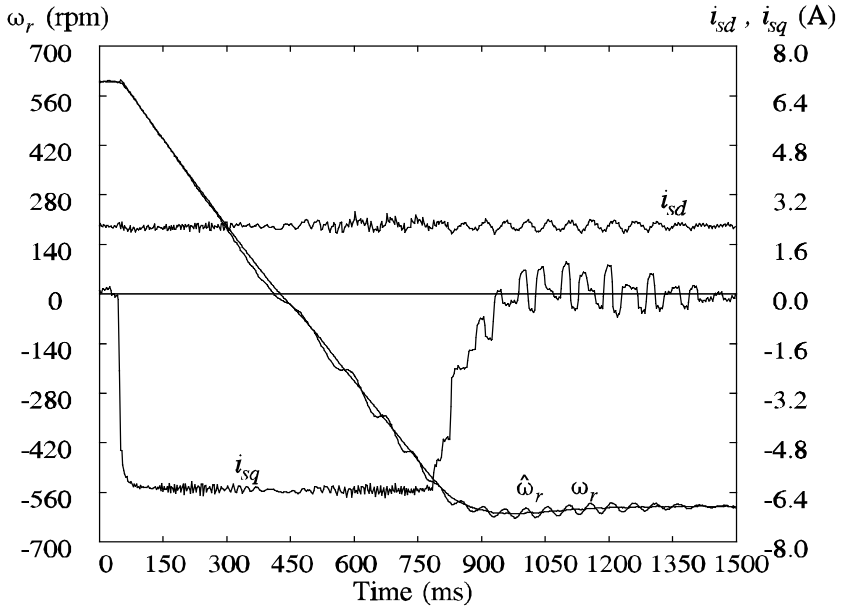

Figure 7.19 Sensorless DRFO speed reversal under no load. -10% error in σL_s

the under and overestimated case (although they are slightly larger in the underestimated case). The corresponding pole-zero loci are shown in Figs. 4.13 and 4.14. In spite of these oscillations the increase on the overall transient time is almost negligible when compared to Fig. 7.14, pointing to good field orientation through zero speed.

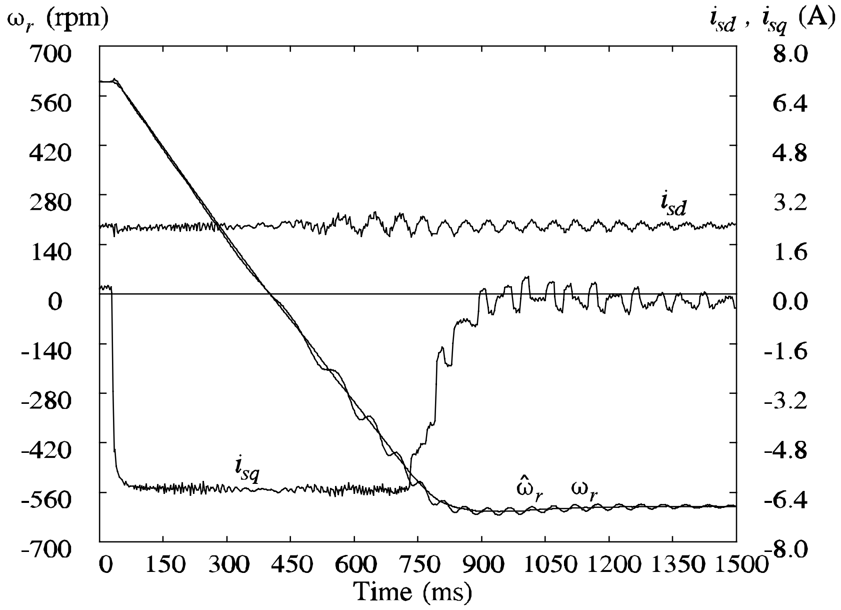

Figure 7.20 Sensorless DRFO speed reversal under no load. +10% error in L_0

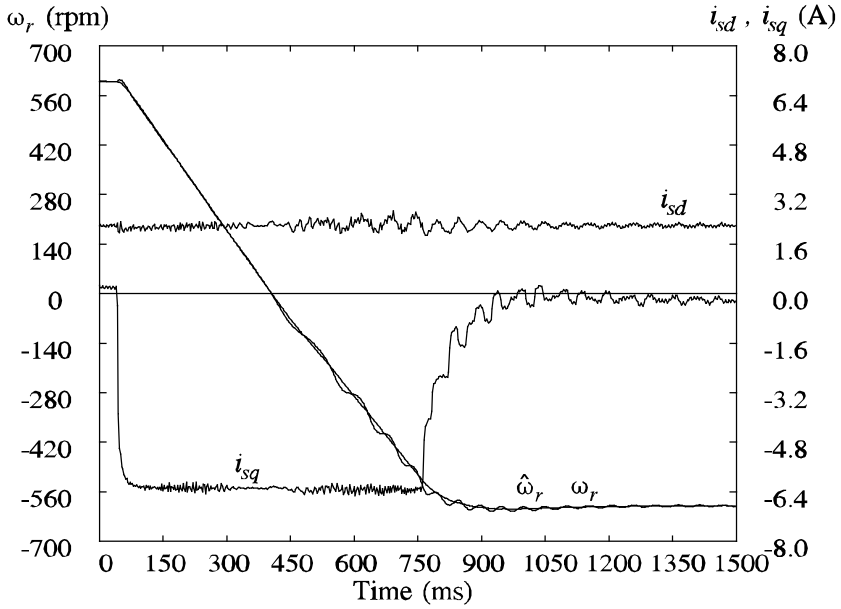

Figure 7.21 Sensorless DRFO speed reversal under no load. -10% error in L_0

Finally the results for L_0 (Figs. 7.20 and 7.21) and T_r (Figs. 7.22 and 7.23) are shown. The same consideration as for the transients with errors in σL_s apply here, i.e. the effect of the variations in L_0 and T_r on the overall transient time are very small and the magnitude of the oscillations appears to be related to the

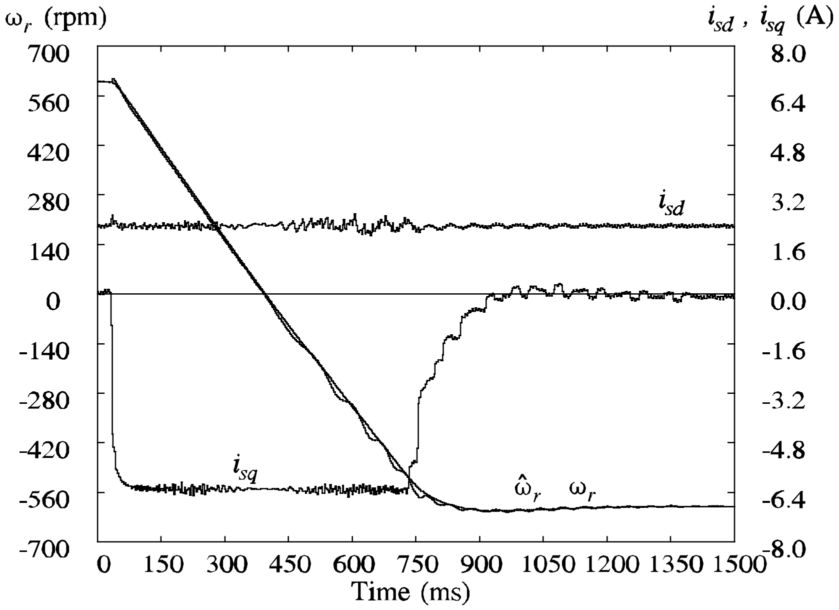

Figure 7.22 Sensorless DRFO speed reversal under no load. +10% error in T_r

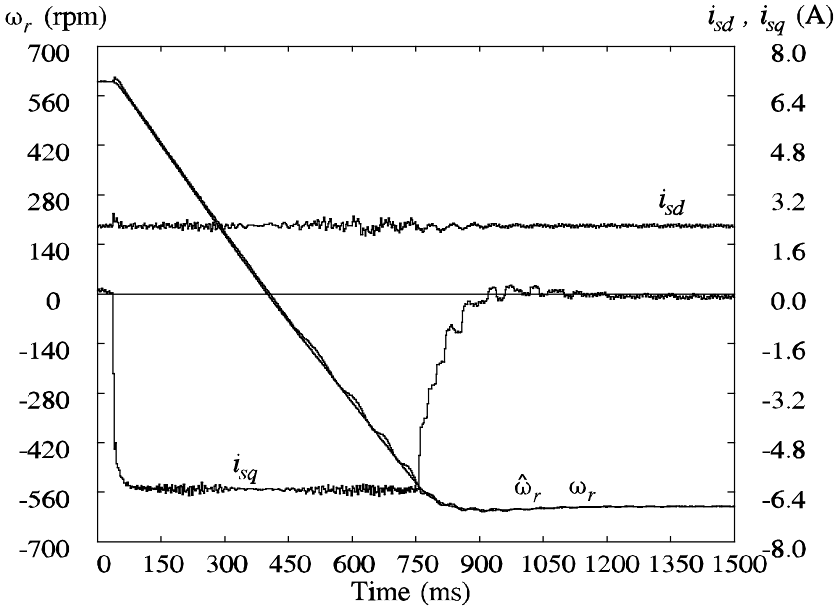

Figure 7.23 Sensorless DRFO speed reversal under no load. -10% error in T_r

corresponding small signal pole-zero loci shown in Figs. 4.9 and 4.10 for L_0 and Figs. 4.11 and 4.12 for T_r.

The results presented in this section are consistent with the calculated pole-zero loci obtained in Section 4.4, however these practical results cannot be held as a definitive validation of the theoretical results because it is not possible to separate the effects of incorrect stator resistance being used for calculation of the rotor flux (Section 6.3.2) and the effects of lightly damped speed dependent poles caused by incomplete cancellation of estimator poles and zeroes (Section 4.4). Moreover, all the results in these section use a speed feedback low pass filter that distorts the pole-zero loci shown in Section 4.4, generally damping the oscillations that otherwise would be of larger magnitude. To address these problems, the results in the next section are obtained without using a speed feedback filter and without reversing the machine.

7.5 Non-Reversal Speed Transients

The effect of different parameter errors on speed transients is shown in Figs. 7.24 to 7.30. The speed loop bandwidth (ω_n) is 4 rads^{-1} and the adaptive loop bandwidth (ω_{ad}) is 125 rads^{-1} in all the transients in this section. No speed feedback filter is used. All the parameters have been properly tuned for each transient, except for the one of interest. Figures 7.24 and 7.25 show the speed transients for ±10% error in L_0. These transients exhibit some ripple in the estimated slip and in the torque producing current. When L_0 is overestimated (Fig. 7.25) these oscillations are slightly larger than in the underestimated case, in agreement with the pole-zero loci of Figs. 4.9 and 4.10.

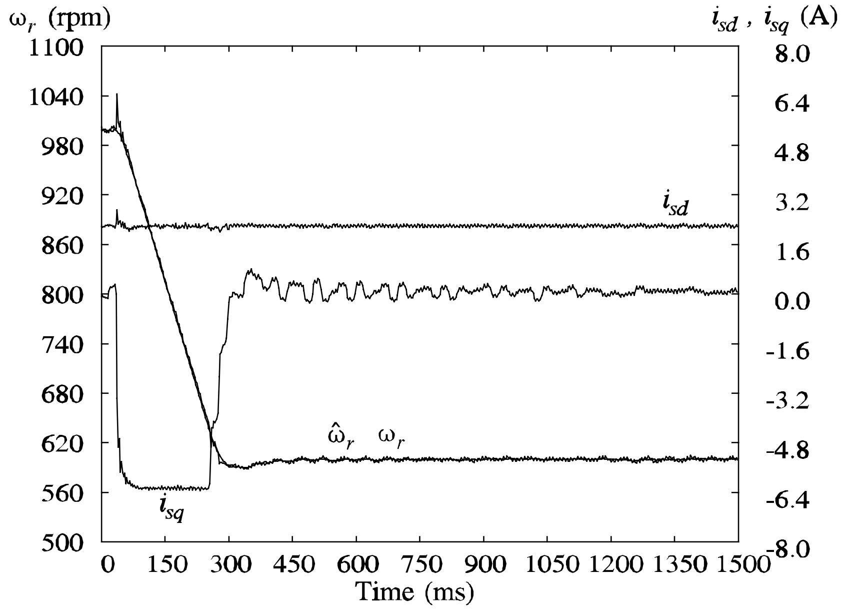

Figure 7.24 Sensorless DRFO speed transient from 1000 to 600 rpm with -10% error on L_0

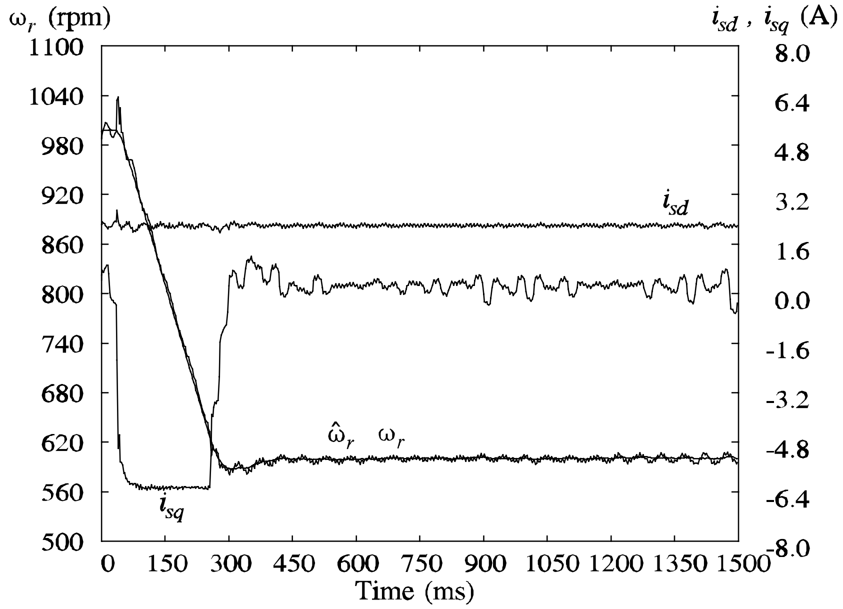

Figure 7.25 Sensorless DRFO speed transient from 1000 to 600 rpm with +10% error on L_0

The effect of errors in the rotor time constant are shown in Figs. 7.26 and 7.27. The oscillations are slightly larger in Fig. 7.26 (pole-zero loci in Fig. 4.12) than in Fig. 7.27 (pole-zero loci in Fig. 4.11). The speed overshoot in Figs. 7.26 and 7.27 is different, although the same speed controller was used in both cases. The

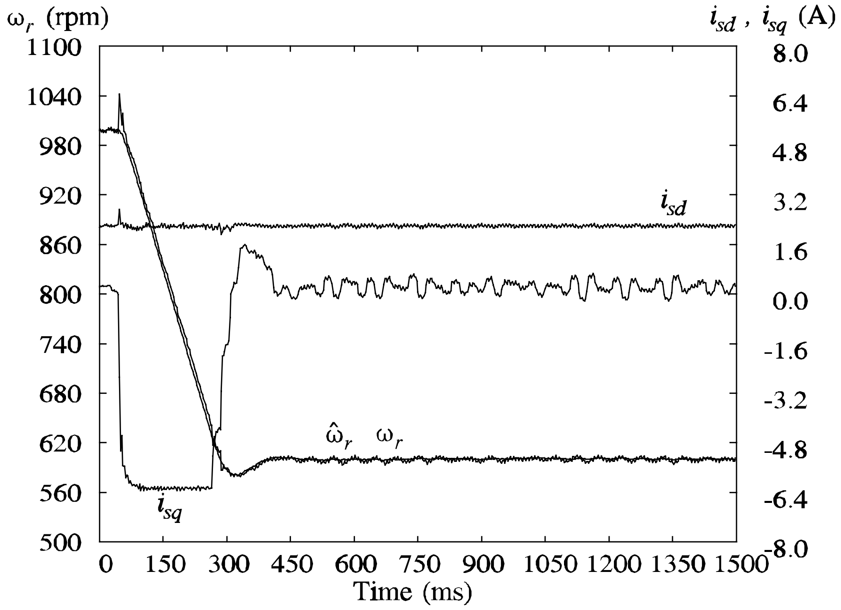

Figure 7.26 Sensorless DRFO speed transient from 1000 to 600 rpm with -10% error on T_r

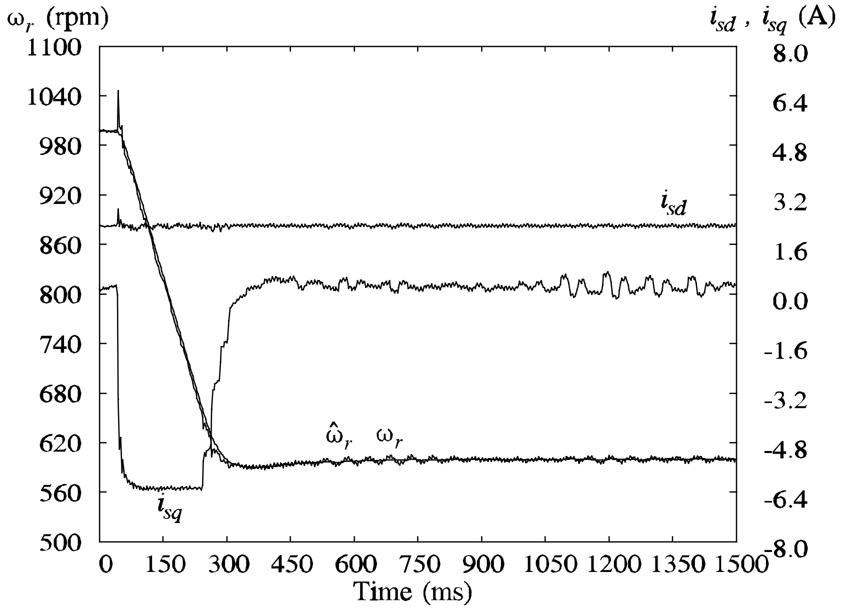

Figure 7.27 Sensorless DRFO speed transient from 1000 to 600 rpm with +10% error on T_r

different overshoot is due to the estimated speed error caused by the incorrect value of T_r being used in the speed estimator.

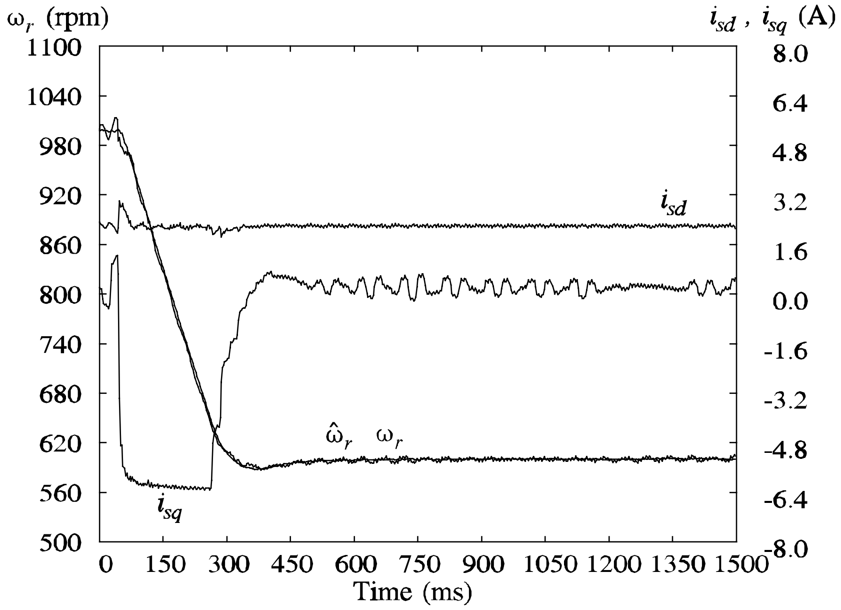

Figure 7.28 Sensorless DRFO speed transient from 1000 to 600 rpm with -10% error on σL_s

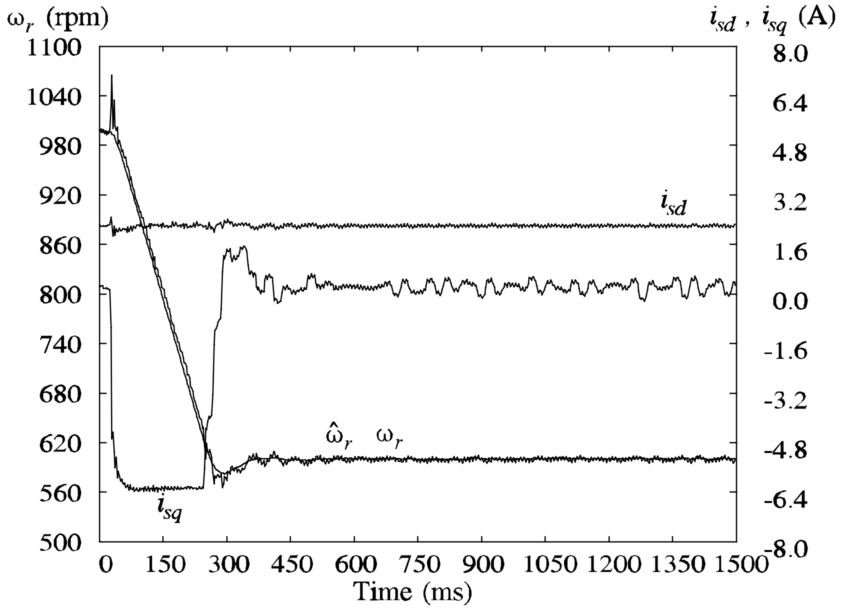

Figure 7.29 Sensorless DRFO speed transient from 1000 to 600 rpm with +10% error on σL_s

Figures 7.28 and 7.29 show the effect of variations on σL_s on a speed transient from 1000 to 600 rpm. As in the previous case (errors in T_r) the overshoot in the speed transient is different in both figures, again for the same reason: the steady state speed error caused by σL_s errors. The ripple in both figures is almost the same, in agreement with the pole-zero loci of Figs. 4.13 and 4.14.

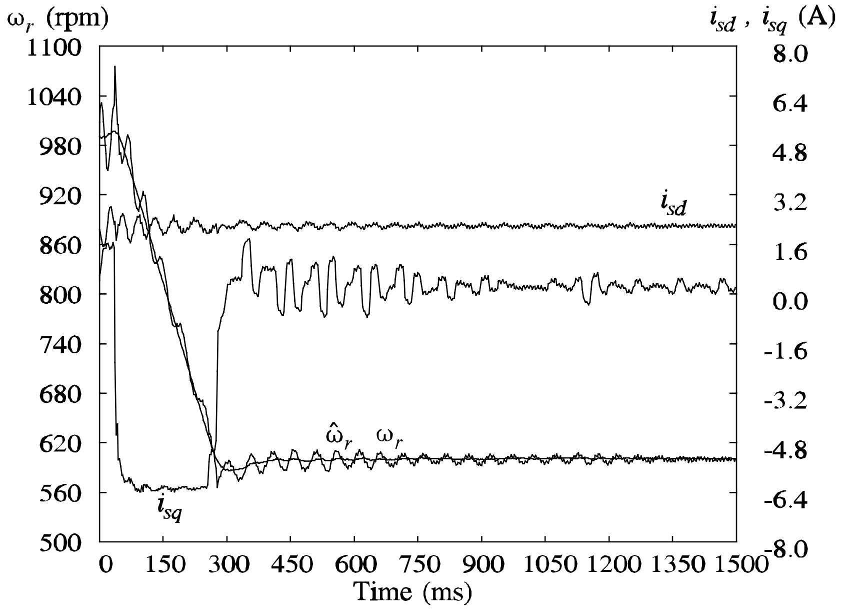

Figure 7.30 Sensorless DRFO speed transient from 1000 to 600 rpm with -10% error on R_s

Figure 7.30 illustrates the effect of R_s underestimation. The transient oscillations are larger than any of the cases shown previously, as expected from the pole-zero loci of Fig. 4.15. Note the frequency of the oscillations is very close to ω_e, as predicted by the aforementioned pole-zero loci. This is also the case for all the previous transients. The speed transient for the ovestimated R_s could not be carried out, since the system was unstable (see pole-zero loci in Fig. 4.16). System instability caused by R_s overestimation is illustrated in Fig. 4.17.

7.6 Performance Measure for Sensored and Sensorless Drives

In a generic sensored drive, the maximum natural frequency (loosely termed "bandwidth") for a speed loop is limited by speed encoder resolution, noise considerations and the drive inertia. System noise is dependent on many factors including signal resolution, A/D resolution, drive torque harmonics (which may feed through onto the speed) and the closed loop controllers. For simplicity this work is restricted to the resolution of the ω_r and i_{sq}^* signals which is a large determining factor in the system noise and one which is also simple to predict.

If one considers a PI speed controller $k_p(s+a)/s$ controlling a simple inertial load J, it is easily shown that $k_p=2\zeta\omega_n J$, where ζ, ω_n are the closed loop parameters. Hence a speed signal quantisation ω_q is amplified on to the torque demand as

$$T_q = 2\zeta\omega_n J\omega_q \tag{7.2}$$

In order to express the torque resolution as a proportion of the base torque, (7.2) can be expressed in per unit terms. Defining $T_q^{pu} = T_q/T_b$, $\omega_q^{pu} = \omega_q/\omega_b$ and $J^{pu} = J\omega_b/T_b$ then

$$T_q^{pu} = 2\zeta\omega_n J^{pu}\omega_q^{pu} \tag{7.3}$$

Note that the integral control component does not contribute to (7.3) in steady state. If an N-line encoder is used with pulses being counted over a T_s sample period, then the speed resolution (or maximum truncation error) is $2\pi/NT_s$ rads^{-1}. Hence

$$T_q^{pu} = \frac{4\pi\zeta\omega_n J^{pu}}{NT_s\omega_b} \tag{7.4}$$

For a 4-pole motor with a nominal damping of 0.7 then

$$\omega_n J^{pu} \approx 18(NT_s)T_q^{pu} \tag{7.5}$$

from which a limiting value of $\omega_n J^{pu}$ can be attained for a given T_q^{pu}. A large scale speed transient is not a good test for the experimental measure of $\omega_n J$ since such transients often involve the drive reaching torque limit and hence the control is open loop under such a condition. On the other hand the speed loop normally remains linear (i.e. does not go into torque limit) during a load torque rejection transient. This is easily seen for an inertial load, in which the motor torque is equal to value of the step disturbance at the maximum speed excursion. Given that the torque disturbance does not exceed the controller torque limit, then the speed loop must be linear prior to the maximum excursion. We can assume therefore that the use of a step load disturbance is an appropriate measure of the closed loop natural frequency for the speed loop.

The maximum speed excursion under step load torque disturbance for closed loop second order systems is derived as follows. Consider a first order mechanical load driven by a converter with fast torque loop dynamics and subject to a mechanical load disturbance. Given a PI speed controller, the resulting closed loop transfer function between the speed ω_r and the load torque $T_L(s)$ is

$$\omega_r(s) = \frac{T_L(s)}{J\omega_n^2}\left(\frac{s\omega_n^2}{s^2 + 2\zeta\omega_n s + \omega_n^2}\right) \tag{7.6}$$

If T_L is a step of T_l Nm then it is easily shown that the maximum speed excursion from the demand speed is given by

$$\omega_{\max} = \frac{T_l e^{-f(\zeta)}}{J\omega_n} \tag{7.7}$$

where

$$f(\zeta) = \frac{\zeta}{\sqrt{1-\zeta^2}}\arctan\left(\frac{\sqrt{1-\zeta^2}}{\zeta}\right) \tag{7.8}$$

Defining the per unit inertia as $J^{pu}=J\omega^b/T^b$ where ω^b and T^b are the rated or base values of the speed and torque respectively, then (7.7) can be written in per unit as

$$\omega_{\max}^{pu} = \frac{T_l^{pu} g(\zeta)}{J^{pu}\omega_n} \tag{7.9}$$

For a damping factor range of 0.5 to 0.8, $g(\zeta)$ varies approximately linearly from 0.54 to 0.425 ($g(\zeta)$=0.46 for ζ=0.7). The above expressions are independent of load friction.

For a step load disturbance, we can therefore derive a nominal second order equivalent measure of $\omega_n J$ assuming ζ=0.7. Equation (7.9) becomes

$$\omega_n J^{pu} = \omega_n J_2^{pu}(0.7) = \frac{0.46\, T_e^{pu}}{\omega_{\max}^{pu}} \tag{7.10}$$

7.7 Load Disturbance Rejection

With ω_n = 4 rads^{-1}, J = 0.3 kgm^2 and T_L = 22 Nm, the maximum speed excursion for a 100% step increase in load torque is approximately 70 rpm as derived from (7.10). This is seen in Figs. 7.31 and 7.32 showing the response of the sensorless system for ω_r at 1000 rpm and 40 rpm, all with tuned parameters. Note that 40 rpm corresponds to a rotor frequency of 1.3 Hz (electrical) and Fig. 7.32 illustrates an excellent performance. The $\omega_n J^{pu}$ value is ~8. This is of course achievable with a sensored system. For example, with NT_s = 50 (a sampling time of 5 ms with a 10000 line encoder) the results for ω_n = 10 and 20 rads^{-1} are shown in Fig. 7.33. Figure 7.34 shows the i_{sq}^* demand signal for the case of 20 rads^{-1} where the resolution is seen to be 1.6 N or 7% of rated torque as predicted from (7.3). This is probably considered slightly high and a maximum resolution of 5% is probably deemed acceptable for most applications.

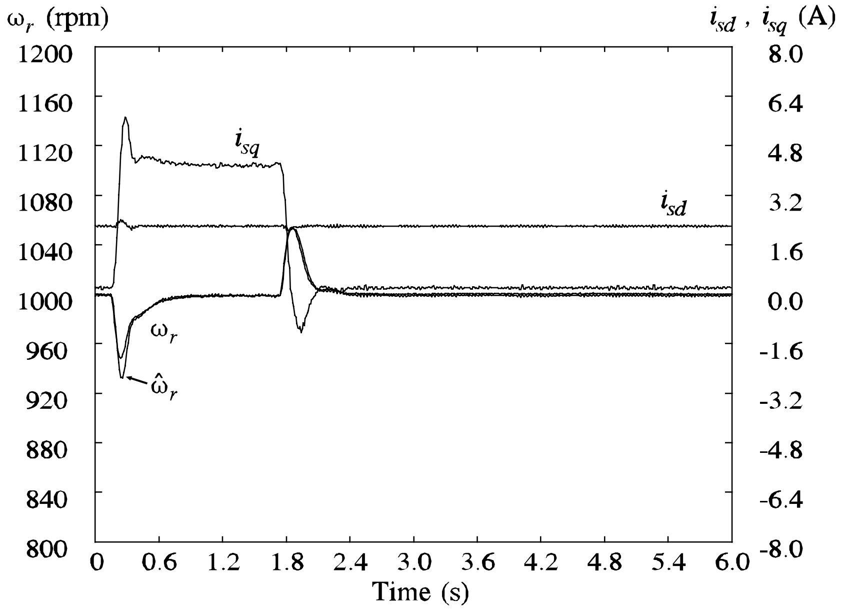

Figure 7.31 Sensorless DRFO response to a 100% load increase at 1000 rpm with tuned parameters

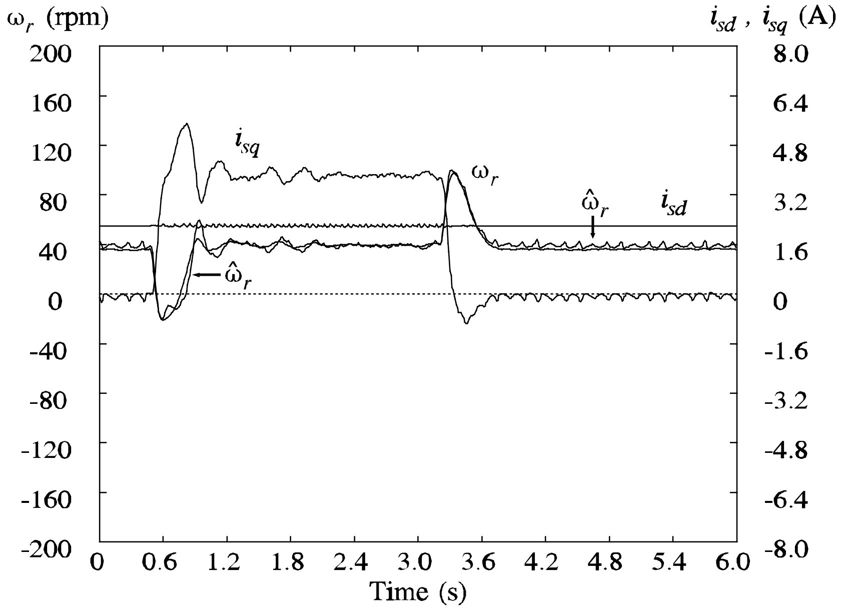

Figure 7.32 Sensorless DRFO response to a 100% load increase at 40 rpm with tuned parameters

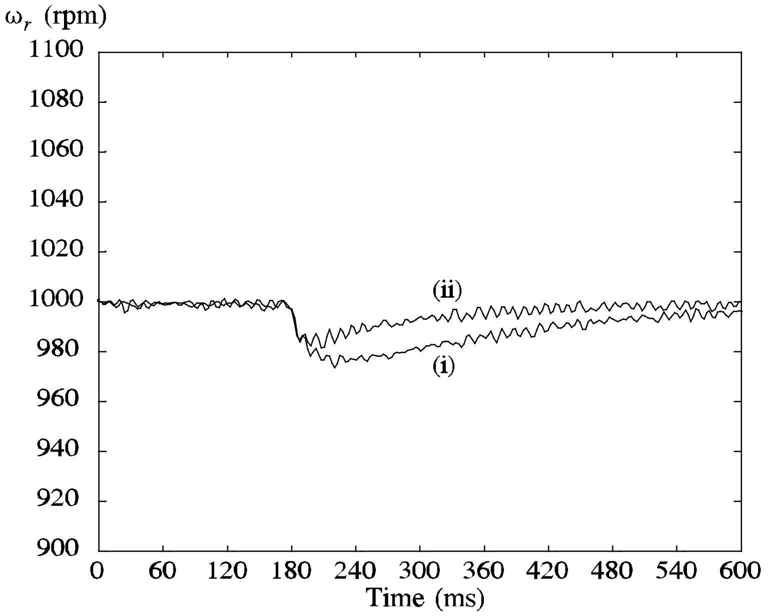

Figure 7.33 Sensored IRFO response to a 100% load increase. (i) ω_n = 10 rads^{-1}, (ii) ω_n = 20 rads^{-1}. (Note: expanded time scale)

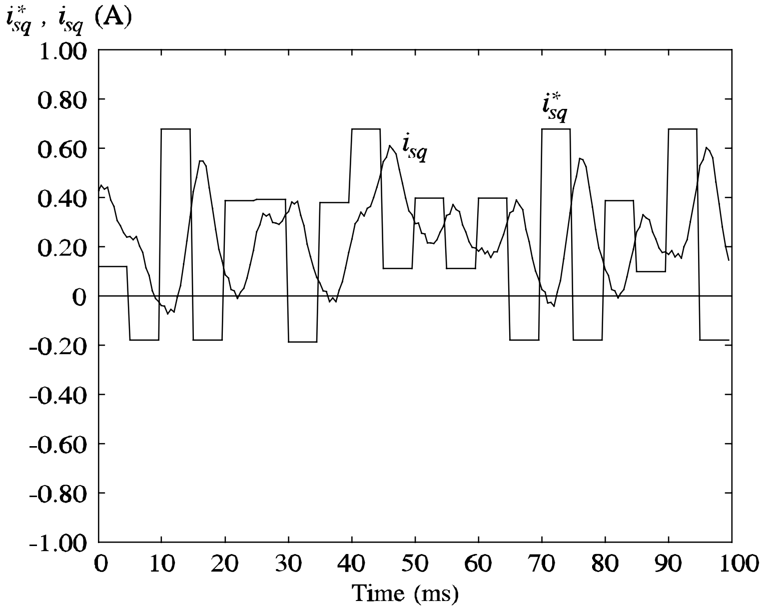

Figure 7.34 Sensored IRFO response to a 100% load increase. ω_n = 20 rads^{-1} with i_{sq}^* magnified

The $\omega_n J^{pu}$ of ~8 hitherto presented is found to give good, reliable and repeatable performance in terms of load disturbance rejection, speed transients through zero and speed transients to zero under load. In terms of load disturbance rejection, the drive has the same dynamic speed performance as a sensored drive with NT~10 (e.g. a 2000 line encoder with T = 5 ms) which is generally regarded as a respectable, although not outstanding, sensored vector drive. It is emphasised that increasing NT, and hence the dynamic capability of a sensored drive, only enhances the performance when the torque demand does not reach its limit value; for large speed transients, the sensorless drive will give nearly identical performance to a sensored drive, albeit with a slower final settling.

The value of $\omega_n J^{pu}$~8 is higher than most, if not all sensorless drives hitherto reported. However the aim of this work is to illustrate and explain the limitations in dynamic performance attainable from a MRAS system, rather than merely maximize $\omega_n J^{pu}$. It is noted that $\omega_n J^{pu}$~8 is itself only attainable given prior identification of L_0 and σL_s through self-commissioning and on-line tuning of T_r and R_s. The author has however found that $\omega_n J^{pu}$~12 is attainable (Fig. 7.35 shows a load disturbance rejection response with this condition) as long as there are frequent transients through zero speed for R_s tuning to yield reliable results. The fact that this may not occur in practice means that $\omega_n J^{pu}$ will be derated. All results so far shown are with an adaptive loop natural frequency ω_{ad} of 125 rads^{-1}.

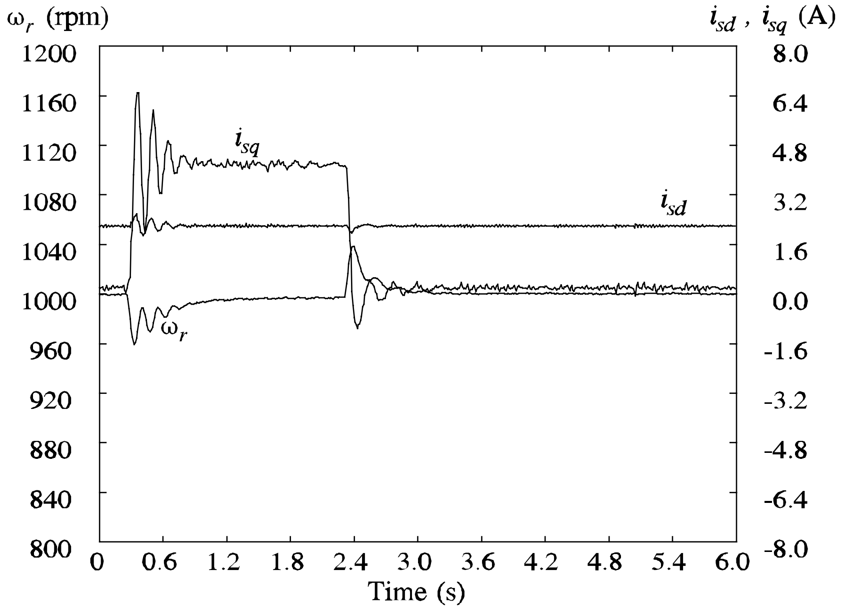

Figure 7.35 Sensorless DRFO response to a 100% load increase (ω_n = 6 rads^{-1}, ω_{ad} = 125 rads^{-1})

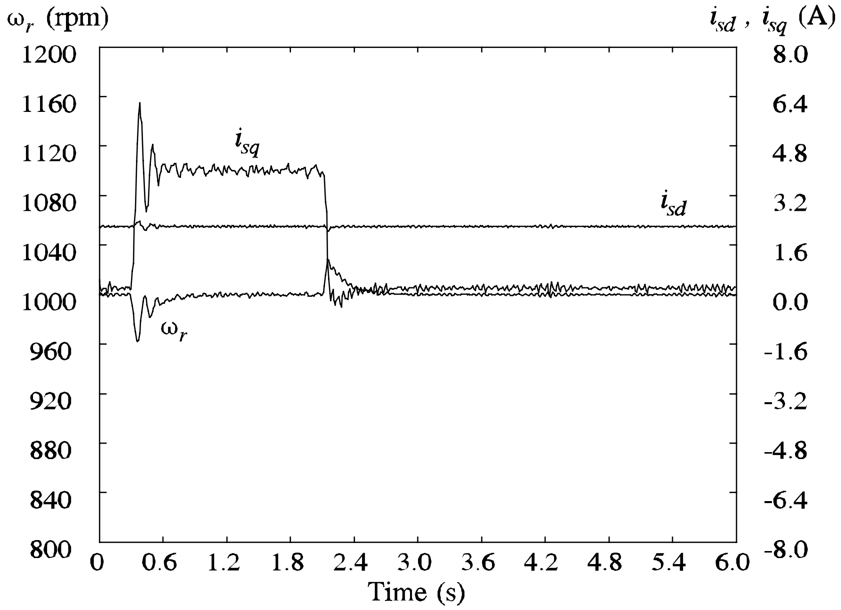

Figure 7.36 Sensorless DRFO response to a 100% load increase (ω_n = 8 rads^{-1}, ω_{ad} = 60 rads^{-1})

Figure 7.36 shows a load torque rejection response for $\omega_n J^{pu}$~16 and ω_{ad} = 60 rads^{-1} and operation under these conditions is found to be reliable. However for a 4 kW drive in which the load inertia is approximately matched to the machine, the condition corresponds to an ω_n ~ 50 rads^{-1}. This transgresses the rule that observer bandwidths should be significantly higher than those of the quantities that they are attempting to observe. The effects of having the two bandwidths of similar magnitudes have not been investigated.

7.8 Discussion and Conclusions

The practical results presented in this chapter show that very good performance can be achieved from a sensorless vector control drive provided that the machine parameters are accurately known. Extremely good performance in speed reversal transients, torque rejection transients and even zero speed operation has been shown. The dynamic performance of such a sensorless system in terms of speed bandwidth has been found to be comparable to sensored IRFO implementations, although not outstanding.

The achievement of a high $\omega_n J^{pu}$ depends on an accurate knowledge of the machine parameters. Inaccurate parameters produce oscillations and limit the gain of the speed controller, therefore limiting the speed bandwidth. The parameter T_r is considered to be tracked very accurately, even down to periods of a few seconds under dynamic operation. Likewise the effects of σL_s errors have in practice been small which is an encouraging result. The parameter having substantial effect has been found to be R_s, introducing larger oscillations than any other single parameter, and deteriorating greatly field orientation at low speeds. Even though the R_s tuner presented in this paper has yielded accuracies of 1 or 2%, the tuning is still dependent upon appropriate speed cycling during operation. With load duty cycling for long periods away from zero speed, larger errors in R_s will return.

The adaptive loop bandwidth (ω_{ad}) exhibits also an important influence on the maximum achievable speed loop bandwidth (ω_n). In general higher values of ω_n can be obtained with lower adaptive loop bandwidth. However the value of ω_{ad} is determined by the mechanical system time constant and by ω_n itself and therefore cannot be lowered at will.

The speed estimate accuracy and speed holding capability are also determined by the degree of accuracy by which the different parameters of the machine are known. The most influential parameter by far is the rotor time constant T_r, followed by the overall leakage reactance σL_s. The stator resistance and the magnetising

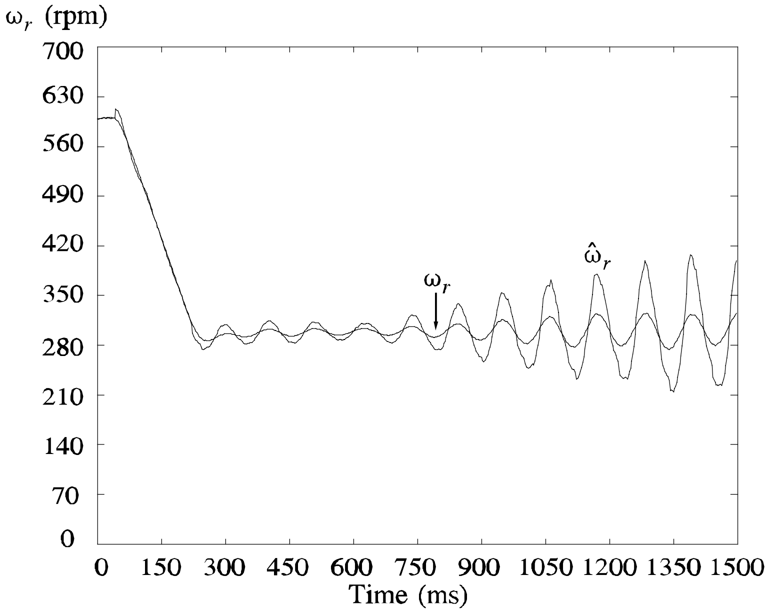

Figure 7.37 Sensorless DRFO with 25 Hz filter in the estimated speed feedback path. +10% R_s error

inductance have in general little effect on the speed accuracy at all but very low speed.

The importance of high signal-to-noise ratios for a quality sensorless drive may also be stressed. Careful design and layout of interface circuitry, good anti-aliasing filters and floating point arithmetic are all factors leading to the "clean" results presented in this paper. Indeed if floating point arithmetic is not used, arithmetic truncation noise may well swamp many of the small transient oscillations seen in this paper. In such a case, as the speed bandwidth is increased, the noise will suddenly appear to "blow up" with little indication of what has caused it to do so.

The transient oscillation problem is easily ameliorated by the inclusion of a 20-25 Hz filter in the $\hat{\omega}_r$ feedback path. This has the effect of bringing the oscillatory poles and zeroes back together again at speeds above the filter bandwidth (see Fig. 4.26 in Section 4.5). High speed operation (eg. field weakening) is therefore not a problem. Of course as the speed is reduced to a frequency within the filter bandwidth, the transient oscillations may reappear. This is shown in Fig. 7.37 in which a 25 Hz filter is included ($\hat{R}_s = 1.1 R_s$, $\omega_n = 4\,\text{rads}^{-1}$, $\omega_{ad} = 125\,\text{rads}^{-1}$); the transient oscillations are unstable for this case.

The practical results shown in this chapter are consistent with the predicted theoretical results shown in Chapter 4 in terms of speed accuracy, system stability, speed feedback filter and effect of the different loop bandwidths on the maximum attainable closed loop speed bandwidth. In view of these theoretical results, the practical results shown in this chapter also confirm the necessity of T_r and R_s adaption in order to obtain a good performance from the proposed sensorless drive.

The results illustrating the performance limitations of the sensorless drive do of course relate quantitatively to the MRAS-CLFO used as the speed and flux angle estimator. It has been found that the problem of transient oscillations also affects other flux-based MRAS estimators [20, 77]. It is also conjectured that the limiting oscillations will afflict conventional or EKF observer systems as well. It is however not claimed that the MRAS system will yield the best speed bandwidth or that the problem of transient oscillations cannot be overcome by using other estimator structures. It is hoped that the results presented can be viewed as a benchmark and a challenge for further research.

Chapter 8 Discussion and Conclusions

The objective of this project was to develop a speed sensorless drive with performance comparable to that of sensored drives. In order to achieve this goal, an experimental rig was constructed using a transputer network to control it. Once the appropriate sensorless strategy was chosen, a small signal analysis of the resulting control system was carried out in order to investigate the effect of parameter errors. On-line tuning of two machine parameters (T_r and R_s) has been investigated and implemented. For the tuning of the rotor time constant and to obtain good speed holding capability, an independent speed measurement from the rotor slot harmonics present in the stator line current has been developed. The accuracy of this all-digital speed measurement technique was found to be very good. Finally the performance of the tuned system has been compared with that of a standard IRFO scheme. In the course of the research the following findings became apparent.

8.1 Microprocessor Implementation

The sensorless vector control system hitherto proposed requires a reasonably fast microprocessor for its real time implementation. It has been found that a transputer network is particularly suitable for research in power electronics in general and vector control in particular. The transputer has the advantage of being able to execute several programs in parallel and moreover is extremely flexible and scalable. The T800 transputers used in this work are 32-bit microprocessors and can perform a single floating point multiplication in approx. 450 ns. On the other hand transputers are relatively expensive and it is extremely unlikely that they will be used in mass produced sensorless drives. Conversely 8-bit microcontrollers are considered not to be powerful enough to perform all the control tasks and at the same time provide for a reasonable switching frequency. The solution for an industrial implementation points therefore to either 16-bit microcontrollers like the SAB166/SAB167 or to fast integer DSP's (for instance some of the TMS320 family). Obviously the real time measurement of the machine speed from the rotor slot harmonics requires a dedicated processor since a single processor would not be capable of performing both vector control and intensive real-time digital signal processing. The obvious choice for a commercial application would be a DSP.

8.2 Comparative Investigation of Vector Control Structures

The comparative studies of different vector control strategies lead to the practical implementation of Direct Stator Field Orientation (DSFO), Indirect Rotor Field Orientation (IRFO), sensored DRFO and sensorless DRFO. The comparative investigations showed that from the point of view of field orientation rotor flux orientation is to be preferred to stator flux orientation when a high bandwidth flux controller is not being used. The reason is that rotor flux orientation provides a higher degree of decoupling between flux magnitude and torque generating current (i_{sq}). Moreover it was also found that the sensitivity to parameter errors of a particular sensorless flux orientation method depends on whether stator or rotor dynamic equations are being used for field orientation purposes. The stator equation (voltage model) depends on the stator resistance (R_s) and on the leakage inductance (σL_s) and it is more robust at medium and high speed, when the influence of the stator resistance is smaller. The rotor equation (current model) depends on the rotor time constant (T_r) and on the magnetising inductance (L_0) and it exhibits a better performance at low speed. Based on the previous considerations it was found that a DRFO sensorless system based on the MRAS-CLFO scheme provides a good degree of field orientation, even at low speeds. From the research carried out there is no evidence to suggest that similar performance could not be achieved by using methods like the Extended Luenberger Observer (ELO) or the Extended Kalman Filter (EKF), however this research work used the MRAS-CLFO due to its greater simplicity.

8.3 Slot Harmonic Speed Tracking System

It was already known from previous studies within the Power Electronics, Machines and Control Group at the University of Nottingham that slot harmonics are easily detectable by Discrete Fourier Transform (DFT) techniques even for closed slot cage motors [31]. Several investigative studies have been taken in this work, all of which constitute new and previously unpublished work:

i) *Steady state accuracy:* the accuracy of the DFT is constrained by the acquisition time T_{aq}, therefore a general expression has been obtained relating the steady state accuracy of the RSH speed calculator with T_{aq}. It was found that accuracy improvement for a given T_{aq} could be obtained by interpolation in the discrete frequency domain. Interpolation techniques vary depending on the windowing function used for the signal frequency analysis, therefore a general interpolation expression was derived for the important kind of time windows obtained by addition of Dirichlet kernels. The performance of seven different windows were investigated in terms of accuracy and resolution, the best proving to be the Hanning window. With this window accuracies ranged from 0.2 rpm for T_{aq} = 0.5 s to 0.02 rpm for T_{aq} = 5.6 s.

ii) *Resolution:* this determines how close a slot harmonic can be to a larger inverter harmonic before accurate speed detection is lost. Results are translated into practical consequences for robust detection, namely the low-load limit and the low-speed limit in which the slot harmonics start to cross the low order inverter harmonics. Using the Hanning window/interpolation, detection down to natural no-load (i.e. the motor loaded by its own bearing friction and windage) was attainable. Non-robust detection occurred at speeds below 2 Hz. Assuming a significant amplitude of the rotor slot harmonic, the low speed limit in any machine is determined by the maximum allowable T_{aq} and by the number of rotor slots, hence speed measurement at lower frequencies could be obtained by using a larger T_{aq} or by using a machine with more rotor slots.

iii) *Speed tracking algorithms:* these are simple until the slot harmonics cross the low order inverter harmonics at lower speed. Two algorithms were written, one exploiting the existence of two slot harmonics and retaining robustness down to 2 Hz.

iv) *Behaviour during speed transients:* studies were done using a recursive DFT algorithm, known as the Short Time Discrete Fourier Transform (ST-DFT). The ST-DFT was updated every 30 ms and its performance was analyzed using different transient slew rates and acquisition times T_{aq}. The ST-FFT performance was entirely predictable, tracking the speed with a fixed delay $T_d = T_c + T_{aq}/2$. For transient durations less than T_d, the detection jumped to the new speed at T_d.

The above work has resulted in a slot harmonic speed detector capable of high accuracies in steady state and robust down to natural no-load and down to excitation frequencies of 2 Hz. The dynamic performance is significant with entirely predictable delays. This was beyond original expectations.

After this work was published in [11, 13] and submitted for journal publication [14], a research group in the USA [44] reported a method in which all inverter and slot harmonics were down sampled to a single slot harmonic and a single inverter harmonic by using intentional spectral aliasing. The author was aware of this possibility but had dismissed it on account of the huge increase in spectral leakage that the process introduces. Extremely long T_{aq} times are necessary (36 s for a fundamental stator frequency of 1 Hz). Accuracy and resolution are likewise poor, and it was concluded that this method is not better than the use of the DFT without interpolation techniques.

8.4 Tuning of the MRAS-CLFO Speed Estimator

The speed signal detected from the rotor slot harmonics $\omega_{r(sh)}$ is used to tune the MRAS-CLFO speed estimator principally against variations in the rotor time constant T_r. An adaptive loop was designed in which the value of T_r in the MRAS is adjusted to drive the error between MRAS speed estimate and $\omega_{r(sh)}$ to zero. This adaptive loop has a bandwidth of about 1 Hz for T_{aq} = 1 s, giving a speed accuracy of 0.08 rpm (faster tuning bandwidths are possible with reduced accuracy). This bandwidth is significant in that it allows tuning during changes in T_r due to cross-saturation and leakage effects when large values of torque current are used. In steady state, the resulting sensorless drive has the same speed accuracy than the slot harmonic speed estimator. It is worth remarking that the 0.08 rpm steady state speed accuracy was obtained independently of the load conditions. This implies an extremely good speed regulation during sensorless operation.

A completely new method of stator resistance identification was developed which yielded accuracies of 1-2% (experimentally confirmed). This method exhibits the major advantage of not requiring of the knowledge of any other machine parameter for its operation. This method does not require speed information either, and is therefore suitable for sensorless drives. One important drawback of this method is the necessity of speed cycling for its operation and hence its inability of estimating R_s in steady state. The effects of a wrong stator resistance estimate being used for flux calculation during speed transients through zero speed were thoroughly studied.

It was found that DC terms appear in the flux estimates during dynamic transients when the wrong value of R_s is used, which in turn cause oscillations on the estimated flux angle and on the estimated flux magnitude. An analytical expression to quantify the effect of inaccurate R_s estimates was derived and its predictions were verified by simulation and experimentally. This result is also new and previously unpublished.

8.5 Small Signal Analysis of the Closed Loop Drive

The speed signal from the tuned MRAS speed estimator was used as a feedback signal for a classical speed controller and the closed natural frequency ω_n maximised in comparison with a sensored IRFO vector drive. Increasing ω_n towards that of the sensored drive led to increasing torque and speed oscillations (even in steady state) and ultimately to drive instability. Drive oscillations were reproduced in simulations when the machine parameters used in the MRAS estimator were in error. A full mathematical model of the closed loop vector control and MRAS system was then derived and linearised about quiescent drive operating points using the symbolic maths package MAPLE. The linearised equations were passed to MATLAB and the closed loop pole-zero positions plotted for variations in speed and parameter errors. The results showed that with perfect parameters the observer poles and zeroes cancel each other with only the mechanical pole remaining (a phenomena well known in observer theory). Imperfect parameters caused imperfect cancellation with the underdamped machine poles causing a non-zero residue leading to the effects observed. The residues increased with increasing load and were more pronounced with variations of the stator resistance, although errors in all parameters contributed to oscillations. Most significantly, the oscillations were found to increase with the design parameter $\omega_n J$, where ω_n is the natural frequency of the speed loop and J is the system inertia. In addition the oscillations were also found to increase with the adaptive loop bandwidth ω_{ad}.

Moreover, the small signal analysis confirmed that errors in the estimated parameters (especially on T_r) cause torque dependent speed estimate errors. This confirms the necessity of an independent speed measurement system (in our case from the rotor slot harmonics) in order to obtain speed holding characteristics similar to sensored drives.

8.6 Speed Dynamics Comparison of Sensored and Sensorless Drives

An excellent performance measure of the speed dynamics was found to be $\omega_n J$ since this allows performance to be compared independently of the system inertia. It is directly measurable from the load torque transient response which is a good experimental test for the speed loop bandwidth. For sensored drives, the maximum value of $\omega_n J$ is a function of the resolution of the line encoder N, the sample time T, and the maximum allowable noise on the torque demand. The developed sensorless drive yielded a per unit value of $\omega_n J$ of about 8 without R_s identification and about 16 with identification. For a sensored drive with an allowable 5% noise on the torque demand, this corresponds to $NT = 10$ and 20 respectively. In general practical terms, a 4 kW sensorless MRAS drive with matched load inertia and tuned parameters can perform to a speed bandwidth of about 15 Hz. It is noted that the speed bandwidth of sensored drives can generally be improved by the use of high resolution speed encoders. The attainable bandwidth of the tuned sensorless system however is such as to be comparable to sensored DC and AC vector drives as found in many if not the majority of applications.

Using the tuned sensorless drive, zero speed operation was found to be possible with loads equal or higher than 75% rated torque. The speed accuracy at zero speed steady state was found to be ±8 rpm with the machine fully fluxed.

8.7 Research Results and Future Direction

This research has resulted in 5 conference publications [12, 11, 13, 7, 8], 2 journal publications [9, 10] with one journal publication pending. The direction of future work may be divided into three aspects:

i) Investigation of the proposed sensorless system in field weakening operation.
ii) The enhancement in measurement bandwidth of the slot harmonic derived speed signal.
iii) Improvement in accuracy at zero speed. This can be done by exploiting rotor asymmetry, which will also yield true sensorless position control.

Appendix 1 Vector Control Theory

The voltage across a coil at any instant is equal to the resistive drop plus the induced e.m.f. For the stator coils we have

$$\underline{v}_s^s = R_s \underline{i}_s^s + \frac{\mathrm{d}\underline{\lambda}_s^s}{\mathrm{d}t} \tag{A1.1}$$

where the superscript *s* denotes quantities in the stator fixed reference frame. For a cage rotor, or short circuit wound rotor we have

$$0 = R_r \underline{i}_r^r + \frac{\mathrm{d}\underline{\lambda}_r^r}{\mathrm{d}t} \tag{A1.2}$$

where the superscript *r* denotes quantities in the rotor fixed reference frame. The rotor and stator flux linkages can be expressed as functions of stator and rotor currents

$$\underline{\lambda}_s^s = L_s \underline{i}_s^s + L_0 \underline{i}_r^r e^{j\theta_r} \tag{A1.3}$$

$$\underline{\lambda}_r^r = L_r \underline{i}_r^r + L_0 \underline{i}_s^s e^{-j\theta_r} \tag{A1.4}$$

where θ_r is the rotor angular position.Substituting (A1.3) in the stator and rotor dynamic equations (eqs. (A1.1) and (A1.2) respectively) we obtain

$$\underline{v}_s^s = R_s \underline{i}_s^s + L_s p \underline{i}_s^s + L_0 p(\underline{i}_r^r e^{j\theta_r}) \tag{A1.5}$$

$$0 = R_r \underline{i}_r^r + L_r p \underline{i}_r^r + L_0 p(\underline{i}_s^s e^{-j\theta_r}) \tag{A1.6}$$

To complete the dynamic equations of the induction machine, we just need to add the expressions for torque and mechanical load

$$T_e = 3\frac{p_n}{2}L_0 \ \mathrm{Im}\left\{\underline{i}_s^s(\underline{i}_r^r e^{j\theta_r})^*\right\} \tag{A1.7}$$

$$\frac{2}{p_n}(Jp+B)\omega_r = T_e - T_L \tag{A1.8}$$

where T_e is the electromagnetic torque, T_L is the load torque, J is the machine-load inertia and B is the mechanical friction coefficient. The relationship between rotor angular position and rotor speed is $p\theta_r = \omega_r$.

Equations (A1.5), (A1.6) and (A1.7) can be expressed in a frame of reference rotating at synchronous speed to yield

$$\underline{v}_s = R_s\underline{i}_s + \sigma L_s(j\omega_e+p)\underline{i}_s + \frac{L_0}{L_r}(j\omega_e+p)\underline{\lambda}_r \tag{A1.9}$$

$$0 = -\frac{L_0}{L_r}R_r\underline{i}_s + \frac{R_r}{L_r}\underline{\lambda}_r + (j\omega_{sl}+p)\underline{\lambda}_r \tag{A1.10}$$

$$T_e = 3\frac{p_n}{2}\frac{L_0}{L_r}\ \mathrm{Im}\{\underline{i}_s\underline{\lambda}_r^*\} \tag{A1.11}$$

where the leakage coefficient σ is defined as

$$\sigma = \frac{L_sL_r - L_0^2}{L_sL_r} \tag{A1.12}$$

and the slip frequency ω_{sl}

$$\omega_{sl} = \omega_e - \omega_r = p(\theta_e - \theta_r) \tag{A1.13}$$

In this case stator currents and rotor flux linkage have been chosen as state variables, however similar expressions can be obtained from (A1.5), (A1.6) and (A1.7) using other state variables (e.g. stator currents and stator flux linkage).

Expressing (A1.9), (A1.10) and (A1.11) in real and imaginary components we have

$$v_{sd} = (R_s + \sigma L_s p)i_{sd} - \sigma L_s \omega_e i_{sq} + \frac{L_0}{L_r} p \lambda_{rd} - \omega_e \frac{L_0}{L_r} \lambda_{rq} \qquad \text{(A1.14)}$$

$$v_{sq} = (R_s + \sigma L_s p)i_{sq} + \sigma L_s \omega_e i_{sd} + \frac{L_0}{L_r} p \lambda_{rq} + \omega_e \frac{L_0}{L_r} \lambda_{rd} \qquad \text{(A1.15)}$$

$$0 = -\frac{L_0}{L_r} R_r i_{sd} + \left(\frac{R_r}{L_r} + p \right) \lambda_{rd} - \omega_{sl} \lambda_{rq} \qquad \text{(A1.16)}$$

$$0 = -\frac{L_0}{L_r} R_r i_{sq} + \left(\frac{R_r}{L_r} + p \right) \lambda_{rq} + \omega_{sl} \lambda_{rd} \qquad \text{(A1.17)}$$

$$T_e = 3 \frac{p_n}{2} \frac{L_0}{L_r} \{ i_{sq} \lambda_{rd} - i_{sd} \lambda_{rq} \} \qquad \text{(A1.18)}$$

By aligning the rotor flux with the real axis of the synchronous frame, λ_{rq} equals zero and the previous equations are reduced to

$$v_{sd} = (R_s + \sigma L_s p)i_{sd} - \sigma L_s \omega_e i_{sq} + \frac{L_0}{L_r} p \lambda_{rd} \qquad \text{(A1.19)}$$

$$v_{sq} = (R_s + \sigma L_s p)i_{sq} + \sigma L_s \omega_e i_{sd} + \omega_e \frac{L_0}{L_r} \lambda_{rd} \qquad \text{(A1.20)}$$

$$0 = -\frac{L_0}{L_r} R_r i_{sd} + \left(\frac{R_r}{L_r} + p \right) \lambda_{rd} \qquad \text{(A1.21)}$$

$$0 = -\frac{L_0}{L_r} R_r i_{sq} + \omega_{sl} \lambda_{rd} \qquad \text{(A1.22)}$$

$$T_e = 3\frac{p_n}{2}\frac{L_0}{L_r}\lambda_{rd}\, i_{sq} \tag{A1.23}$$

The last three equations are particularly interesting. Equation (A1.21) provides a means of controlling the rotor flux linkage by using i_{sd}, eq. (A1.23) provides a means of controlling the electromagnetic torque by using i_{sq}, and the machine slip can be obtained from (A1.22). The flux angle deternining the position of the synchronous reference framte and therefore needed for calculating i_{sd} and i_{sq} can be obtained using

$$\theta_e = \int(\omega_r + \omega_{sl})\,\mathrm{d}t \tag{A1.24}$$

Note this particular derivation corresponds to Indirect Rotor Field Orientation (IRFO). Using the same procedure, the corresponding equations for Stator Field Orientation can be easily obtained. Expressing (A1.9) and (A1.10) as functions of the stator current and flux and considering $\lambda_{sq} = 0$ yields

$$\begin{aligned} v_{sd} &= R_s i_{sd} + \frac{d}{dt}\lambda_{sd} \\ v_{sq} &= R_s i_{sq} + \omega_e \lambda_{sd} \end{aligned} \tag{A1.25}$$

$$0 = (1 + T_r p)\lambda_{sd} - (L_s + \sigma L_s T_r p)\, i_{sd} + \omega_s \sigma L_s T_r i_{sq} \tag{A1.26}$$

$$0 = -(L_s + \sigma L_s T_r p)\, i_{sq} - \omega_s \sigma L_s T_r i_{sd} + \omega_s T_r \lambda_{sd} \tag{A1.27}$$

Appendix 2 Circuit Diagrams

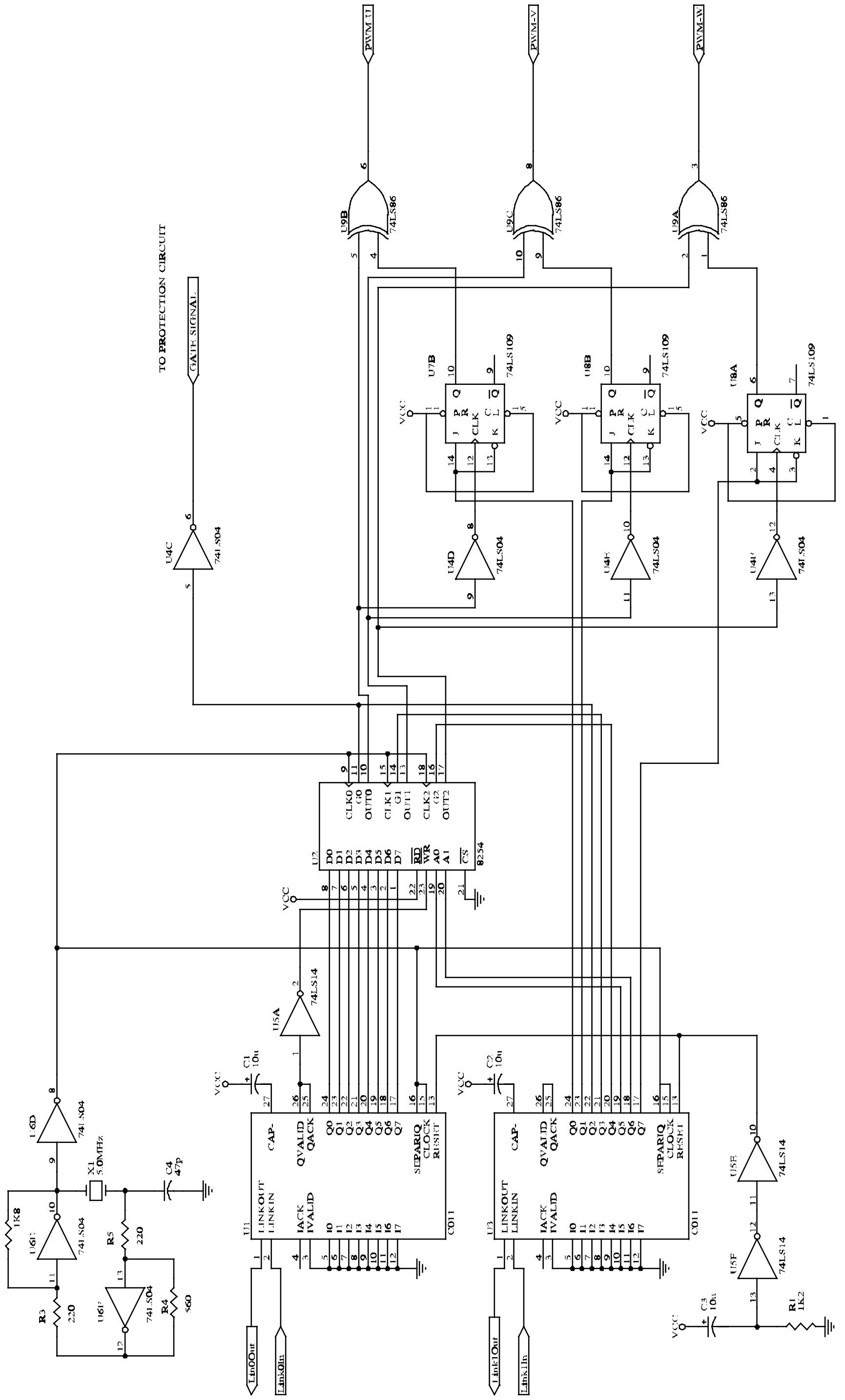

Figure A2.1 PWM Counter Circuit

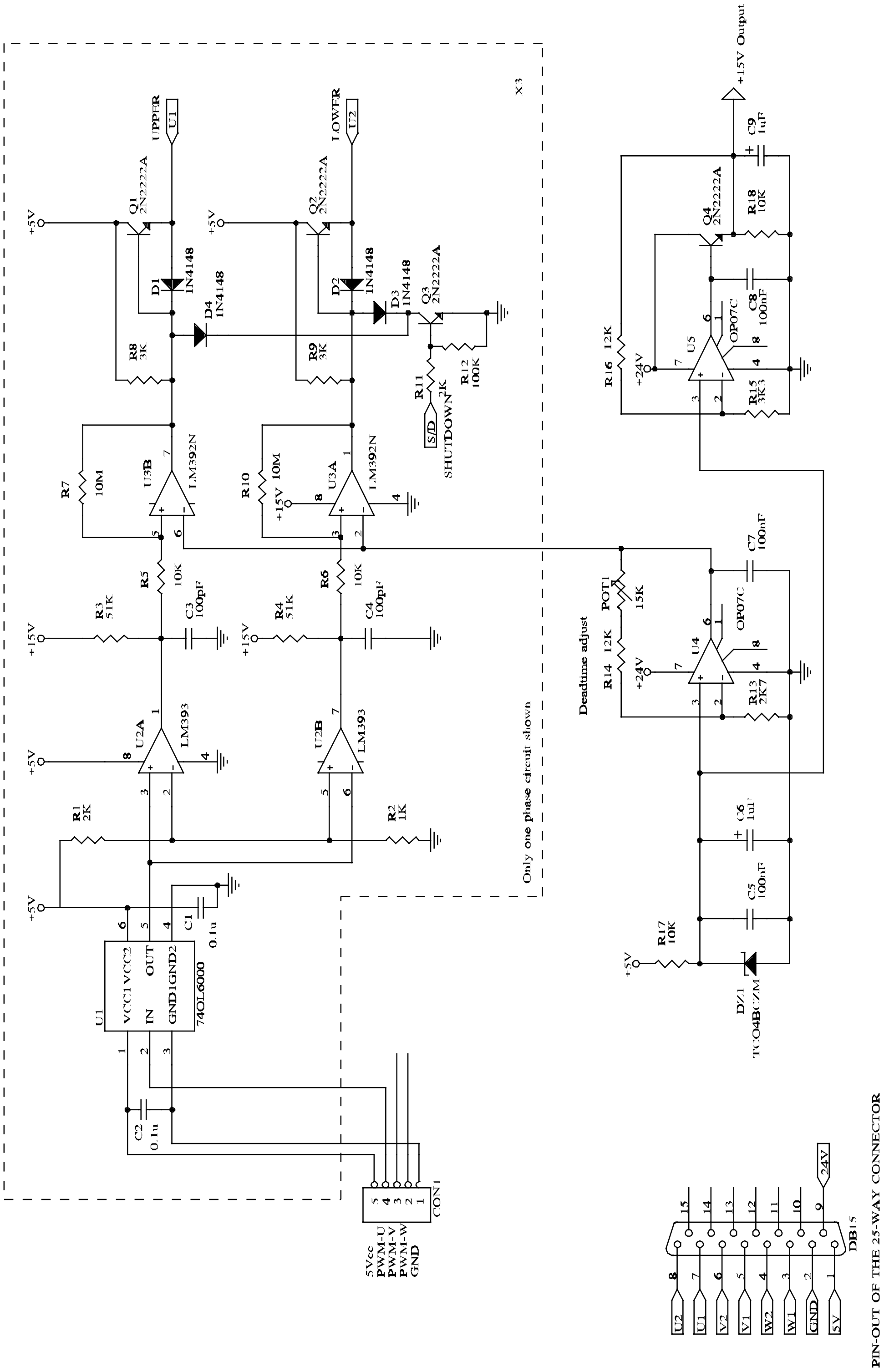

Figure A2.2 Interlock Delay Circuit

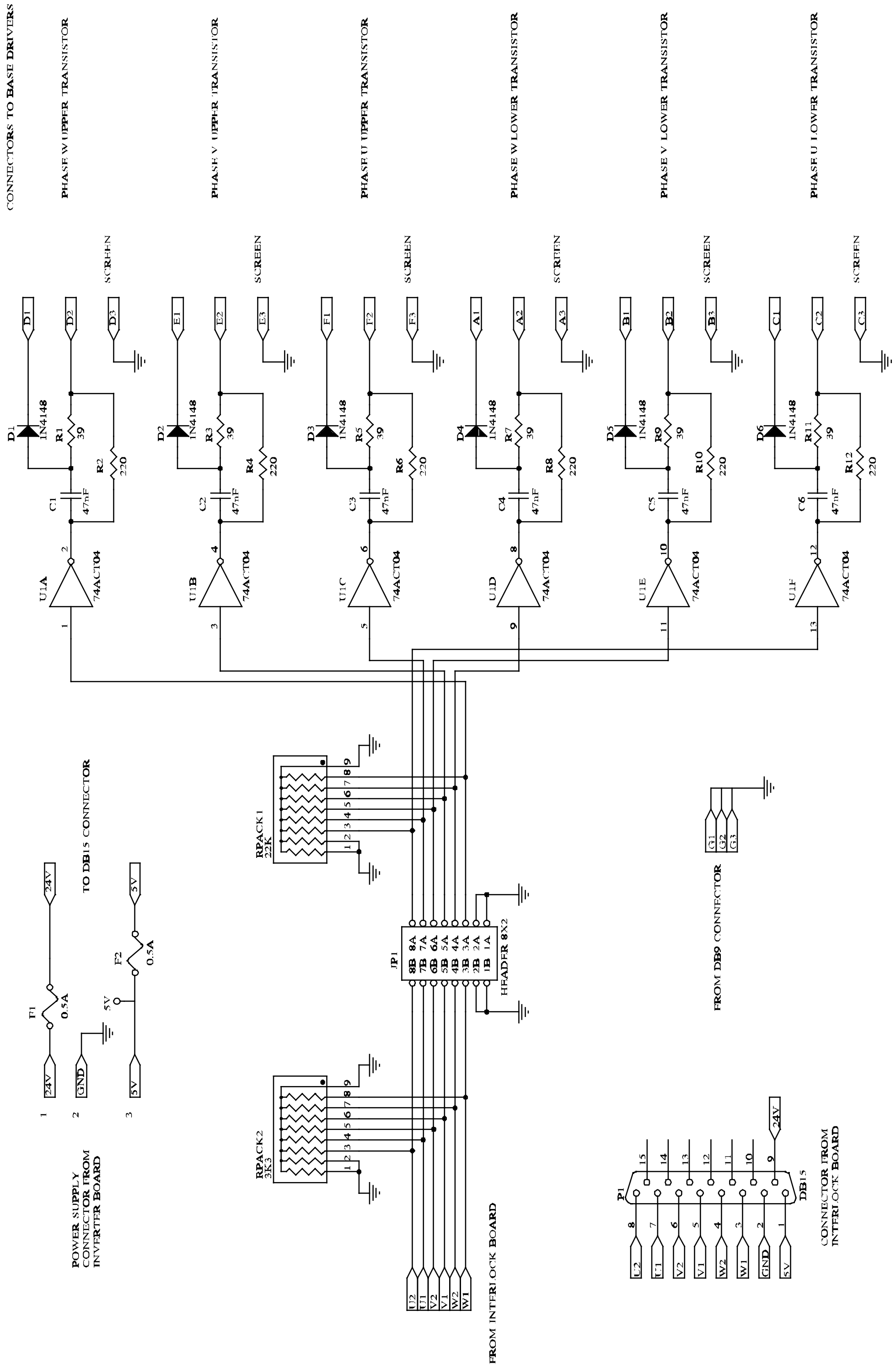

Figure A2.3 Inverter Interface Circuit

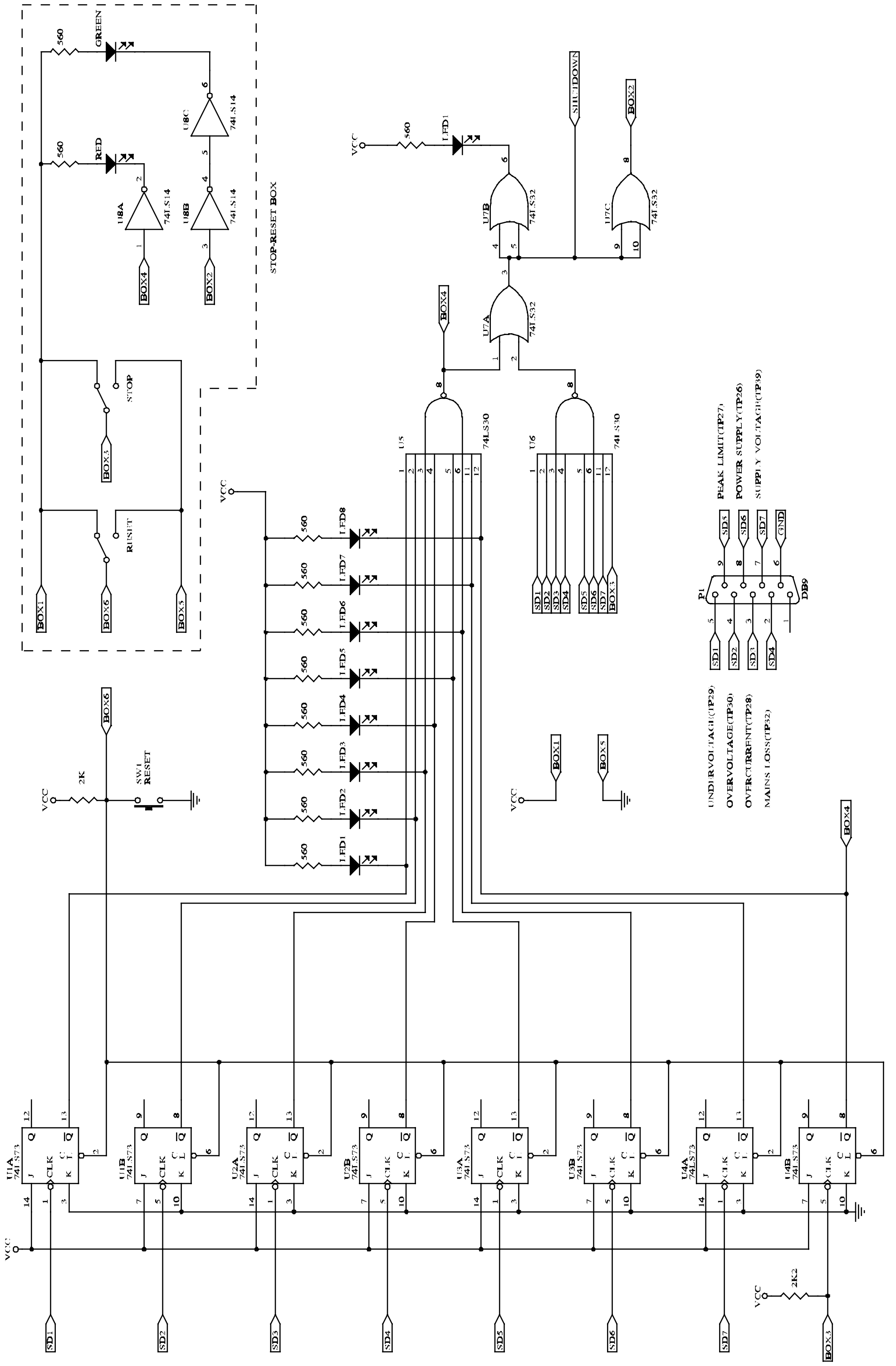

Figure A2.4 Protection Circuit

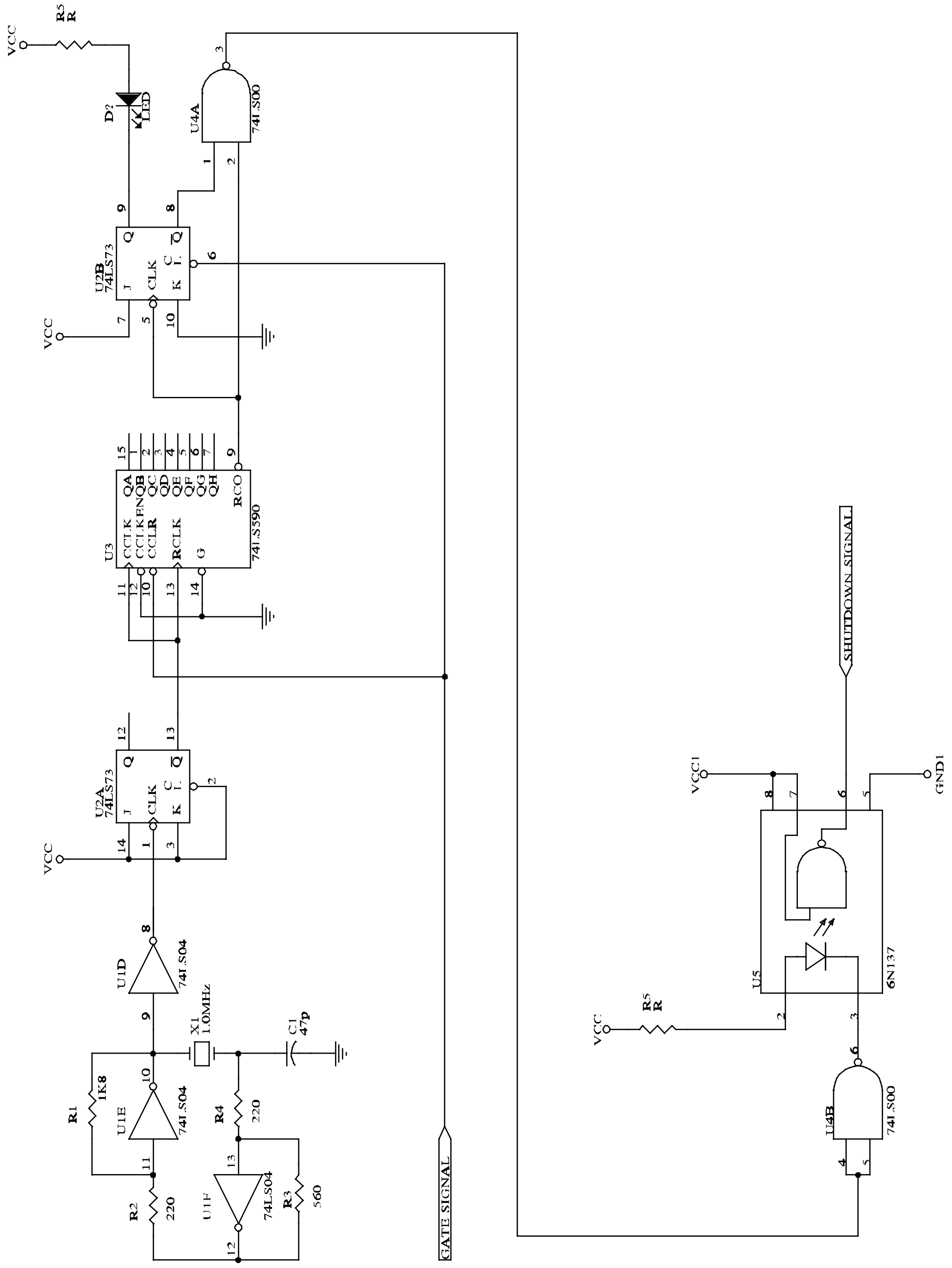

Figure A2.5 Dead-lock Protection Circuit

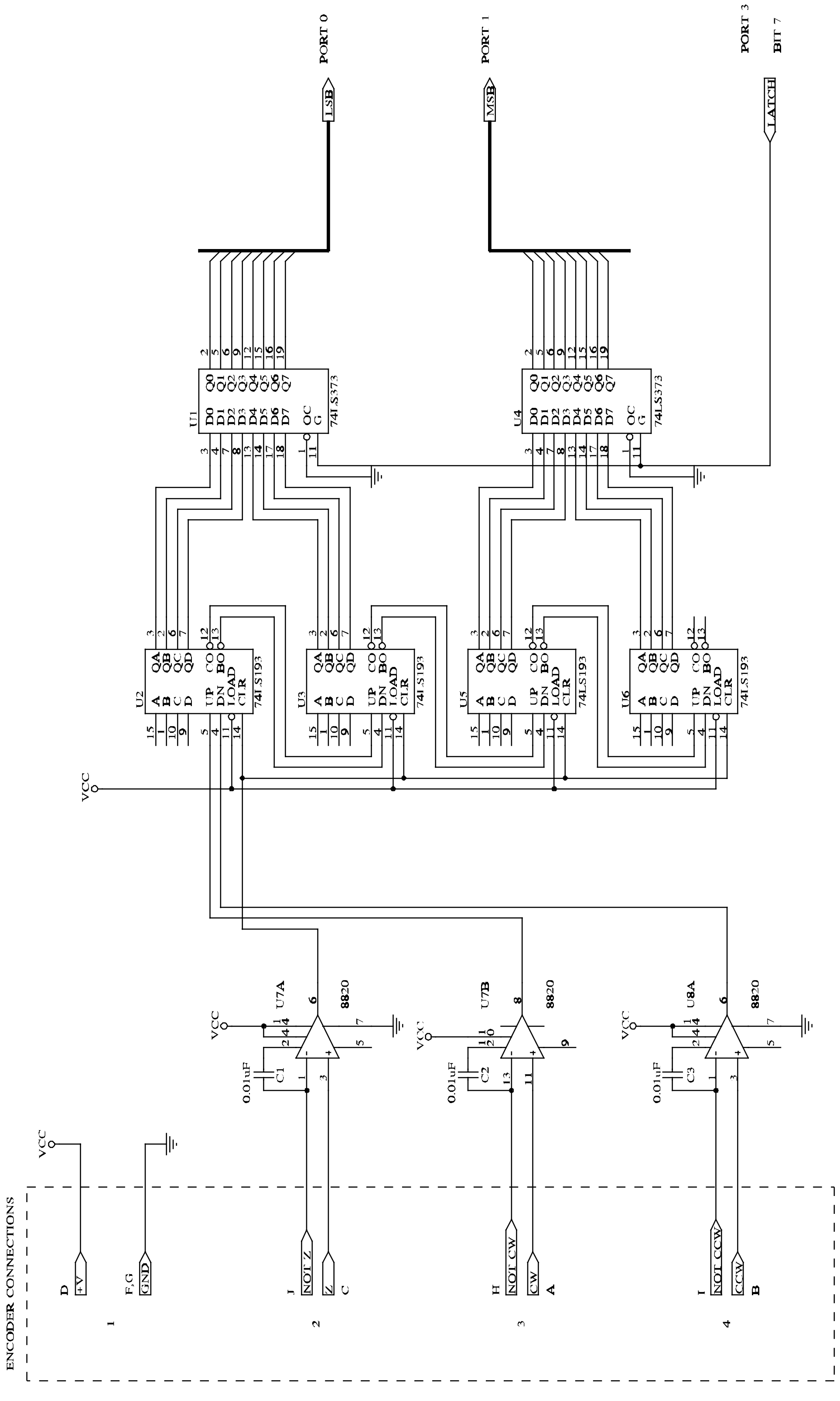

Figure A2.6 Encoder Interface Circuit

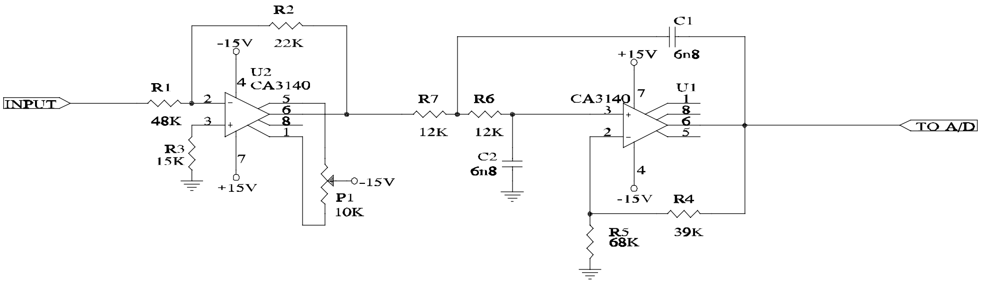

C1=C2 R6=R7
CUT-OFF FREQUENCY: 1/(2*PI*R6*C1)

Figure A2.7 Antialiasing Filter

Appendix 3 Linearisation of the MRAS-CLFO Dynamic Equations

The deduction of the linearised equations has been carried out as follows. Let the MRAS-CLFO be defined as follows

$$\dot{x} = \begin{pmatrix} f_1(x,u) \\ f_2(x,u) \\ \vdots \\ f_9(x,u) \end{pmatrix}; \qquad y = g(x) \tag{A3.1}$$

where

$$\begin{gathered} x = (\omega_r \quad \hat{\lambda}_{rd}^C \quad \hat{\lambda}_{rq}^C \quad x_{sd} \quad x_{sq} \quad x_{ed} \quad x_{eq} \quad x_2 \quad x_3)^T \\ u = i_{sq} \\ y = \hat{\omega}_r \end{gathered} \tag{A3.2}$$

$$f_1(x,u) = -\frac{B}{J}\omega_r + \frac{K_T\left(\underline{\lambda}_r \times \underline{i}_s\right)}{J} - \frac{T_m}{J} \tag{A3.3}$$

$$f_2(x,u) = \mathrm{Re}\left\{-\left[\frac{1}{\hat{T}_r} + j(\omega_e - \hat{\omega}_r)\right]\underline{\hat{\lambda}}_r^C + \frac{\hat{L}_0}{\hat{T}_r}\underline{i}_s\right\} \tag{A3.4}$$

$$f_3(x,u) = \mathrm{Im}\left\{-\left[\frac{1}{\hat{T}_r} + j(\omega_e - \hat{\omega}_r)\right]\underline{\hat{\lambda}}_r^C + \frac{\hat{L}_0}{\hat{T}_r}\underline{i}_s\right\} \tag{A3.5}$$

$$f_4(x,u) = \mathrm{Re}\left\{K_2\underline{x}_e - \left(K_1\frac{\hat{L}_r}{\hat{L}_0} + j\omega_e\right)\underline{x}_s + K_1\underline{\hat{\lambda}}_r^C - K_1\underline{\hat{\lambda}}_r^{/} + \left(K_1\frac{\hat{L}_r}{\hat{L}_0}\Delta\sigma L_s - \Delta R_s\right)\underline{i}_s\right\} \tag{A3.6}$$

$$f_5(x,u) = \mathrm{Im}\left\{K_2\underline{x}_e - \left(K_1\frac{\hat{L}_r}{\hat{L}_0} + j\omega_e\right)\underline{x}_s + K_1\underline{\hat{\lambda}}_r^C - K_1\underline{\hat{\lambda}}_r^{/} + \left(K_1\frac{\hat{L}_r}{\hat{L}_0}\Delta\sigma L_s - \Delta R_s\right)\underline{i}_s\right\} \tag{A3.7}$$

$$f_6(x,u) \;=\; \mathrm{Re}\left\{ -j\omega_e \underline{x}_e + \underline{\hat{\lambda}}_r^{C} - \underline{\hat{\lambda}}_r^{\prime} - \frac{\hat{L}_r}{\hat{L}_0}\underline{x}_s + \frac{\hat{L}_r}{\hat{L}_0}\Delta\sigma L_s \underline{i}_s \right\} \tag{A3.8}$$

$$f_7(x,u) \;=\; \mathrm{Im}\left\{ -j\omega_e \underline{x}_e + \underline{\hat{\lambda}}_r^{C} - \underline{\hat{\lambda}}_r^{\prime} - \frac{\hat{L}_r}{\hat{L}_0}\underline{x}_s + \frac{\hat{L}_r}{\hat{L}_0}\Delta\sigma L_s \underline{i}_s \right\} \tag{A3.9}$$

$$f_8\,(x,u) \;=\; (\underline{\hat{\lambda}}_r^{C} \times \underline{\hat{\lambda}}_r^{V}) \tag{A3.10}$$

$$f_9\,(x,u) \;=\; K_t(\underline{\hat{\lambda}}_r^{V} \times \underline{i}_s) + K_5 x_2 + K_4 \dot{x}_2 - \hat{B}\hat{\omega}_r \tag{A3.11}$$

$$g\,(x,u) \;=\; \frac{1}{\hat{J}}x_3 + K_3 \dot{x}_2 \tag{A3.12}$$

From these equations, the coefficients of the linearised system matrices in (4.22) are obtained conventionally

$$a_{ij} \;=\; \frac{\partial f_i}{\partial x_j}, \quad b_i \;=\; \frac{\partial f_i}{\partial u}, \quad c_j \;=\; \frac{\partial g}{\partial x_j} \tag{A3.13}$$

The matrices ***A***, ***B*** and ***C*** are evaluated at the operating point (x_0,u_0), obtained by solving

$$0 \;=\; f_i(x_0, u_0) \tag{A3.14}$$

The actual state space matrices depend on the errors on the observer parameters and on the operating point, that can be determined by setting the values of i_{sq0}, ω_{r0} and λ'_{rd0}. An explicit expression for ***A***, ***B*** and ***C*** is in general too cumbersome, and therefore will not be included here. For this work, the explicit expressions have been obtained by solving the above equations using MAPLE and by subsequent numerical evaluation with MATLAB. The MAPLE programs used for the computation of the linearised system and the initial conditions are listed in Appendix 4.

Appendix 4 MAPLE Programs

Appendix 4 MAPLE Programs

Appendix 4 MAPLE Programs

Appendix 4 MAPLE Programs

Appendix 4 MAPLE Programs

Appendix 4 MAPLE Programs

Appendix 4 MAPLE Programs

Appendix 4 MAPLE Programs

Appendix 4 MAPLE Programs

Appendix 4 MAPLE Programs

Appendix 4 MAPLE Programs

Appendix 4 MAPLE Programs

Appendix 4 MAPLE Programs

Appendix 4 MAPLE Programs

Appendix 4 MAPLE Programs

Appendix 4 MAPLE Programs

Appendix 4 MAPLE Programs

Appendix 4 MAPLE Programs

Appendix 4 MAPLE Programs

Appendix 4 MAPLE Programs

Appendix 4 MAPLE Programs

Appendix 4 MAPLE Programs

Appendix 4 MAPLE Programs

Appendix 5 Software Description

To implement the different algorithms and control systems more than 13,000 lines of sofware code have been written. Three different programming languages have been used, Occam for the transputers, Pascal for the host PC and Fortran for the i860 vector processor. A detailed explanation of the different routines would be too cumbersome to be useful, however a functional description of the different software blocks can give a valuable insight into the complexity of the developed software.

The description of the Occam software will be carried out using "pseudo-Occam" listings. A line beginning with three dots "`...`" denotes a "fold" or functional block, whereas any text following two hyphens "`--`" is a comment.

A5.1 PWM Transputer

The **PWM** receives the voltage command from the **CONTROL** transputer and calculates the three timing values that will be loaded into the counters in order to generate the desired **PWM** pattern. The voltage commands are two voltages in a synchronous frame (V_d and V_q) and the corresponding flux angle which determines the position of the synchronous frame (θ_e).

```
PROC pwm (CHAN OF REAL32 control.to.pwm, pwm.to.control,
                         i860.to.pwm, pwm.to.i860)

  #USE "snglmath.lib" -- library files for sine table generation
  ...  variable declarations

  SEQ
    ...  sine table generation
    ...  set initial values

    PRI PAR  --PRI PAR merely used to access the high priority timer
      ...  pwm generation
      ...  dummy
:
```

Figure A5.1 PWM Program structure

The listing in Fig. A5.1 shows the general structure of the program running in the **PWM** transputer. First of all the single precision mathematical library is used in order to access the sine function for generating the sine lookup table. Then the different variables, constants and links are defined. Afterwards the initialisation procedures will first generate the sine lookup table and set the initial values of the different variables and initial settings of the PWM counters. Then a high priority parallel construct (PRI PAR) is used in order to access the high precision timer of the transputer, which provides a timing resolution of 1 µs.

```
SEQ
  TIMER clock:
  WHILE TRUE
    SEQ

      clock ? now
      ...  calculate l-h during actual carrier h - l
      clock ? AFTER (now PLUS delay.slot)

      clock ? now
      ...  calculate h-l during actual carrier l - h
      clock ? AFTER (now PLUS delay.slot)
```

Figure A5.2 PWM generation procedure

Figure A5.2 shows the PWM generation procedure. First of all, a timer is declared ("clock"), then the pwm generation consists of an endless loop. Within the loop, the value of the timer first loaded into the variable "now", then the calculation for the low to high transition of the PWM are carried out while the counters are generating the high to low PWM transition. Once all the calculations are carried out, the transputer will wait until the overall processing time reaches the value "delay.slot", which determines the switching frequency. The same procedure is carried out again for the high to low calculations.

```
SEQ
  ...  update reference values from control

  clock ? AFTER (now PLUS sync.delay)

  ...  enable counters high to low
  ...  increment the pointers to sine table
  ...  access sine look up table
  ...  calculate abc voltages
  ...  calculate Tab1,Tab2,Tab3
  ...  output pulses
```

Figure A5.3 PWM Half cycle generation

The generation of one of the previously mentioned transitions (or half cycles) is shown in Fig. A5.3. Firstly, the reference values are received from the control transputer. Then a synchronisation delay is introduced to allow for current and voltage measurement before the counters are triggered. This will ensure that current and voltage measurement will not occur while the transistors are switching. Once the counters are enabled with the previously calculated switching times, the reference angle is used to calculate the adequate pointers to the sine lookup table, in order to obtain the sine and cosine of the reference angle. Then the three phase voltages (V_a, V_b, V_c) are obtained from the reference voltages (V_d, V_q). Afterwards the three counting values (Tab1,Tab2,Tab3) are calculated from the phase voltages. Moreover the "tab" values are checked to be between acceptable limits, and modified if pulsedropping is requires. Finally the "tab" values are downloaded to the counters. The counting of the new "tab" values will be triggered in the next PWM half cycle.

A5.2 CONTROL Transputer

The **CONTROL** transputer carries out voltage and current measurements, control calculations, MRAS-CLFO speed and flux estimation, rotor time constant adaption, speed and current control and generation of voltage references for the PWM transputer.

```
PROC control (CHAN OF ANY comms.to.control,
              CHAN OF ANY control.to.comms,
              CHAN OF REAL32 pwm.to.control,control.to.pwm)
  #USE "snglmath.lib"  --library files for lookup table generation
  ...  Link definition and configuration
  ...  Procedures and variables
  SEQ
    ...  Initialize A/D converters
    ...  Obtain the offset of each channel
    ...  Sine table generation
    ...  Generate square root table
    ...  Generate arc cos table
    ...  Initialize SCOPE variables

    PRI PAR  -- access High Priority timer
      SEQ
        ...  Set initial values
        ...  Vector control
      SKIP
:
```

Figure A5.4 **CONTROL** transputer software structure

The software structure of the **CONTROL** transputer is shown in Fig. A5.4. Firstly the single precision maths library is used to generate the sine, arc cosine and square root lookup tables. Then the transputer links are defined and configured. Afterwards all the different variables and procedures are declared. The initialisation part of the program comprises initialisation of analog to digital converters, measurement offset correction and look up table generation. Moreover the variables used for data capture (SCOPE variables) are also initialised. Once again the PRI-PAR construction is used to access the high priority timer. Then the different variables are initialised. The initialisation process involves the communication of the machine MRAS-CLFO and controller parameters from the host, via the **OVERSEER** and **COMMS** transputers. Then the vector control routines are carried out.

```
SEQ
  WHILE TRUE
    SEQ
      control.to.pwm ! thetaflux

      --Communicate with COMMS to synchronise speed measurement
      control.to.comms ! variabl[selected[0]]

      ...  communication with PWM
      ...  other communications (COMMS and A/D converters)
      ...  scale measurements and obtain alpha/beta quantities
      ...  Obtain Back-emf
      ...  Send back emf values to comms
      ...  decode supervisor instructions

      ...  scale rotor angle + wrap around
      ...  calculate speed using filter

      ...  Low-pass filter integration of currents and voltages

      ...  Tr identification (using RSH speed measurement)
      ...  MRAS-CLFO Flux and Velocity observer
      ...  Obtain estimated flux angle
      ...  Obtain estimated flux magnitude

      ...  speed and flux control (Ts = 20ms)
      ...  slip calculation and current control

      ...  SCOPE
```

Figure A5.5 Vector Control routines

The control routines are carried out in an endless software loop, shown in Fig. A5.5. Firstly, the execution of the control routines is synchronised with the PWM generation by waiting for the **PWM** transputer to read the flux angle value. Then a communication is established with the **COMMS** transputer to sychroncronise the speed measurement carried out by the named transputer. Once the synchronisation has been carried out, the rest of the communications are performed, first with the PWM generation routines and then with the A/D converters and with the **COMMS** transputer. At this stage the **COMMS** transputer sends the measured rotor position to the **CONTROL** transputer. Once the voltages and currents have been measured, they are scaled and transformed to two axis quantities. Then the back e.m.f. is calculated and sent to the **COMMS** transputer for further processing. Afterwards the commands received from the **OVERSEER** transputer via the **COMMS** transputer are decoded and appropriate actions are taken. Afterwards the rotor angle is scaled and checked for wrap around. Then the rotor speed is calculated by differentiation of the rotor angle and subsequent low pass filtering. Then voltages and currents are integrated using low pass filters, in order to provide a measurement of the stator resistance, as described in Section 6.3.5. The next step is the identification of the rotor time constant using the speed measurement from the rotor slot harmonics, in order to tune the MRAS-CLFO. Afterwards the estimation of the rotor flux and rotor speed is carried out. The estimated flux angle and flux magnitude is subsequently obtained. Next, the flux and speed control routines are carried out at a sampling time that can be varied between 5 and 20 ms. The last step of the control routines is the calculation of the machine slip, in order to obtain the flux angle for Indirect Rotor Field Orientation; the current demodulation into a synchronous frame, using the flux angle; and the current control. Lastly the SCOPE variables are updated.

A5.3 COMMS Transputer

The **COMMS** transputer carries out the measurement of the rotor position and the Least Squares Circular Regression Algorithm (LSCRA). The basic structure of the **COMMS** procedure is shown in Fig. A5.6.

```
PROC comms(CHAN OF ANY supervisor.to.comms,
           CHAN OF ANY comms.to.supervisor,
           CHAN OF ANY control.to.comms,
           comms.to.control)

  ...  variable declarations
  ...  procedures definitions
  ...  SCOPE variable declarations
  SEQ
    ...  Iot setup

    ...  pass initial values to control
    ...  get CLFO/MRAC parameters from overseer
    ...  send SCOPE parameters to overseer

    ...  Initialize least squares algorithm variables

    WHILE TRUE
      PRI PAR   --Used only to access the high priority timer
        ...  Main loop
        SKIP
:
```

Figure A5.6 **COMMS** Procedure

The initialisation part of this program consists of the declaration of the different variables and procedures, as well as the declaration of the "SCOPE" variables. Then the parallel I/O module is configured. Afterwards the machine parameters and the initial control values are received from the **SUPERVISOR** and passed down to the **CONTROL** transputer. The same happens with the initial MRAS-CLFO parameters. Afterwards the names of the variables that can be monitored is passed from the **CONTROL** transputer to the host via the **SUPERVISOR**. Then the variables to use in the LSCRA are initialised. The main body of the program is again an endless loop, shown in Fig. A5.7.

```
SEQ
  control.to.comms ? variabl[0]
  ...  latch rotor angle reading

  PAR
    SEQ
      ...  communications with control and supervisor
    SEQ
      ...  read rotor position

  ...  Send angle reading to control transputer
  ...  Get back emf from control transputer
  ...  Decode supervisor instructions
  ...  Least squares algorithm (LSCRA)
  ...  SCOPE
```

Figure A5.7 **COMMS** Main loop

Firstly the variable sent from the **CONTROL** transputer is read, to provide synchronisation for the subsequent latching of the speed reading. Then the communications between with the **CONTROL** and **SUPERVISOR** transputers are carried out in parallel with the reading of the rotor angle. Once the rotor angle has been read, it is sent to the **CONTROL** transputer, which in turn sends the calculated back e.m.f. to the **COMMS** transputer for later use by the LSCRA routines. Then the commands received from the supervisor are decoded and appropriate action is taken. Lastly the LSCRA is carried out and the "SCOPE" variables are updated.

A5.4 OVERSEER Transputer

The **OVERSEER** transputer carries out the interfacing of the host routines, the vector control routines carried out by the **COMMS**, **CONTROL** and **PWM** transputers; and the rotor slot harmonic speed measurement routines. The **OVERSEER** software procedures are reflected in Fig. A5.8.

The initialisation stages comprise the variable and procedure definitions, the definition of the "SCOPE" variables and procedures; the resetting of the data buffers. Then the machine parameters and controller values are received from the host PC and transmitted to the **CONTROL** transputer via the **COMMS** transputer. The same is done with the MRAS-CLFO parameters. Afterwards the "SCOPE" parameters are sent from the **COMMS** transputer to the host. Then the three main parts of the **OVERSEER** program are carried out in parallel. These three routines carry out the

```
PROC overseer (CHAN OF ANY from.host, to.host,
               comms.to.supervisor,
               supervisor.to.comms)

  ...  variable declaration
  ...  define procedures
  ...  SCOPE

  SEQ
    ...  Reset data buffers
    ...  get machine parameters from host and pass them to comms
    ...  get CLFO/MRAC parameters from host
    ...  get SCOPE parameters from comms and send them to host

    PRI PAR
      SEQ
        ... buffer (interface with the rest of the transp. network)
      PAR
        SEQ
          ...  display (interface with the host PC)
        SEQ
          ...  i860 interface
:
```

Figure A5.8 **OVERSEER** Procedure

interfacing between the **COMMS** transputer, PC host and the rotor slot harmonic speed measurement carried out by the i860.

```
...  local variable declarations for buffer
SEQ
  ...  setup initial values
  WHILE TRUE
    SEQ
      ...  communicate with COMMS Transputer
      clock ? now
      ALT
        inter.to.buffer ? FFT.speed
          SKIP
        display.to.buffer ? c.variable.int
          ...  communicate with display
        clock ? AFTER (now PLUS 150 )
          SKIP
```

Figure A5.9 Buffer Procedure

The "buffer" procedure which interfaces with the **COMMS** transputer is shown in Fig. A5.9. After the local variable definitions and the setup of initial values, the main loop starts with the communication with the **COMMS** transputer in order to send the host commands and to obtain the values of upto eight "SCOPE" variables.

Then the ALT construct is introduced to wait for the arrival of one of the following three events:

- Arrival of a rotor slot harmonic speed measurement update.
- Arrival of a command from the "display" procedure (interface to the host). If a command is received, it is decoded and transmitted to the **COMMS** transputer. Then the values of the monitored variables is sent to the "display" procedure for later transmission to the host.
- Time out if none of the previous events occur during the next 150 µs.

```
...  local variable declarations
SEQ
  ...  initialise local variables
  WHILE TRUE
    SEQ
      from.host ? choice16
      SEQ
        IF
          choice16 = (INT16 (’c’)) -- change frequency
            SEQ
              ...  Obtain speed ref. from host and pass it to buffer
          ...  Other commands
```

Figure A5.10 Display Procedure

The "display" procedure is shown in Fig. A5.10. After the declaration and initialisation of local variables, the procedure enters in an endless loop. In this loop, the program waits for a command to be sent from the host and then acts accordingly. As an example, when the host sends the ASCII value ’*c*’, it is signalling a change on the machine speed. The detailed procedure for the change on speed reference is shown in Fig. A5.11.

```
SEQ
  from.host ? speed
  control.value := speed
  c.variable.int := 1

  -- Send command to buffer procedure and at the same time fetch
  -- transient data from buffer
  GetData(DataFactor,c.variable.int,control.value)

  --Send obtained data to host
  SendData.toHost()
```

Figure A5.11 Change in speed reference

When the "display" procedure detects that the host wants to change the machine speed, it asks for the new speed reference to the host and then passes it to the **CONTROL** transputer via "buffer" procedure and **COMMS** transputer. This is done by setting the "control.value" and "c.variable.int" to their corresponding values. Then the "GetData" procedure is called in order to pass the commands to the "buffer" and at the same time fetch the transient data caused by the change in speed. Once the data is obtained, it is sent back to the host for visualisation.

```
...  Define local variables

WHILE TRUE
  PRI ALT

    from.i860 ? FFT.speed
      inter.to.buffer ! FFT.speed

    ovs.to.i860 ? c.val16
      ...  Send display commands to i860
```

Figure A5.12 i860 Interface Procedure

The "i860 interface" procedure is shown in Fig. A5.12. This is a simple routine, and basically waits for data to be sent from or to the transputer in the i860 board (**i860-SERVER**). If there is an speed measurement available from the i860, then it is sent to the "buffer" procedure, which in turn sends it to the **CONTROL** transputer. If there is a command from the "display" procedure, it is fetch and sent to the **i860-SERVER**.

A5.5 i860-SERVER Transputer

This transputer carries out all the needed interfacing with the i860 processor. Its two main tasks are the high frequency sampling of the stator line current and the interfacing with the i860 which is mainly done by memory mapping different input and output buffers. The program running on this transputer is illustrated in Fig. A5.13.

The first step is to declare the variables and the procedures that are going to be used in the program. Then a linear array is defined in order to access the memory shared by the transputer and i860. Then the different variables are initialised and the A/D converter is properly configured. The next step involves the configuration of the FORTRAN program running on the i860. To do that, the initial values of FFT record length and sampling frequency are sent to the i860, which will return the addresses of the different input output buffers. Then the previous addresses are converted into Occam arrays for direct use by the transputer. Once the initialisation is concluded, two main procedures are carried out in parallel; the first one, named "SAMPLER", carries out the sampling, filtering and frequency decimation of the stator line current. The second procedure, named "MAIN", interfaces the "SAMPLER"

```
PROC i860(CHAN OF REAL32 pwm.to.i860, i860.to.pwm,
          CHAN OF INT from.FORTRAN,CHAN OF INT16 to.FORTRAN)

  ...  Variable declaration
  ...  Procedure definitions
  ...  ACCESS TO SHARED MEMORY

  SEQ
    ...  Initialize variables
    ...  Set up A/D converter

    ...  Send initial record length to FORTRAN
    ...  Obtain buffer addresses from FORTRAN
    ...  Define buffers based on the previous addresses
    PAR
      ...  Sampling and filtering "SAMPLER"
      ...  Main program "MAIN"

:
```

Figure A5.13 **i860-SERVER** Procedure

procedure, the i860 Fortran program and the overseer. The listing of the "SAMPLER" procedure is shown in Fig. A5.14.

```
WHILE TRUE
  SEQ
    IF
      Adt.on
        ...  Receive value from A/D converter and LP filter
      TRUE
        SKIP

    clock ? now
    ALT
      -- Get control word from MAIN program
      sampler.control ? control.word
        SEQ
          ...  Decode command from MAIN program

      clock ? AFTER (now PLUS delay)
        SKIP

    ...  Check buffer limits and buffer wrapping
```

Figure A5.14 "SAMPLER" Procedure

Firstly, if the A/D converter is on, the program will read the current value and will low pass filter it. Then the program will wait for a command form the "MAIN" program for a period of time determined by the variable "delay". If no command is received during this time, the program will continue with its normal execution, and if a command is received, it will be decoded and appropriate action will take place. Lastly the checking of the buffer pointers ensures that the buffer limits are kept, doing the appropriate wrap around if necessary. This will create a circular buffer for the input data.

```
SEQ
  ...  Initial settings of the sampler
  clock1 ? last.FFT
  WHILE TRUE
    ALT
      ovs.to.i860 ? command
        ...  Decode command received from overseer

      Recursive & clock1 ? AFTER (last.FFT PLUS us.FFT.Delay)
        ...  Read speed value from FORTRAN in recursive mode
```

Figure A5.15 "MAIN" Procedure

The program listing of the "MAIN" procedure is shown in Fig. A5.15. First of all the initial record length and sampling frequency are sent to the "SAMPLER". Then the programs waits for one of the following events to happen:

- A command sent from the **OVERSEER** transputer, which will be decoded and sent to the i860 Fortran program if necessary.
- If recursive speed measurement is enabled, after a determined period of time the i860 Fortran program will be polled to check if a new speed measurement is available, in which case it will be sent to the **OVERSEER** transputer.

Bibliography

[1] Andria, G., Savino, M. and Trotta, A., “Windows and Interpolation Algorithms to Improve Electrical Measurement Accuracy”, *IEEE Transactions on Instrumentation and Measurement*, 1989, Vol.38, No. 4, pp. 856-863.

[2] Asher, G.M. and Sumner, M., “Parallelism and the Transputer for Real-Time High-Performance Control of AC Induction Motors”, *IEE Proceedings-D*, 1990, Vol.137, No. 4, pp. 179-188.

[3] Atkinson, DJ; Acarnley, PP; Finch, JW , “Observers for Induction-Motor State and Parameter-Estimation”, *IEEE Transactions on Industry Applications*, 1991, Vol.27, No. 6, pp. 1119-1127.

[4] Binns, KJ., “Calculation of some Basic Flux Quantities in Induction and other Doubly-Slotted Electrical Machines”, *Proceedings of the IEE*, 1964, Vol.111, No. 11, pp. 1847-1858.

[5] Blackman, R.B. and Tukey, J.W., *The Measurement of Power Spectra*. Dover Publications, New York, 1958.

[6] Blaschke, F., “The Principle of Field Orientation as Applied to the New Transvector Closed Loop Control for Rotating Machines”, *Siemens Rev.*, 1972, Vol.39, No. 5, pp. 217-220.

[7] Blasco-Giménez, R., Asher, G.M., and Sumner, M., “A New Method of Stator Resistance Estimation for Enhanced Dynamic Performance of Sensorless Vector Control Drives”, *Proceedings of the EPE Conference*, Seville, 1995, Vol.1, pp. 1.689-1.694.

[8] Blasco-Giménez, R., Asher, G.M., and Sumner, M., “Rotor Time Constant Identification in Sensorless Vector Control Drives using Rotor Slot Harmonics”, *Proceedings of the EPE Conference*, Sevilla, 1995, Vol.1, pp. 1.083-1.088.

[9] Blasco-Giménez, R., Asher, G.M., Sumner, M. and Bradley, K.J., “Dynamic Performance Limitations for MRAS Based Sensorless Induction Motor Drives. Part 1: Stability analysis”, *Accepted for IEE-Proceedings B*, 1995,.

[10] Blasco-Giménez, R., Asher, G.M., Sumner, M. and Bradley, K.J., "Dynamic Performance Limitations for MRAS Based Sensorless Induction Motor Drives. Part 2: On-line Parameter Tuning and Dynamic Performance Studies", *Accepted for IEE-Proceedings B,* 1995,.

[11] Blasco-Giménez, R., Sumner, M. and Asher, G.M., "Non-Intrusive Real-Time Speed Measurement of Inverter Fed Induction Motors Using Spectral Estimation and Rotor Slot Harmonics", *UPEC Conference Proceedings*, Galway, 1994, Vol.2, pp. 569-572.

[12] Blasco-Giménez, R., Sumner, M. and Asher, G.M., "Sensorless Vector Control of Induction Motor Drives Using an Intel i860 Connected to a Transputer Network", *Proceedings of the WTC,* Como, 1994, pp. 657-671.

[13] Blasco-Giménez, R., Sumner, M. and Asher, G.M., "Speed Measurement of Inverter Fed Induction Motors Using the FFT and the Rotor Slot Harmonics", *Proceedings of the IEE-PEVD Conference*, London, 1994, pp. 470-475.

[14] Blasco-Giménez, R.; Asher, G.M.; Sumner M. and Bradley K.J., "The Performance of the FFT-Rotor Slot Harmonic Speed Detector for Sensorless Induction Motor Drives", *Submitted for publication in IEE-Proc. B*, 1994,.

[15] Brunsbach, BJ; Henneberger, G , "Field-Oriented Control of an Induction-Motor Without Mechanical Sensors using a Kalman-Filter", *Archiv Fur Elektrotechnik*, 1990, Vol.73, No. 5, pp. 325-335.

[16] Casadei, D., Grandi, G. and Serra, G., "Rotor Flux Oriented Torque-Control of Induction Machines Based on Stator Flux Vector Control", *Proceedings of the EPE Conference,* Brighton, 1993, Vol.5, pp. 67-72.

[17] Chai, H. and Acarnley, P.P., "Induction Motor Parameter Estimation Algorithm using Spectral Analysis", *IEE Proceedings-B*, 1992, Vol.139, No.3, pp. 165-174.

[18] Chan, CC; Wang, HQ , "An Effective Method for Rotor Resistance Identification for High-Performance Induction-Motor Vector Control", *IEEE Transactions on Industrial Electronics*, 1990, Vol.37, No. 6, pp. 477-482.

[19] Chrzan, PJ; Kurzynski, P , "A Rotor Time Constant Evaluation for Vector-Controlled Induction-Motor Drives", *IEEE Transactions on Industrial Electronics*, 1992, Vol.39, No. 5, pp. 463-465.

[20] Cilia, J., *Simulink Library for Induction Motor Control*. Internal Report, University of Nottingham, 1995.

[21] Claessens, P. and Mathys, P., “An Optimized, Adaptative, Reduced-Order Flux Observer”, *Proceedings of the EPE Conference*, Brighton, 1993, Vol.5, pp. 422-427.

[22] Copson, E.T., *Asymptotic Expansions*. Cambridge Press, New York, 1965.

[23] Cuyvers, R., and Lauwereins, R., “Hardware Faul-Tolerance: Possibilities and Limitations offered by Transputers”. Chapter in *Transputers in Real-Time Control*. Research Studies Press Ltd., London, 1992.

[24] Cuzner, R.M., Lorenz, R.D. and Novotny, D.W., “Application of Non-linear Observers for Rotor Position Detection on an Induction Motor using Machine Voltages and Currents”, *IEEE Industry Applications Society Annual Meeting*, Seattle, 1990, Vol.1, pp. 416-421.

[25] Depenbrock, M., “Direct Self-Control (DSC) of Inverter-Fed Induction Machine”, *IEEE Transactions in Power Electronics*, 1988, Vol.3, No. 4, pp. 420-429.

[26] Dittrich, A , “Parameter Sensitivity of Procedures for Online Adaptation of The Rotor Time Constant of Induction Machines with Field-Oriented Control”, *IEE Proceedings-Electric Power Applications*, 1994, Vol.141, No. 6, pp. 353-359.

[27] Du, T. and Brdys, M.A., “Implementetion of Extended Luenberger Obsertvers for Joint State and Parameter Estimation of PWM Induction Motor Drive”, *Proceedings of the EPE Conference*, Brighton, 1993, Vol.5, pp. 439-444.

[28] Elten, D; Filbert, D , “Identification of Electrical Parameters and the Speed of Small 3 Phase Induction-Motors”, *ETZ Archiv*, 1990, Vol.12, No. 12, pp. 379-383.

[29] Erdman, WL; Hoft, RG , “Induction Machine Field Orientation along Airgap and Stator Flux”, *IEEE Transactions on Energy Conversion*, 1990, Vol.5, No. 1, pp. 115-121.

[30] Fay, A.G., *Simulation of Vector Control of Induction Machines*. Studienarbeit, Dept. of Elec. Eng. University of Nottingham, 1994.

[31] Ferrah, A., Bradley, K.J. and Asher, G.M., “An FFT-Based Novel Approach to Noninvasive Speed Measurement in Induction Motor Drives”, *IEEE Transactions on Instrumentation and Measurement*, 1992, Vol.41, No. 6, pp. 797-802.

[32] Fudeh, H.R., “Modeling and Analysis of Induction Machines Containing Space Harmonics, Parts I, II and III”, *IEEE Transactions on Power Apparatus and Systems*, 1983, Vol.102, No. 8, pp. 2608-2628.

[33] Gabriel, R; Leonhard, W; Nordby, C, “Microprocessor Control of the Converter-Fed Induction Motor”, *Process Automation I*, 1980, pp. 35.

[34] Garcés, L.J., “Parameter Adaption for the Speed-Controlled Static AC Drive with a Squirrel-Cage Induction Motor”, *IEEE Transactions on Industry Applications*, 1980, Vol.IA-15, No. 2, pp. 173-178.

[35] Habetler, T.G., Profumo, F., Griva, G., Pastorelli, M. and Bettini, A., “Stator Resistance Tuning in a Stator Flux Field Oriented Drive using an Instantaneous Hybrid Flux Estimator”, *Proceedings of the EPE Conference*, Brighton, 1993, Vol.4, pp. 292-299.

[36] Habetler, T.G, Profumo, F., Pastorelli, M. and Tolbert, L.M., “Direct Torque Control of Induction Machines Using Space Vector Modulation”, *IEEE Transactions on Industry Applications*, 1992, Vol.28, No. 5, pp. 1045-1053.

[37] Harris, F.J., “On the Use of Windows for Harmonic Analysis with the Discrete Fourier Transform”, *Proceedings of the IEEE*, 1978, Vol.66, No. 1, pp. 51-83.

[38] Hasse, K., *Zur Dynamik drehzahlgerelter Antriebe mit stromrichter-gespeisten Asynchron-Kurzschlussläufermaschinen (on dynamic of the speed controlled static ac drive with squirrel-cage induction machine)*. PhD thesis, Techical University Darmstadt, 1969.

[39] Heller, B. and Hamata, V, *Harmonic Field Effects in Induction Machines*. Elsevier Scientific Publishing Co., Amsterdam, 1977.

[40] Henneberger, G., Brunsbach, B.J. and Klepsch, T., “Field-Oriented Control of Synchronous and Asynchronous Drives Without Mechanical Sensors using a Kalman Filter”, *Proceedings of the EPE Conference*, Firenze, 1991, Vol.3, pp. 664-671.

[41] Ho, E.Y.Y. and Sen, P.C., “Decoupling Control of Induction Motor Drives”, *IEEE Transactions on Industrial Electronics*, 1988, Vol.35, No. 2, pp. 253-262.

[42] Holliday, D., Fletcher, J.E. and Williams, B.W., “Non-Invasive Rotor Position and Speed Sensing of Asynchronous Motors”, *Proceedings of EPE ’95*, Sevilla, 1995, Vol.1, pp. 1.333-1.337.

[43] Holtz, J. and Thimm, T., “Identification of the Machine Prameters in a Vector-Controlled Induction Motor Drive”, *IEEE Transactions on Industry Applications*, 1991, Vol.27, No. 6, pp. 1111-1118.

[44] Hurst, H.D. and Habetler, G.H., “Sensorless Speed Measurement using Current Harmonic Spectral Estimation in Induction Machine Drives”, *Power Electronics Spectialists Conference Records*, Taipei, Taiwan, 1994, Vol.1, pp. 10-15.

[45] Ishida, M. and Iwata, K., “A New Frequency Detector of an Induction Motor Utilizing Rotor Slot Harmonics”, *IEEE Transactions on Industry Applications*, 1984, Vol.20, No. 3, pp. 575-582.

[46] Jansen, P.L. and Lorenz, R.D., “Accuracy Limitations of Velocity and Flux Estimation in Direct Field Oriented Induction Machines”, *Proceedings of the EPE Conference*, Brighton, 1993, Vol.1, pp. 312-318.

[47] Jansen, P.L. and Lorenz, R.D., “Transducerless Position and Velocity Estimation in Induction and Salient AC Machines”, *IEEE Transactions on Industry Applications*, 1995, Vol.31, No. 2, pp. 240-247.

[48] Jansen, PL; Lorenz, RD; Novotny, DW , “Observer-Based Direct Field Orientation - Analysis and Comparison of Alternative Methods”, *IEEE Transactions on Industry Applications*, 1994, Vol.30, No. 4, pp. 945-953.

[49] Jotten, R. and Schierling, H., “Adaptive and Self-Commissioning control for a Drive with Induction Motor and Voltage Source Inverter”, *Proceedings of the EPE Conference*, Grenoble, 1987, pp. 883-889.

[50] Kanmachi, T. and Takahashi, I., “Sensor-less Speed Control of an Induction Motor with no Influence of Secondary Resistance Variation”, *IEEE Industry Application Society Annual Meeting*, 1993, Vol.1, pp. 408-413.

[51] Kim, YR; Sul, SK; Park, MH , “Speed Sensorless Vector Control of Induction-Motor using Extended Kalman Filter”, *IEEE Transactions on Industry Applications*, 1994, Vol.30, No. 5, pp. 1225-1233.

[52] Klaes, N.R., “Parameter Identification of an Induction Machine with Regard to Dependencies on Saturation”, *IEEE Transactions on Industry Applications*, 1993, Vol.29, No. 6, pp. 1135-1140.

[53] Koyama, M; Yano, M; Kamiyama, I; Yano, S , “Microprocessor-Based Vector Control-System for Induction-Motor Drives with Rotor Time Constant Identification Function”, *IEEE Transactions on Industry Applications*, 1986, Vol.22, No. 3, pp. 453-459.

[54] Kreindler, L; Moreira, JC; Testa, A; Lipo, TA , “Direct Field Orientation Controller using the Stator Phase Voltage 3rd Harmonic”, *IEEE Transactions on Industry Applications*, 1994, Vol.30, No. 2, pp. 441-447.

[55] Kubota, H. and Matsuse, K., “Speed Sensorless Field Oriented Control of Induction Motor with Rotor Resistance Adaption”, *IEEE Industry Applications Society Annual Meeting*, 1993, Vol.1, pp. 414-418.

[56] Kubota, H., Matsuse, K. and Nakano, T., “DSP-Based Speed Adaptive Flux Observer of Induction Motor”, *IEEE Transactions on Industry Applications*, 1993, Vol.29, No. 2, pp. 344-348.

[57] Lanczos, C., *Discourse on Fourier Series*. Hafner Publishing Co., New York, 1966.

[58] Landau, Y.D., *Adaptive Control: The Model Reference Approach*. Marcel Dekker Inc., 1979.

[59] Levi, E., “Magnetic Saturation in Rotor-Flux-Oriented Induction-Motor Drives. Operating Regimes, Consequences and Open-Loop Compensation”, *European Transactions on Electrical Power Engineering*, 1994, Vol.4, No. 4,, pp. 277-286.

[60] Loron, L. and Laliberte, G., “Application of the Extended Kalman Filter to Parameters Estimation of Induction Motors”, *Proceedings of the EPE Conference*, Brighton, 1993, Vol.5, pp. 85-90.

[61] Luenberger, D.G., “An Introduction to Observers”, *IEEE Transactions on Automatic Control*, 1971, Vol.Ac-16, No. 6, pp. 596-602.

[62] Matsuo, T; Blasko, V; Moreira, JC; Lipo, TA , “Field-Oriented Control of Induction Machines Employing Rotor End Ring Current Detection”, *IEEE Transactions on Power Electronics*, 1994, Vol.9, No. 6, pp. 638-645.

[63] Miyashita, I. and Ohmori, Y., “Improvement of Robustuness on Speed Sensorless Vector Control of Induction Motor Drives”, *Proceedings of the EPE Conference*, Firenze, 1991, Vol.4, pp. 660-665.

[64] Moreira, J.C. and Lipo, T.A., “A New Method for Rotor Time Constant Tuning in Indirect Field Oriented Control”, *IEEE Transactions on Industry Applications*, 1993, Vol.8, No. 4, pp. 626-631.

[65] Ohtani, T; Takada, N; Tanaka, K , “Vector Control of Induction-Motor Without Shaft Encoder”, *IEEE Transactions on Industry Applications*, 1992, Vol.28, No. 1, pp. 157-164.

[66] Peña, R.S., *State and Parameter Estimation for Induction Motor Drives using Kalman Filter*. MSc Dissertation, Dept. of Electrical and Electronic Engineering. University of Nottingham, 1992.

[67] Peng, F. and Fukao, T., “Robust Speed Identification for Speed Sensorless Vector Control of Induction Motors”, *IEEE Industry Applications Society Annual Meeting*, 1993, Vol.1, pp. 419-426.

[68] Profumo, F; Griva, G; Pastorelli, M; Moreira, J; DeDoncker, R , "Universal Field-Oriented Controller Based on Air-Gap Flux Sensing Via 3rd Harmonic Stator Voltage", *IEEE Transactions on Industry Applications*, 1994, Vol.30, No. 2, pp. 448-455.

[69] Renders, H., Schoukens, J. and Vilain, G., "High-Accuracy Spectrum Analysis of Sampled Discrete Frequency Signals by Analitical Leakage Compensation", *IEEE Transactions on Intrumentation and Measurement*, 1984, Vol.IM-33, No. 4, pp. 287-292.

[70] Rife, D.C. and Vincent, A, "Use of the Discrete Fourier Transform in the Measurement of Frequencies and Level of Tones", *Bell System Technical Journal*, 1970, Vol.49, No. 2, pp. 197-228.

[71] Rowan, TM; Kerkman, RJ; Leggate, D , "A Simple Online Adaption for Indirect Field Orientation of an Induction Machine", *IEEE Transactions on Industry Applications*, 1991, Vol.27, No. 4, pp. 720-727.

[72] Schauder, C., "Adaptive Speed Identification for Vector Control of Induction Motors Without Rotational Transducers", *IEEE Industry Applications Society Annual Meeting*, 1989, pp. 493-499.

[73] Schoukens, J., Pintelon, R. and Van Hamme, H., "The Interpolated Fast Fourier Transform: A Comparative Study", *IEEE Transactions on Instrumentation and Measurement*, 1992, Vol.41, No. 2, pp. 226-232.

[74] Schroedl, M., "Sensorless Control of Induction Motors at Low Speed and Standstill", *Proceedings ICEM '92*, 1992, pp. 863-867.

[75] Sorensen, H.V., Jones, D.L., Heideman, M.T. and Burrus, S., "Real-Valued Fast Fourier Transform Algorithms", *IEEE Transactions on Acoustics, Speech and Signal Processing*, 1987, Vol.ASSP-35, No. 6, pp. 849-863.

[76] Stein, E., "A Speed Sensing and Controlling System for Inverted Fed Induction Machine by Evaluating the Rotor Slot Harmonics", *Proceedings of the Electric Energy Conference*, Adelaide, 1987,.

[77] Stubener, D., *Analysis and Simulation of Adaptive Speed Estimators*. Studienarbeit, Dept. of Elec. Eng. University of Nottingham, 1995.

[78] Sumner, M. and Asher, G.M., “The Experimental Investigation of Multi-Parameter Identification Methods for Cage Induction Motors”, *Proceedings of the EPE Conference*, Florence, 1991, Vol.3, pp. 389-394.

[79] Sumner, M. and Asher, G.M. , “Autocommissioning for Voltage-Referenced Voltage-Fed Vector- controlled induction-Motor drives”, *IEE Proceedings-B Electric Power Applications*, 1993, Vol.140, No. 3, pp. 187-200.

[80] Sumner, M; and Asher, G.M., “PWM Induction Motor Drive Using the INMOS Transputer Parallel Processor”, *Proceedings of the APEC Conference*, New Orleans, 1988, pp. 121-129.

[81] Tajima, H; Hori, Y , “Speed Sensorless Field-Orientation Control of the Induction Machine”, *IEEE Transactions on Industry Applications*, 1993, Vol.29, No. 1, pp. 175-180.

[82] Tamai, S., Sugimoto H. and Yano, M., “Speed Sensor-Less Vector Control of Induction Motors with Model Reference Adaptive System”, *IEEE Industry Applications Society Annual Meeting*, 1987, pp. 189-195.

[83] Umanand, L; Bhat, SR , “Online Estimation of Stator Resistance of an Induction-Motor for Speed Control Applications”, *IEE Proceedings-Electric Power Applications*, 1995, Vol.142, No. 2, pp. 97-103.

[84] Vélez-Reyes, M., Minami, K. and Verghese, G.C., “Recursive Speed and Parameter Estimation for Induction Machines”, *IEEE Industry Applications Society Annual Meeting*, Denver, 1989, pp. 607-611.

[85] Wang, C.; Novotny, D.W. and Lipo, T.A., “An Automated Rotor Time Constant Measurement System for Indirect Field Orientated Drives”, *IEEE Transactions on Industry Applications*, 1988, Vol.24, pp. 151-159.

[86] Williams, B.W.; Goodfellow, J.K. and Green, T.C., “Sensorless Speed Measurement of Inverter Driven Squirrel Cage Induction Motors without Rotational Transducers”, *Proceedings of the 4th International Conference on Power Electronics and Variable Speed Drives*, 1990, pp. 297-300.

[87] Xu, X. and Novotny, D.W., “Implementation of Direct Stator Flux Orientation Control on a Versatile DSP Based System”, *IEEE Transactions on Industry Applications*, 1991, Vol.27, No. 4, pp. 694-700.

[88] Xue, Y., Xu, X., Habetler, T.G. and Divan, D.M., “A Stator Flux-Oriented Voltage Source Variable-Speed Drive Based on DC Link Measurement”, *IEEE Transactions on Industry Applications*, 1991, Vol.27, No.5, pp. 962-968.

[89] Yang, G., and Chin, T., “Adaptive-Speed Identification Scheme for a Vector-Controlled Speed Sensorless Inverter-Induction Motor Drive”, *IEEE Transactions on Industry Applications*, 1993, Vol.29, No.4, pp. 820-825.

[90] Zinger, D., Profumo, F., Lipo, T.A. and Novotny D.W., “A Direct Field Oriented Controller for Induction Motor Drives Using Tapped Stator Windings”, *Proceedings of the IEEE Power Electronics Specialists Conference*, Kyoto, 1988, pp. 855-861.